

ISSN 2667-4211

ESKİŞEHİR TECHNICAL UNIVERSITY
JOURNAL OF SCIENCE AND TECHNOLOGY
A – Applied Sciences and Engineering

Volume **25** Number **3** - September - **2024**



Volume: 25 / Number: 3 / June - 2024

Eskişehir Technical University Journal of Science and Technology A - Applied Sciences and Engineering (Other variant title: **Estuscience-Se**) is a peer-reviewed and refereed international journal published by Eskişehir Technical University. Since 2000, it has been regularly published and distributed biannually and it has been published quarterly and only electronically since 2016.

The journal accepts only manuscripts written in English.

The journal issues are published electronically in **March, June, September, and December**.

Eskişehir Technical University Journal of Science and Technology A - Applied Sciences and Engineering is an international peer-reviewed and refereed journal published by Eskişehir Technical University.

The journal is dedicated to the dissemination of knowledge in applied sciences and engineering disciplines.

The journal aims to publish high quality, original international scientific research articles with specific contributions to the literature in the field of engineering and applied sciences. The journal publishes research papers in the fields of applied science and technology such as Physics, Biology, Mathematics, Statistics, Chemistry and Chemical Engineering, Environmental Sciences and Engineering, Civil Engineering, Earth and Atmospheric Sciences, Electrical and Electronical Engineering, Computer Science and Informatics, Materials Sciences and Engineering, Mechanical Engineering, Mining Engineering, Industrial Engineering, Aeronautics and Astronautics, Pharmaceutical Sciences.

The journal publishes original research articles and special issue articles. All articles are peer-reviewed and the articles that have been evaluated are ensured to meet with researchers as soon as possible.

Eskişehir Technical University holds the copyright of all published material that appear in Eskişehir Technical University Journal of Science and Technology A - Applied Sciences and Engineering.

"Anadolu Üniversitesi Bilim ve Teknoloji Dergisi A - Uygulamalı Bilimler ve Mühendislik (Anadolu University Journal of Science and Technology A - Applied Sciences and Engineering)" published within Anadolu University started to be published within Eskişehir Technical University which was established due to statute law 7141, in 2018. Hence, the name of the journal is changed to " Eskişehir Technical University Journal of Science and Technology A - Applied Sciences and Engineering (Eskişehir Teknik Üniversitesi Bilim ve Teknoloji Dergisi A - Uygulamalı Bilimler ve Mühendislik)".

The Journal's Other Variant Title: **Estuscience-Se**; approved by ISSN National Centre for Türkiye on April 30, 2024.

Indexed by **ULAKBIM TR Dizin**,



ESKİŞEHİR TECHNICAL UNIVERSITY JOURNAL OF SCIENCE AND TECHNOLOGY

A- APPLIED SCIENCES AND ENGINEERING

Estuscience – Se



Volume: 25 / Number: 3 / September - 2024

Owner / Publisher: Prof. Dr. Adnan ÖZCAN for Eskişehir Technical University

EDITOR-IN-CHIEF

Prof. Dr. Semra KURAMA

Eskişehir Technical University, Institute of Graduate Programs, 26555 - Eskişehir, TURKEY

Phone: +90 222 213 7470

e-mail: skurama@eskisehir.edu.tr

CO-EDITOR IN CHIEF

Prof. Dr. Tahir Hikmet KARAKOÇ

Eskişehir Technical University, Faculty of Aeronautics and Astronautics, 26555 - Eskişehir, TURKEY

Phone: +90 222 213 8466

e-mail: hkarakoc@eskisehir.edu.tr

CO-EDITOR IN CHIEF

Assoc. Prof. Dr. Gülçin IŞIK

Eskişehir Technical University, Institute of Graduate Programs, 26555 - Eskişehir, TURKEY

Phone: +90 222-213 7472

e-mail: gulciny@eskisehir.edu.tr

CO-EDITOR IN CHIEF

Assit. Prof. Dr. Hüseyin Ersin EROL

Eskişehir Technical University, Institute of Graduate Programs, 26555 - Eskişehir, TURKEY

Phone: +90 222-213 7473

e-mail: heerol@eskisehir.edu.tr

CONTACT INFORMATION

Eskişehir Technical University Journal of Science and Technology

Eskişehir Technical University, Institute of Graduate Programs, 26555 Eskişehir, TURKEY

Phone: +90 222 213 7485

e-mail : btada@eskisehir.edu.tr



Volume: 25 / Number: 3 / September - 2024

OWNER

Adnan ÖZCAN, The Rector of Eskişehir Technical University

EDITORIAL BOARD

Semra KURAMA, Editor in Chief

T. Hikmet KARAKOÇ, Co-Editor in Chief

Gülçin IŞIK, Co-Editor in Chief

Hüseyin Ersin EROL, Co-Editor in Chief

LANGUAGE EDITOR-ENGLISH

Burcu ERDOĞAN

İlker DEMİROĞLU

SECTION EDITORS

Sibel AKAR (Eskişehir Osmangazi University, Turkey)
Ziya AKÇA (Eskişehir Osmangazi University, Turkey)
İpek AKIN (İstanbul Teknik University, Turkey)
Sema AKYALÇIN (ESTU, Turkey)
Mehmet ALEGÖZ (ESTU, Turkey)
Suna AVCIOĞLU (Yıldız Teknik University, Turkey)
Uğur AVDAN (ESTU, Turkey)
Zehra YİĞİT AVDAN (ESTU, Turkey)
Ayşe H. BİLGE (Kadir Has University, Turkey)
Müjdat ÇAĞLAR (ESTU, Turkey)
Çağatay DENGİZ (Ortadoğu Teknik University, Turkey)
Rasime DEMİREL (ESTU, Turkey)
Elif Begüm ELÇİOĞLU (ESTU, Turkey)
Barış ERBAŞ (ESTU, Turkey)
Hüseyin Ersin EROL (ESTU, Turkey)
Metin GENÇTEN (Yıldız Teknik University, Turkey)
Ömer Nezih GEREK (ESTU, Turkey)
Özer GÖK (ESTU, Turkey)
Cihan KALELİ (ESTU, Turkey)
Gordona KAPLAN (ESTU, Turkey)

T. Hikmet KARAKOÇ (ESTU, Turkey)
Elif KORUYUCU (ESTU, Turkey)
Semra KURAMA (ESTU, Turkey)
Hakan Ahmet NEFESLİOĞLU (ESTU, Turkey)
Anatoly NĪKANOV (Saratov State Technical University, Slovenia)
Murad OMAROV (Kharkiv National University of Radio Electronics, Ukraine)
Mehmet İnanç ONUR (ESTU, Turkey)
Seyhan ÖNDER (Eskişehir Osmangazi University, Turkey)
Zahide BAYER ÖZTÜRK (Nevşehir Hacı Bektaş Veli Univ., Turkey)
Emrah PEKKAN (ESTU, Turkey)
Najeeb REHMAN (Comsat University, Pakistan)
İsmail Hakkı SARPÜN (Akdeniz University, Turkey)
Aydın SİPAHİOĞLU (Eskişehir Osmangazi University, Turkey)
İlkin YÜCEL ŞENGÜN (Ege University, Turkey)
Sevil ŞENTÜRK (ESTU, Turkey)
Gülsüm TOPATEŞ (Ankara Yıldırım Beyazıt University Turkey)
Önder TURAN (ESTU, Turkey)
Muammer TÜN (ESTU, Turkey)
Fatma TÜRSEK (Eskişehir Osmangazi University, Turkey)
Berna ÜSTÜN (ESTU, Turkey)

Secretary/Typeset

Handan YİĞİT



Volume: 25 / Number: 3 / September - 2024

ABOUT

Eskişehir Technical University Journal of Science and Technology A - Applied Sciences and Engineering (Estuscience-Se) is a peer-reviewed and refereed international journal published by Eskişehir Technical University. Since 2000, it has been regularly published and distributed biannually and it has been published quarterly and only electronically since 2016.

The journal accepts only manuscripts written in English.

The journal issues are published electronically in **MARCH, JUNE, SEPTEMBER, and DECEMBER.**

AIM AND SCOPE

Eskişehir Technical University Journal of Science and Technology A - Applied Sciences and Engineering is an international peer-reviewed and refereed journal published by Eskişehir Technical University.

The journal is dedicated to the dissemination of knowledge in applied sciences and engineering disciplines.

The journal aims to publish high quality, original international scientific research articles with specific contributions to the literature in the field of engineering and applied sciences. The journal publishes research papers in the fields of applied science and technology such as Physics, Biology, Mathematics, Statistics, Chemistry and Chemical Engineering, Environmental Sciences and Engineering, Civil Engineering, Earth and Atmospheric Sciences, Electrical and Electronical Engineering, Computer Science and Informatics, Materials Sciences and Engineering, Mechanical Engineering, Mining Engineering, Industrial Engineering, Aeronautics and Astronautics, Pharmaceutical Sciences.

The journal publishes original research articles and special issue articles. All articles are peer-reviewed and the articles that have been evaluated are ensured to meet with researchers as soon as possible.

PEER REVIEW PROCESS

Manuscripts are first reviewed by the editorial board in terms of its its journal's style rules scientific content, ethics and methodological approach. If found appropriate, the manuscript is then send to at least two renown referees by editor. The decision in line with the referees may be an acceptance, a rejection or an invitation to revise and resubmit. Confidential review reports from the referees will be kept in archive. All submission process manage through the online submission systems.

OPEN ACCESS POLICY

This journal provides immediate open access to its content on the principle that making research freely available to the public supports a greater global exchange of knowledge. Copyright notice and type of licence : **CC BY-NC-ND**.

PRICE POLICY

Eskişehir Technical University Journal of Science and Technology A - Journal of Applied Sciences and Engineering is an English, peer-reviewed, scientific, free of charge open-access-based journal. The author is not required to pay any publication fees or article processing charges (APCs) for peer-review administration and management, typesetting, and open-access. Articles also receive Digital Object Identifiers (DOIs) from the CrossRef organization to ensure they are always available.

ETHICAL RULES

You can reach the Ethical Rules in our journal in full detail from the link below:

<https://dergipark.org.tr/en/pub/estubtda/policy>

Ethical Principles and Publication Policy

Policy & Ethics

Assessment and Publication

As a peer-reviewed journal, it is our goal to advance scientific knowledge and understanding. We have outlined a set of ethical principles that must be followed by all authors, reviewers, and editors.

All manuscripts submitted to our journals are pre-evaluated in terms of their relevance to the scope of the journal, language, compliance with writing instructions, suitability for science, and originality, by taking into account the current legal requirements regarding copyright infringement and plagiarism. Manuscripts that are evaluated as insufficient or non-compliant with the instructions for authors may be rejected without peer review.

Editors and referees who are expert researchers in their fields assess scientific manuscripts submitted to our journals. A blind peer review policy is applied to the evaluation process. The Editor-in-Chief, if he/she sees necessary, may assign an Editor for the manuscript or may conduct the scientific assessment of the manuscript himself/herself. Editors may also assign referees for the scientific assessment of the manuscript and make their decisions based on reports by the referees. Articles are accepted for publication on the understanding that they have not been published and are not going to be considered for publication elsewhere. Authors should certify that neither the manuscript nor its main contents have already been published or submitted for publication in another journal.

The Journal; Implements the Publication Policy and Ethics guidelines to meet high-quality ethical standards for authors, editors and reviewers:

Duties of Editors-in-Chief and co-Editors

The crucial role of the journal Editor-in-Chief and co-Editors is to monitor and ensure the fairness, timeliness, thoroughness, and civility of the peer-review editorial process. The main responsibilities of Editors-in-Chief are as follows:

- Selecting manuscripts suitable for publication while rejecting unsuitable manuscripts,
- Ensuring a supply of high-quality manuscripts to the journal by identifying important,
- Increasing the journal's impact factor and maintaining the publishing schedule,
- Providing strategic input for the journal's development,

Duties of Editors

The main responsibilities of editors are as follows:

- An editor must evaluate the manuscript objectively for publication, judging each on its quality without considering the nationality, ethnicity, political beliefs, race, religion, gender, seniority, or institutional affiliation of the author(s). Editors should decline any assignment when there is a potential for conflict of interest.
- Editors must ensure the document(s) sent to the reviewers does not contain information of the author(s) and vice versa.
- Editors' decisions should be provided to the author(s) accompanied by the reviewers' comments and recommendations unless they contain offensive or libelous remarks.
- Editors should respect requests (if well reasoned and practicable) from author(s) that an individual should not review the submission.
- Editors and all staff members should guarantee the confidentiality of the submitted manuscript.
- Editors should have no conflict of interest with respect to articles they reject/accept. They must not have a conflict of interest with the author(s), funder(s), or reviewer(s) of the manuscript.
- Editors should strive to meet the needs of readers and authors and to constantly improve the journal.

Duties of Reviewers/Referees

The main responsibilities of reviewers/referees are as follows:

- Reviewers should keep all information regarding papers confidential and treat them as privileged information.
- Reviews should be conducted objectively, with no personal criticism of the author.
- Reviewers assist in the editorial decision process and as such should express their views clearly with supporting arguments.
- Reviewers should complete their reviews within a specified timeframe (maximum thirty-five (35) days). In the event that a reviewer feels it is not possible for him/her to complete the review of the manuscript within a stipulated time, then this information must be communicated to the editor so that the manuscript could be sent to another reviewer.
- Unpublished materials disclosed in a submitted manuscript must not be used in a reviewer's personal research without the written permission of the author. Information contained in an unpublished manuscript will remain confidential and must not be used by the reviewer for personal gain.
- Reviewers should not review manuscripts in which they have conflicts of interest resulting from competitive, collaborative, or other relationships or connections with any of the authors, companies, or institutions connected to the papers.

- Reviewers should identify similar work in published manuscripts that has not been cited by the author. Reviewers should also notify the Editors of significant similarities and/or overlaps between the manuscript and any other published or unpublished material.

Duties of Authors

The main responsibilities of authors are as follows:

- The author(s) should affirm that the material has not been previously published and that they have not transferred elsewhere any rights to the article.
- The author(s) should ensure the originality of the work and that they have properly cited others' work in accordance with the reference format.
- The author(s) should not engage in plagiarism or in self-plagiarism.
- On clinical and experimental humans and animals, which require an ethical committee decision for research in all branches of science;

All kinds of research carried out with qualitative or quantitative approaches that require data collection from the participants by using survey, interview, focus group work, observation, experiment, interview techniques,

Use of humans and animals (including material/data) for experimental or other scientific purposes,

- Clinical studies on humans,
- Studies on animals,
- Retrospective studies in accordance with the law on the protection of personal data, (Ethics committee approval should have been obtained for each individual application, and this approval should be stated and documented in the article.)

Information about the permission (board name, date, and number) should be included in the "Method" section of the article and also on the first/last page.

During manuscript upload, the "Ethics Committee Approval" file should be uploaded to the system in addition to the manuscript file.

In addition, in case reports, it is necessary to include information on the signing of the informed consent/ informed consent form in the manuscript.

- The author(s) should suggest no personal information that might make the identity of the patient recognizable in any form of description, photograph, or pedigree. When photographs of the patient were essential and indispensable as scientific information, the author(s) have received consent in written form and have clearly stated as much.
- The author(s) should provide the editor with the data and details of the work if there are suspicions of data falsification or fabrication. Fraudulent data shall not be tolerated. Any manuscript with suspected fabricated or falsified data will not be accepted. A retraction will be made for any publication which is found to have included fabricated or falsified data.
- The author(s) should clarify everything that may cause a conflict of interests such as work, research expenses, consultant expenses, and intellectual property.
- The author(s) must follow the submission guidelines of the journal.
- The author(s) discover(s) a significant error and/or inaccuracy in the submitted manuscript at any time, then the error and/or inaccuracy must be reported to the editor.
- The author(s) should disclose in their manuscript any financial or other substantive conflicts of interest that might be construed to influence the results or interpretation of their manuscript. All sources of financial support should be disclosed under the heading of "Acknowledgment" or "Contribution".
- The corresponding author(s) must ensure that all appropriate co-authors are not included in the manuscript, that author names are not added or removed and that the authors' address information is not changed after the review begins and that all co-authors see and approve the

final version of the manuscript at every stage of the manuscript. All significant contributors should be listed as co-authors. Other individuals who have participated in significant aspects of the research work should be considered contributors and listed under “Author Contribution”.

Cancellations/Returns

Articles/manuscripts may be returned to the authors in order to increase the authenticity and/or reliability and to prevent ethical breaches, and even if articles have been accepted and/or published, they can be withdrawn from publication if necessary. The Editor-in-Chief of the journal has the right to return or withdraw an article/manuscript in the following situations:

- When the manuscript is not within the scope of the journal,
- When the scientific quality and/or content of the manuscript do not meet the standards of the journal and a referee review is not necessary,
- When there is proof of ruling out the findings obtained by the research, (When the article/manuscript is undergoing an assessment or publication process by another journal, congress, conference, etc.,)
- When the article/manuscript was not prepared in compliance with scientific publication ethics,
- When any other plagiarism is detected in the article/manuscript,
- When the authors do not perform the requested corrections within the requested time (maximum twenty-one (21) days),
- When the author does not submit the requested documents/materials/data etc. within the requested time,
- When the requested documents/materials/data etc. submitted by the author are missing for the second time,
- When the study includes outdated data,
- When the authors make changes that are not approved by the editor after the manuscript was submitted,
- When an author is added/removed, the order of the authors is changed, the corresponding author is altered, or the addresses of the authors are changed in the article that is in the evaluation process,
- When a statement is not submitted indicating that approval of the ethics committee permission was obtained for the following (including retrospective studies):
- When human rights or animal rights are violated,

ETHICAL ISSUES

Plagiarism

The use of someone else’s ideas or words without a proper citation is considered plagiarism and will not be tolerated. Even if a citation is given, if quotation marks are not placed around words taken directly from other authors’ work, the author is still guilty of plagiarism. Reuse of the author’s own previously published words, with or without a citation, is regarded as self-plagiarism.

All manuscripts received are submitted to iThenticate®, which compares the content of the manuscript with a database of web pages and academic publications. Manuscripts are judged to be plagiarized or self-plagiarized, based on the iThenticate® report or any other source of information, will be rejected. Corrective actions are proposed when plagiarism and/or self-plagiarism is detected after publication. Editors should analyze the article and decide whether a corrected article or retraction needs to be published.

Open-access theses are considered as published works and they are included in the similarity checks.

iThenticate® report should have a maximum of 11% from a single source, and a maximum of 25% in total.

Conflicts of Interest

Eskişehir Technical University Journal of Science and Technology A - Applied Sciences and Engineering should be informed of any significant conflict of interest of editors, authors, or reviewers to determine whether any action would be appropriate (e.g. an author's statement of conflict of interest for a published work, or disqualifying a referee).

Financial

The authors and reviewers of the article should inform the journal about the financial information that will bring financial gain or loss to any organization from the publication of the article.

*Research funds; funds, consulting fees for a staff member; If you have an interest, such as patent interests, you may have a conflict of interest that needs to be declared.

Other areas of interest

The editor or reviewer may disclose a conflict of interest that, if known, would be embarrassing (for example, an academic affiliation or rivalry, a close relationship or dislike, or a person who may be affected by the publication of the article).

Conflict of interest statement

Please note that a conflict of interest statement is required for all submitted manuscripts. If there is no conflict of interest, please state “There are no conflicts of interest to declare” in your manuscript under the heading “Conflicts of Interest” as the last section before your Acknowledgments.

AUTHOR GUIDELINES

All manuscripts must be submitted electronically.

You will be guided stepwise through the creation and uploading of the various files. There are no page charges. Papers are accepted for publication on the understanding that they have not been published and are not going to be considered for publication elsewhere. Authors should certify that neither the manuscript nor its main contents have already been published or submitted for publication in another journal. We ask a signed copyright to start the evaluation process. After a manuscript has been submitted, it is not possible for authors to be added or removed or for the order of authors to be changed. If authors do so, their submission will be cancelled.

Manuscripts may be rejected without peer review by the editor-in-chief if they do not comply with the instructions to authors or if they are beyond the scope of the journal. After a manuscript has been accepted for publication, i.e. after referee-recommended revisions are complete, the author will not be permitted to make any changes that constitute departures from the manuscript that was accepted by the editor. Before publication, the galley proofs are always sent to the authors for corrections. Mistakes or omissions that occur due to some negligence on our part during final printing will be rectified in an errata section in a later issue.

This does not include those errors left uncorrected by the author in the galley proof. The use of someone else's ideas or words in their original form or slightly changed without a proper citation is considered plagiarism and will not be tolerated. Even if a citation is given, if quotation marks are not placed around words taken directly from another author's work, the author is still guilty of plagiarism. All manuscripts received are submitted to iThenticateR, a plagiarism checking system, which compares the content of the manuscript with a vast database of web pages and academic publications. In the received iThenticateR report; The similarity rate is expected to be below 25%. Articles higher than this rate will be rejected.

Uploading Articles to the Journal

Authors should prepare and upload 2 separate files while uploading articles to the journal. First, the Author names and institution information should be uploaded so that they can be seen, and then (using the additional file options) a separate file should be uploaded with the Author names and institution information completely closed. When uploading their files with closed author names, they will select the "Show to Referee" option, so that the file whose names are closed can be opened to the referees.

Preparation of Manuscript

Style and Format

Manuscripts should be **single column** by giving one-spaced with 2.5-cm margins on all sides of the page, in Times New Roman font (font size 11). Every page of the manuscript, including the title page, references, tables, etc., should be numbered. All copies of the manuscript should also have line numbers starting with 1 on each consecutive page.

Manuscripts must be upload as word document (*.doc, *.docx vb.). **Please avoid uploading texts in *.pdf format.**

Symbols, Units and Abbreviations

Standard abbreviations and units should be used; SI units are recommended. Abbreviations should be defined at first appearance, and their use in the title and abstract should be avoided. Generic names of chemicals should be used. Genus and species names should be typed in italic or, if this is not available, underlined.

Please refer to equations with capitalisation and unabbreviated (e.g., as given in Equation (1)).

Manuscript Content

Articles should be divided into logically ordered and numbered sections. Principal sections should be numbered consecutively with Arabic numerals (1. Introduction, 2. Formulation of problem, etc.) and subsections should be numbered 1.1., 1.2., etc. Do not number the Acknowledgements or References sections. The text of articles should be, if possible, divided into the following sections: Introduction, Materials and Methods (or Experimental), Results, Discussion, and Conclusion.

Title and contact information

The first page should contain the full title in sentence case (e.g., Hybrid feature selection for text classification), the full names (last names fully capitalised) and affiliations (in English) of all authors (Department, Faculty, University, City, Country, E-mail), and the contact e-mail address for the clearly identified corresponding author. The first page should contain the full title, abstract and keywords (both English and Turkish).

Abstract

The abstract should provide clear information about the research and the results obtained, and should not exceed 300 words. The abstract should not contain citations and must be written in Times New Roman font with font size 9.

Keywords

Please provide 3 to 5 keywords which can be used for indexing purposes.

Introduction

The motivation or purpose of your research should appear in the “Introduction”, where you state the questions you sought to answer, and then provide some of the historical basis for those questions.

Methods

Provide sufficient information to allow someone to repeat your work. A clear description of your experimental design, sampling procedures, and statistical procedures is especially important in papers describing field studies, simulations, or experiments. If you list a product (e.g., animal food, analytical device), supply the name and location of the manufacturer. Give the model number for equipment used.

Results

Results should be stated concisely and without interpretation.

Discussion

Focus on the rigorously supported aspects of your study. Carefully differentiate the results of your study from data obtained from other sources. Interpret your results, relate them to the results of previous research, and discuss the implications of your results or interpretations.

Conclusion

This should state clearly the main conclusions of the research and give a clear explanation of their importance and relevance. Summary illustrations may be included.

Acknowledgments

Acknowledgments of people, grants, funds, etc. should be placed in a separate section before the reference list. The names of funding organizations should be written in full.

Conflict of Interest Statement

The authors are obliged to present the conflict of interest statement at the end of the article after the acknowledgments section.

CRediT Author Statement

Write the authors' contributions in detail using the specified CRediT notifications. Authors may have contributed in more than one role. The corresponding author is responsible for ensuring that descriptions are accurate and accepted by all authors.

CRediT Notifications	Explanation
Conceptualization	Ideas; formulation or evolution of overarching research goals and aims
Methodology	Development or design of methodology; creation of models
Software	Programming, software development; designing computer programs; implementation of the computer code and supporting algorithms; testing of existing code components

Validation	Verification, whether as a part of the activity or separate, of the overall replication/ reproducibility of results/experiments and other research outputs
Formal analysis	Application of statistical, mathematical, computational, or other formal techniques to analyse or synthesize study data
Investigation	Conducting a research and investigation process, specifically performing the experiments, or data/evidence collection
Resources	Provision of study materials, reagents, materials, patients, laboratory samples, animals, instrumentation, computing resources, or other analysis tools
Data Curation	Management activities to annotate (produce metadata), scrub data and maintain research data (including software code, where it is necessary for interpreting the data itself) for initial use and later reuse
Writing – Original Draft	Preparation, creation and/or presentation of the published work, specifically writing the initial draft (including substantive translation)
Writing – Review & Editing	Preparation, creation and/or presentation of the published work by those from the original research group, specifically critical review, commentary, or revision – including pre-or post-publication stages
Visualization	Preparation, creation and/or presentation of the published work, specifically visualization/ data presentation
Supervision	Oversight and leadership responsibility for the research activity planning and execution, including mentorship external to the core team
Project administration	Management and coordination responsibility for the research activity planning and execution
Funding acquisition	Acquisition of the financial support for the project leading to this publication

References

Writing Style; **AMA; References Writing format** should be used in the reference writing of our journal. If necessary, at this point, the reference writings of the articles published in our article can be examined.

Citations in the text should be identified by numbers in square brackets. The list of references at the end of the paper should be given in order of their first appearance in the text. All authors should be included in reference lists unless there are 10 or more, in which case only the first 10 should be given, followed by ‘et al.’. Do not use individual sets of square brackets for citation numbers that appear together, e.g., [2,3,5–9], not [2], [3], [5]–[9]. Do not include personal communications, unpublished data, websites, or other unpublished materials as references,

although such material may be inserted (in parentheses) in the text. In the case of publications in languages other than English, the published English title should be provided if one exists, with an annotation such as “(article in Turkish with an abstract in English)”. If the publication was not published with an English title, cite the original title only; do not provide a self-translation. References should be formatted as follows (please note the punctuation and capitalisation):

Journal articles

Journal titles should be abbreviated according to ISI Web of Science abbreviations.

Guyon I, Elisseeff A. An introduction to variable and feature selection. *J Mach Learn Res* 2003; 3: 1157-1182.

Izadpanahi S, Ozcinar C, Anbarjafari G, Demirel H. Resolution enhancement of video sequences by using discrete wavelet transform and illumination compensation. *Turk J Elec Eng & Comp Sci* 2012; 20: 1268-1276.

Books

Haupt RL, Haupt SE. *Practical Genetic Algorithms*. 2nd ed. New York, NY, USA: Wiley, 2004.
Kennedy J, Eberhart R. *Swarm Intelligence*. San Diego, CA, USA: Academic Press, 2001.

Chapters in books

Poore JH, Lin L, Eschbach R, Bauer T. Automated statistical testing for embedded systems. In: Zander J, Schieferdecker I, Mosterman PJ, editors. *Model-Based Testing for Embedded Systems*. Boca Raton, FL, USA: CRC Press, 2012. pp. 111-146.

Conference proceedings

Li RTH, Chung SH. Digital boundary controller for single-phase grid-connected CSI. In: *IEEE 2008 Power Electronics Specialists Conference*; 15–19 June 2008; Rhodes, Greece. New York, NY, USA: IEEE. pp. 4562-4568.

Theses

Boynukalin Z. *Emotion analysis of Turkish texts by using machine learning methods*. MSc, Middle East Technical University, Ankara, Turkey, 2012.

Tables and Figures

All illustrations (photographs, drawings, graphs, etc.), not including tables, must be labelled “Figure.” Figures must be submitted in the manuscript.

All tables and figures must have a caption and/or legend and be numbered (e.g., Table 1, Figure 2), unless there is only one table or figure, in which case it should be labelled “Table” or “Figure” with no numbering. Captions must be written in sentence case (e.g., Macroscopic appearance of the samples.). The font used in the figures should be Times New Roman. If symbols such as \times , μ , η , or v are used, they should be added using the Symbols menu of Word.

All tables and figures must be numbered consecutively as they are referred to in the text. Please refer to tables and figures with capitalisation and unabbreviated (e.g., “As shown in Figure 2...”, and not “Fig. 2” or “figure 2”).

The resolution of images should not be less than 118 pixels/cm when width is set to 16 cm. Images must be scanned at 1200 dpi resolution and submitted in jpeg or tiff format. Graphs and diagrams must be drawn with a line weight between 0.5 and 1 point. Graphs and diagrams with

a line weight of less than 0.5 point or more than 1 point are not accepted. Scanned or photocopied graphs and diagrams are not accepted.

Figures that are charts, diagrams, or drawings must be submitted in a modifiable format, i.e. our graphics personnel should be able to modify them. Therefore, if the program with which the figure is drawn has a “save as” option, it must be saved as *.ai or *.pdf. If the “save as” option does not include these extensions, the figure must be copied and pasted into a blank Microsoft Word document as an editable object. It must not be pasted as an image file (tiff, jpeg, or eps) unless it is a photograph.

Tables and figures, including caption, title, column heads, and footnotes, must not exceed 16 × 20 cm and should be no smaller than 8 cm in width. For all tables, please use Word’s “Create Table” feature, with no tabbed text or tables created with spaces and drawn lines. Please do not duplicate information that is already presented in the figures.

Article Corrections and Uploading to the System

Authors should upload the desired edits for their articles without destroying or changing the Template file of the article, by selecting and specifying the relevant edits as Colored, and also submit the Clean version of the article in 2 separate files (using the Additional file option if necessary). * In case of submitting a corrected article, a separate File in Reply to the Referees must be prepared and the "Reply to the Referees" option in the Add additional file option should be checked and uploaded. If a separate file is not prepared in response to the referees, the Author will definitely be asked to upload the relevant file again and the evaluation will be in the pending phase.

CONTENTS

RESEARCH ARTICLE


AN ALGEBRAIC APPROACH FOR REFINED NEUTROSOPHIC RANDOM VARIABLES <i>A. Hatip</i>	331
MXENE 2D Ti₃C₂T_x PRODUCTION AND SPIN-ORBIT EFFECT (SOI) OF Ti₃C₂(OH)₂ IN THE ELECTRONIC STRUCTURE <i>M. R. Ekici, H. Y. Uzunok, E. Bulut, H. M. Tütüncü, A. Atasoy</i>	341
EFFICIENT DRUG CARRIER FOR ACETYLSALICYLIC ACID FROM CHITOSAN-BASED COMPOSITES PREPARED WITH MONTMORILLONITE, CELLULOSE AND HYDROXYAPATITE <i>D. Sezer, Z. Aktaş, S. Hoşgün, E. Z. Hoşgün, B. Bozan</i>	368
LAMBERT AZIMUTHAL EQUAL-AREA PROJECTION <i>E. Öztürk</i>	380
DETERMINATION OF DEEP RED REMOVAL POTENTIAL OF ACTIVATED CARBON PRODUCED FROM WHEAT BRAN <i>İ. Demiral, C. Şamdan, F. B.Kus</i>	390
FIBONACCI AND LUCAS NUMBERS AS PRODUCTS OF THEIR ARBITRARY TERMS <i>A. Daşdemir, A. Emin</i>	407
PRODUCTIVITY, EFFICIENCY AND ENTREPRENEURIAL - INNOVATIVE UNIVERSITY INDEX: AN ANALYSIS FOR UNIVERSITIES IN TÜRKİYE <i>İ. Yenilmez</i>	415
MULTI-LEVEL CLASSIFICATION BASED ON DEEP LEARNING FOR ACCURATE RISK STRATIFICATION OF ARRHYTHMIAS <i>E. Ş. Sadık</i>	427
END-TO-END AUTOMATIC MUSIC TRANSCRIPTION OF POLYPHONIC QANUN AND OUD MUSIC USING DEEP NEURAL NETWORK <i>E. Germen, C. Karadoğan</i>	442
IMPACT OF THE OBJECTIVE ATTRIBUTE WEIGHTING ON FIVE POPULAR MULTI-CRITERIA DECISION-MAKING METHODS: AN EMPIRICAL STUDY <i>H. Merkepçi</i>	456
NUMERICAL SOLUTIONS OF BOUSSINESQ TYPE EQUATIONS BY MESHLESS METHODS <i>M. Ari, Y. Dereli</i>	471
GEOMETRIC PATTERN OF POWERS OF THREE VIA SIERPINSKI TRIANGULAR NUMBERS <i>T. Ermiş</i>	485
AN ANALYSIS ON THE USE OF MODIFIED EXPANDED PERLITE AND PUMICE IN INORGANIC BONDED FIBROUS COMPOSITE BOARDS <i>L. Gündüz, Ş. O. Kalkan</i>	490
SOME GEOMETRIC STRUCTURES RELATED TO DESARGUES CONFIGURATION IN PG(2,5) <i>E. Altuntaş Kahrıman, A. Bayar</i>	511



RESEARCH ARTICLE

AN ALGEBRAIC APPROACH FOR REFINED NEUTROSOPHIC RANDOM VARIABLES

Ahmed HATİP^{1,*}

¹ Department of Mathematics, Faculty of Arts and Sciences, University of Gaziantep, Gaziantep, Türkiye
kollnaar5@gmail.com -  [0000-0001-9132-9845](https://orcid.org/0000-0001-9132-9845)

Abstract

In this article, we are going to extend the definition of literal neutrosophic random variables to literal refined neutrosophic random variables and we will study its new properties. We derive and present various concepts including refined neutrosophic probability distribution function in the continuous case, refined neutrosophic cumulative distribution function of continuous refined neutrosophic random variables, refined neutrosophic expected value, refined neutrosophic variance, refined neutrosophic standard deviation, refined neutrosophic mean deviation, refined neutrosophic r^{th} quartiles, refined neutrosophic moments generating function, and refined neutrosophic characteristic function. Additionally, the paper includes many solved examples and applications. This paper opens the road to generalizing many concepts in neutrosophic probability theory specially neutrosophic reliability theory, neutrosophic stochastic processes, and neutrosophic queuing theory.

Keywords

Refined neutrosophic expected value,
Refined neutrosophic variance,
Refined standard neutrosophic deviation,
Refined neutrosophic probability density function,
Refined neutrosophic cumulative distribution

Time Scale of Article

Received :26 August 2023
Accepted : 28 August 2024
Online date : 30 September 2024

1. INTRODUCTION

Neutrosophic field of reals is a generalization of classical field reals adding an indeterminacy element(I), where $I^2 = I$, $I^n = I$; $n \in N$ and I^{-1} is undefined [1, 2]. Neutrosophic has been applied in many areas, such as decision-making [3, 4], artificial intelligence and machine learning [5, 6], intelligent disease diagnosis [7, 8], communication services [9], artificial pattern recognition [10], e-learning [11], physics [12, 13], and more.

In [14], the single-valued neutrosophic probability was introduced by F. Smarandache as a function $P_N: X \rightarrow [0,1]^3$ where X is a space that contains indeterminant components, i.e., neutrosophic sample space and defined the neutrosophic probability function of event A by $P_N(A) = (T(A), I(neutA), F(antiA)) = (T, I, F)$ where $0 \leq T, I, F \leq 1$ and $0 \leq T + I + F \leq 3$. Many other studies depended on the definition that assumes a neutrosophic distribution function is a function whose parameters contain indeterminacy (see [15])

Researchers have explored the foundation of neutrosophic queueing theory as a branch of neutrosophic stochastic modeling, as discussed in [16, 17]. Furthermore, researchers presented many concepts related to neutrosophic probability theory and its applications in [18]. Additionally, they have researched neutrosophic time series prediction and modeling in various scenarios, including neutrosophic moving averages, neutrosophic logarithmic models, neutrosophic linear models, and more, as presented in [19-

*Corresponding Author: kollnaar5@gmail.com

21]. These studies contribute to advancing understanding and utilizing neutrosophic principles in stochastic modeling.

Agboola proposed the idea of refined neutrosophic algebraic structures and specifically investigated refined neutrosophic groups in [22]. Since then, numerous researchers in the field of neutrosophic logic have explored and analyzed various refined neutrosophic algebraic structures. Adeleke et al. investigated refined neutrosophic rings and refined neutrosophic subrings, presenting their fundamental properties in [23]. Additionally, in [24], Adeleke et al. studied refined neutrosophic ideals and refined neutrosophic homomorphisms, providing an exploration of their basic properties.

In this research, by incorporating an indeterminacy component, we propose a generalization of classical random variables to handle imprecision, uncertainty, ambiguity, vagueness, and enigmatic aspects. This leads to the introduction of refined neutrosophic random variables. We explore various characteristics of these refined neutrosophic random variables, such as refined expected value, refined variance, refined standard deviation, refined moments generating function, and refined characteristic function. Furthermore, we investigate the properties associated with these characteristics

2. PRELIMINARIES

This section provides some definitions of neutrosophic logic and neutrosophic probability. Preliminaries
Definition 2.1. [25] Let $X \neq \Phi$ be. A neutrosophic set $NS(A)$ it can be defined by its elements with triples of the form $\{x, (T_{NS(A)}(x), I_{NS(A)}(x), F_{NS(A)}(x)): x \in X\}$, where $T_{NS(A)}$, $I_{NS(A)}(x)$ and $F_{NS(A)}(x)$ represent the degree of membership, degree of indeterminacy, and degree of non-membership, respectively, of each element $x \in X$ to the set $NS(A)$.

Definition 2.2. [26] Let F be a field, the neutrosophic field $NS(F)$ is a field that is generated by $\langle F \cup I \rangle$ and we usually denote it by $NS(F) = \langle F \cup I \rangle$.

Definition 2.3. [27] The literal neutrosophic number has the form $X(I) = x + \alpha I$ where x, α are real or complex numbers, and I is an algebraic element that satisfies $0 \cdot I = 0$ and $I^2 = I$.

Definition 2.4. [14] The single-valued neutrosophic probability of event A is $P_N(A) = (T(A), I(neutA), F(antiA))$ where T, I, F take its values in $[0,1]$.

Definition 2.5. [22] Let $(X(I_1, I_2), +, \cdot)$ be a refined neutrosophic field where $+$ and \cdot are ordinary addition and multiplication respectively we call I_1, I_2 the split indeterminacy elements of the original indeterminacy I where $I = \alpha I_1 + \beta I_2$ and $\alpha, \beta \in R$. Moreover, I_1 and I_2 preserve the following: $I_1^2 = I_1, I_2^2 = I_2$ and $I_1 I_2 = I_2 I_1 = I_1$.

For any two elements, we define

$$i. X(I_1, I_2) + Y(I_1, I_2) = x + \alpha I_1 + \beta I_2 + y + \alpha^* I_1 + \beta^* I_2 = x + y + (\alpha + \alpha^*) I_1 + (\beta + \beta^*) I_2$$

$$ii. X(I_1, I_2) \cdot Y(I_1, I_2) = (x + \alpha I_1 + \beta I_2) \cdot (y + \alpha^* I_1 + \beta^* I_2) = x \cdot y + (x\alpha^* + \alpha y + \alpha\alpha^* + \alpha\beta^* + \beta\alpha^*) I_1 + (x\beta^* + \beta y + \beta\beta^*) I_2.$$

Definition 2.6. [28] The square root of a refined neutrosophic positive real number can be computed and defined as follows:

$$\sqrt{X(I_1, I_2)} = \sqrt{x + \alpha I_1 + \beta I_2} = \sqrt{x} + (\sqrt{x + \alpha + \beta} - \sqrt{x + \alpha})$$

3. ON THE REFINED NEUTROSOPHIC RANDOM VARIABLES

In this section, we are going to generalize the previous definition of neutrosophic random variables to the concept of refined neutrosophic random variables taking into consideration that I is split into I_1 and I_2 .

Definition 3.1. Refined Neutrosophic Random Variable

Take the classical random variable X defined on Ω the events space as follows:

$$X: \Omega \rightarrow R$$

We will define refined-neutrosophic random variable NX as follows:

$$NX: \Omega \rightarrow R(I_1, I_2)$$

and

$$NX = X + \alpha I_1 + \beta I_2$$

where I_1 and I_2 are the split components of the original indeterminacy I .

Theorem 3.2. PDF and CDF of Refined Neutrosophic Random Variables

We here prove that NCDF(Neutrosophic Cumulative distribution function) of a refined-neutrosophic random variable and NPDF(Neutrosophic Probability Density Functions), respectively, are as follows:

$$F_{NX}(x) = F_X(x - (\alpha I_1 + \beta I_2))$$

$$f_{NX}(x) = f_X(x - (\alpha I_1 + \beta I_2))$$

PROOF.

$$F_{NX}(x) = P(NX \leq x) = P(X + \alpha I_1 + \beta I_2 \leq x) = P(X \leq x - (\alpha I_1 + \beta I_2)) = F_X(x - (\alpha I_1 + \beta I_2))$$

and taking the derivative to the last equation concerning x we find:

$$f_{NX}(x) = \frac{dF_{NX}(x)}{dx} = \frac{dF_X(x - (\alpha I_1 + \beta I_2))}{dx} \cdot \frac{d(x - (\alpha I_1 + \beta I_2))}{dx} = f_X(x - (\alpha I_1 + \beta I_2))$$

Theorem 3.3. The Expectation of Refined-Neutrosophic Random Variable

The expectation of refined-neutrosophic random variable $NX = X + \alpha I_1 + \beta I_2$ is:

$$E(NX) = E(X) + \alpha I_1 + \beta I_2$$

PROOF.

Here, in the continuous case, we have:

$$E(NX) = E(X + \alpha I_1 + \beta I_2)$$

$$= \int_x (x + \alpha I_1 + \beta I_2) f(x) dx$$

$$= \int_x x f(x) dx + (\alpha I_1 + \beta I_2) \int_x f(x) dx$$

$$= E(X) + \alpha I_1 + \beta I_2$$

where $\int_x f(x) dx = 1$.

In discrete case:

$$E(NX) = E(X + \alpha I_1 + \beta I_2)$$

$$= \sum_x (x + \alpha I_1 + \beta I_2) f(x)$$

$$= \sum_x x f(x) + (\alpha I_1 + \beta I_2) \sum_x f(x)$$

$$= E(X) + \alpha I_1 + \beta I_2$$

where $\sum_x f(x) = 1$.

Proposition 3.4.

i. $E(aNX + b + \alpha I_1 + \beta I_2) = aE(NX) + b + \alpha I_1 + \beta I_2 ; a, \alpha, \beta \in R$

ii. If NX, NY are two refined-neutrosophic random variables, then

$$E(NX \pm NY) = E(NX) \pm E(NY)$$

iii. $E[(a + \alpha I_1 + \beta I_2)NX] = E(aV + (\alpha I_1 + \beta I_2)NX) = E(aNX) + E((\alpha I_1 + \beta I_2)NX)$
 $= aE(NX) + (\alpha I_1 + \beta I_2) E(NX) ; a, \alpha, \beta \in R$

iv. $|E(NX)| \leq E|NX|$

PROOF.

If NX is continuous:

$$|E(NX)| = \left| \int_x (x + \alpha I_1 + \beta I_2) f(x) dx \right| \leq \int_x |(x + \alpha I_1 + \beta I_2)| f(x) dx = E|NX|$$

where $|f(x)| = f(x)$ since it is a positive function. If NX is discrete:

$$|E(NX)| = \left| \sum_x (x + \alpha I_1 + \beta I_2) f(x) \right| \leq \sum_x |(x + \alpha I_1 + \beta I_2)| f(x) = E|NX|$$

Definition 3.5. The Variance of a refined-neutrosophic random variable

A variance of refined-neutrosophic variables is:

$$V(NX) = V(X)$$

Here, we can always write:

$$V(NX) = E[NX - E(NX)]^2 = E[X + \alpha I_1 + \beta I_2 - E(X) - (\alpha I_1 + \beta I_2)]^2 = E[X - E(X)]^2 = V(X)$$

Example 3.6. Let X be a classical random variable defined by its pdf as follows:

$$f_X(x) = 2x; 0 \leq x \leq 1$$

i. Find a PDF of $NX = X + \alpha I_1 + \beta I_2$ and prove that it's a density function.

$$f_{NX}(x) = f_X(x - (\alpha I_1 + \beta I_2)) = 2(x - (\alpha I_1 + \beta I_2)); 0 \leq x - (\alpha I_1 + \beta I_2) \leq 1$$

$$f_{X_N}(x) = 2x - 2(\alpha I_1 + \beta I_2); \alpha I_1 + \beta I_2 \leq x \leq 1 + \alpha I_1 + \beta I_2$$

Prove that $f_{NX}(x)$ is a density function

$$\int_{\alpha I_1 + \beta I_2}^{1 + \alpha I_1 + \beta I_2}$$

$$\begin{aligned} \int_{\alpha I_1 + \beta I_2}^{1 + \alpha I_1 + \beta I_2} (2x - 2(\alpha I_1 + \beta I_2)) dx &= [x^2 - 2(\alpha I_1 + \beta I_2)x] \Big|_{\alpha I_1 + \beta I_2}^{1 + \alpha I_1 + \beta I_2} \\ &= (1 + \alpha I_1 + \beta I_2)^2 - 2(\alpha I_1 + \beta I_2)(1 + \alpha I_1 + \beta I_2) \\ &\quad - (\alpha I_1 + \beta I_2)^2 \\ &\quad + 2(\alpha I_1 + \beta I_2)^2 \\ &= 1 + (\alpha I_1 + \beta I_2)^2 + 2(\alpha I_1 + \beta I_2) - 2(\alpha I_1 + \beta I_2) \\ &\quad - 2(\alpha I_1 + \beta I_2)^2 \\ &\quad - (\alpha I_1 + \beta I_2)^2 + 2(\alpha I_1 + \beta I_2)^2 \\ &= 1 \end{aligned}$$

ii. Find the refined expected value of NX .

$$E(NX) = E(X) + \alpha I_1 + \beta I_2 = \int_0^1 2x^2 dx + \alpha I_1 + \beta I_2 = \frac{2}{3} + \alpha I_1 + \beta I_2$$

iii. Find the refined variance of NX .

$$V(NX) = V(X) = \int_0^1 \left(x - \frac{2}{3}\right)^2 2x dx = \frac{1}{18}$$

Theorem 3.7. The Mean deviation of a refined-neutrosophic random variable

The mean deviation of refined-neutrosophic random or $M.D(NX)$ is:

$$M.D(NX) = M.D(X) = E|X - E(X)|$$

PROOF.

$$\begin{aligned} M.D(NX) &= E|X_N - E(NX)| \\ &= E|X + \alpha I_1 + \beta I_2 - E(X + \alpha I_1 + \beta I_2)| \\ &= E|X + \alpha I_1 + \beta I_2 - E(X) - \alpha I_1 - \beta I_2| \\ &= M.D(X) \end{aligned}$$

Definition 3.8. The r^{th} quartile of a refined-neutrosophic continuous random variable:

The r^{th} quartile of a refined-neutrosophic random variable or Q_N^r is:

$$\int_{-\infty}^{Q_N^r} f_{X_N}(x) dx = \frac{r}{4}; r = 1, 2, 3$$

We call Q_N^1, Q_N^2 and Q_N^3 the on refined neutrosophic first, second, and third quartiles, respectively.

Example 3.9. Let NX be the refined-neutrosophic random variable defined in Example 3.6 and find its three quartiles. We have

$$f_{NX}(x) = 2x - 2(\alpha I_1 + \beta I_2); (\alpha I_1 + \beta I_2) \leq x \leq 1 + (\alpha I_1 + \beta I_2)$$

Therefore,

$$\int_{\alpha I_1 + \beta I_2}^{Q_N^r} (2x - 2(\alpha I_1 + \beta I_2)) dx = \frac{r}{4}; r = 1, 2, 3$$

For $r = 1$, we get:

$$\int_{\alpha I_1 + \beta I_2}^{Q_N^1} (2x - 2(\alpha I_1 + \beta I_2)) dx = \frac{1}{4}$$

$$[x^2 - 2(\alpha I_1 + \beta I_2)x]_{\alpha I_1 + \beta I_2}^{Q_N^1} = \frac{1}{4}$$

$$Q_N^{1^2} - 2(\alpha I_1 + \beta I_2)Q_N^1 - (\alpha I_1 + \beta I_2)^2 + 2(\alpha I_1 + \beta I_2)^2 = \frac{1}{4}$$

$$Q_N^{1^2} - 2(\alpha I_1 + \beta I_2)Q_N^1 + (\alpha I_1 + \beta I_2)^2 - \frac{1}{4} = 0$$

Dealing with a previous refined-neutrosophic equation concerning Q_N^1 we obtain:

$$\Delta = b^2 - 4ac = 4(\alpha I_1 + \beta I_2)^2 - 4\left((\alpha I_1 + \beta I_2)^2 - \frac{1}{4}\right) = 1$$

$$(Q_N^1)_1 = \frac{-b - \sqrt{\Delta}}{2a} = \frac{2(\alpha I_1 + \beta I_2) - 1}{2} = \alpha I_1 + \beta I_2 - \frac{1}{2}$$

And this solution is ejected because $\alpha I_1 + \beta I_2 \leq x \leq 1 + \alpha I_1 + \beta I_2$.

$$(Q_N^1)_2 = \frac{-b + \sqrt{\Delta}}{2a} = \frac{2(\alpha I_1 + \beta I_2) + 1}{2} = \alpha I_1 + \beta I_2 + \frac{1}{2}$$

And this solution is accepted because $\alpha I_1 + \beta I_2 \leq x \leq 1 + \alpha I_1 + \beta I_2$.

For $r = 2$, we get:

$$Q_N^{2^2} - 2(\alpha I_1 + \beta I_2)Q_N^2 + (\alpha I_1 + \beta I_2)^2 = \frac{2}{4} = \frac{1}{2}$$

Dealing with a refined-neutrosophic equation concerning Q_N^2 we obtain:

$$\Delta = b^2 - 4ac = 4(\alpha I_1 + \beta I_2)^2 - 4\left((\alpha I_1 + \beta I_2)^2 - \frac{1}{2}\right) = 2$$

$$(Q_N^2)_1 = \frac{-b - \sqrt{\Delta}}{2a} = \frac{2(\alpha I_1 + \beta I_2) - \sqrt{2}}{2} = \alpha I_1 + \beta I_2 - \frac{\sqrt{2}}{2}$$

Rejected.

$$(Q_N^2)_2 = \frac{-b + \sqrt{\Delta}}{2a} = \frac{2(\alpha I_1 + \beta I_2) + \sqrt{2}}{2} = \alpha I_1 + \beta I_2 + \frac{\sqrt{2}}{2}$$

Accepted.

For $r = 3$, we get:

$$Q_N^{3^2} - 2(\alpha I_1 + \beta I_2)Q_N^3 + (\alpha I_1 + \beta I_2)^2 = \frac{3}{4}$$

Dealing with a refined-neutrosophic equation concerning Q_N^3 we obtain:

$$\Delta = b^2 - 4ac = 4(\alpha I_1 + \beta I_2)^2 - 4\left((\alpha I_1 + \beta I_2)^2 - \frac{3}{4}\right) = 6$$

$$(Q_N^3)_1 = \frac{-b - \sqrt{\Delta}}{2a} = \frac{2(\alpha I_1 + \beta I_2) - \sqrt{6}}{2} = \alpha I_1 + \beta I_2 - \frac{\sqrt{6}}{2}$$

Rejected.

$$(Q_N^3)_2 = \frac{-b + \sqrt{\Delta}}{2a} = \frac{2(\alpha I_1 + \beta I_2) + \sqrt{6}}{2} = \alpha I_1 + \beta I_2 + \frac{\sqrt{6}}{2}$$

Accepted.

Theorem 3.10. MGF of a refined-neutrosophic random variable

Take into account the refined-neutrosophic random $NX = X + \alpha I_1 + \beta I_2$ then its corresponding MGF will be:

$$M_{NX}(t) = e^{t(\alpha I_1 + \beta I_2)} M_X(t)$$

PROOF.

$$\begin{aligned} M_{NX}(t) &= E(e^{tNX}) \\ &= E(e^{t(X + \alpha I_1 + \beta I_2)}) \\ &= E(e^{tX} e^{t(\alpha I_1 + \beta I_2)}) \\ &= e^{t(\alpha I_1 + \beta I_2)} E(e^{tX}) \\ &= e^{t(\alpha I_1 + \beta I_2)} M_X(t) \end{aligned}$$

Proposition 3.11.

- i. $M_{NX}(0) = 1$
- ii. $\frac{dM_{NX}(0)}{dt} = E(NX)$

PROOF.

$$\begin{aligned} \frac{dM_{NX}(t)}{dt} \Big|_{t=0} &= \frac{de^{t(\alpha I_1 + \beta I_2)} M_X(t)}{dt} \Big|_{t=0} \\ &= \frac{de^{t(\alpha I_1 + \beta I_2)}}{dt} M_X(t) \Big|_{t=0} + \frac{dM_X(t)}{dt} e^{t(\alpha I_1 + \beta I_2)} \Big|_{t=0} \\ &= (\alpha I_1 + \beta I_2) e^{t(\alpha I_1 + \beta I_2)} M_X(t) \Big|_{t=0} + M'_X(t) e^{t(\alpha I_1 + \beta I_2)} \Big|_{t=0} \\ &= (\alpha I_1 + \beta I_2) M_X(0) + M'_X(0) \\ &= (\alpha I_1 + \beta I_2) + E(X) \\ &= E(NX) \end{aligned}$$

Theorem 3.12. CF of Refined-Neutrosophic Random Variables

Let us consider the refined-neutrosophic random $NX = X + \alpha I_1 + \beta I_2$ then its CF will be:

$$\varphi_{NX}(t) = e^{it(\alpha I_1 + \beta I_2)} \varphi_X(t) ; i = \sqrt{-1}$$

PROOF.

$$\begin{aligned} \varphi_{NX}(t) &= E(e^{itNX}) \\ &= E(e^{it(X + \alpha I_1 + \beta I_2)}) \\ &= E(e^{itX} e^{it(\alpha I_1 + \beta I_2)}) \\ &= e^{it(\alpha I_1 + \beta I_2)} E(e^{itX}) \\ &= e^{it(\alpha I_1 + \beta I_2)} \varphi_X(t) \end{aligned}$$

Proposition 3.13.

- i. $\varphi_{NX}(0) = 1$
- ii. $|\varphi_{NX}(t)| \leq 1$, which means that CF always exists.

PROOF.

$$|\varphi_{NX}(t)| = |E(e^{itNX})| \leq E|e^{itNX}| = E|\cos tNX + i \sin tNX| = E|1| = 1$$

- iii. $\frac{d\varphi_{NX}(t)}{dt} \Big|_{t=0} = iE(NX)$

PROOF.

$$\begin{aligned} \frac{d\varphi_{NX}(t)}{dt} \Big|_{t=0} &= \frac{de^{it(\alpha I_1 + \beta I_2)} \varphi_X(t)}{dt} \Big|_{t=0} \\ &= \frac{de^{it(\alpha I_1 + \beta I_2)}}{dt} \varphi_X(t) \Big|_{t=0} + \frac{d\varphi_X(t)}{dt} e^{it(\alpha I_1 + \beta I_2)} \Big|_{t=0} \\ &= i(\alpha I_1 + \beta I_2) e^{it(\alpha I_1 + \beta I_2)} \varphi_X(t) \Big|_{t=0} + \varphi'_X(t) e^{it(\alpha I_1 + \beta I_2)} \Big|_{t=0} \\ &= i(\alpha I_1 + \beta I_2) + iE(X) \\ &= i(\alpha I_1 + \beta I_2 + E(X)) \end{aligned}$$

$$= iE(NX)$$

$$iv. \frac{d^n \varphi_{X_N}(t)}{dt^n} \Big|_{t=0} = i^n E(NX)^n$$

$$v. \varphi_{NX}(t) = M_{NX}(it)$$

Example 3.14. Let NX be the refined-neutrosophic random variable defined in Example 3.6.

i. Find $M_{NX}(t)$.

$M_{NX}(t) = e^{t(\alpha I_1 + \beta I_2)} M_X(t)$, but:

$$M_X(t) = \int_0^1 e^{tx} 2x dx = \frac{2(te^t - e^t + 1)}{t^2}$$

Therefore:

$$M_{NX}(t) = e^{t(\alpha I_1 + \beta I_2)} \frac{2(te^t - e^t + 1)}{t^2} = 2 \frac{te^{t(1+\alpha I_1 + \beta I_2)} - e^{t(1+\alpha I_1 + \beta I_2)} + e^{t(\alpha I_1 + \beta I_2)}}{t^2}$$

ii. Depending on the properties of $M_{X_N}(t)$ find $E(NX)$.

$$\begin{aligned} M'_{NX}(t) &= 2 \frac{t^2 (e^{t(1+\alpha I_1 + \beta I_2)} + (1 + \alpha I_1 + \beta I_2)e^{t(1+\alpha I_1 + \beta I_2)}t - (1 + \alpha I_1 + \beta I_2)e^{t(1+\alpha I_1 + \beta I_2)} + (\alpha I_1 + \beta I_2)) - 2t(te^{t(1+\alpha I_1 + \beta I_2)} - e^{t(1+\alpha I_1 + \beta I_2)} + e^{t(\alpha I_1 + \beta I_2)})}{t^4} \\ &= 2 \frac{t(e^{t(1+\alpha I_1 + \beta I_2)} + (1 + (\alpha I_1 + \beta I_2))e^{t(1+\alpha I_1 + \beta I_2)}t - (1 + (\alpha I_1 + \beta I_2))e^{t(1+\alpha I_1 + \beta I_2)} + (\alpha I_1 + \beta I_2)e^{tI}) - 2(te^{t(1+\alpha I_1 + \beta I_2)} - e^{t(1+\alpha I_1 + \beta I_2)} + e^{t(\alpha I_1 + \beta I_2)})}{t^3} \\ &= 2 \frac{te^{t(1+\alpha I_1 + \beta I_2)} + (1 + \alpha I_1 + \beta I_2)e^{t(1+\alpha I_1 + \beta I_2)}t^2 - (1 + \alpha I_1 + \beta I_2)te^{t(1+\alpha I_1 + \beta I_2)} + (\alpha I_1 + \beta I_2)te^{t(\alpha I_1 + \beta I_2)} - 2te^{t(1+\alpha I_1 + \beta I_2)} + 2e^{t(1+\alpha I_1 + \beta I_2)} - 2e^{t(\alpha I_1 + \beta I_2)}}{t^3} \end{aligned}$$

$$M'_{NX}(0) = \frac{2}{3} + \alpha I_1 + \beta I_2 = E(NX)$$

iii. Conclude $\varphi_{NX}(t)$ formula.

$$\varphi_{NX}(t) = M_{NX}(it) = 2 \frac{ite^{it(1+\alpha I_1 + \beta I_2)} - e^{it(1+\alpha I_1 + \beta I_2)} + e^{it(\alpha I_1 + \beta I_2)}}{-t^2}$$

4. DISCUSSION FOR BENEFITS AND FUTURE APPLICATIONS OF REFINED NEUTROSOPHIC RANDOM VARIABLES

Some phenomena in nature may consist of three independent categories of data which can be modeled as a random variable that follows a certain probability distribution, and therefore it can be represented as a single random variable of the type of refined neutrosophic, which facilitates calculations and arriving at predictions and results related to this phenomenon through the laws and mathematical formulas that we have proven in this research paper.

On the other hand, merging processes through one process contributes to reducing the cost of algorithms and reducing the number of large calculations in a clear and tangible way. This helps computers carry out this study and produce results more easily and without consuming computer hardware.

5. POSSIBLE CHALLENGES AND LIMITATIONS

The biggest challenge facing the application of the results of this study in the future is for computers to be introduced to the number system of refined neutrosophic numbers, and for it to be entered programmatically into the computer.

Therefore, before these results can be applied in statistical studies, computers must be introduced to this type of random variables and the mathematical formulas that we have proven must be introduced in order to provide the basic benefit from them in improving traditional algorithms and reducing their programming and computational costs.

4. CONCLUSION

In this paper, we have presented a generalized definition of what is known by refined-neutrosophic random variables, and we have successfully introduced the main concepts of its characteristics, including PDF and CDF. Our focus was on the refined-neutrosophic representation, and we proved several properties associated with it. Additionally, we demonstrated the applicability of these results in various domains, including quality control, stochastic modeling, reliability theory, queueing theory, electrical engineering, and more. In future researches, we will study the effectiveness of this generalization to many fields of probability theory, especially in stochastic processes and their applications and we will study the ability to generalize this definition to the plithogenic sets concept.

CONFLICT OF INTEREST

The author stated that there are no conflicts of interest regarding the publication of this article.

CRedit AUTHOR STATEMENT

Ahmed Hatip: Formal analysis, Writing - original draft, Visualization, Investigation, Supervision, Conceptualization.

REFERENCES

- [1] Smarandache F. Introduction to Neutrosophic Statistics. USA: Sitech & Education Publishing 2014; 3: 31-55.
- [2] Kandasamy WBV, Smarandache F. Neutrosophic Rings. Hexis, Phoenix, Arizona: Infinite Study 2006; 3: 7-20.
- [3] Kamaci H. Neutrosophic Cubic Hamacher Aggregation Operators and Their Applications in Decision Making. Neutrosophic Sets and Systems 2020; 33: 234-255.
- [4] Salama A, Sharaf Al-Din A, Abu Al-Qasim I, Alhabib R, Badran M. Introduction to Decision Making for Neutrosophic Environment Study on the Suez Canal Port. Egypt. Neutrosophic Sets and Systems 2020; 35: 22-44.
- [5] Anuradha J. Neutrosophic Fuzzy Hierarchical Clustering for Dengue Analysis in Sri Lanka. Neutrosophic Sets and Systems 2020; 31: 179-199.
- [6] Sahin R. Neutrosophic Hierarchical Clustering Algorithms. Neutrosophic Sets and Systems 2014; 2: 19-24.
- [7] Shahzadi G, Akram M, Saeid AB. An Application of Single-Valued Neutrosophic Sets in Medical Diagnosis. Neutrosophic Sets and Systems 2017; 18 (3): 80-88.
- [8] Ejaita OA, Asagba P. An Improved Framework for Diagnosing Confusable Diseases Using Neutrosophic Based Neural Network. Neutrosophic Sets and Systems 2017; 16: 28-34.
- [9] Chakraborty A, Banik B, Mondal SP, Alam S. Arithmetic and Geometric Operators of Pentagonal Neutrosophic Number and its Application in Mobile Communication Service Based MCGDM Problem. Neutrosophic Sets and Systems 2020; 32: 61-79.

- [10] Sahin M, Olgun N, Uluçay V, Kargin A, Smarandache F. A New Similarity Measure Based on Falsity Value between Single Valued Neutrosophic Sets Based on the Centroid Points of Transformed Single Valued Neutrosophic Numbers with Applications to Pattern Recognition, Neutrosophic Sets and Systems 2017; 15: 31-48.
- [11] Lotfy MM, ELhafeez S, Eisa M, Salama A. A. Review of Recommender Systems Algorithms Utilized in Social Networks based e-Learning Systems & Neutrosophic System. Neutrosophic Sets and Systems 2015; 08: 32-41.
- [12] Yuhua F. Neutrosophic Examples in Physics. Neutrosophic Sets and Systems 2013; 01: 26-33.
- [13] Yuhua F. Examples of Neutrosophic Probability in Physics. Neutrosophic Sets and Systems 2015; 07: 32-33.
- [14] Smarandache F. Introduction to Neutrosophic Measure, Neutrosophic Integral and Neutrosophic Probability. Craiova. Romania. Sitech – Education 2013; 3: 27-114. .
- [15] Alhabib R, Ranna MM, Farah H., Salama A. Some Neutrosophic Probability Distributions. Neutrosophic Sets and Systems 2018; 22: 30-38.
- [16] Zeina MB. Neutrosophic Event-Based Queueing Model. International Journal of Neutrosophic Science 2020; 06 (01): 48-55.
- [17] M. B. Zeina, Erlang Service Queueing Model with Neutrosophic Parameters, International Journal of Neutrosophic Science 2020; 06 (01): 106-112.
- [18] Zeina MB, Abobala M, Hatip A, Broumi S, Mosa SJ. Algebraic Approach to Literal Neutrosophic Kumaraswamy Probability Distribution. Neutrosophic Sets and Systems 2023; 54: 124-138.
- [19] Alhabib R, Salama AA. The Neutrosophic Time Series-Study Its Models (Linear-Logarithmic) and Test the Coefficients Significance of Its linear model. Neutrosophic Sets and Systems 2020; 33: 105-115.
- [20] Alhabib R, Salama AA. Using Moving Averages To Pave The Neutrosophic Time Series. International Journal of Neutrosophic Science 2020; 3(01): 14-20.
- [21] Esther Valencia Cruzaty L, Reyes Tomalá M, Manuel Castillo Gallo C. A Neutrosophic Statistic Method to Predict Tax Time Series in Ecuador. Neutrosophic Sets and Systems 2020; 34(3): 33-39.
- [22] Agboola AAA, On Refined Neutrosophic Algebraic Structures. Neutrosophic Sets and Systems 2015; 10: 99-101.
- [23] Adeleke EO, Agboola AAA, Smarandache F. Refined Neutrosophic Rings I. International Journal of Neutrosophic Science 2020; 02(3): 77-81.
- [24] Adeleke EO, Agboola AAA, Smarandache F. Refined Neutrosophic Rings II. International Journal of Neutrosophic Science 2020; 02(3): 89-94.
- [25] Smarandache F. Neutrosophic Set a Generalization of the Intuitionistic Fuzzy Sets, Inter. J. Pure Appl. Math 2005; 2: 287-297.

- [26] Ali M, Smarandache F, Shabir M, Vladareanu L. Generalization of Neutrosophic Rings and Neutrosophic Fields. *Neutrosophic Sets and Systems* 2014; 5: 9-14.
- [27] Smarandache F. Neutrosophic Measure and Neutrosophic Integral. *Neutrosophic Sets and Systems* 2013; 01: 3-7.
- [28] Celik M, Hatip A. On the Refined AH-Isometry and Its Applications in Refined Neutrosophic Surfaces. *Galoitica Journal of Mathematical Structures and Applications* 2022; 02(01): 21-28.



RESEARCH ARTICLE

MXENE 2D $Ti_3C_2T_x$ PRODUCTION AND SPIN-ORBIT EFFECT (SOI) OF $Ti_3C_2(OH)_2$ IN THE ELECTRONIC STRUCTURE

Mesut Ramazan EKİCİ^{1,*}, Hüseyin Yasin UZUNOK², Emrah BULUT^{3,4}, Hüseyin Murat TÛTÛNCÛ⁵, Ahmet ATASOY⁶

¹ Sakarya University, Metallurgical and Materials Engineering, Sakarya, Türkiye.

mekici@sakarya.edu.tr - [0000-0002-3024-2567](https://orcid.org/0000-0002-3024-2567)

² Sakarya University, Faculty of Sciences, Physics, Sakarya, Türkiye

hyuzunok@sakarya.edu.tr - [0000-0002-2130-1748](https://orcid.org/0000-0002-2130-1748)

³ Sakarya University, Faculty of Sciences, Chemistry, Sakarya, Türkiye

⁴ Sakarya University Research Development & Application Center-SARGEM, Sakarya, Türkiye

ebulut@sakarya.edu.tr - [0000-0002-7623-8088](https://orcid.org/0000-0002-7623-8088)

⁵ Sakarya University, Faculty of Sciences, Physics, Sakarya, Türkiye

tutuncu@sakarya.edu.tr - [0000-0003-1979-1626](https://orcid.org/0000-0003-1979-1626)

⁶ Sakarya University of Applied Sciences, Faculty of Technology, Metallurgical and Materials Engineering, Sakarya, Türkiye

atasoy@sakarya.edu.tr - [0000-0003-1564-8793](https://orcid.org/0000-0003-1564-8793)

Abstract

Research on new-generation materials to meet the energy needs has begun to attract attention. Recently, energy storage in materials has become the most researched area. As a result of the reaction of the MAX phase 312 Ti_3SiC_2 powder with hydrofluoric acid, a new 2D nanosized layered powder called MXene, similar to graphene, was obtained. MXenes, which have been studied in various sectors, especially energy, have attracted the attention of researchers owing to their multilayered structures. When Ti_3SiC_2 powder was treated with hydrofluoric acid (HF), an accordion-like two-dimensional $Ti_3C_2T_x$ MXene structure was formed. In MXenes, surface coatings such as $-O$, $-OH$, and $-F$ groups, which determine and affect various aspects of 2D materials, such as conductivity, constitute the application area. In this study, $Ti_3C_2(OH)_2-O$ and/or $-OH$ surface terminations were examined using density functional theory (DFT) with the effect of the hydrofluoric acid etching time. Quantum Espresso program was used for DFT calculation. X-ray diffraction (XRD) and scanning electron microscopy (SEM and FESEM) were used to examine the MXene-phase $Ti_3C_2T_x$ powder and first-principles calculations were performed. The structural and electronic properties of MAX and MXene compounds were determined. The spin-orbit effect (SOI) was examined in the electronic structure of MXene. The total and partial densities of states (DOS) with and without spin orbit were calculated.

Keywords

MXene,
 Ti_3SiC_2 ,
Spin-orbit,
DFT,
2D Material

Time Scale of Article

Received : 16 December 2023
Accepted : 20 July 2024
Online date : 30 September 2024

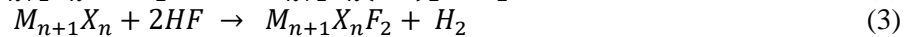
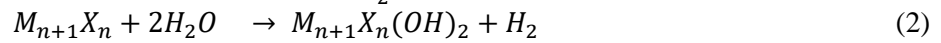
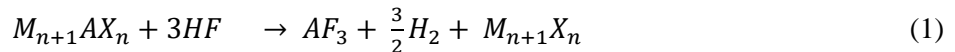
*Corresponding Author: mekici@sakarya.edu.tr

1. INTRODUCTION

In 2011, a team led by Drexel University's Yury Gogotsi and Michel W. Barsoum discovered that selective etching of the MAX phase could yield a novel 2-dimensional transition metal carbide phase. The removal of the A layer from the MAX phase (MX) and its similarity to graphene (ene) resulted in the formation of MXene, a novel 2-dimensional carbide/nitride phase transition metal. Selective etching of Al was achieved by immersing Al-containing MAX phases in hydrofluoric (HF) acid, resulting in two-dimensional (2D) materials called MXenes [1], [2], [11]–[14], [3]–[10]. MXenes, the most researched materials, have been used in lithium-ion batteries, electrochemical capacitors, and fuel cells. Furthermore, the rich chemistry of MXenes, along with their ability to modify the composition, even along a single atomic plane, provide intriguing qualities for "temporary" battery designs, where the electrode can operate depending on the material used [15]–[17]. By integrating Li-ions into MXene layers, MXene appears to be a good candidate for electrode materials for Lithium-ion batteries (LIBs) and supercapacitors. MXene reveals that it has the potential to be an excellent high-capacity anode material [15], [18]–[21].

MAX phases are carbides or nitrides with three layers, and their theoretical formula is $M_{n+1}AX_n$ ($n = 1, 2, 3$). Where M is an early transition metal, A is a group A element, and X is either carbon or nitrogen. MAX Phases have good electrical and thermal conductivities (e.g., metals), easy machinability, flexibility, good thermal shock resistance (e.g., ceramics), high strength, toughness, high temperature, and thermal and chemical stability. It is a fantastic material that combines the qualities of metals and ceramics [22]–[25]. MXene is a two-dimensional (2D) transition metal carbide and nitride nanomaterial with the chemical formula $M_{n+1}X_nT_x$. T_x represents the surface group. T_x surface terminations include fluorine (–F), hydroxyl (–OH), and oxygen (–O) [26]–[32].

MXenes are used in a wide range of applications. Field effect transistors [7], [33]–[36], biomaterial [6], [37], [38], suitable substrate for paints [13], [35], electromagnetic interface screensavers [32], [39], electrodes [7], [8], [26], [40], [41], catalyst [28], [32], [42], optical [32], [43], batteries [26], [44]–[47], composites [26], [32], reactor [30], [48], [49], sensor (gas sensor, biosensor, pressure sensor, strain sensor) [6], [8], [26], [50]–[52], water treatment [6], [8], [14], [26], [50], super capacitor [28], [32], transparent conductors [6], [32] is used. Finishing processes for MXene production (–F, –O, and/or –OH);



The supernatant (AF_3) and $\frac{3}{2}H_2$ were removed from the MAX phase when combined with hydrofluoric acid (Equation 1) to produce $M_{n+1}X_n$. MXene is produce when the $M_{n+1}X_n$ phase combines with either water (Equation 2) or hydrofluoric acid (Equation 3). The surface termination in Equation 2 is oxygen (–O) and/or hydroxyl (–OH). The surface termination in Equation 3 is fluorine (–F) [34], [53]. The surface-finishing processes of Ti_3SiC_2 are presented in Tables 1 [29], [50], [54], [55]. The T_x component of $Ti_3C_2T_x$ formed as a result of these reactions can be –F ($Ti_3C_2F_2$), –O ($Ti_3C_2O_2$), or –OH ($Ti_3C_2(OH)_2$) [56]–[60].

Table 1. Different surface finishing processes of Ti₃SiC₂ [61]–[63].

Step 1	Step 2
Ti ₃ SiC ₂ + 3HF = Ti ₃ C ₂ + SiF ₃ + 3/2H ₂	Ti ₃ C ₂ + 2HF = Ti ₃ C ₂ F ₂ + H ₂
	Ti ₃ C ₂ + O ₂ = Ti ₃ C ₂ O ₂
	Ti ₃ C ₂ + 2H ₂ O = Ti ₃ C ₂ (OH) ₂ + H ₂

Owing to their ceramic properties, MXenes are chemically and mechanically stable. MXenes have various shapes and sizes, including single- and multilayered structures. It can be made as a complex material from a mix of light and heavy transition metals, allowing the number of valence electrons and relativistic spin-orbit coupling to be adjusted. This improved the electronic performance and mechanical stability of the devices. Thus, the thickness of the MXene layer can be changed. MXene surfaces can be functionalized with various chemical groups, allowing surface state engineering. Some MXenes exhibit massless Dirac dispersions in bands close to the Fermi level. This broadens the scope of dirac-based physics and its applications. These characteristics distinguish MXene from other compounds. The electrical properties of MXenes, such as conductivity, band gap, and operational function, are determined by their terminal groups and X-elements, which determine whether they are metallic or semiconducting [32], [64].

MAX-phase bonding generally involves metallic, covalent, and ionic interactions. A strong M - X link is covalent, metallic, and ionic, whereas an M - A bond is metallic. The weak ionic-covalent connections between M and X are too strong to break easily. They were separated into three groups: 2 (211), 3 (312), and 4 (413), corresponding to the M layer, depending on the number of M layers separating the A layers. MAX phases have structures that are composed of several metals. Ionic M-A bonds are connected by weak covalent M-X bonds. Consequently, the atoms of element A are far more reactive than those of elements M and X. The most basic principle for accessing MXenes is selective etching; using an acidic fluoride solution, removing A element layers without damaging the M-X bonds is possible. MAX phases have high binding strength owing to their metallic, ionic, and covalent bonds. Because the metallic link between Ti and Si is weaker than the covalent bond between Ti and C, HF etching selectively eliminates the Si layer from Ti₃SiC₂. The Ti₃C₂ layers were joined with Si atomic layers, which acted as mirror planes in Ti₃SiC₂. Si-Ti bonds are weak, but Ti-C bonds are significantly more durable. Ti₃SiC₂ exhibits exceptional mechanical characteristics and chemical stability at high temperatures. The structure combines metallic and ceramic characteristics with layered crystalline metallic (M-A) and covalent (M-X) links. The MAX phases are good thermal and electrical conductors. M-X bonds are among the most powerful in nature [14], [15], [42], [52].

The addition of metal ions or organic molecules and the combination of inorganic particles and MXene layers control and optimize the MXene properties [50]. MXene (Ti₃C₂T_x) layers can be intercalated in various ways owing to the weak bonds between the M_{n+1}X_n layers [6], [34]. The number of hydrogen bonds and/or the bonds between the Van der Waals Ti₃C₂T_x layers decreased after joining dimethyl sulfoxide (DMSO) [65], [66]. Inorganic molecules (metal cations and water) can easily combine with MXene, widening the space between layers [6], [34], [67]. MXenes with these molecules, followed by mechanical vibration or sonication in water, form colloidal monolayers and multilayer MXenes [26]. After intercalation, single or few layers of Ti₃C₂T_x were split into layers (nanosheets/flakes) by direct handshaking or mechanical vibration (bath sonication stage), and a stable colloidal solution was formed [34], [65], [68], [69].

2. EXPERIMENTAL PROCEDURES

MAX phase powder-mixing ratio was used for MXene synthesis. The MAX-phase powder was mixed with 10 mL of acid solution [2], [55], [61]–[63], [70], [71]. In the experiments, Teflon Magnetic Fish (PTFE) and plastic beakers did not react. The mixture was stirred using a magnetic stirrer with Teflon magnetic fish in a plastic bottle [45], [72].

MAX-phase Ti_3SiC_2 powder with a 200-mesh size and 98 per cent purity (2% TiC) was obtained from Forsman Scientific (Beijing) Co., Ltd. For 1 g of Ti_3SiC_2 powder, 10 ml of acid solution was used. Acid (50 per cent) was used as an acid. The powder was slowly added to the solution owing to the exothermic reaction. The resultant solution was mixed for 8 h and 32 h in a fume hood with a magnetic stirrer set at 750 rpm. Table 2 lists the codes for the sample samples prepared based on the mixing time.

Table 2. Mixing times of Ti_3SiC_2 and $\text{Ti}_3\text{C}_2\text{T}_x$ powders.

Sample	Acid/Solution	Hours	Code
Sample 1	-	-	Ti_3SiC_2
Sample 2	HF	8	HF-8
Sample 3	HF	32	HF-32
Sample 4	HF+HF	8+8	HF-HF-8
Sample 5	HF+HF	32+32	HF-HF-32
Sample 6	HF+HF+DMSO	8+8+18	HF-HF-DMSO-8
Sample 7	HF+HF+DMSO	32+32+18	HF-HF-DMSO-32

The PTFE was placed in a beaker to mix the plastic. The powders obtained after HF treatment were subjected to HF (HF-HF) treatment. Centrifugation with deionized water was rounded off in MXene manufacturing to neutralize the acidic environment caused by the reaction of MAX-phase particles with acid. A link exists between the pH level and the mixing process. The pH of the supernatant determines the time required for centrifugation. The pH value of the supernatant solution is 4–6 [6], [8], pH value is between 5–6 [18], [29], [34], [42], [65], [69], pH value is between 6–7 [15], [35], [46]. In some studies, the pH was considered sufficient to achieve neutrality [9], [36]. More centrifugation was required to achieve an appropriate pH shift, which was directly affected by centrifugation the HF reactions. Numerous elements influence the MXene production. Many factors alter the physical and chemical properties of MXenes, which, in turn, affect their quality. The solution ratio, mixing duration, acid variety, organic chemicals, temperature, pressure, and surface finishing are the most critical variables. One of the most important factors that determines the quality and yield of MXenes is the solution ratio. The chemical stability of MXene increases as the number of layers increases. $\text{Ti}_3\text{C}_2\text{T}_x$ has 50 per cent HF and 100 per cent efficiency, whereas Ti_2CT_x has 60 per cent efficiency with only 10% HF [20]. For MXenes, the mixing time is effective for surface finishing. Increasing the -O terminations while lowering the HF concentration lowers the -F terminations [14]. Some XRD peaks may vanish, whereas others may return because of mixing time. The processing time increased with HF to attain higher angle values. This indicates that when the processing time with HF increases, the d-distances of the planes decrease [73]. The increased mixing time reduces the particle size, resulting in a faster transition from the MAX phase to the MXene phase. Although there was no notable change in the mixing after a short period, the MXene phase was created with alterations in the MAX phase structure over long mixing times [52]. The mixing time decreased with an increase in the temperature of the mixture. Temperature and time showed an inverse relationship. For example, mixing for 48 h at 35 °C is comparable to mixing for 24 h at 60 °C [1].

The Al layers were replaced with surface terminal groups presumed to be -O, -OH, and/or -F during the chemical etching of the MAX phases to form the MXene phases. According to DFT calculations, surface terminations can directly or indirectly modify the electronic characteristics of MXenes from

semiconductors with small bandgaps to semiconductors with wide bandgaps. Termination causes variations in the bandgap. The capacity of oxygen-terminated MXenes was calculated to be higher than those of hydroxyl- and F-terminated MXenes [14]. Centrifugation is necessary for manufacturing MXenes. After combining with acid, the centrifugation speed and time helped the solution to become neutral (pH 5-6). Although the centrifuge speed varied, it was typically set to 3500 rpm [34]–[36], [69]. The fluid and powder were mixed using a magnetic stirrer and transferred to a centrifuge tube. Centrifugation was performed at 3500 rpm for 5 min [62], [63]. pH measurements were performed in the supernatant of the centrifuge tube before it was emptied. The pH meter was washed with distilled water for each particle size. Centrifugation was performed for 5 min until the pH level reached 5-6. After centrifugation, the pH of the MXene powder increased logarithmically. There was a proportionate variance between the time spent mixing with HF and the time spent centrifuging (Fig. 1).

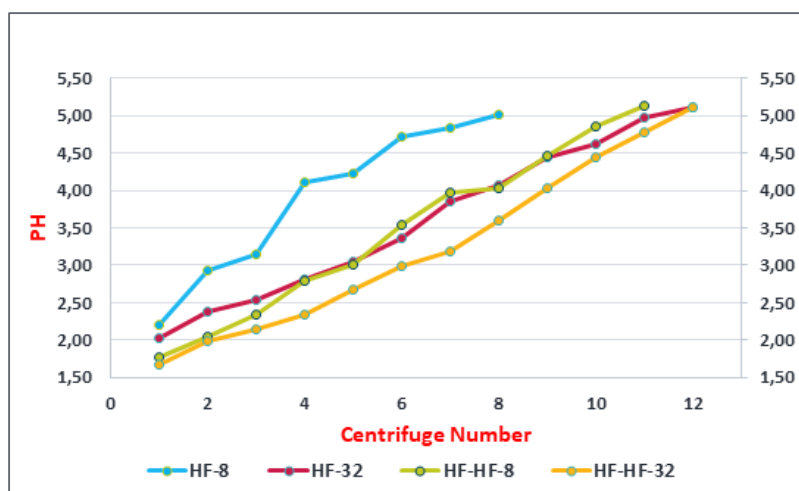


Figure 1. pH change in the powder produced with hydrofluoric acid (HF) by centrifugation.

Filtering removes the MXene particle solution from deionized water. A mud (clay)-like structure was formed after filtration [33], [36], [42], [52], [74], [75]. After mixing, the supernatant was filtered using a filter. The liquid waste portion of the supernatant was emptied into other containers. Following centrifugation of the solution obtained by mixing it with HF, the supernatant-colored turquoise was obtained. The amount of silicon in the supernatant was determined by chemical analysis. The layers generated by breaking the Van der Waals bonds between the layers were split into further layers by sonication after intercalation with an organic solvent (e.g. dimethyl sulfoxide). This enables mechanical vibration or hand shaking to open layers [26], [34], [66].

Ethyl alcohol (40 mL) was poured into a glass beaker. The sonicator was sonicated for 6 hours in 1-hour chunks. Each hour, four cycles were completed at 15-minute intervals, with sonication creating 5-second pulses.

Each cycle included a 5-minute rest time after the warm-ups. The mixture was submerged in an ultrasonic bath for one hour. For one gramme of MXene particles, 500 ml of deionized water was placed in an ultrasonic bath at a frequency of 37 kHz. The MXene particles broke and were delaminated in both the ultrasonic treatments. The layered MXene structures were mixed with DMSO for 18 h at room temperature. To 1 g of MXene, 20 ml DMSO was used [42], [52], [64], [65], [76]. The mixture was centrifuged at 4000 rpm for 10 min to separate the DMSO from the mixture. This phenomenon is known as delamination [14], [15], [21], [67]. After centrifugation, the mixture was filtered through a 200 nm porous membrane filter. It was then dried in a vacuum oven at 70 °C for 24 h [15], [34], [35], [67], [77]. Figure 2 shows the MXene phase.

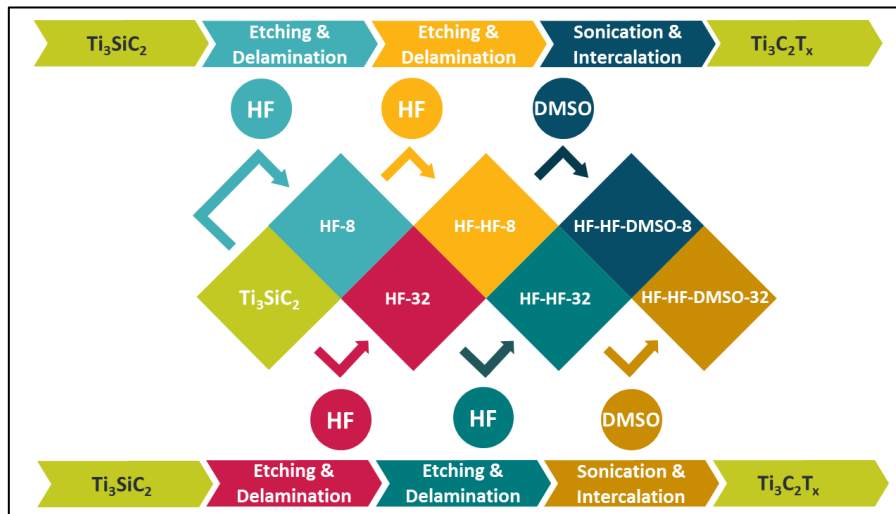


Figure 2. MXene production steps

After centrifugation and filtration, a moist, clay-like texture was observed. The powders were dried in a vacuum oven for 24 hours at a temperature of 70-80 °C [34], [65], [66], [78]. To filter the clay (mud) from the powder and separate it from the liquid, vacuum filtration was conducted for approximately one hour. Subsequently, it was dried in a vacuum oven at 70 °C for 24 h. Table 3 lists the chemical methods used for the powders.

Table 3. Processes used in the manufacture of MAX Phase Ti3SiC2 powders using MXene.

Code	Etching	Delamination	Sonication	Intercalation
Ti3SiC2	-	-	-	-
HF-8	+	+	-	-
HF-32	+	+	-	-
HF-HF-8	++	++	+	-
HF-HF-32	++	++	+	-
HF-HF-DMSO-8	++	++	+	+
HF-HF-DMSO-32	++	++	+	+

There are losses in the powder production when MXene is produced from the MAX phase. One gram of Ti3SiC2 contained 0.140852 g silicon. The loss of silicon or the amount of silicon in the supernatant was determined using EDX analysis. The amount of silicon in the supernatant was measured.

The silicon ratio in the supernatant solution is measured in ppm using the Spectro Arcos FHE16 model Inductively Coupled Plasma (ICP)-Optical Emission Spectrometer (OES) equipment (Figure 3). First, reference silicon standard solutions were prepared. The silicon content in the model (supernatant) was determined by comparing the ratio of the sample to the standard solution (Figure 3). Because of the reaction with HF, the MAX phase powders removed Si from the atmosphere; however, some Si remained in the powder.

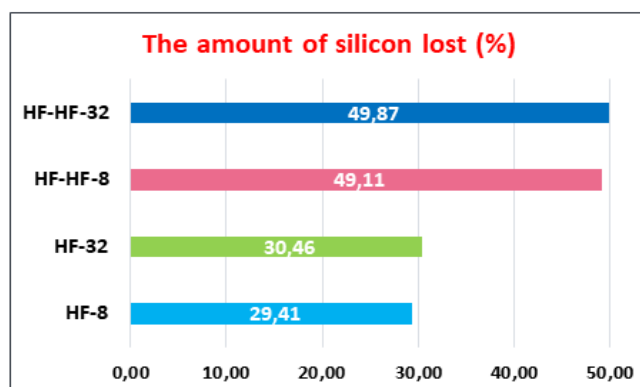


Figure 3. MXene synthesis from the MAX phase resulted in a percentage weight loss of silicon in $Ti_3C_2T_x$ powder.

Because of the fluorine ratio in HF etching, a lower HF acid ratio results in more oxygen. In the etching process with 10% HF, more oxygen and less fluorine are observed than in the etching process with 50% HF. The most important factor in surface finishing is acidity [26], [42]. Because the etching process involves an exothermic reaction, vigilance should be exercised and the reaction vessel should be thoroughly ventilated [9], [50]. Owing to the risk associated with HF, other acids can be used as alternative corrosives. The MXene layer developed flaws because of HF's high etching ability of HF [32], [50]. The functional groups in the generated MXenes impart hydrophilicity to surface terminations [68].

2.1. Theoretical Calculations

This study was carried out using the Quantum-Espresso [79], [80] simulation package based on density functional theory. The electron–electron interaction was processed by GGA using the existing Perdew-Burke-Ernzerhof [81]. Coulomb interactions between valence electrons and ionic nuclei were described using full and scalar relativistic ultrasoft pseudopotentials to determine the effects of spin–orbit interaction (SOI) on the physical properties of all compounds studied. The maximum plane-wave cutoff energy was set at 60 Ry, whereas the electronic charge density was expanded on a basic cutoff basis up to 600 Ry. Self-consistent solutions of the Kohn-Sham equations were determined using Monkhorst-Pack special k-points [82] within the Brillouin zone (BZ). While the total energy calculations for all compounds examined were performed on a $(12 \times 12 \times 12)$ k-point network, this network was increased to $(24 \times 24 \times 24)$ for electronic measurements.

2.2. Structural and Electronic Properties

The studied Ti_3SiC_2 and its MXene-phase $Ti_3C_2(OH)_2$ compounds crystallized in a hexagonal $p63/mmc$ (Wyckoff number of 194) structure, as shown in Figure 4. As shown in Figure 4 (a), the polyhedral was formed into an octahedral pyramid, with the Ti atom placed at its center. Some of the C atoms from the neighboring unit cells are also shown to better understand these polyhedra and bonds. Crossing Ti atoms formed six bonds with neighboring C and Si atoms. For $Ti_3C_2(OH)_2$, polyhedra occur between Ti and C atoms and have a triangular pyramid shape. The coordinates of the Ti atoms were 2a (0.00,0.00,0.00), 4f ($1/3, 2/3, z_{Ti}$), Si atoms were 2b (0.00, 0.00, $1/4$), C atoms were 4f ($1/3, 2/3, z_C$), O atoms were 4e (0.00, 0.00, z_O), and H atoms were 4e (0.00, 0.00, z_H). The lattice parameters of Ti_3SiC_2 were obtained from a previous experimental study [82]. Structural relaxation calculations were performed for $Ti_3C_2(OH)_2$; structural relaxation calculations were performed, and the obtained values for its lattice parameters were $a = 3.21 \text{ \AA}$, and $c = 22.38 \text{ \AA}$. The inner parameters for atoms are $z_{Ti} = 0.6122$, $z_C = 0.5746$, $z_O = 0.4133$, and $z_H = 0.2151$ for $Ti_3C_2(OH)_2$. The C atoms formed three bonds with O atoms and one bond with a Ti atom, with a total of four bonds. The bond length between Ti-C in $Ti_3C_2(OH)_2$ is 2.088 \AA , which is longer than the corresponding value of 2.081 \AA in Ti_3SiC_2 . Because the electronegativities of the atoms

are different in both compounds, we can say that the bonding in the studied compounds is an admixture of covalent, ionic, and metallic behaviors.

The calculated electronic band structure of the MAX Phase Ti_3SiC_2 compound is presented in Figure 5 along with the high-symmetry directions of the Brillouin region of the hexagonal system. The Fermi level was set to 0 eV and is indicated by dashed blue lines with significantly high symmetry points. Because several bands cross the Fermi level along all symmetry directions, it was concluded that this compound exhibits a metallic behavior. These results agree with those of previous studies of this compound [83]. While the red dashed lines are obtained by including the SOI, the dashed black lines represent the electronic structure without the SOI. As shown in Figure 5., the SOI had almost no effect on the electronic band structure of the compound.

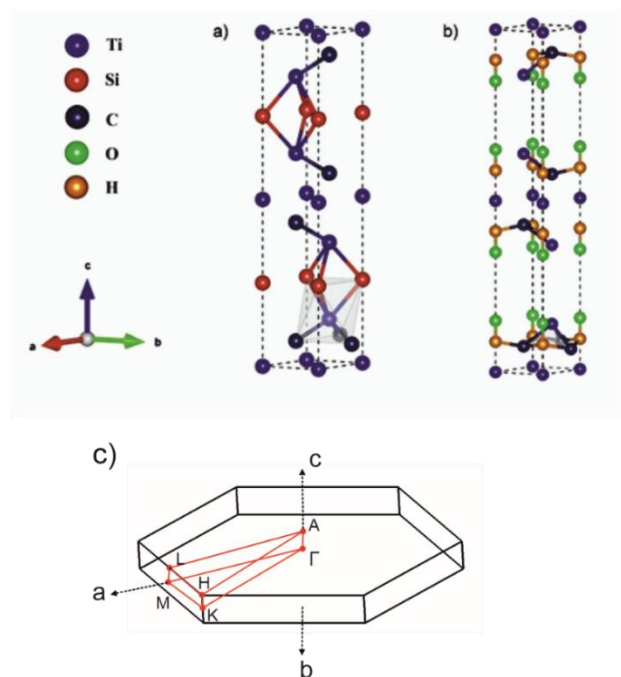


Figure 4. Crystal structures of a) Ti_3SiC_2 , b) $Ti_3C_2(OH)_2$ compounds, and (c) high-symmetry points of the hexagonal structure

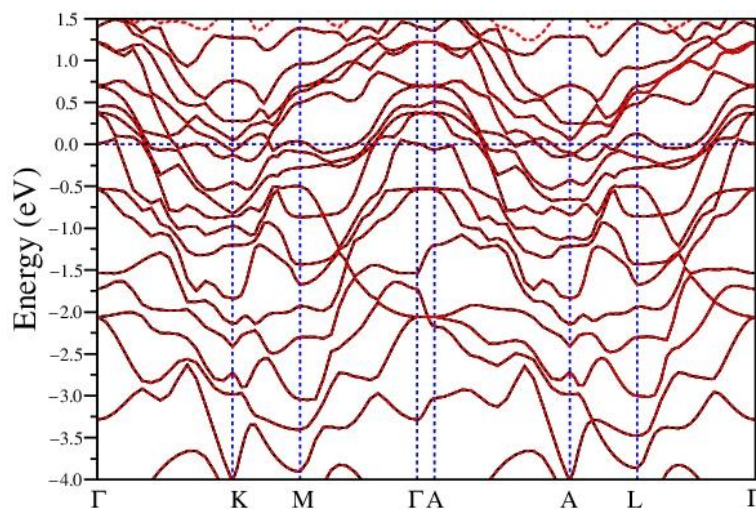


Figure 5. Electronic structures of Ti_3SiC_2 with (red dashed lines) and without (solid black lines) spin-orbit interactions

However, the electronic structure of $\text{Ti}_3\text{C}_2(\text{OH})_2$ exhibits features different from those of its MAX phase, as shown in Figure 6. Splitting due to the SOI increases the electronic bands that cross the E_F and enhances the free electrons near this energy level. The highest splitting between the energy bands due to SOI is about 0.3 eV at high-symmetry points. Therefore, it is crucial to include SOI when calculating the MXene phase of $\text{Ti}_3\text{C}_2(\text{OH})_2$.

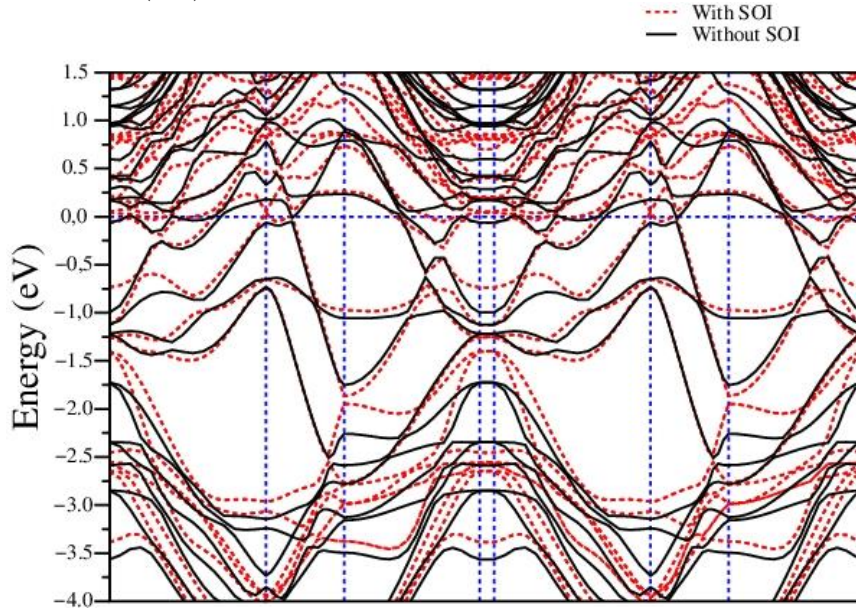


Figure 6. Electronic structures of $\text{Ti}_3\text{C}_2(\text{OH})_2$ with (red dashed lines) and without (solid black lines) spin-orbit interactions

The high-symmetry points and Fermi surface (FS) sheets of the Ti_3SiC_2 compound are presented in Figure 7, and are consistent with previous results [83]. Because SOI is not effective for this compound, the FS sheets with SOI are not shown in Figure 7. Six electronic bands crossed the E_F , forming six different FS. The first four FS had simple nesting around the Γ point. First, the FS enclosed the Γ -point in a spherical shape. The other three have a cylindrical shape, which also circles the Γ point. The fifth FS has more complex nesting than the first four FS. Although it rotates at the Γ point, it has a flower-like shape. The last FS has an enclosed shape around the K high-symmetry point. All the FS had both hole and electron pocket characteristics.

The FS sheets for $\text{Ti}_3\text{C}_2(\text{OH})_2$ differ from the MAX phase owing to the effectiveness of the SOI. When the SOI is not considered, only two electronic bands cross the E_F and form two FS sheets, as shown in the left panel of Figure 8. The first one forms a flower-like nesting away from the zone center. The second has a similar shape away from the zone center, but also has two closed shapes around the Γ high-symmetry point.

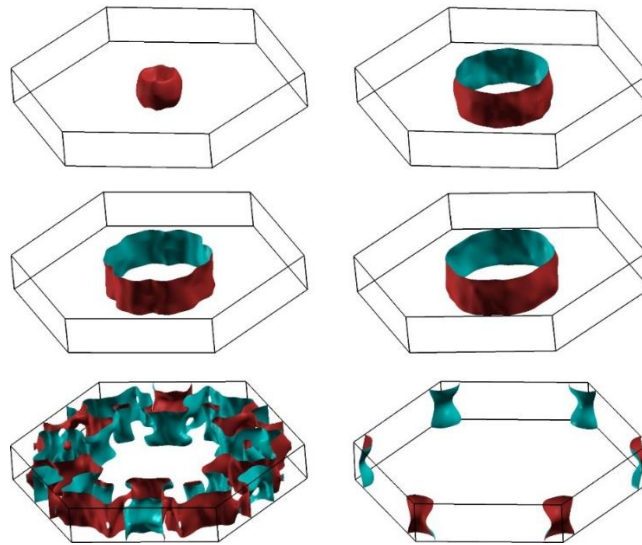


Figure 7. The Fermi Surface sheets for Ti_3SiC_2 compound

The number of FS sheets increased when the SOI was included. The shape of the first FS does not change owing to the SOI, but the second one seems to be split into two different FS sheets that enhance the number of free electrons near the E_F . Nesting along the $\Gamma - H$ direction can increase the scattering of electrons, which can increase the electron-phonon interaction. While the first FS with SOI had mainly hole-pocket features, the second and third FS sheets had electron-pocket features within the hexagonal MXene $Ti_3C_2(OH)_2$.

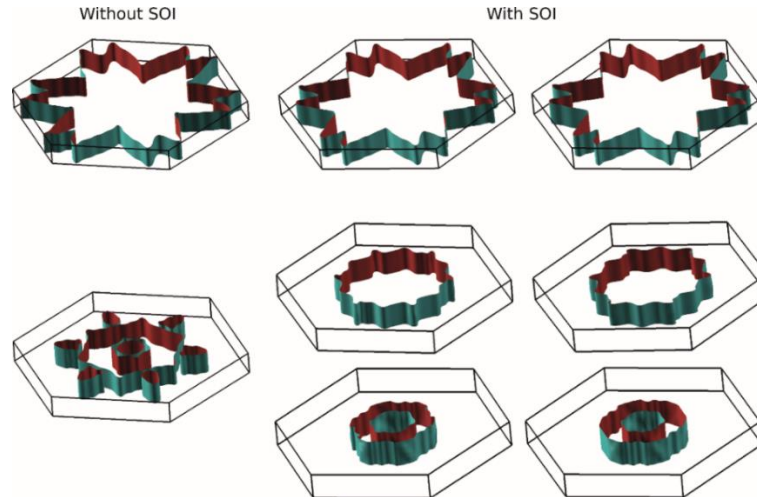


Figure 8. Fermi Surface sheets for $Ti_3C_2(OH)_2$. While the left column shows the sheets obtained without SOI, the middle and right columns correspond to the Fermi surface sheets obtained with SOI

The total and partial densities of state (DOS) of Ti_3SiC_2 are shown in Figure 9. Because all atoms in the compound contribute to the DOS at the Fermi level ($N(E_F)$), we can say that it exhibits a 3D-metallic electronic behavior. No gaps are observed in the valence bands of this compound. The $N(E_F)$ value mainly consists of Ti 3d orbitals contributing to C 2p and Si 3p hybridization. The $N(E_F)$ value for Ti_3SiC_2 was calculated as 10.7 States/eV. The Ti 3d shell contributes approximately %65 (6.95 States/eV), the C 2p shell contributes around %17 (1.82 States/eV), and the Si 3p shell contributes to the $N(E_F)$ around %15 (1.61 States/eV) of the Ti_3SiC_2 compound. Although the d-orbital dominates the Fermi energy level, because the mass of the compound is relatively low, the SOI is not as effective as

that in a heavier mix. Hybridization occurred between the d- and p-orbitals in all energy regions. This hybridization is more distinctive in the valence region, suggesting solid bonding between Ti, C, and Si compounds. As the electronic structure implies, the SOI has a negligible effect on the electronic properties of this compound. Hence, only the DOS without the SOI is shown in Figure 9. The DOS and partial DOS features of $\text{Ti}_3\text{C}_2(\text{OH})_2$ with and without SOI are shown in Figure 9. It can be seen that the multilayer structure is slightly disturbed after mixing with dimethylsulfoxide (Fig. 9).

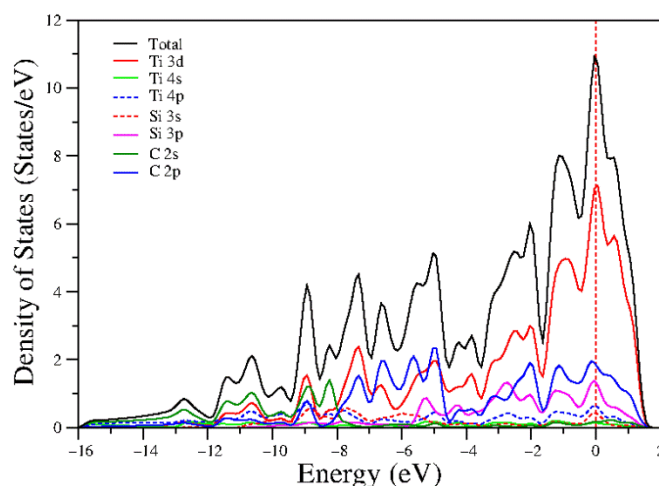


Figure 9. The total and partial density of states in Ti_3SiC_2 orbitals

In Figure 10 (a), the DOS features of this compound are calculated using the SOI. Between -8.5 eV and -4.2 eV, O 2p shell makes the largest contribution the DOS features of the valence band. After this energy level to -2.5 eV, both Ti 3d and C 2p orbitals contribute equally to the DOS value. Near E_F , the Ti 3d shell dominated the electronic properties of $\text{Ti}_3\text{C}_2(\text{OH})_2$. A similar observation was made for the DOS properties calculated without an SOI, as shown in Figure 10 (b). The DOS features of $\text{Ti}_3\text{C}_2(\text{OH})_2$ with and without SOI are shown in Figure 10. In Figure 10 (a), the DOS features of this compound were calculated using the SOI. Between -8.5 eV and -4.2 eV, the O 2p shell makes the most significant contribution to the DOS features of the valence band. After this energy level to -2.5 eV, the Ti 3d and C 2p orbitals contribute equally to the DOS value. Near E_F , the Ti 3d shell dominated the electronic properties of the $\text{Ti}_3\text{C}_2(\text{OH})_2$ compound. A similar observation can be made for the DOS properties calculated without the SOI, as shown in Figure 10 (b). The main difference between these two graphs is the $N(E_F)$ values. The $N(E_F)$ value with SOI was calculated as 8.0 States/eV, whereas the corresponding value without SOI was obtained as 7.2 States/eV. This enhancement due to SOI can be explained by the gathering of split bands around E_F . The contribution of the Ti 3d shell to $N(E_F)$ was approximately %74 with the SOI and %76 without the SOI. The C and O 2p orbitals contributed equally to $N(E_F)$ in both calculations. We can say that even though the mass of the compound does not change significantly from the MAX phase to the MXene phase, because of the changing bonding features and contribution rates, SOI is much more effective in the MXene phase.

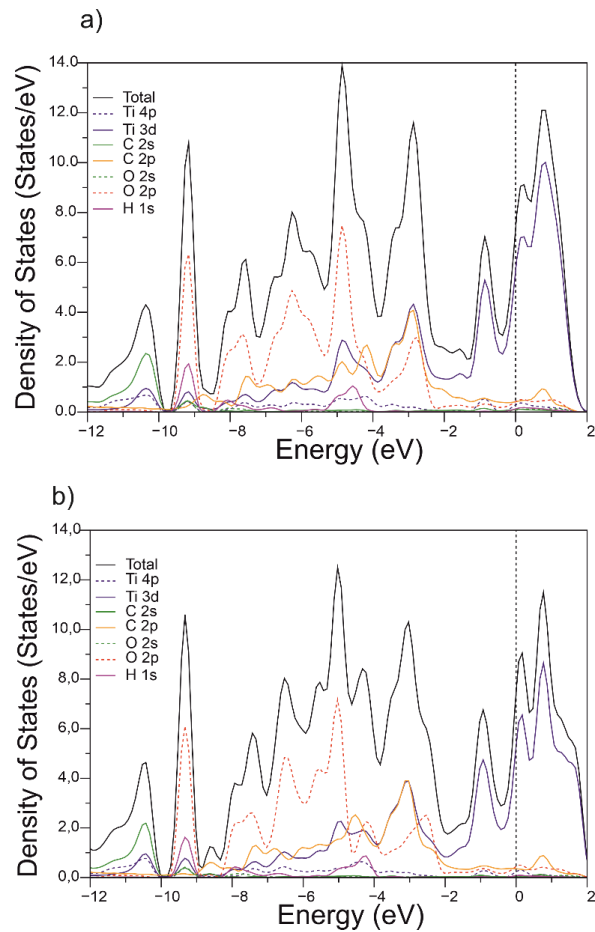


Figure 10. The density of states in $\text{Ti}_3\text{C}_2(\text{OH})_2$ compounds (a) with and (b) without SOI

3. RESULTS AND DISCUSSION

The MAX phase starting powder broke the titanium-silicon bonds. Strong bonds existed between titanium and carbide, whereas weak bonds existed between titanium and silicon. In the $\text{Ti}_3\text{C}_2\text{T}_x$ layers formed, MXenes exhibited weak Van der Waals bonds. The particles formed after hydrofluoric acid exfoliation were then exfoliated. Exfoliation results in an accordion-like shape [42], [52], [67]. The powders were coated with 80% gold and 20% palladium prior to SEM using Quorum Q150R ES brand coating equipment and a Polaron Range SC7620 Mini Sputter Coater. The researchers used a JEOL JSM-6060LV scanning electron microscope (SEM). Figure 11 shows SEM images of the Ti_3SiC_2 MAX phase powder, which is referred to as the primary material.

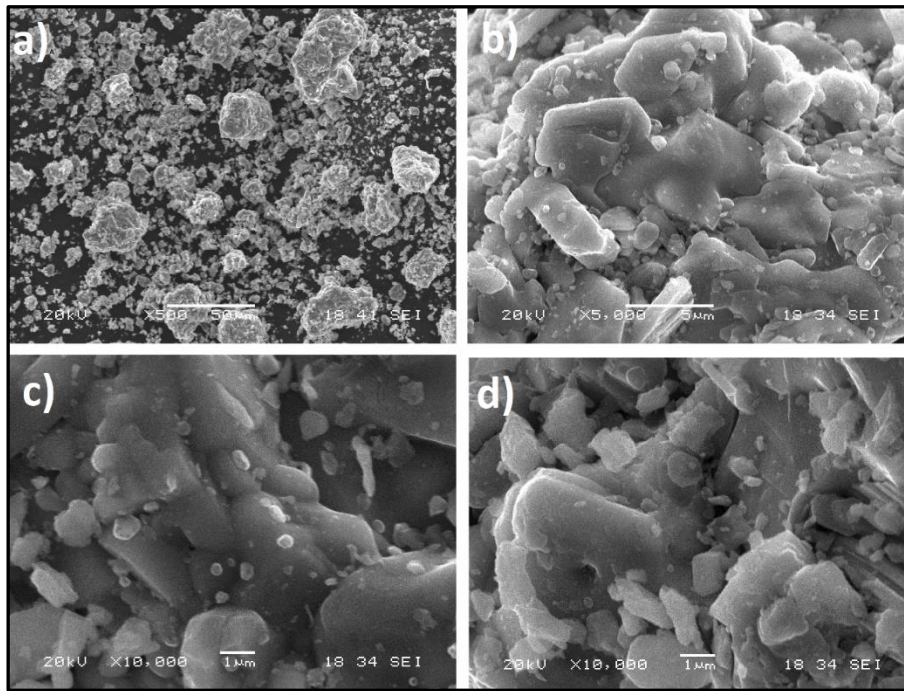


Figure 11. SEM images of Ti_3SiC_2 MAX phase powder.

The samples were coded based on their operation. Hydrofluoric acid (HF) and dimethyl sulfoxide (DMSO) were used for coding. The mixing time with the acids was indicated by the sample code numbers (8 and 32 h). If treated with hydrofluoric acid, it is referred to as HF. It is classified as HF-HF if it has previously been treated with hydrofluoric acid and chemically treated with hydrofluoric acid. It was labelled with DMSO after treatment with acids and then combined with dimethyl sulfoxide. The powders were aggregated and the forms were more spherical, as shown in the SEM image of the basic material. The structures in which the stacked layers were best observed were the samples treated with a high mixing time, as shown by the SEM morphologies of the MXene powders (Figure 12).

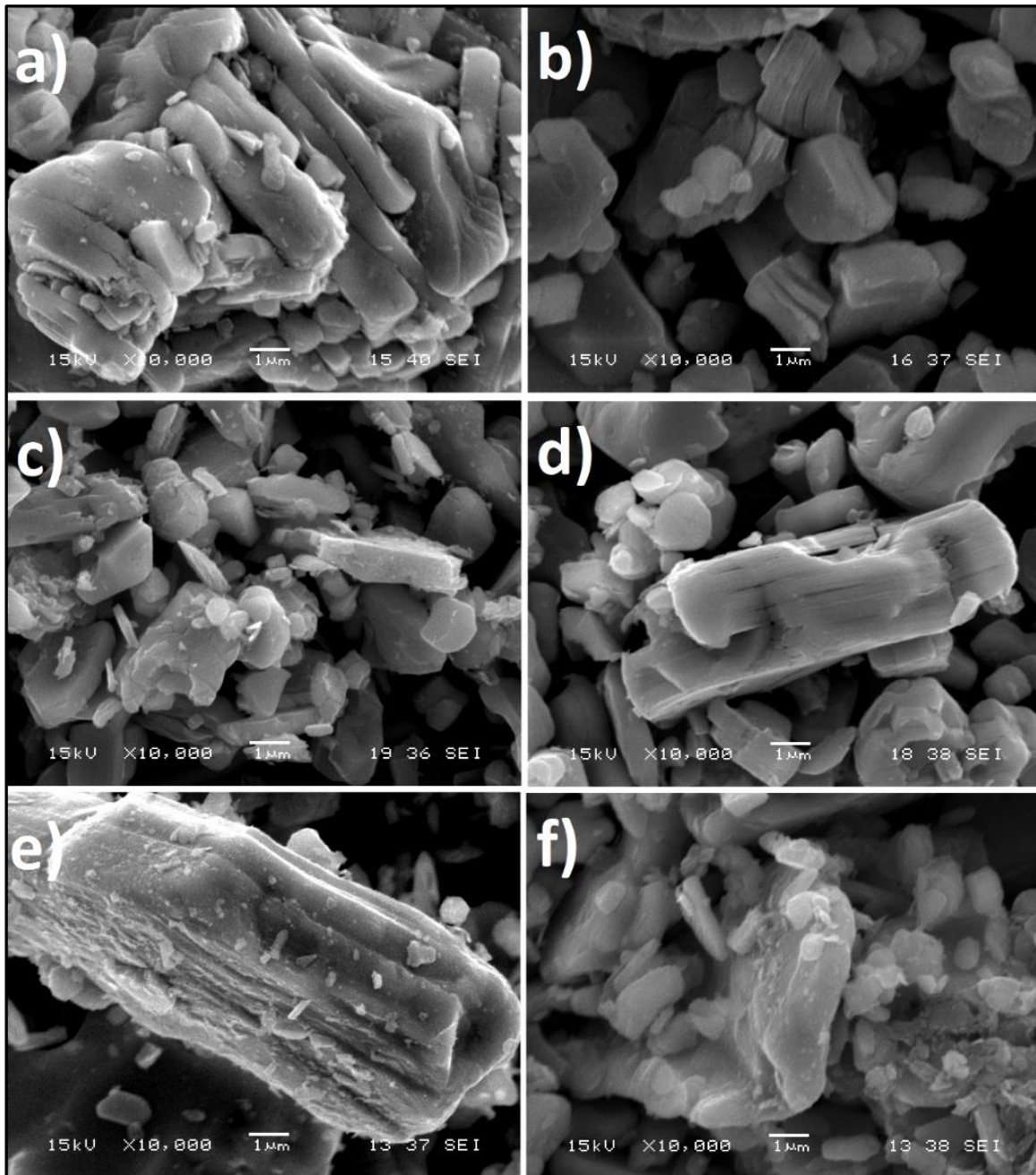


Figure 12. MXene structure ($Ti_3C_2T_x$) powders a) HF-8, b) HF-32, c) HF-HF-8, d) HF-HF-32, e) HF-HF-DMSO-2, f) HF-HF-DMSO-32, SEM pictures

The powders acquired after 32 h of mixing were used to create SEM images, which clearly showed a layered structure (Figure 13). Field Emission Scanning Electron Microscopy (FE-SEM, FEI Quanta FEG 450) was used to characterize the materials. Figure 14 shows FE-SEM images of the MAX-phase Ti_3SiC_2 sample used as the starting powder [63].

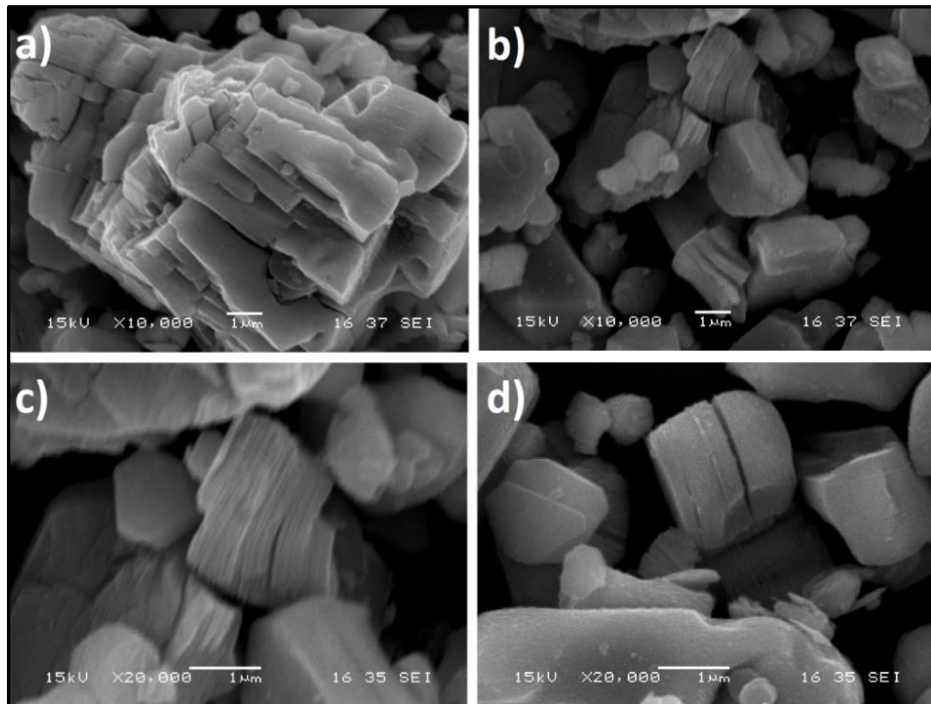


Figure 13. SEM images of HF-32 sample in MXene structure ($Ti_3C_2T_x$)

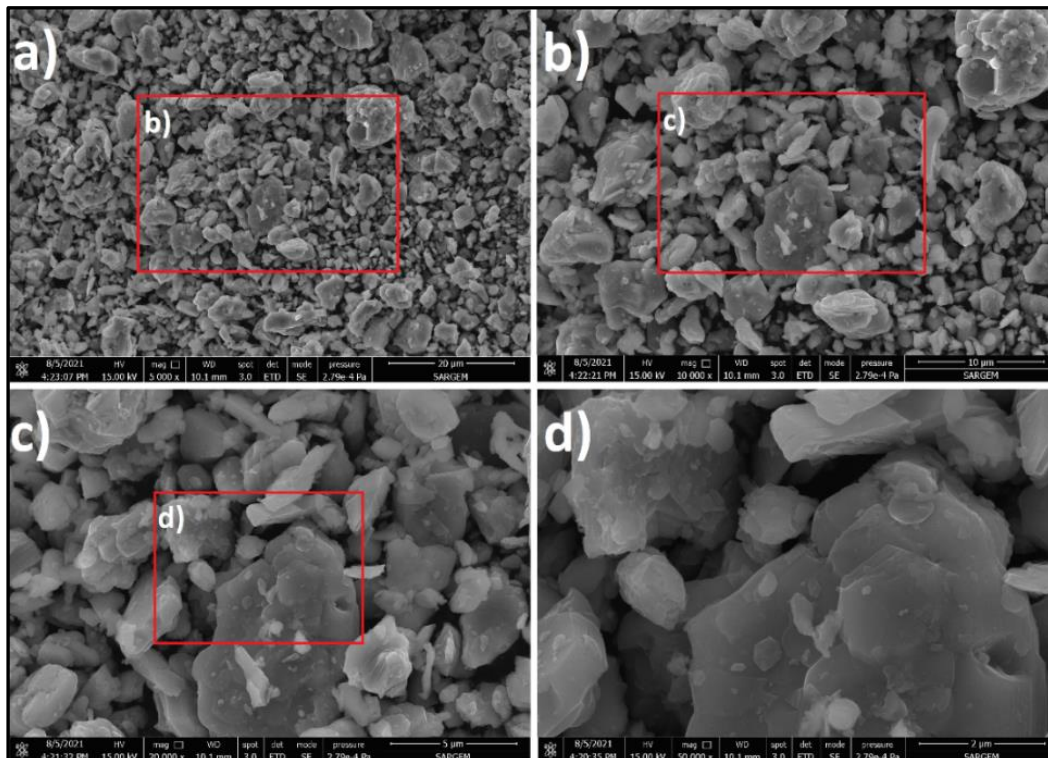


Figure 14. FE-SEM images of Ti_3SiC_2 MAX phase powder.

Figure 15 shows FE-SEM EDX pictures of the MAX phase Ti_3SiC_2 sample. According to the EDX images, the Ti content is approximately 70%. A layered structure was not observed in the initial powder.

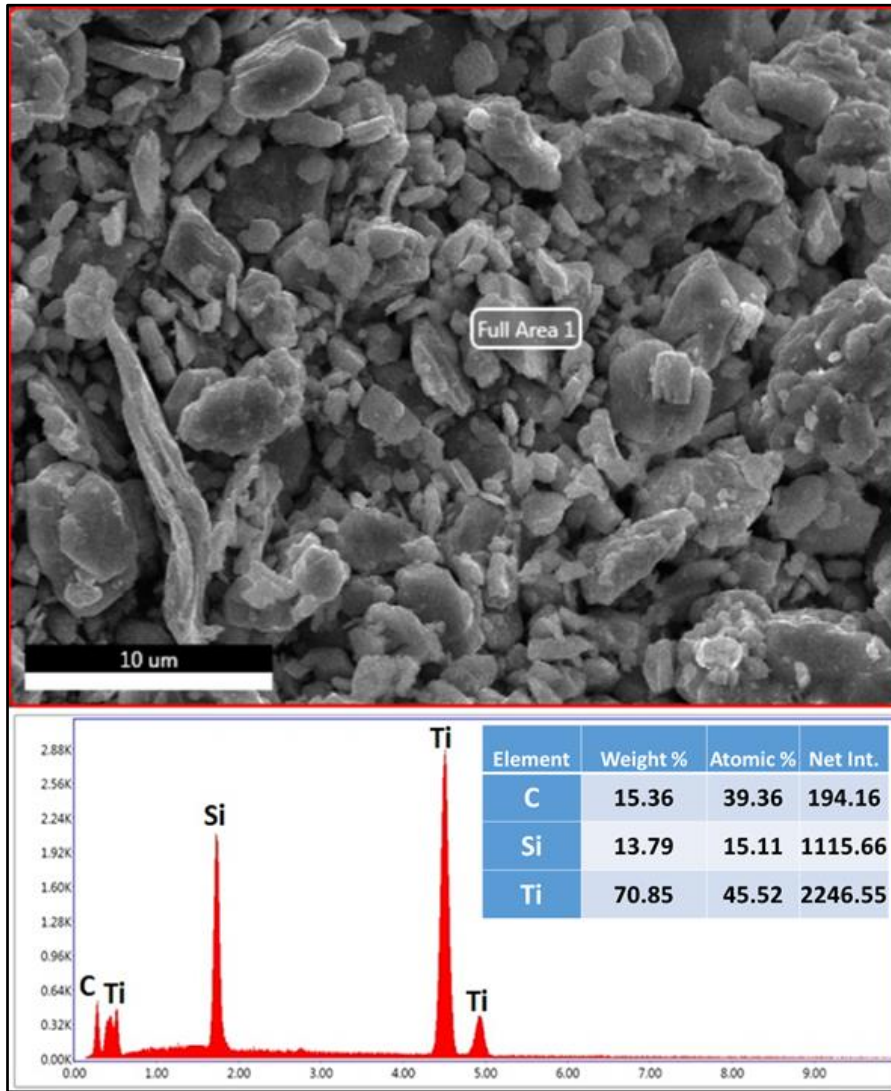


Figure 15. FE-SEM EDX images of Ti_3SiC_2 MAX phase powder

Figure 16 shows the FE-SEM images of the samples prepared by mixing the MAX phase powder with hydrofluoric acid (HF) and then dimethyl sulfoxide (DMSO) for 8 and 32 h. The layered structures were formed after 32 h. At higher mixing speeds, the paper-like 2D structures, known as MXenes, became more dominant (Figure 17). Delamination is observed in the SEM and FE-SEM images as overlapping layers, which appear to have been sliced sharply with a metal blade [20]. The effect of the hydrofluoric acid mixing period was apparent in the HF-32 (Figure 16) [63] and HF-HF-32 (Figure 17) samples, where the layered structure was preserved, weak bonds were destroyed, and new layers were generated. The layered structures of HF-HF-DMSO-8 and HF-HF-DMSO-32 (Figure 16) with dimethyl sulfoxide were not entirely visible after mixing with hydrofluoric acid for 8 and 32 h, respectively.

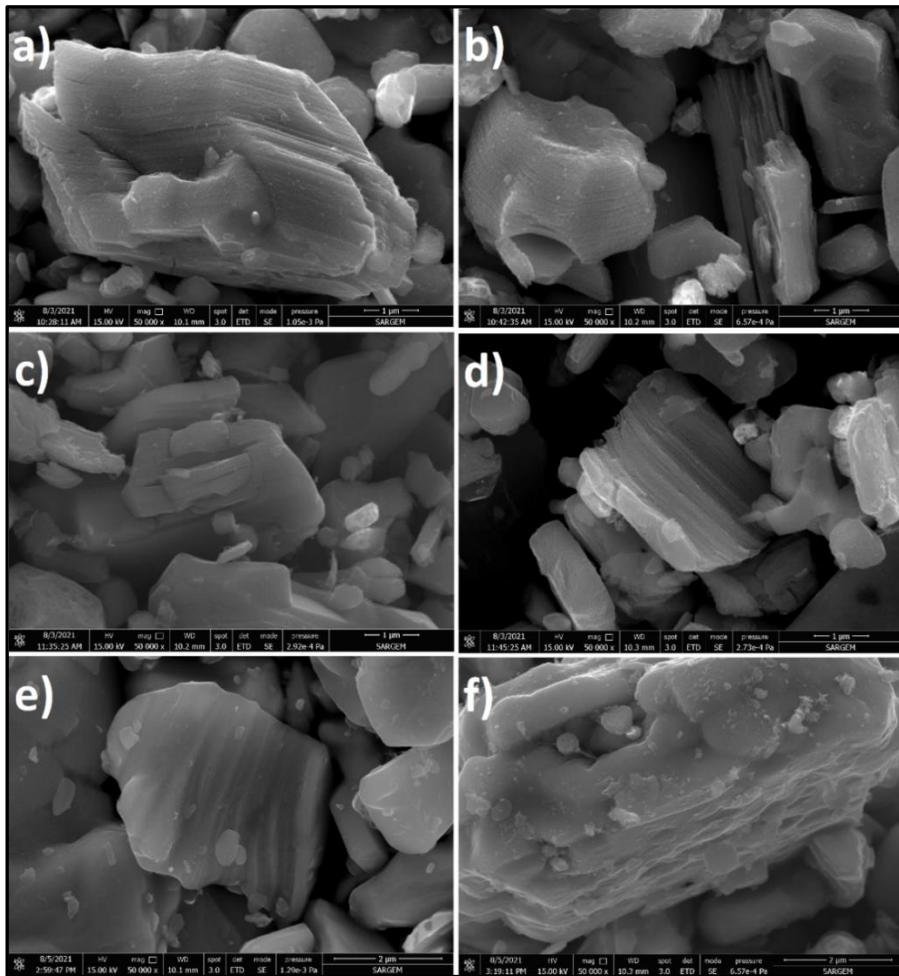


Figure 16. Powders with MXene structure ($Ti_3C_2T_x$) a) HF-8, b) HF-32, c) HF-HF-8, d) HF-HF-32, e) HF-HF-DMSO-8, and f) HF-HF-DMSO-32, FE-SEM images

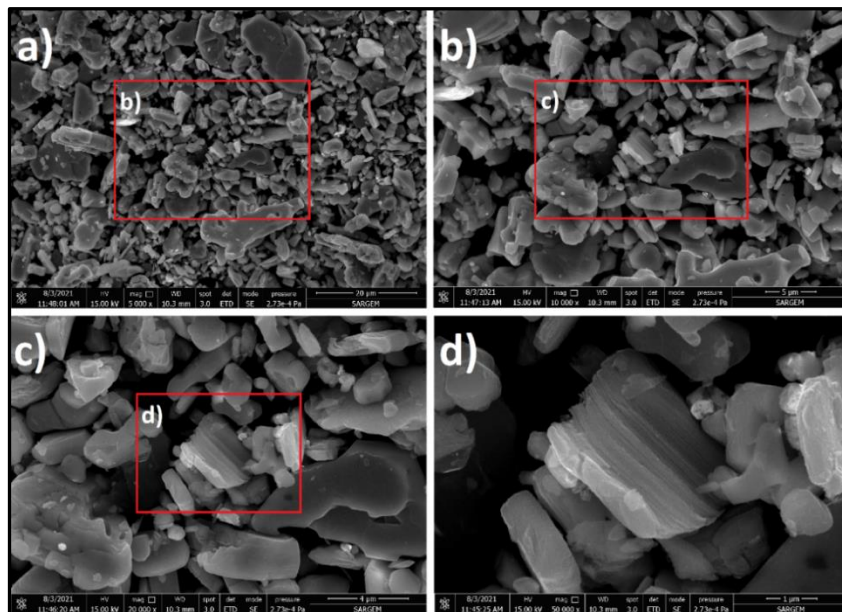


Figure 17. FE-SEM images of HF-HF-32 sample

At four points selected from different locations in the SEM-EDX point analysis of the HF-HF-32 sample, there was a considerable drop in Si compared with the initial powder (Figure 18). Breaking Ti-Si bonds and eliminating Si from the environment are the main reasons for this.

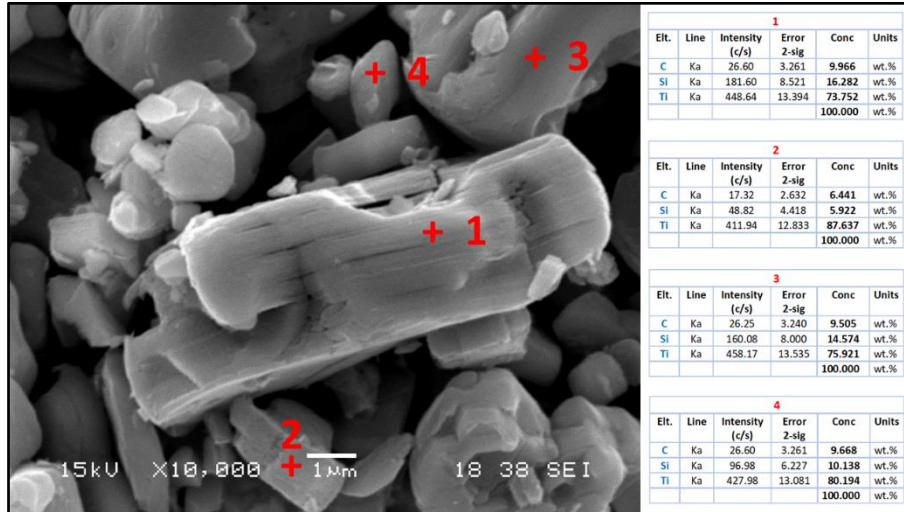


Figure 18. SEM EDX Spot Analysis of HF-HF-32 sample

Changes in Ti, Si, and C are visible in the SEM-EDX line analysis of the HF-HF-32 sample (Figure 19). The rate of silicon difference between the layers varied significantly. A linear relationship is observed between titanium and carbon. The elimination of Si from the environment due to reactions at specific locations is one of the most prominent reasons for this.

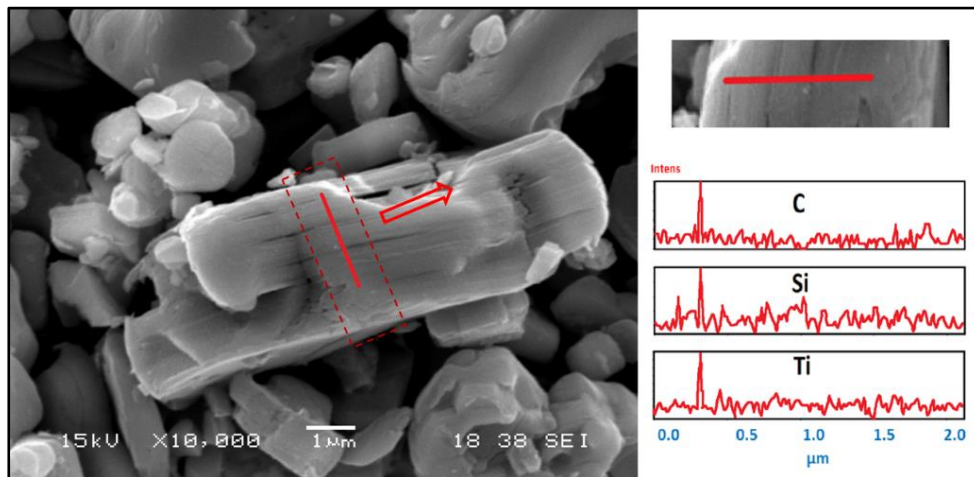


Figure 19. SEM EDX Line Analysis of HF-HF-32 sample

XRD analyses were performed using a RIGAKU D/MAX/2200/PC equipment and a Cu-supplied X-ray tube ($\lambda = 1.54056$). The only MXene that has been successfully delaminated in substantial quantities is $Ti_3C_2T_x$ [34]. XRD and EDS analyses confirmed the conversion of the MAX phase into MXene [8]. XRD studies of MAX-phase Ti_3SiC_2 powder revealed similar characteristics [73]. Figure 20 shows XRD images of the MAX-phase Ti_3SiC_2 sample used as the starting powder. The Ti_3SiC_2 peak at 39.779° was the highest (104). The d value of this peak is 2.2642 \AA [63].

In general, XRD can identify intercalation because the interlayer spacing changes as a result of intercalation, which increases the c-lattice parameter (c-LP) and shifts the corresponding peak at two coordinates to the left [42]. The weakening or removal of all X-ray diffraction (XRD) peaks from the preceding MAX phase indicates effective etching from a crystallographic standpoint [15]. As the mixing temperature and duration were increased, d decreased. The XRD model will only have (0001) peaks (showing material loss in non-basal directions) if the MAX phase is completely converted to MXene, and all other heights will weaken or disappear. The (0001) elevations were initially broad and then narrowed as the angle decreased, suggesting that the lattice parameter increased [8]. The (002) and (004) peaks were split into two when the etching time was increased [1]. Figure 21 shows an XRD comparison of the MAX phase starting powder with MXene-based powders.

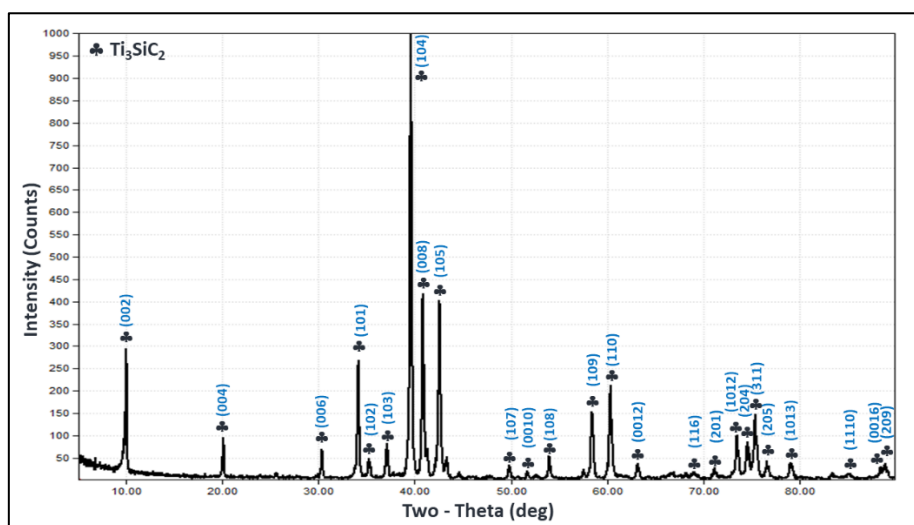


Figure 20. XRD Analysis of MAX phase Ti_3SiC_2 sample

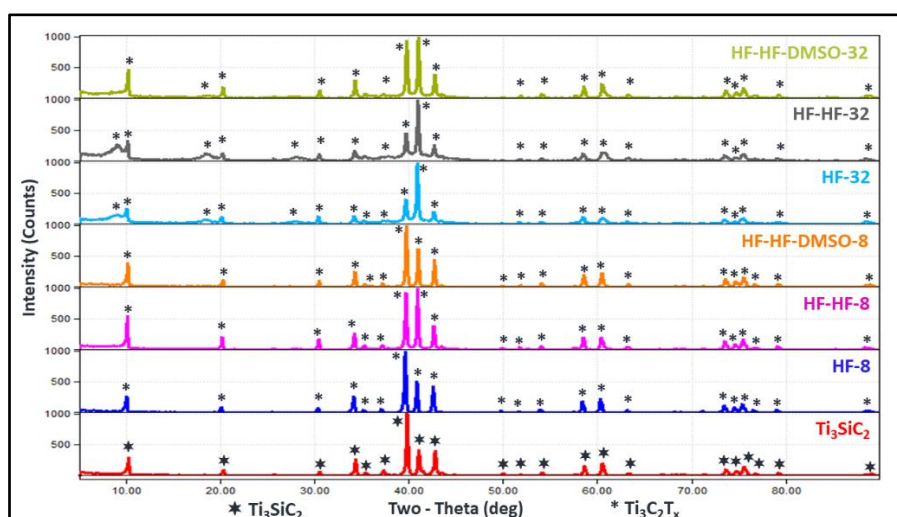


Figure 21. XRD analysis of MAX phase starting powder and other samples

The first (002) peak of the MAX phase shifted downward for $Ti_3C_2T_x$ generated by direct HF exfoliation [13]. The (002), (004), and (006) planes of MXene are assigned to $Ti_3C_2T_x$. The (002) peak was considerably displaced in the spectra of the modified $Ti_3C_2T_x$ and MXene. The high-order (004) and

(006) peaks behaved similarly. The lattice parameters of the modified samples illustrate the expansion of the c-plane distance [84]. (002), (004), (006), (008), and (009) are the XRD patterns of MXenes (110). With the addition of DMSO to MXene and sonication, the (002) pattern was exfoliated [64]. The peaks of the Ti_3SiC_2 sample are displaced to the left by those of the hydrofluoric-acid-treated samples. Some of the peaks are smaller (Figure 22). The peaks at 39.8° , 41° , and 42.7° showed an apparent shift. Compared to the initial powder, the peaks appeared to shift to the left.

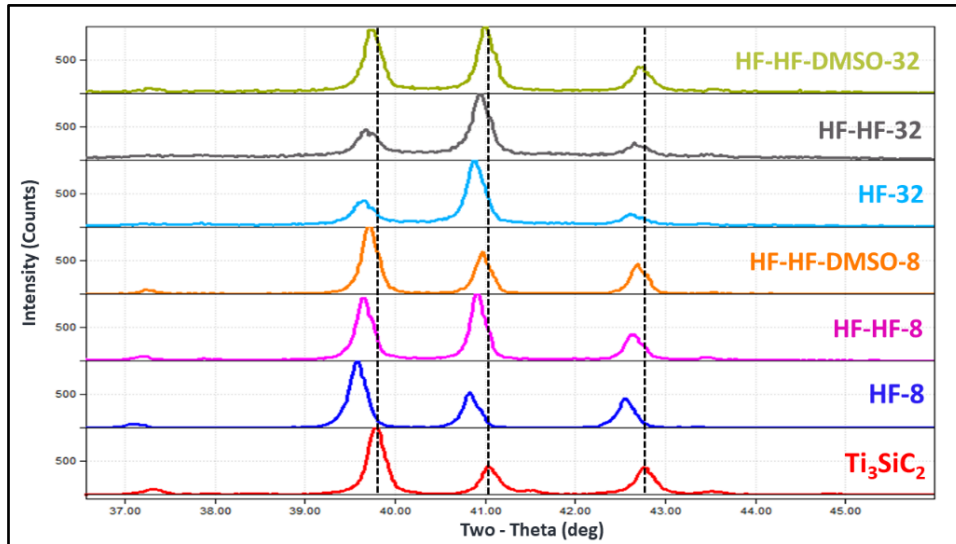


Figure 22. XRD analysis of MAX phase starting powder and other samples

After exfoliation, XRD analysis of the $Ti_3C_2T_x$ sample revealed typical (0001) peaks, indicating that a layered structure was well formed. Dispersion and ultrasonication in ethanol and DMSO increased the intensity of the (002) peak [5]. Peaks (001), such as (002), (004), and (0010), on the other hand, expanded, lost intensity, and shifted to lower angles than their pre-processing positions [55]. MXene peaks are typically seen at 9° and 19° [1], [34], [78]. The XRD analysis of the HF-32 [63] and HF-HF-32 samples revealed MXene production (Figure 23).

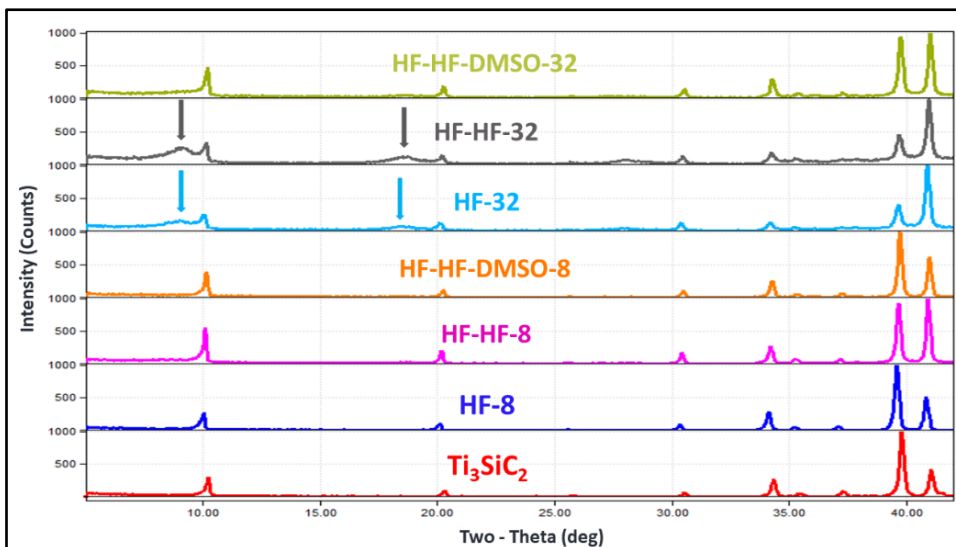


Figure 23. XRD analysis of Starting Powder and other samples

4. CONCLUSIONS

The production of MXene is affected by the long mixing period with hydrofluoric acid. The Si concentration in the powder decreased after being treated twice with hydrofluoric acid. It is clear that MXene conversion occurred at high mixing speeds, resulting in silicon loss. An increase in the mixing time resulted in the formation of multilayer structures. Stratified structures did not form after 8 h of mixing. The inclusion of spin-orbit interaction in the theoretical calculations shows that even though the mass of the compound does not change significantly from the MAX phase to the MXene phase, because of the change in bonding features and density of states contribution rates, SOI is significantly more effective in the MXene phase. The effect of mixing time was observed in obtaining MXene. The structure formed after 32 h of mixing was more stable and two dimensional. This structure provides a positive change in the electronic properties. This is in agreement with the theoretical calculations. New generations of MXene materials are expected to be pioneers in electronic studies. Future studies on MXene compounds will focus on understanding the impact of various surface terminations and intercalations on the electronic, magnetic, and catalytic properties of these materials. . Research will continue to enhance the photocatalytic performance of $Ti_3C_2(OH)_2$ for applications such as hydrogen production, CO_2 reduction, and pollutant degradation. This includes the development of novel Ti_3C_2 -based composites with materials like TiO_2 to improve charge separation and photocatalytic efficiency.

Data Availability

The datasets used and/or analysed during the current study available from the corresponding author on reasonable request.

CONFLICT OF INTEREST

The author stated that there are no conflicts of interest regarding the publication of this article.

CRedit AUTHORSHIP CONTRIBUTION STATEMENT

Mesut Ramazan Ekici: Investigation, Methodology, Writing - original draft, Formal analysis, Writing - review & editing. **Hüseyin Yasin Uzunok:** Conceptualisation, Data curation, Methodology, Writing - review. **Emrah Bulut:** Writing, Supervision, Data Curation, Formal analysis. **Hüseyin Murat Tütüncü:** Writing, Formal analysis, Visualisation. **Ahmet Atasoy:** Writing, Supervision, Data Curation, Formal analysis.

REFERENCES

- [1] Su X, Zhang J, Mu H, et al. Effects of etching temperature and ball milling on the preparation and capacitance of Ti_3C_2 MXene. *Journal of Alloys and Compounds*. 2018;752:32-39. doi:10.1016/j.jallcom.2018.04.152.
- [2] Zhu H. Functional metal carbide nano structures with unique thermal and electrical chemical properties. Published online 2018.
- [3] Shein IR, Ivanovskii AL. Graphene-like titanium carbides and nitrides $Ti_{n+1}C_n$, $Ti_{n+1}N_n$ ($n = 1, 2$, and 3) from de-intercalated MAX phases: First-principles probing of their structural, electronic properties and relative stability. *Computational Materials Science*. 2012;65:104-114. doi:10.1016/j.commatsci.2012.07.011.
- [4] Agartan L, Hantanasirisakul K, Buczek S, et al. Influence of operating conditions on the

- desalination performance of a symmetric pre-conditioned $Ti_3C_2T_x$ -MXene membrane capacitive deionization system. *Desalination*. 2020;477. doi:10.1016/j.desal.2019.114267.
- [5] Lv G, Wang J, Shi Z, Fan L. Intercalation and delamination of two-dimensional MXene ($Ti_3C_2T_x$) and application in sodium-ion batteries. *Materials Letters*. 2018;219:45-50. doi:10.1016/j.matlet.2018.02.016.
- [6] Salim O, Mahmoud KA, Pant KK, Joshi RK. Introduction to MXenes: synthesis and characteristics. *Materials Today Chemistry*. 2019;14:100191. doi:10.1016/j.mtchem.2019.08.010.
- [7] Eklund P, Rosen J, Persson POÅ. Layered ternary $M_{n+1}AX_n$ phases and their 2D derivative MXene: An overview from a thin-film perspective. *Journal of Physics D: Applied Physics*. 2017;50(11). doi:10.1088/1361-6463/aa57bc.
- [8] Venkateshalu S, Grace AN. MXenes-A new class of 2D layered materials: Synthesis, properties, applications as supercapacitor electrode and beyond. *Applied Materials Today*. 2020;18:100509. doi:10.1016/j.apmt.2019.100509.
- [9] Alhabe M, Maleski K, Mathis TS, et al. Selective Etching of Silicon from Ti_3SiC_2 (MAX) To Obtain 2D Titanium Carbide (MXene). *Angewandte Chemie - International Edition*. 2018;57(19):5444-5448. doi:10.1002/anie.201802232.
- [10] Cui G, Zheng X, Lv X, Jia Q, Xie W, Gu G. Synthesis and microwave absorption of $Ti_3C_2T_x$ MXene with diverse reactant concentration, reaction time, and reaction temperature. *Ceramics International*. 2019;45(17):23600-23610. doi:10.1016/j.ceramint.2019.08.071.
- [11] Gogotsi Y, Anasori B. The Rise of MXenes. *ACS Nano*. 2019;13(8):8491-8494. doi:10.1021/acsnano.9b06394.
- [12] Zhao S, Nivetha R, Qiu Y, Guo X. Two-dimensional hybrid nanomaterials derived from MXenes ($Ti_3C_2T_x$) as advanced energy storage and conversion applications. *Chinese Chemical Letters*. 2020;31(4):947-952. doi:10.1016/j.cclet.2019.11.045.
- [13] Rasool K, Pandey RP, Rasheed PA, Buczek S, Gogotsi Y, Mahmoud KA. Water treatment and environmental remediation applications of two-dimensional metal carbides (MXenes). *Materials Today*. 2019;30(November):80-102. doi:10.1016/j.mattod.2019.05.017.
- [14] Halim J, Cook KM, Naguib M, et al. X-ray photoelectron spectroscopy of select multi-layered transition metal carbides (MXenes). *Applied Surface Science*. 2016;362:406-417. doi:10.1016/j.apsusc.2015.11.089.
- [15] Collini P. Deposizione Elettroforetica Di Film Di Mxene Per Applicazioni Funzionali. *MaxMaterialsDrexelEdu*. Published online 2017. http://max.materials.drexel.edu/wp-content/uploads/Pieralberto_Collini.pdf.
- [16] Tang J, Yi W, Zhong X, et al. Laser writing of the restacked titanium carbide MXene for high performance supercapacitors. *Energy Storage Materials*. 2020;32(July):418-424. doi:10.1016/j.ensm.2020.07.028.
- [17] Wild M, Gregory J. *Offe. Lithium-Sulfur Batteries*. John Wiley & Sons Ltd; 2019.

- [18] Shi L. From MAX phases to MXenes : synthesis, characterization and electronic properties. Published online 2017.
- [19] Jo G. Proton Hopping in a Single Layer Water Between MXene Layers Using ReaxFF MD Simulation. 2017;(May).
- [20] Halim J. Synthesis and Characterization of 2D Nanocrystals and Thin Films of Transition Metal Carbides (MXenes). 2014;(1679). doi:10.3384/lic.diva-111128.
- [21] Magné D. Synthèse et structure électronique de phases MAX et MXènes. Published online 2016. <http://nuxeo.edel.univ-poitiers.fr/nuxeo/site/esupversions/83ffbfba-e881-4604-9aff-2875945e1f3b>.
- [22] M. Higashi, S. Momono, K. Kishida, N. L. Okamoto, and H. Inui, “Anisotropic plastic deformation of single crystals of the MAX phase compound Ti_3SiC_2 investigated by micropillar compression,” *Acta Materialia*, vol. 161, pp. 161–170, 2018, doi: 10.1016/j.actamat.2018.09.024.
- [23] Zhu M, Wang R, Chen C, Zhang HB, Zhang GJ. Comparison of corrosion behavior of Ti_3SiC_2 and Ti_3AlC_2 in NaCl solutions with Ti. *Ceramics International*. 2017;43(7):5708-5714. doi:10.1016/j.ceramint.2017.01.111.
- [24] Sun ZM, Zou Y, Tada S, Hashimoto H. Effect of Al addition on pressureless reactive sintering of Ti_3SiC_2 . *Scripta Materialia*. 2006;55(11):1011-1014. doi:10.1016/j.scriptamat.2006.08.019.
- [25] Zhang J, Wang L, Jiang W, Chen L. Effect of TiC content on the microstructure and properties of Ti_3SiC_2 -TiC composites in situ fabricated by spark plasma sintering. *Materials Science and Engineering A*. 2008;487(1-2):137-143. doi:10.1016/j.msea.2007.12.004.
- [26] Anasori B, Lukatskaya MR, Gogotsi Y. 2D metal carbides and nitrides (MXenes) for energy storage. *Nature Reviews Materials*. 2017;2(2). doi:10.1038/natrevmats.2016.98.
- [27] Li J, Kurra N, Seredych M, Meng X, Wang H, Gogotsi Y. Bipolar carbide-carbon high voltage aqueous lithium-ion capacitors. *Nano Energy*. 2019;56(November 2018):151-159. doi:10.1016/j.nanoen.2018.11.042.
- [28] Hu T, Yang J, Wang X. Carbon vacancies in Ti_2CT_2 MXenes: Defects or a new opportunity? *Physical Chemistry Chemical Physics*. 2017;19(47):31773-31780. doi:10.1039/c7cp06593k.
- [29] Wang Y, Feng W, Chen Y. Chemistry of two-dimensional MXene nanosheets in theranostic nanomedicine. *Chinese Chemical Letters*. 2020;31(4):937-946. doi:10.1016/j.ccllet.2019.11.016.
- [30] Ward J, Middleburgh S, Topping M, et al. Crystallographic evolution of MAX phases in proton irradiating environments. *Journal of Nuclear Materials*. 2018;502:220-227. doi:10.1016/j.jnucmat.2018.02.008.
- [31] Jung Y II, Park DJ, Park JH, Park JY, Kim HG, Koo YH. Effect of $TiSi_2/Ti_3SiC_2$ matrix phases in a reaction-bonded SiC on mechanical and high-temperature oxidation properties. *Journal of the European Ceramic Society*. 2016;36(6):1343-1348. doi:10.1016/j.jeurceramsoc.2016.01.015.
- [32] Khazaei M, Ranjbar A, Arai M, Sasaki T, Yunoki S. Electronic properties and applications of MXenes: a theoretical review. *Journal of Materials Chemistry C*. 2017;5(10):2488-2503. doi:10.1039/c7tc00140a.

- [33] Acerce M. Electrochemical Charge Storage and Electrochemomechanical Behavior of Chemically Exfoliated & Restacked MoS₂ Nanosheets. Published online 2016.
- [34] Abdelmalak MN. MXenes: A New Family of Two-Dimensional Materials and its Application as Electrodes for Li-ion Batteries. Published online 2014.
- [35] Boota M. Redox-Active Hybrid Materials for Pseudocapacitive Energy Storage. ECS Meeting Abstracts. 2017;(September). doi:10.1149/ma2017-01/43/2013.
- [36] Ghidui MJ. Ions in MXene: Characterization and Control of Interlayer Cations and their Effects on Structure and Properties of 2D Transition Metal Carbides. 2018;(June).
- [37] Colón MG. Max-Phase Slurry Coatings For High Temperature Oxidation Protection of Ti Based Alloys. Published online 2014.
- [38] Lane NJ. Lattice Dynamical Studies of Select MAX Phases. 2013;(April).
- [39] Karlsson L. Transmission Electron Microscopy of 2D Materials: Structure and Surface Properties. 2016;(1745). doi:10.3384/diss.diva-127526.
- [40] Zhang X, Liu Y, Dong S, Yang J, Liu X. Flexible electrode based on multi-scaled MXene (Ti₃C₂T_x) for supercapacitors. *Journal of Alloys and Compounds*. 2019;790:517-523. doi:10.1016/j.jallcom.2019.03.219.
- [41] Wen Y, Rufford TE, Chen X, et al. Nitrogen-doped Ti₃C₂T_x MXene electrodes for high-performance supercapacitors. *Nano Energy*. 2017;38(June):368-376. doi:10.1016/j.nanoen.2017.06.009.
- [42] Lukatskaya MR. Capacitive Performance of Two-Dimensional Metal Carbides. 2015;(December). doi:10.1145/3132847.3132886.
- [43] Ahmed B. Surface Modification of MXenes: A Pathway to Improve MXene Electrode Performance in Electrochemical Energy Storage Devices. Published online 2017.
- [44] Rajagopalan Kannan DR, Terala PK, Moss PL, Weatherspoon MH. Analysis of the Separator Thickness and Porosity on the Performance of Lithium-Ion Batteries. *International Journal of Electrochemistry*. 2018;2018:1-7. doi:10.1155/2018/1925708.
- [45] Meng J, Zhang F, Zhang L, et al. Rolling up MXene sheets into scrolls to promote their anode performance in lithium-ion batteries. *Journal of Energy Chemistry*. 2020;46:256-263. doi:10.1016/j.jechem.2019.10.008.
- [46] Wang CH, Kurra N, Alhabeb M, Chang JK, Alshareef HN, Gogotsi Y. Titanium Carbide (MXene) as a Current Collector for Lithium-Ion Batteries. *ACS Omega*. 2018;3(10):12489-12494. doi:10.1021/acsomega.8b02032.
- [47] Tang H, Li W, Pan L, et al. A Robust, Freestanding MXene-Sulfur Conductive Paper for Long-Lifetime Li-S Batteries. *Advanced Functional Materials*. 2019;29(30):1-10. doi:10.1002/adfm.201901907.
- [48] Jiang W, Henager CH, Varga T, et al. Diffusion of Ag, Au and Cs implants in MAX phase

- Ti₃SiC₂. Journal of Nuclear Materials. 2015;462:310-320. doi:10.1016/j.jnucmat.2015.04.002
- [49] Jacques S, Fakih H, Viala JC. Reactive chemical vapor deposition of Ti₃SiC₂ with and without pressure pulses: Effect on the ternary carbide texture. Thin Solid Films. 2010;518(18):5071-5077. doi:10.1016/j.tsf.2010.02.059.
- [50] Cao MS, Cai YZ, He P, Shu JC, Cao WQ, Yuan J. 2D MXenes: Electromagnetic property for microwave absorption and electromagnetic interference shielding. Chemical Engineering Journal. 2019;359(November 2018):1265-1302. doi:10.1016/j.cej.2018.11.051.
- [51] Min B. Broadly defined synthesis and properties of phase change materials. Published online 2018.
- [52] Mashtalir O. Chemistry of Two-Dimensional Transition Metal Carbides (MXenes). Published online 2015.
- [53] Jaffari ZH, Abuabdou SMA, Ng D-Q, Bashir MJK. Insight into two-dimensional MXenes for environmental applications: Recent progress, challenges, and prospects. FlatChem. 2021;28(April):100256. doi:10.1016/j.flatc.2021.100256.
- [54] Ashton M. Computational Methods for the Discovery and Characterization of Two-Dimensional Materials. Published online 2017.
- [55] Naguib M, Kurtoglu M, Presser V, et al. Two-Dimensional Nanocrystals Produced by Exfoliation of Ti₃AlC₂. Advanced Materials. 2011;23(37):4248-4253. doi:10.1002/adma.201102306.
- [56] Liao Y, Qian J, Xie G, et al. 2D-layered Ti₃C₂ MXenes for promoted synthesis of NH₃ on P₂₅ photocatalysts. Applied Catalysis B: Environmental. 2020;273(February):119054. doi:10.1016/j.apcatb.2020.119054.
- [57] Wen Y, Li R, Liu J, et al. A temperature-dependent phosphorus doping on Ti₃C₂T_x MXene for enhanced supercapacitance. Journal of Colloid and Interface Science. 2021;604:239-247. doi:10.1016/j.jcis.2021.06.020.
- [58] Chen Y-H, Qi M-Y, Li Y-H, et al. Activating two-dimensional Ti₃C₂T_x-MXene with single-atom cobalt for efficient CO₂ photoreduction. Cell Reports Physical Science. 2021;2(3):100371. doi:10.1016/j.xcrp.2021.100371.
- [59] Zhao X, Chen J, Zhao C, et al. Construction ZnIn₂S₄/Ti₃C₂ of 2D/2D heterostructures with enhanced visible light photocatalytic activity: A combined experimental and first-principles DFT study. Applied Surface Science. 2021;570(August):151183. doi:10.1016/j.apsusc.2021.151183.
- [60] Mondal K, Ghosh P. Exfoliation of Ti₂C and Ti₃C₂ Mxenes from bulk trigonal phases of titanium carbide: A theoretical prediction. Solid State Communications. 2019;299(March):113657. doi:10.1016/j.ssc.2019.113657.
- [61] Ekici MR, Atasoy A. Graphene Alternative 2D Materials: MXene. In: 20th International Metallurgy and Materials Congress. ; 2021:396-400.
- [62] Ekici MR, Atasoy A. Effect of HF Acid on The Formation of New 2D Ti₃C₂ Mxene From Ti₃SiC₂. Selcuk University Journal of Engineering Sciences. 2020;Special Is(1):1-23. <https://sujes.selcuk.edu.tr/sujes/article/view/512>.

- [63] Ekici MR, Tabar E, Atasoy A, Bulut E, Hoşgör G. Effect of hydrochloric acid and hydrofluoric acid treatment on the morphology, structure and gamma permeability of 2D MXene $Ti_3C_2T_x$ electrodes. *Canadian Metallurgical Quarterly*. Published online September 16, 2022:1-22. doi:10.1080/00084433.2022.2124108.
- [64] Chae A, Jang H, Koh DY, Yang CM, Kim YK. Exfoliated MXene as a mediator for efficient laser desorption/ionization mass spectrometry analysis of various analytes. *Talanta*. 2020;209(November 2019):120531. doi:10.1016/j.talanta.2019.120531.
- [65] Ren C (Evelyn). Interaction of Ions with Two-Dimensional Transition Metal Carbide (MXene) Films. ProQuest Dissertations and Theses. 2017;(July).
- [66] Dall'Agnese Y. Study of Early Transition Metal Carbides for Energy Storage Applications. 2016;(March).
- [67] Steinberg J a. Formation of Thin Films from MXene Flakes. Published online 2013.
- [68] Zhang C (John), Nicolosi V. Graphene and MXene-based transparent conductive electrodes and supercapacitors. *Energy Storage Materials*. 2019;16(May 2018):102-125. doi:10.1016/j.ensm.2018.05.003.
- [69] Shah JB. Synthesis of MXene-Epoxy Nanocomposites. 2017;(June).
- [70] Hatter CB, Shah J, Anasori B, Gogotsi Y. Micromechanical response of two-dimensional transition metal carbonitride (MXene) reinforced epoxy composites. *Composites Part B: Engineering*. 2020;182(June 2019):107603. doi:10.1016/j.compositesb.2019.107603.
- [71] Rosenkranz A, Grützmacher PG, Espinoza R, et al. Multi-layer $Ti_3C_2T_x$ -nanoparticles (MXenes) as solid lubricants - Role of surface terminations and intercalated water. *Applied Surface Science*. 2019;494(July):13-21. doi:10.1016/j.apsusc.2019.07.171.
- [72] Zhang S. Study of chemical reactivity of MAX phase single crystals. Published online 2018.
- [73] Aghamohammadi H, Heidarpour A, Jamshidi R. The phase and morphological evolution of Ti_3SiC_2 MAX phase powder after HF treatment. *Ceramics International*. 2018;44(15):17992-18000. doi:10.1016/j.ceramint.2018.06.278.
- [74] Piechowiak MA, Henon J, Durand-Panteix O, et al. Growth of dense Ti_3SiC_2 MAX phase films elaborated at room temperature by aerosol deposition method. *Journal of the European Ceramic Society*. 2014;34(5):1063-1072. doi:10.1016/j.jeurceramsoc.2013.11.019.
- [75] Schultheiß J, Dermeik B, Filbert-Demut I, et al. Processing and characterization of paper-derived Ti_3SiC_2 based ceramic. *Ceramics International*. 2015;41(10):12595-12603. doi:10.1016/j.ceramint.2015.06.085.
- [76] Guo J, Zhao Y, Liu A, Ma T. Electrostatic self-assembly of 2D delaminated MXene (Ti_3C_2) onto Ni foam with superior electrochemical performance for supercapacitor. *Electrochimica Acta*. 2019;305:164-174. doi:10.1016/j.electacta.2019.03.025.
- [77] Rangom YP. Double Layer Formation and Cation Pseudo- Intercalation Supercapacitor Carbon Nanotube Composite Electrodes with Enhanced Electrochemical Performances. Published online

2014.

- [78] Li Z, Wang L, Sun D, et al. Synthesis and thermal stability of two-dimensional carbide MXene Ti_3C_2 . *Materials Science and Engineering B: Solid-State Materials for Advanced Technology*. 2015;191(C):33-40. doi:10.1016/j.mseb.2014.10.009.
- [79] Giannozzi P, Baroni S, Bonini N, et al. QUANTUM ESPRESSO: a Modular and Open-source Software project for Quantum Simulations of Materials. *Journal of Physics: Condensed Matter*. 2009;21(39):395502. doi:10.1088/0953-8984/21/39/395502.
- [80] Giannozzi P, Andreussi O, Brumme T, et al. Advanced Capabilities for Materials Modelling With Quantum ESPRESSO. *Journal of Physics: Condensed Matter*. 2017;29(46):465901. doi:10.1088/1361-648X/aa8f79.
- [81] Perdew JP, Burke K, Ernzerhof M. Generalized Gradient Approximation Made Simple. *Physical Review Letters*. 1996;77(18):3865-3868. doi:10.1103/PhysRevLett.77.3865.
- [82] Arunajatesan S, Carim AH. Symmetry and crystal structure of Ti_3SiC_2 . *Materials Letters*. 1994;20(5-6):319-324. doi:10.1016/0167-577X(94)90037-X.
- [83] Pinek D, Ito T, Furuta K, et al. Near Fermi Level Electronic Structure of Ti_3SiC_2 Revealed by Angle-resolved Photoemission Spectroscopy. *Physical Review B*. 2020;102(7):075111. doi:10.1103/PhysRevB.102.075111.
- [84] Zhang L, Su W, Shu H, et al. Tuning the photoluminescence of large $Ti_3C_2T_x$ MXene flakes. *Ceramics International*. 2019;45(9):11468-11474. doi:10.1016/j.ceramint.2019.03.014.



RESEARCH ARTICLE

EFFICIENT DRUG CARRIER FOR ACETYLSALICYLIC ACID FROM CHITOSAN-BASED COMPOSITES PREPARED WITH MONTMORILLONITE, CELLULOSE AND HYDROXYAPATITE

Dilay SEZER^{1,*}, **Zeynep AKTAŞ**², **Seda HOŞGÜN**³, **Emir Zafer HOŞGÜN**^{4,*}, **Berrin BOZAN**⁵

¹ Chemical Engineering Department, Engineering Faculty, Eskişehir Technical University, Eskişehir, Türkiye
dilaaaysezer@gmail.com - [0000-0003-1537-0744](https://orcid.org/0000-0003-1537-0744)

² Chemical Engineering Department, Engineering Faculty, Eskişehir Technical University, Eskişehir, Türkiye
zeynep.aktas@eskisehir.edu.tr - [0000-0002-1070-5560](https://orcid.org/0000-0002-1070-5560)

³ Chemical Engineering Department, Engineering and Architecture Faculty, Eskişehir Osmangazi University, Eskişehir, Türkiye.
serol@ogu.edu.tr - [0000-0002-5884-9723](https://orcid.org/0000-0002-5884-9723)

⁴ Chemical Engineering Department, Engineering Faculty, Eskişehir Technical University, Eskişehir, Türkiye
ezhosgun@eskisehir.edu.tr - [0000-0002-3810-701X](https://orcid.org/0000-0002-3810-701X)

⁵ Chemical Engineering Department, Engineering Faculty, Eskişehir Technical University, Eskişehir, Türkiye
bbozan@eskisehir.edu.tr - [0000-0002-3112-5784](https://orcid.org/0000-0002-3112-5784)

Abstract

In this study, chitosan-based hydroxyapatite/chitosan (HAP/CHI), cellulose/chitosan (CEL/CHI) and montmorillonite/chitosan (MMT/CHI) composites were synthesized and characterized by Fourier Transform Infrared Spectroscopy (FTIR), Scanning Electron Microscopy (SEM) and Thermogravimetric Analysis (TGA). Acetylsalicylic acid (ASA) was used as a drug for loading and desorption studies to determine the release behavior of the synthesized composites. The maximum adsorption capacities (qe) were obtained as 251.5 mg/g, 197.7 mg/g and 288.95 mg/g for HAP/CHI, CEL/CHI and MMT/CHI, respectively. In vitro release studies of ASA from the composites HAP/CHI, CEL/CHI, and MMT/CHI were carried out phosphate buffer solution (PBS) and gastric juice (GJ). In the intestinal medium (PBS) controlled drug release continued for 72 hours (4320 minutes), and burst release was observed in the first 5 minutes in all composites. 19.16%, 47.15% and 37.32% of the active ingredient from HAP/CHI, CEL/CHI and MMT/CHI composites, respectively, were released in the first 5 minutes. After 5 minutes, the release slowed down and became more controlled for all three composites. At the end of the release, the highest releasing composite was CEL/CHI, with 95.77% ASA release. A total drug release of 87.48% was achieved with MMT/CHI and 87.37% with HAP/CHI. In the gastric environment (GJ) Controlled drug release continued for 72 hours (4320 minutes), and burst release was observed in the first 5 minutes in all composites. 52.51%, 72.30% and 44.87% of the active ingredient from HAP/CHI, CEL/CHI and MMT/CHI composites, respectively, were released in the first 5 minutes. After 5 minutes, the release slowed down and became more controlled for all three composites. At the end of the release, the highest releasing capacity was found with the CEL/CHI composite, with 96.05% ASA release. A total drug release of 93.26% was achieved with HAP/CHI and 84.89% with MMT/CHI.

Keywords

Chitosan,
Drug delivery,
Composite,
Acetylsalicylic acid,
Montmorillonite

Time Scale of Article

Received :31 January 2024
Accepted : 06 August 2024
Online date : 30 September 2024

1. INTRODUCTION

Recently, biopolymer composite minerals have attracted considerable research interest for biomedical and pharmaceutical applications [1]. Compared to synthetic polymers, natural polymers have benefits like biocompatibility, biodegradability, and biologically identifiable components that promote cellular functions [2]. Chitosan (CHI), one of the biopolymers, is a potential option for creating artificial bone scaffolds because of its superior hemostasis, adsorptive qualities, biocompatibility, and antibacterial activity. These qualities are widely used in biomedical, cosmetic, and water treatment applications [3-5]. Although chitosan has advanced the development of safe and effective drug delivery systems [6], its properties, including adsorption capacity, weak mechanical strength, irregular size, lack of process repeatability and chemical resistance need to be enhanced. Consequently, in order to produce chitosan beads, microspheres, films, or fibers with a stable size and enhanced mechanical qualities, physical and chemical modifications have been suggested [7].

According to recent research, clay minerals such magnesium aluminum silicate, montmorillonite, and laponite enhance chitosan's mechanical and thermal resilience as well as its rate of drug release and encapsulation. This is mostly because of their advantageous characteristics, which include mechanical stability, high specific surface areas, biocompatibility, huge pore volumes, and chemical inertness [1]. The inorganic calcium phosphate substance known as hydroxyapatite (HAP) is a crucial part of human bones and teeth. HAP can be obtained from natural sources or through chemical synthesis and is a biodegradable material with very good bioactive properties. Due to its numerous beneficial properties, including excellent biocompatibility, bioactivity, osteo conductivity, and anti-inflammatory properties, HAP has been extensively studied for biomedical applications [8,9]. Considering these properties, HAP, which can be obtained synthetically using a suitable calcium and phosphate source, is used as a good adsorbent for many substances such as proteins, antitoxins, antibiotics and growth factors.

Montmorillonite (MMT) supports drug release by strongly adsorbing to the drug molecules and improves the bioavailability and dissolution rate of hydrophobic drugs [10]. Because of their great adsorption capacity, high specific surface area, swelling ability, and ability to create appropriate particle sizes for embolization, MMT particles are perfectly suited for the creation of drug carrier embolization agents [11].

The most prevalent biopolymer in nature is cellulose (CEL), which may be dissolved and transformed into regenerated useful materials in a variety of shapes and sizes, including films, hydrogels, microspheres, and fibers. However, the lack of antimicrobial activity and poor bioactivity of cellulose restricts its use in antibacterial packaging and biomaterials. In order to address this issue and optimize cellulose's use, it is typically combined or altered with other polymers [4].

Aspirin, which was chosen as the model drug in this study, obtained by the acetylation of salicylic acid, has a long history as an antipyretic and analgesic drug. Acetylsalicylic acid (ASA) is a nonsteroidal drug with anti-inflammatory, analgesic, and antipyretic effects. Furthermore, taking a large amount of ASA orally can have unfavorable side effects such as ulcers, bleeding in the stomach, and tinnitus. Consequently, it would be preferable if the medications containing ASA, and its controlled release feature were combined. This would allow the ASA to be released gradually and create the proper drug concentration in plasma. Consequently, a great option for the polymeric drug to generate the controlled release of ASA would be to combine the chitosan drug carrier with the ASA drug [12]. To our knowledge, there are no other studies using chitosan composites for the release of acetylsalicylic acid.

In this study, chitosan-based composites hydroxyapatite/chitosan (HAP/CHI), cellulose/chitosan (CEL/CHI) and montmorillonite/chitosan (MMT/CHI) were synthesized to improve the resistance and drug delivery properties of chitosan for pharmaceutical systems, and the loading capacity and release behavior of acetylsalicylic acid in phosphate buffer solution (PBS) and gastric environment (GJ) medium were investigated.

2. MATERIALS AND METHODS

2.1. Materials

The following materials were used without further purification: Calcium nitrate ($\text{Ca}(\text{NO}_3)_2$) (98%) from Carlo Erba. Phosphoric acid (H_3PO_4) (85%) from J.T. Baker. Ammonia solution (NH_4OH) (25%), sodium chloride (NaCl) and cellulose (CEL) from Merck. Potassium phosphate monobasic (KH_2PO_4) and sodium phosphate dibasic heptahydrate ($\text{Na}_2\text{HPO}_4 \cdot 7\text{H}_2\text{O}$) from Riedel-de Haën. Acetylsalicylic acid (ASA) (99%) from Alfa Aesar. Cetyltrimethylammonium bromide (CTAB), montmorillonite (MMT) and chitosan (CHI) (high molecular weight) from Sigma-Aldrich.

2.2. Synthesis of Hydroxyapatite (HAP)

The HAP samples were synthesized by the chemical precipitation technique. The surfactants were used at an estimated yield of 1% (w/w) HAP after being dissolved in water. The target Ca/P ratio was 1.67. While the H_3PO_4 solution (0.72 M) was added dropwise, the $\text{Ca}(\text{NO}_3)_2$ (1.2 M) solution was stirred constantly. A pH of 10 was maintained with NH_4OH (25%) [13]. At this point, the solution became milky and for surface modification 0.1 mM CTAB solution was added, and it was stirred for 30 min before being allowed at room temperature for a day. After filtration, the HAP samples underwent washing with distilled water, followed by drying in oven, and finally calcined at 550 °C for 6 hours, with a heating rate of 2 °C/min.

2.3. Preparation of Composites

All of the composites were synthesized with chitosan solution which is prepared same methodology that given below.

10 mL of 1% (v/v) acetic acid (CH_3COOH) and 100 mg of chitosan were stirred on a magnetic stirrer at 1000 rpm for 30 min until it became transparent, and then treated in an ultrasonic water bath for 5 min.

100 mg of HAP, CEL, MMT and 100 mL of distilled water were added and then placed in an ultrasonic water bath for 30 min. Composite suspensions were added to the prepared chitosan solution and then stirred on a magnetic stirrer at 1500 rpm for 24 hours. Then 2M NaOH solution was added dropwise with a syringe and stirred on a magnetic stirrer at 500 rpm. After 24 h, the samples were centrifuged at 4000 rpm for 20 min and washed with distilled water until pH neutral. The samples were collected and dried at 60 °C for 24 hours. After 24 hours, the samples were completely dried and the composites were collected, stored for further analysis and labeled as HAP/CHI, CEL/CHI and MMT/CHI.

2.4. ASA Loading

To investigate ASA's adsorption capability on the chitosan-based composites, 50 mg of acetylsalicylic acid was dissolved in 100 mL of distilled water, and 300 mg of each composite (HAP/CHI, CEL/CHI, and MMT/CHI) was submerged in a 500 mL ASA solution (0.5 mg/mL) for 24 hours at 25 °C in a shaking water bath. On the chitosan-based composites, the adsorption capability was ascertained. Following the adsorption procedure, the liquid phase was filtered, and a UV spectrophotometer (Shimadzu UV-1800) set to 275 nm was used to measure the concentration of ASA in the solution.

The amount of ASA adsorbed per gram of composite, q_e (mg/g), was calculated according to Equation 1.

$$q_e = V \times \frac{(C_o - C_t)}{m} \quad (1)$$

Where V is the solution volume (L), C_o is the initial concentration of ASA (mg/L), C_t is the concentration of ASA at a given time, and m is the amount of composite (g).

2.5. In vitro Drug Release Studies

To investigate the ASA release, 10 mL of phosphate-buffered saline (PBS) (pH = 7.4) and GJ (pH = 1.2) were mixed with approximately 20 mg of the samples loaded with ASA HAP/CHI, CEL/CHI, and MMT/CHI. To make the PBS solution, distilled water was mixed with KH_2PO_4 , $\text{Na}_2\text{HPO}_4 \cdot 7\text{H}_2\text{O}$, and NaCl. To make GJ solution, 0.01 M HCl solution with pH 1.2 was used. The experiments were conducted in a shaking bath at 37 °C and 50 rpm. A sample was taken from solution, and it was measured with the UV spectrophotometer at a prearranged time interval. The system was then replenished with fresh solution in order to maintain a steady volume. The total amount of ASA released within each time interval was determined based on the absorbance values, allowing for the calculation of the concentration and subsequent mass of ASA released [14,15].

2.6. Characterizations of Composites

For characterization studies of composites, FT-IR, SEM and TGA analyzes were used. Thermoscientific Nicolet IS10 FT-IR, which is outfitted with a universal ATR sample adapter, was utilized for conducting FT-IR analyses. 64 scans of ATR-FT-IR spectra were obtained at a resolution of 4 cm^{-1} , covering the spectral range of 4000-650 cm^{-1} . Using a HITACHI TM 3030 Plus SEM apparatus, pictures were captured to gather data on the materials' surface morphology. The produced samples were subjected to a Thermogravimetric Analysis in nitrogen atmosphere (N_2) using a TGA instrument (TGA 4000, Perkin Elmer) from 40 to 800 °C at a heating rate of 10 °C/min.

3. RESULTS AND DISCUSSION

3.1. Characterization of Composites

The synthesized HAP/CHI, CEL/CHI, and MMT/CHI samples were characterized by FT-IR, TGA and SEM analysis. The sample's functional groups were ascertained by FT-IR analysis. All of the synthetic composites' spectra showed characteristic bands at about 3570 cm^{-1} , which corresponded to the distinct stretching vibration modes of the OH- groups. (Figure 1). According to the HAP/CHI spectra, the bands at 3343 and 1654 cm^{-1} belong to adsorbed water, which could be OH- groups present in HAP dust and reacting with atmospheric carbon dioxide [16]. A strong band appeared at 3568 cm^{-1} , which was due to $(\text{PO}_4)^{3-}$ ions. The bands at 1028 cm^{-1} were characteristic of phosphate stretch vibrations, and the bands observed at 603 cm^{-1} and 568 cm^{-1} were due to phosphate bending vibrations. The peaks around 1400 cm^{-1} in the FTIR spectra indicate the $(\text{CO}_3)^{2-}$ groups. The peaks at about 1600 cm^{-1} and 2800 show the spectral features of the -NH groups and -CH group of chitosan [17, 18].

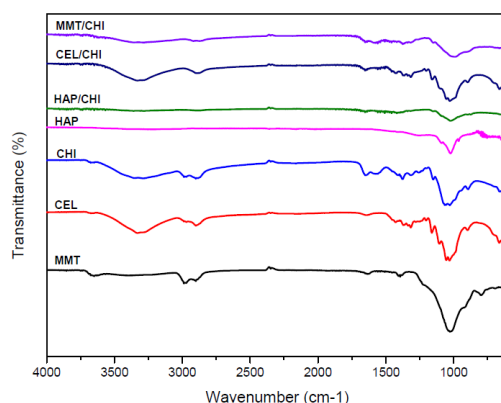


Figure 1. FTIR spectra of HAP, CHI, CEL, MMT, HAP/CHI, CEL/CHI and MMT/CHI

According to the CEL/CHI spectra, the strong vibrational band at 3330 cm^{-1} is considered to be O-H stretching. The band at 2901 cm^{-1} corresponds to the C-H stretching of the aliphatic groups. The vibrational bands at 1656 cm^{-1} and 1457 cm^{-1} in the FTIR spectrum of the cellulose/chitosan composite are expressions of the vibrations associated with the O-H and the N-H group, respectively. Although the molecular structure of chitosan and cellulose is quite similar, the main difference between them can be explained by the spectra of NH stretching at 3330 cm^{-1} and 1457 cm^{-1} , which arise from the NH groups that chitosan possesses [19].

The 3352 cm^{-1} peak in the MMT/CHI composite seen in the FTIR spectrum in Figure 1 is considered to be the vibrational band combined with the N-H stretching vibrational band and the O-H stretching vibrational band. The spectra of the N-H stretching created by the amine groups of chitosan may both account for the peak at 1581 cm^{-1} . While the aliphatic C-H stretching was observed at peaks of 2930 cm^{-1} , the C-H bending was observed at peaks of 1379 cm^{-1} and the C-O stretching at peaks of 1151 cm^{-1} . The peaks for the amide I and amide II bands bending were observed at 1655 cm^{-1} and 1581 cm^{-1} . The peaks at 1013 cm^{-1} which represent the middle OH bending, CO, NH (amine) and NH_2 (amino), respectively, are comparable to those seen in chitosan [12, 20, 21].

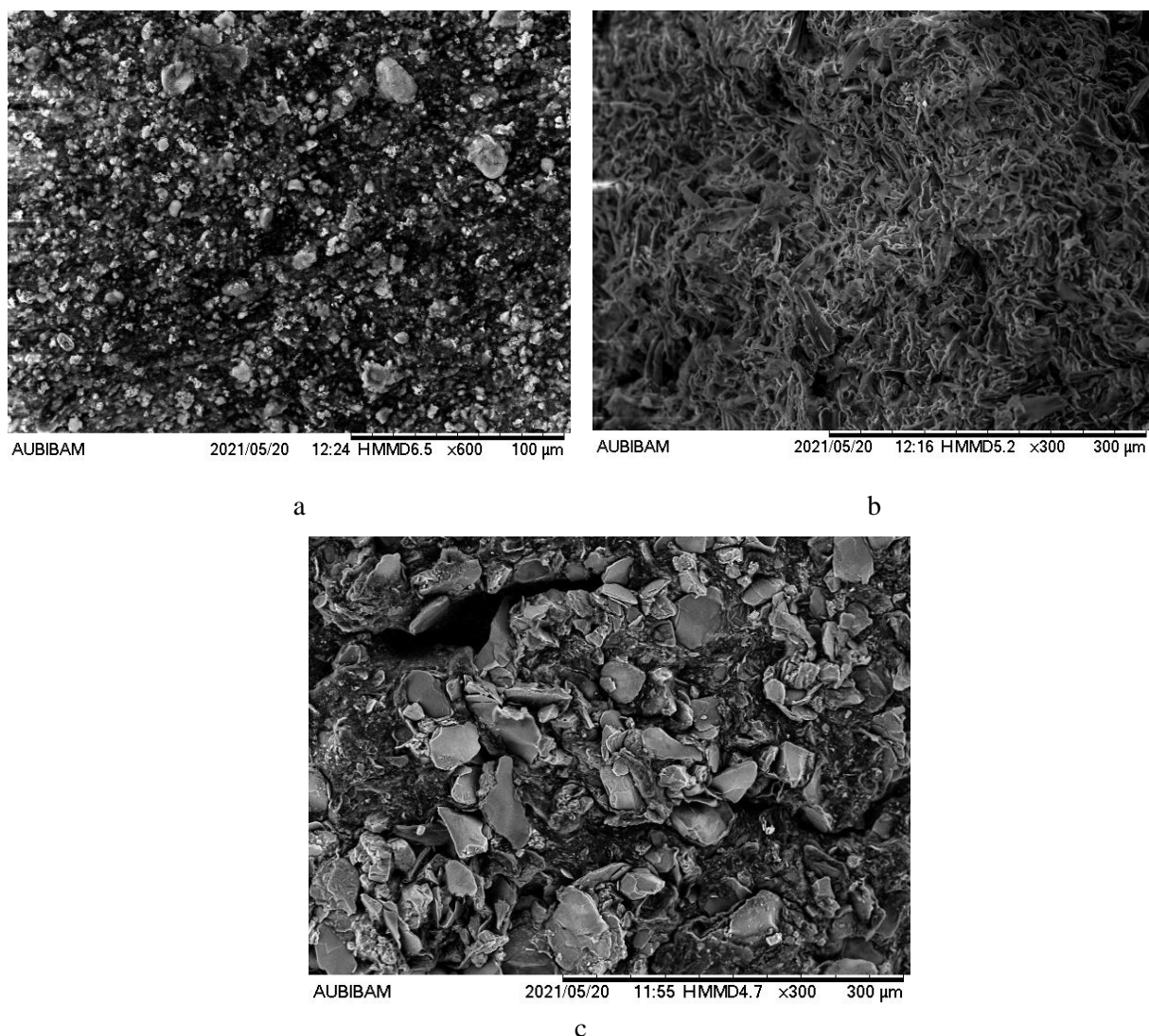


Figure 2. SEM images of HAP/CHI (a) CEL/CHI (b) and MMT/CHI (c)

The SEM images of HAP/CHI, CEL/CHI and MMT/CHI are shown in Figure. 2. As can be seen in the SEM images, HAP/CHI shows a relatively smooth surface with some agglomerates. On the other hand, the surface of MMT/CHI exhibits deep voids and non-uniform pores characterized by long, non-uniform hollow bodies. As we can see MMT/CHI has more pores than the other two composites. It means that using MMT in CHI composites increased the porosity. This increased porosity is the reason why clay adsorbents are preferred for the adsorption process. The CEL/CHI surface shows an irregular and dense morphology with a high pore density and heterogeneity together with reinforced and clearly visible pores.

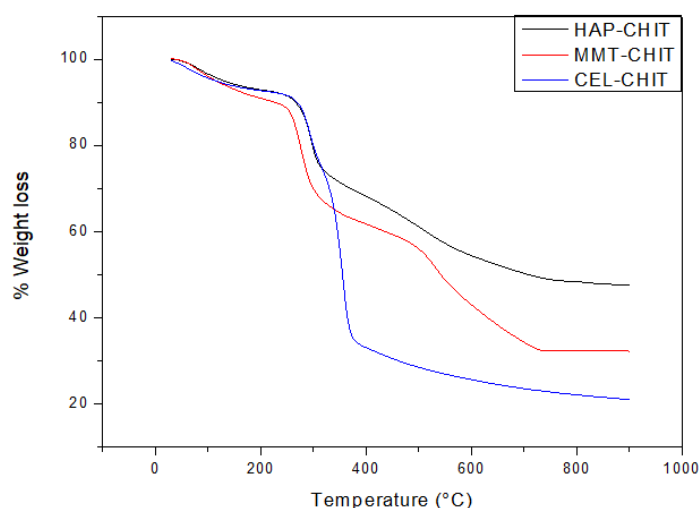


Figure 3. TGA profiles of HAP/CHI, CEL/CHI and MMT/CHI

TGA analyses were performed to observe the thermal behavior of the produced HAP/CHI, CEL/CHI and MMT/CHI materials. As can be seen in Figure 3, the highest mass loss and degradation at high temperatures were observed for CEL/CHI. For the CEL/CHI composite, a rapid mass loss of 60% was observed between 200-400 °C in a single step. From 400 °C to 1000 °C, a mass loss of 10 % was observed. Similarly, for the HAP/CHI composition, a rapid mass loss of 20 % was observed between 200-300 °C in a single step and then a mass loss of 40 % from 300 °C to 1000 °C. For the MMT/CHI composition, the mass loss occurred rapidly in 2 steps. The first step was observed between 200-300 °C and the second step between 450-750 °C. A mass loss of 20 % was observed in the first step and 25 % in the second step. The mass loss of all three composites began to accelerate after 200 °C. The first stage (30–200 °C) is associated with the loss of adsorbed and bound water and acetic acid residues. The second stage (200–400 °C) is due to the degradation of chitosan [22].

3.2. Loading of ASA

The maximum adsorption capacities (q_e) were 251.5 mg/g, 197.7 mg/g and 288.95 mg/g for the composites HAP/CHI, CEL/CHI and MMT/CHI, respectively (Figure 4.). The amount of adsorbed ASA increased with time in both composites. The maximum amount of q_e was obtained with the composite MMT/CHI. This is related to the functional groups and structural properties of MMT/CHI, which were evaluated in the characterization section.

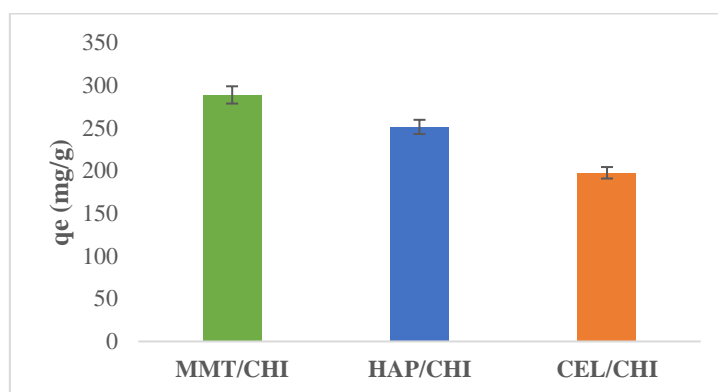


Figure 4. ASA adsorption capacity on the different composites (0.2 mg/mL ASA at 25 °C in 60 min)

3.3. In vitro Release of ASA

3.3.1. In the PBS medium

The release investigations used ASA-loaded HAP/CHI, CEL/CHI and MMT/CHI that were achieved at maximum ASA loading, as mentioned in the section 'Loading with ASA'. Prolonged release in PBS medium was achieved with the composites obtained (Figure 5.). In the study, 1 gram of HAP/CHI, CEL/CHI and MMT/CHI contained 251.5 mg, 197.7 mg and 288.95 mg of the active substance (ASA), respectively. The controlled release of the active substance lasted 72 hours (4320 minutes), with a sudden release observed in the first 5 minutes for all composites. 19.16%, 47.15% and 37.32% of the active substance of HAP/CHI, CEL/CHI and MMT/CHI were released in the first 5 minutes. After 5 minutes, the release slowed down and became more controlled for all three composites. At the end of the release, the composite CEL/CHI was the one with the highest release with 95.77% ASA release. A total release of 87.48% was achieved with MMT/CHI and 87.37% with HAP/CHI. When investigating the release profiles, it was assumed that HAP/CHI is more suitable for controlled release due to its less explosive release and more controlled release compared to the other two systems.

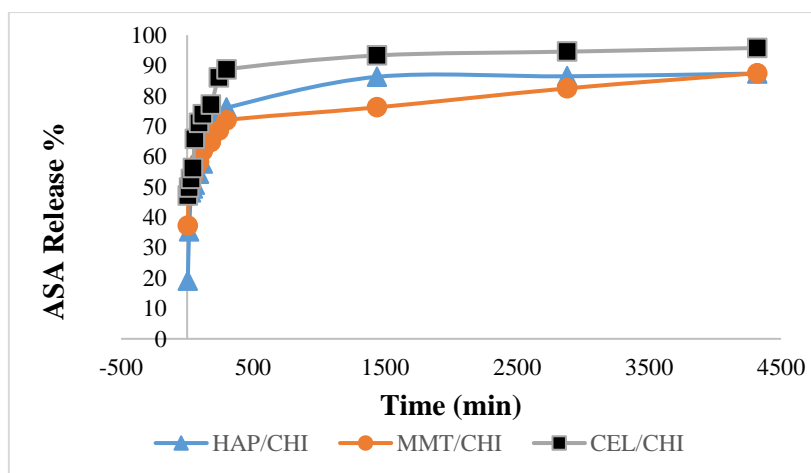


Figure 5. ASA released in the PBS medium with the HAP/CHI, CEL/CHI and MMT/CHI composites.

3.3.2. In the GJ medium

Since the presence of an acidic solution and pepsin in the simulated gastric juice allows the acetylsalicylic acid released from the drug-loaded particles to break down into salicylic acid, both acetylsalicylic acid and salicylic acid were found at pH 1.0, and only acetylsalicylic acid at pH 6.8. As a result of our studies, prolonged release was achieved with the obtained composites in both GJ and PBS medium (Figure 5 and Figure 6). In the study, 1 gram of the composites HAP/CHI, CEL/CHI and MMT/CHI contained 251.5 mg, 197.7 mg and 288.95 mg of active substance (ASA), respectively. The controlled release of the active substance lasted 72 hours (4320 minutes), whereby a sudden release was observed for all composites in the first 5 minutes. 52.51%, 72.30% and 44.87% of the active substance of HAP/CHI, CEL/CHI and MMT/CHI were released in the first 5 minutes. After 5 minutes, the release slowed down and became more controlled for all three composites. At the end of the release, the composite CEL/CHI was the one with the highest release with 96.05% ASA release. A total release of 93.26% was achieved with HAP/CHI and 84.89% with MMT/CHI. Examination of the release profiles revealed that MMT/CHI was more suitable for controlled release due to its less explosive release and more controlled release compared to the other two systems. The reason for the higher explosive release and more uncontrolled release compared to the PBS environment is that chitosan dissolves at low pH and does not tend to dissolve at high pH. Due to this property, the chitosan will dissolve quickly in the GJ environment and the active component in the composite will be released faster and uncontrolled into the environment.

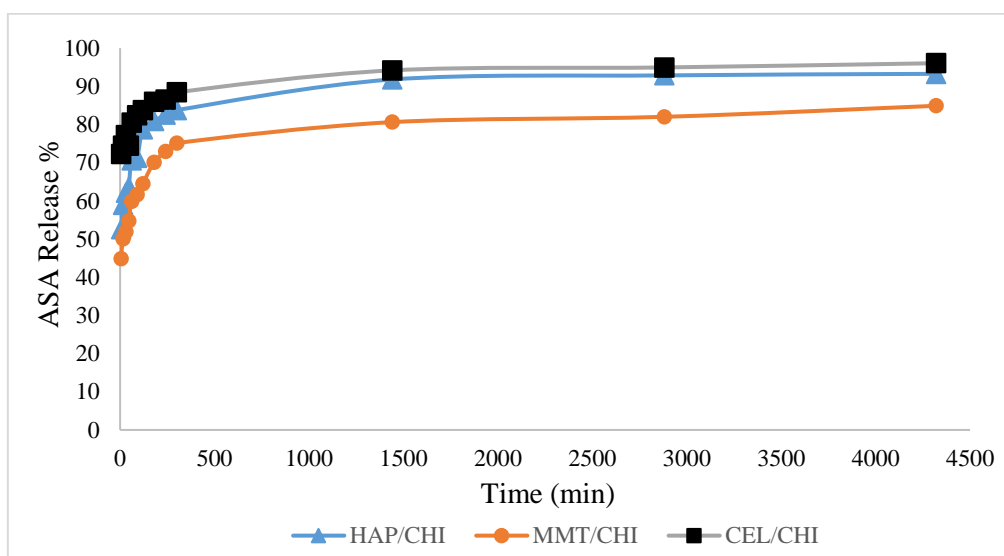


Figure 6. ASA released in the GJ medium with the HAP/CHI, CEL/CHI and MMT/CHI composites.

Compared to similar studies in the literature, the MMT/CHI composite was found to have a more controlled and prolonged release and a higher loading efficiency than many other studies (Table 1). In the release studies, it is evident that most of the studies in the literature were conducted with PBS medium. Although a cumulative release of 100% was achieved in PBS in the study by Gou and Jiaou [27], the duration of this release was considered insufficient for the drug to exert its therapeutic effect. A longer duration of controlled release is important to reduce side effects and improve bioavailability. Therefore, the total release achieved with MMT/CHI at 87.48% and CEL/CHI at 95.77% in PBS medium at the end of 72 hours exceeds that in similar studies in the literature. In GJ medium, a release of 84.89% was achieved with MMT/CHI, which is significantly more successful than in the studies in the literature. In addition, controlled and long-term release was also achieved in studies conducted in gastric medium. Compared to other studies, our study achieved the most suitable release system for ASA in both gastric and intestinal medium.

Table1. Selection of results from studies on the use of ASA-loaded systems

Material	Drug loading capacity	Drug release medium	Release time	Total drug release (%)	References
MMT/CHI	288.95 mg/g	PBS	72 hours	87.48	Our study
		GJ		84.89	
HAP/Cetyltrimethylammonium Bromide	280.27 mg/g	PBS	50 hours	73.91	[13]
Sporopollenin microcapsules	53.4% (270 mg/g)	PBS	10 hours	81.1	[23]
		0.1 M NaOH		66.9	
		GJ		51.7	
CHI/sodiumtripolyphosphate	90.4%	PBS	24 hours	88.3	[24]
MCM-41	350 mg/g	Degassed water	~16 hours	100	[25]
Dextran-layered double hydroxide	28.2%	PBS	1 hour	100	[26]

4. CONCLUSION

In this study new drug delivery systems based on chitosan were developed that can achieve long-term controlled release in both the stomach and the intestine. In these systems, particles modified with chitosan, cellulose, montmorillonite and hydroxyapatite were effectively synthesized and validated using advanced analytical techniques. In this study, the synthesized composites were investigated for the adsorption and controlled release of acetylsalicylic acid. The adsorption and release profiles of ASA-loaded HAP/CHI, CEL/CHI and MMT/CHI samples were compared. In addition, studies were conducted using SEM, FTIR and TGA analysis methods to better investigate the particle structures and chemical interactions.

The results have shown that the best drug carrier system in terms of adsorption or, in other words, drug loading capacity, is the MMT/CHI particles with 288.95 mg/g. The drug release studies showed that all three drug carriers had a more controlled release profile in the intestinal environment (PBS). On the other hand, a prolonged release of up to 2 days was achieved in both release environments, and at the end of release, the CEL/CHI composite was observed to have a higher drug release in the intestine and stomach than the other composites. However, release spurts were observed for all composites in both release environments. The SEM images showed the irregular morphologies of the beads, which could be effective for the adsorption of metal ions. It can be said that HAP/CHI has a relatively smooth surface except for some clusters, while the surface of MMT/CHI is characterized by long, irregular, hollow structures with deep voids and uneven pores. The increased porosity observed here emphasizes the preference for clay adsorbents in adsorption processes. On the other hand, the surface morphology of CEL/CHI shows an irregular and dense structure characterized by clearly visible pores, together with high pore density and heterogeneity. FTIR revealed the main functional groups of pure chitosan, pure cellulose and chitosan–cellulose beads.

The results of these studies indicate that these chitosan-based composites could be a good candidate for advanced drug delivery systems due to their excellent adsorption capacity and release behavior.

ACKNOWLEDGEMENTS

This study was supported by Eskisehir Technical University Scientific Research Projects Commission under grant no: 22ADP087

CONFLICT OF INTEREST

The author(s) stated that there are no conflicts of interest regarding the publication of this article.

CRedit AUTHOR STATEMENT

Dilay Sezer: Investigation, **Zeynep Aktaş:** Investigation, Writing – Original Draft, **Seda Hoşgün:** Writing – Original Draft, Data Curation **Emir Zafer Hoşgün:** Writing – Review & Editing, Supervision, Funding acquisition **Berrin Bozan:** Writing – Review & Editing, Supervision.

REFERENCES

- [1] Ordikhani F, Dehghani M, Simchi A. Antibiotic-loaded chitosan–Laponite films for local drug delivery by titanium implants: cell proliferation and drug release studies. *J Mater Sci: Mater Med.* 2015; 26: 1-12.
- [2] Parhi R. Chitin and Chitosan in Drug Delivery. In: Crini, G. and Lichtfouse, E. (eds.) *Sustainable Agriculture Reviews 36: Chitin and Chitosan: Applications in Food, Agriculture, Pharmacy, Medicine and Wastewater Treatment.* Springer International Publishing, 2019; 175–239.
- [3] Shi J, Zhao H, Wu F, Gan X. Synthesis and characterization of an injectable rifampicin-loaded chitosan/hydroxyapatite bone cement for drug delivery. *Journal of Materials Research.* 2021; 36: 487–498.
- [4] He M, Chen H, Zhang X, Wang C, Xu C, Xue Y, Wang J, Zhou P, Zhao Q.: Construction of novel cellulose/chitosan composite hydrogels and films and their applications. *Cellulose.* 2018; 25: 1987–1996.
- [5] Küçükçalık A, Ünlü CH. Chitosan-Graft-Polyacrylamide Based Release Systems: Effect of pH and Crosslinking. *Journal of the Turkish Chemical Society Section A: Chemistry.* 2022; 9: 121–130.
- [6] Kumari S, Singh RP. Glycolic acid-functionalized chitosan–Co₃O₄–Fe₃O₄ hybrid magnetic nanoparticles-based nanohybrid scaffolds for drug-delivery and tissue engineering. *J Mater Sci.* 2013; 48: 1524–1532.
- [7] Liu X, Zhao X, Liu Y, Zhang T. Review on preparation and adsorption properties of chitosan and chitosan composites. *Polym. Bull.* 2022; 79: 2633–2665.
- [8] Yao AH, Li XD, Xiong L, Zeng JH, Xu J, Wang DP. Hollow hydroxyapatite microspheres/chitosan composite as a sustained delivery vehicle for rhBMP-2 in the treatment of bone defects. *J Mater Sci: Mater Med.* 2015; 26: 1-12.
- [9] Baştan FE. Production and characterization of gelatin functionalized hydroxyapatite composite microspheres for biomedical applications. *Eskişehir Technical University Journal of Science and Technology A-Applied Sciences and Engineering.* 2021; 22: 10–22.
- [10] Sharifzadeh G, Hezaveh H, Muhamad, II, Hashim S, Khairuddin N. Montmorillonite-based polyacrylamide hydrogel rings for controlled vaginal drug delivery. *Materials Science and Engineering: C.* 2020; 110: 110609.

- [11] Bekaroğlu MG, Nurili F, İşçi S. Montmorillonite as imaging and drug delivery agent for cancer therapy. *Applied Clay Science*. 2018; 162: 469–477.
- [12] Haerudin H, Pramono AW, Kusuma DS, Jenie A, Voelcker NH, Gibson C. Preparation and characterization of chitosan/montmorillonite (mmt) nanocomposite systems. 2010. PhD Thesis. University of Indonesia.
- [13] Sezer D, Hoşgün EZ. Controlled release of acetylsalicylic acid via hydroxyapatite prepared with different templates. *J Aust Ceram Soc*. 2023; 59: 153–163.
- [14] Xing G, Shao L, Du Y, Tao H, Qi C. Citric acid crosslinked chitosan/poly(ethylene oxide) composite nanofibers fabricated by electrospinning and thermal treatment for controlled drug release. *Cellulose*. 2021; 28: 961–971.
- [15] Li H, Ke J, Li H, Wei C, Wu X, Li J, Yang Y, Xu L, Liu H, Li S. Mesoporous silicas templated by heterocyclic amino acid derivatives: Biomimetic synthesis and drug release application. *Materials Science and Engineering: C*. 2018; 93: 407–418.
- [16] Cheng ZH, Yasukawa A, Kandori K, Ishikawa T. FTIR Study of Adsorption of CO₂ on Nonstoichiometric Calcium Hydroxyapatite. *Langmuir*. 1998; 14: 6681–6686.
- [17] Luna-Zaragoza D, Romero-Guzmán ET, Reyes-Gutiérrez LR. Surface and Physicochemical Characterization of Phosphates Vivianite, Fe₂(PO₄)₃ and Hydroxyapatite, Ca₅(PO₄)₃OH. *Journal of Minerals and Materials Characterization and Engineering*. 2009; 8: 591–609.
- [18] Paul A, Augustine R, Hasan A, Zahid AA, Thomas S, Agatemor C, Ghosal K. Halloysite nanotube and chitosan polymer composites: Physicochemical and drug delivery properties. *Journal of Drug Delivery Science and Technology*. 2022; 72: 103380.
- [19] Cicek Ozkan, B. Cellulose and chitosan biopolymer composites reinforced with graphene and their adsorption properties for basic blue 41. *Cellulose*. 2022; 29: 9637–9655.
- [20] Bhagath S, Vivek A, Krishna VV, Mittal SS, Balachandran M. Synthesis and characteristics of MMT reinforced chitosan nanocomposite. *Materials Today: Proceedings*. 2021; 46: 4487–4492.
- [21] Günister E, Pestreli D, Ünlü CH, Atıcı O, Güngör N. Synthesis and characterization of chitosan-MMT biocomposite systems. *Carbohydrate Polymers*. 2007; 67: 358–365.
- [22] Paluszkiwicz C, Stodolak E, Hasik M & Blazewicz, M. FT-IR study of montmorillonite–chitosan nanocomposite materials. *Spectrochimica Acta Part A: Molecular and Biomolecular Spectroscopy*. 2011; 79(4): 784–788.
- [23] Mohammed ASY, Dyab AK, Taha F, Abd El-Mageed, A. I. Pollen-derived microcapsules for aspirin microencapsulation: in vitro release and physico-chemical studies. *RSC advances*. 2022; 12(34): 22139–22149.
- [24] Ravi Sankar V, Dachinamoorthi D, Chandra Shekar KB. A Comparative Pharmacokinetic study of Aspirin Suppositories and Aspirin Nanoparticles Loaded Suppositories. *Clinic Pharmacol Biopharm*. 2012; 1(105): 2.

- [25] Vyskočilová E, Luštická I, Paterová I, Machová L, Červený L. Modified MCM-41 as a drug delivery system for acetylsalicylic acid. *Solid state sciences*. 2014; 38: 85-89.

- [26] Dong LE, Gou G, Jiao L. Characterization of a dextran-coated layered double hydroxide acetylsalicylic acid delivery system and its pharmacokinetics in rabbit. *Acta Pharmaceutica Sinica B*. 2013; 3(6): 400-407.



RESEARCH ARTICLE

LAMBERT AZIMUTHAL EQUAL-AREA PROJECTION

Emre ÖZTÜRK^{1,*}

¹ Management Information Systems, Faculty of Economics and Administrative Sciences, Hatay Mustafa Kemal University, Hatay, Türkiye

emre.ozturk@mku.edu.tr -  [0000-0001-6638-3233](https://orcid.org/0000-0001-6638-3233)

Abstract

In the present study, we give the proofs about important properties of Lambert azimuthal projection, for instance conformality, preserve area that important points for characterization. While there are some kind of Lambert projections in the literature (for instance standard, cylindrical), we utilize from the south polar aspect. In our proofs, we use the south polar aspect, and finally we give some visualizations of the inverse of projection as an example.

Keywords

Möbius transformation,
Lambert azimuthal projection,
Visualization

Time Scale of Article

Received : 27 December 2023
Accepted : 27 August 2024
Online date : 30 September 2024

1. INTRODUCTION

Möbius transformations are very useful tool for understanding patterns in Euclidean space. Especially in extended complex plane many kind of curves can be modelled. Möbius transformations also in use tessellations and calculations of distances in hyperbolic geometry. Also it maps circles to circles and preserves cross-ratio, angles and symmetry [1]. Since the angles preserved, Möbius transformation is a conformal map. Moreover, one can compose the Möbius transformations by basic type transformations like translation, rotation, scaling and inversion. Möbius transformations are connected to non-Euclidean geometries (in some models of hyperbolic geometry (e.g. Poincare's disk), isometries are represented by Möbius transforms) and these transformations are connected to Einstein's theory of relativity (via Lorenz transforms) [1]. Closely related to spherical geometry is the geometry of Möbius transformations on the extended complex plane $\mathbb{C}_\infty = \mathbb{C} \cup \{\infty\}$. This connection is provided by the stereographic projection map $\pi: S^2 \rightarrow \mathbb{C}_\infty$ [2]. Many geometricians have studied on Möbius transformation in order to tessellations and create patterns by using different kind of approaches [3,4]. On the other hand, the Lambert azimuthal equal-area projection is one of the normal cylindrical projection who defined by the Swiss mathematician and cartographer Johann Heinrich Lambert [5].

Let us imagine a tangent plane to the unit sphere with center $O(0,0,0)$ at some point S south pole (see, Figure 1). Let P be any point on the sphere differ from antipodal of S and d be the Euclidean distance between S and P in three-dimensional space. Then, the Lambert azimuthal equal-area projection sends point P to only one point P' on the plane that is a distance d from S . Hence, the Lambert projection maps point P to P' at equal distance to S , i.e. $|PS| = |P'S|$. In the general case P' lies on open disk of radius 2 centered at the origin $(0,0)$ in the plane. Moreover, it lies on circle of radius $\sqrt{2}$ centered at

*Corresponding Author: emre.ozturk@mku.edu.tr

(0,0) when P lies on equator. Notice that, while the Lambert projection preserves the area, it is not conformal, i.e. angles are not preserved under the projection. For more details, we refer [6-8].

In the present study, we use the polar aspect of Lambert azimuthal equal-area projection. We choose the projection center as $S(0,0,-1)$ on unit sphere. In section 3, we give the proofs which characterize the important properties of the projection. In the last section, under the inverse Lambert projection, we give some visualizations rely on fixed points of the Möbius transformation.

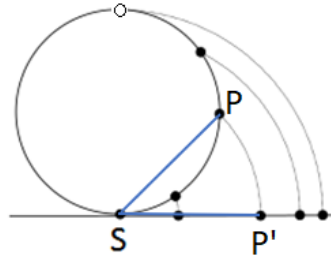


Figure 1: The Lambert azimuthal equal-area projection.

2. PRELIMINARIES

In this section, some basics related with the Möbius transformation are given.

Definition 2.1 Any mapping of the form

$$\mathcal{M}(z) = \frac{az + b}{cz + d}, \quad a, b, c, d \in \mathbb{C}$$

where $ad - bc \neq 0$, is called a Möbius transformation. If $c = 0$, $\mathcal{M}(z)$ is defined for all $z \in \mathbb{C}$; if $c \neq 0$ it is defined for all $z \neq -d/c$. We can avoid this dichotomy by extending \mathcal{M} to a map on the extended complex plane $\mathbb{C}_\infty = \mathbb{C} \cup \{\infty\}$, $\mathcal{M}(\infty) = \infty$ if $c = 0$, $\mathcal{M}(-d/c) = \infty$, $\mathcal{M}(\infty) = a/c$ if $c \neq 0$ [9].

If $ad - bc = 0$ then \mathcal{M} is constant. Note that \mathcal{M} is conformal, i.e., it preserves angles.

The coefficients of \mathcal{M} are not unique. For any $\lambda \neq 0$ real number $\mathcal{M}(z) = \frac{(\lambda a)z + \lambda b}{(\lambda c)z + \lambda d}$. Let the Möbius transformation is not constant. Then, $\lambda = \frac{1}{\sqrt{ad-bc}}$ gives

$$\mathcal{M}(z) = \frac{a'z + b'}{c'z + d'}$$

such that $a'd' - b'c' = 1$. In this case, \mathcal{M} is in normalized form [9].

Lemma 2.2 Let \mathcal{M} be a Möbius transformation in normalized form, i.e., $ad - bc = 1$. Then the fixed points of \mathcal{M} are,

$$\xi_{1,2} = \frac{(a - d) \mp \sqrt{(a + d)^2 - 4}}{2c}.$$

In particular, $|\text{fix}(\mathcal{M})| = 1$ if and only if $a + d = \mp 2$. Otherwise, $|\text{fix}(\mathcal{M})| = 2$ when $\mathcal{M} \neq i. \infty \in \text{fix}(\mathcal{M})$ if and only if $c = 0$.

Proof. Obviously, $z \in \text{fix}(\mathcal{M})$ if and only if $\frac{az+b}{cz+d} = z$ which yields the following:

$$cz^2 + (d - a)z - b = 0. \tag{2.1}$$

Complex roots of the Eq. (2.1) as follows

$$z = \frac{(a - d) \mp \sqrt{(a - d)^2 + 4bc}}{2c}.$$

Since $(a - d)^2 + 4bc = (a + d)^2 - 4$, we get

$$z = \frac{(a - d) \mp \sqrt{(a + d)^2 - 4}}{2c}. \tag{2.2}$$

Hence $z \in \text{fix}(\mathcal{M})$ if and only if z is written by Eq. (2.2). Remain of the proof is obvious.

Let $\infty \in \text{fix}(\mathcal{M})$ or $c = 0$. In this case, the Möbius transformation \mathcal{M} can be written by

$$\mathcal{M}(z) = \omega z + \Omega, \tag{2.3}$$

where $\omega = a/d$, $\Omega = b/d$. By the help of Eqs. (2.1) and (2.3), the following table can be given:

Table 1. Möbius transformation and its fixed points depends on coefficients.

Ω	ω	$\mathcal{M}(z)$	$\text{fix}(\mathcal{M})$
$\Omega \neq 0$	$\omega = 1$	$\mathcal{M}(z) = z + \Omega$ translation on \mathbb{C}	$\{\infty\}$
$\Omega = 0$	$ \omega = 1$	$\mathcal{M}(z) = e^{i\theta}z$ rotation on \mathbb{C}	$\{0, \infty\}$
$\Omega = 0$	$\omega = r \in \mathbb{R}$	$\mathcal{M}(z) = rz$ expansion on \mathbb{C}	$\{0, \infty\}$
$\Omega = 0$	$\omega = re^{i\theta} \in \mathbb{C}$	$\mathcal{M}(z) = re^{i\theta}z$ spiralization on \mathbb{C}	$\{0, \infty\}$

3. LAMBERT AZIMUTHAL EQUAL-AREA PROJECTION

In this section, we give the proofs which characterize the Lambert azimuthal equal-area projection.

Theorem 3.1 The Lambert azimuthal equal-area projection maps points (x, y, z) of unit sphere to the points (X, Y) of plane such that

$$X = \sqrt{\frac{2}{1-z}} x, \quad Y = \sqrt{\frac{2}{1-z}} y.$$

On the other hand, the inverse of Lambert projection maps points (X, Y) of plane to the points (x, y, z) of unit sphere with centre $O(0,0,0)$ such that

$$x = \sqrt{1 - \frac{X^2 + Y^2}{4}} X, \quad y = \sqrt{1 - \frac{X^2 + Y^2}{4}} Y, \quad z = -1 + \frac{X^2 + Y^2}{2},$$

where $X^2 + Y^2 < 4$ and $z \neq 1$.

Proof. In order to calculations, we utilize from Figure 2 (see, [1, p.250]). Notice that the notations we use x, y, z for coordinates of sphere, and capital letters X, Y for coordinates of plane. Let us consider the tangent plane π of unit sphere $\mathbb{S}^2(1)$ with center $O(0,0,0)$ at point S (south pole). Since the plane is tangent to sphere at $S(0,0, -1)$, it is more useful to consider π as $z = -1$. Thus, all $P' \in \pi$ points can be written as $P' = P'(X, Y, -1)$. Note that P and P' lie on the same arc with center S . Therefore, $|PS| = |P'S|$ which yields

$$X^2 + Y^2 = x^2 + y^2 + (z + 1)^2. \tag{3.1}$$

Moreover, $P \in \mathbb{S}^2(1)$, that is

$$x^2 + y^2 + z^2 = 1. \tag{3.2}$$

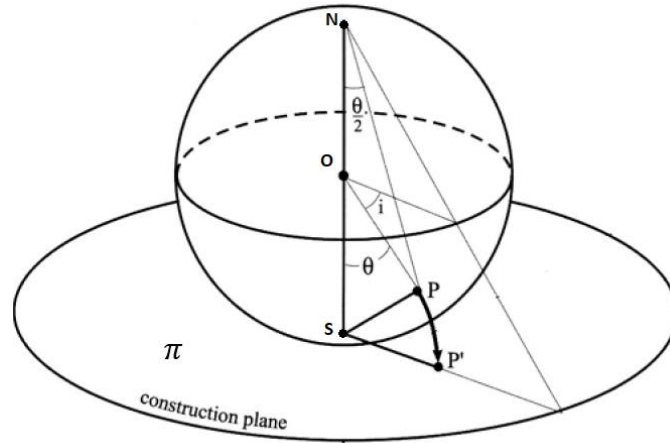


Figure 2: Lambert azimuthal equal-area projection

By Eqs. (3.1) and (3.2) we obtain $z = -1 + \frac{X^2+Y^2}{2}$. On the other hand, well-known cosine theorem in $\triangle POS$ gives $|PS|^2 = 2 - 2\cos\theta = 4\sin^2\frac{\theta}{2}$. Thus, $|P'S|^2 = |PS|^2 = 4\sin^2\frac{\theta}{2}$ and it follows

$$\cos\frac{\theta}{2} = \sqrt{1 - \frac{X^2 + Y^2}{4}}, \tag{3.3}$$

where $0 < \theta < \pi$. Now we orthogonal project P to $[SP']$ at corresponding point $K(x, y, -1)$ on this segment (see Figure 3). Since $\triangle POS$ is isosceles triangle and $[NS]$ orthogonal to $[SP']$, we obtain $m(\widehat{PSP'}) = \frac{\theta}{2}$. Hence,

$$\cos\frac{\theta}{2} = \frac{|KS|}{|PS|} = \frac{\sqrt{x^2 + y^2}}{|PS|}. \tag{3.4}$$

Since $|PS| = |P'S| = \sqrt{X^2 + Y^2}$, Eqs. (3.3) and (3.4) gives

$$x^2 + y^2 = (X^2 + Y^2) \left(1 - \frac{X^2 + Y^2}{4}\right).$$

Now, we consider triangle $\triangle PSP'$ (triangle with P, S, P' vertexes). From cosine theorem it is written, $|PP'|^2 = |PS|^2 + |P'S|^2 - 2|PS||P'S|\cos\frac{\theta}{2}$. If sub $|PP'|^2 = (X - x)^2 + (Y - y)^2 + (z + 1)^2$, $|PS| = |P'S| = 2\sin\frac{\theta}{2}$, and $z + 1 = \frac{X^2+Y^2}{2}$ in equation of cosine theorem, it follows

$$(X - x)^2 + (Y - y)^2 + \left(\frac{X^2 + Y^2}{2}\right)^2 = 8\sin^2\frac{\theta}{2} \left(1 - \cos\frac{\theta}{2}\right). \tag{3.5}$$

From Eq. (3.3), it is easily seen $X^2 + Y^2 = 4\sin^2\frac{\theta}{2}$. If we expand the left-hand side of Eq. (3.5) we obtain

$$X^2 - 2xX + x^2 + Y^2 - 2yY + y^2 + \frac{(X^2 + Y^2)^2}{4} = 8 \sin^2 \frac{\theta}{2} \left(1 - \cos \frac{\theta}{2}\right)$$

and $X^2 + Y^2 = 4 \sin^2 \frac{\theta}{2}$ gives

$$4 \sin^2 \frac{\theta}{2} + 4 \sin^4 \frac{\theta}{2} - 2xX + x^2 - 2yY + y^2 = 8 \sin^2 \frac{\theta}{2} \left(1 - \cos \frac{\theta}{2}\right). \quad (3.6)$$

Now we recall the projection point K .

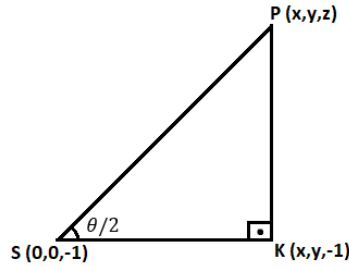


Figure 3: Orthogonal projection of $P(x, y, z)$ onto segment $[SP']$.

Since $|PS| = 2 \sin \frac{\theta}{2}$, it is obvious from Figure 3 that $|KS| = \sin \theta$. Also, $|KS| = \sqrt{x^2 + y^2}$. Then, we have $x^2 + y^2 = \sin^2 \theta$. Let sub this identity in Eq. (3.6) we get

$$4 \sin^2 \frac{\theta}{2} + 4 \sin^4 \frac{\theta}{2} - 2xX - 2yY + \sin^2 \theta = 8 \sin^2 \frac{\theta}{2} - 8 \sin^2 \frac{\theta}{2} \cos \frac{\theta}{2}.$$

By straightforward calculations we obtain

$$2xX + 2yY = 4 \sin \frac{\theta}{2} \sin \theta + \sin^2 \theta - 4 \sin^2 \frac{\theta}{2} + 4 \sin^4 \frac{\theta}{2}.$$

Since $-4 \sin^2 \frac{\theta}{2} + 4 \sin^4 \frac{\theta}{2} = -\sin^2 \theta$, the last equation gives

$$2xX + 2yY = 4 \sin \frac{\theta}{2} \sin \theta = \frac{2 \sin^2 \theta}{\cos \frac{\theta}{2}}. \quad (3.7)$$

By $x^2 + y^2 = \sin^2 \theta$, and Eq. (3.7) it follows

$$xX + yY = \frac{x^2}{\cos \frac{\theta}{2}} + \frac{y^2}{\cos \frac{\theta}{2}}. \quad (3.8)$$

Eq. (3.8) is true if and only if

$$X = \frac{x}{\cos \frac{\theta}{2}} \text{ and } Y = \frac{y}{\cos \frac{\theta}{2}}. \quad (3.9)$$

It follows from Eqs. (3.3), (3.9), and the identity $z = -1 + \frac{X^2 + Y^2}{2}$ that

$$X = \sqrt{\frac{2}{1-z}} x, \quad Y = \sqrt{\frac{2}{1-z}} y.$$

Hence, we get the Lambert azimuthal equal-area projection. On the other hand, from Eqs. (3.3) and (3.9) we obtain

$$x = \sqrt{1 - \frac{X^2 + Y^2}{4}}X, \quad y = \sqrt{1 - \frac{X^2 + Y^2}{4}}Y, \quad z = -1 + \frac{X^2 + Y^2}{2}.$$

Thus, we get the inverse projection, and this completes the proof.

By the help of [8, p.27-28], the following Cauchy-Riemann like condition can be given:

Lemma 3.2 A map projection of the sphere to be equal-area if and only if

$$\frac{\partial y}{\partial \varphi} \frac{\partial x}{\partial \lambda} - \frac{\partial y}{\partial \lambda} \frac{\partial x}{\partial \varphi} = s \cos \varphi, \tag{3.10}$$

where s is constant. Here, φ represents latitude, λ represents longitude and x and y are the projected coordinates for a given (φ, λ) pair.

In spherical coordinates (ψ, θ) on the sphere with ψ the colatitude (complement of the latitude) and θ the longitude, and polar coordinates (R, Θ) on the disk, the map and its inverse are given by [8]:

$$(R, \Theta) = \left(2 \cos \frac{\psi}{2}, -\theta \right) \text{ and } (\psi, \theta) = \left(2 \arccos \frac{R}{2}, -\Theta \right). \tag{3.11}$$

By Eqs. (3.10) and (3.11), the following theorem can be given:

Theorem 3.3 The Lambert azimuthal projection preserves the area. Furthermore, the constant $s = 1$ in Eq. (3.10).

Proof. Let the first deal with the notations by mentioned above. Here, we show the latitude by φ and longitude by λ in the Lambert projection. By Eq. (3.11), the polar coordinates correspond to $\left(2 \cos \frac{\psi}{2}, -\theta \right)$ on the plane which gives us the cartesian coordinates as

$$x = 2 \cos \frac{\psi}{2} \cos (-\theta) \text{ and } y = 2 \cos \frac{\psi}{2} \sin(-\theta). \tag{3.12}$$

Since ψ is the colatitude, and $\lambda = \theta$, we have

$$x = 2 \cos \left(\frac{\pi}{4} - \frac{\varphi}{2} \right) \cos \lambda, \quad y = -2 \cos \left(\frac{\pi}{4} - \frac{\varphi}{2} \right) \sin \lambda.$$

If sub x and y in Eq. (3.10), after the simplifying some calculations, we obtain the following:

$$\frac{\partial y}{\partial \varphi} \frac{\partial x}{\partial \lambda} - \frac{\partial y}{\partial \lambda} \frac{\partial x}{\partial \varphi} = \sin \left(\frac{\pi}{2} - \varphi \right) = \cos \varphi.$$

Hence, the Lambert azimuthal projection satisfies Eq. (3.10) with constant $s = 1$. Thus, the map preserves the area and is equal-area projection.

Proposition 3.4 Let $P_1(x_1, y_1, z_1)$ and $P_2(x_2, y_2, z_2)$ be the points on unit sphere and the corresponding points under the Lambert azimuthal equal-area projection be P_1' and P_2' on the plane. Then the following reads:

$$\theta'' = \mp \theta' + 2k\pi, k \in \mathbb{Z},$$

where θ' is angle between P_1' and P_2' , and θ'' is angle between the orthogonal projection points $P_1''(x_1, y_1, 0)$ and $P_2''(x_2, y_2, 0)$.

Proof. By Theorem 3.1, it is easily seen that

$$\cos\theta' = \frac{x_1x_2 + y_1y_2}{\sqrt{(x_1^2 + y_1^2)(x_2^2 + y_2^2)}}. \tag{3.13}$$

On the other hand, from the orthogonal projection points we have,

$$\cos\theta'' = \frac{x_1x_2 + y_1y_2}{\sqrt{(x_1^2 + y_1^2)(x_2^2 + y_2^2)}}. \tag{3.14}$$

From the Eqs. (3.13) and (3.14), we get the intended.

Theorem 3.5 The Lambert azimuthal equal-area projection is not conformal.

Proof. Let us consider two different points $P_1(x_1, y_1, z_1)$ and $P_2(x_2, y_2, z_2)$ on unit sphere with center O , and assume that the Lambert azimuthal projection is conformal. At least one of z_1 and z_2 differ from zero. Since P_1 and P_2 are unit vectors, it follows:

$$P_1 \cdot P_2 = \cos\theta = x_1x_2 + y_1y_2 + z_1z_2, \tag{3.15}$$

where θ is angle between OP_1 and OP_2 , and “ \cdot ” is Euclidean inner product. On the other hand,

$$\cos\theta' = \frac{x_1x_2 + y_1y_2}{\sqrt{(x_1^2 + y_1^2)(x_2^2 + y_2^2)}}, \tag{3.16}$$

where θ' is angle between projected points SP_1' and SP_2' , S is the projection center. From Eqs. (3.15) and (3.16) it follows:

$$\cos\theta = \sqrt{(1 - z_1^2)(1 - z_2^2)} \cos\theta' + z_1z_2, \tag{3.17}$$

where $x_1^2 + y_1^2 + z_1^2 = x_2^2 + y_2^2 + z_2^2 = 1$. From assumption and Eq. (3.18), $\theta = \theta'$ and so

$$z_1z_2 = 0 \text{ and } (1 - z_1^2)(1 - z_2^2) = 1.$$

The last condition implies $z_1 = z_2 = 0$ which is contradiction. This completes the proof.

4. EXAMPLES

In this section, by the help of Eq. (2.3) and inverse Lambert equal-area projection, we illustrate some samples of surface.

Example 4.1 Recall Eq. (2.3). If $\Omega \neq 0$, $\omega = 1$, then we can write $\Omega = \Omega_r + \Omega_i$ where Ω_r and Ω_i are real and imaginer part of Ω , respectively. If we take $\Omega_r = \Omega_i = 1$ then, inverse Lambert equal-area projection maps points $(X, Y) \in M(z)$ to the following points on unit sphere:

$$(x, y, z) = \left(\sqrt{1 - \frac{(X+1)^2 + (Y+1)^2}{4}} (X + 1), \sqrt{1 - \frac{(X+1)^2 + (Y+1)^2}{4}} (Y + 1), -1 + \frac{(X+1)^2 + (Y+1)^2}{2} \right).$$

This transformation forms Figure 4.

If we take $\Omega_r = -1$, $\Omega_i = 1$ then, inverse Lambert equal-area projection maps points $(X, Y) \in \mathcal{M}(z)$ to the following points on unit sphere:

$$(x, y, z) = \left(\sqrt{1 - \frac{(X-1)^2 + (Y+1)^2}{4}} (X - 1), \sqrt{1 - \frac{(X-1)^2 + (Y+1)^2}{4}} (Y + 1), -1 + \frac{(X-1)^2 + (Y+1)^2}{2} \right).$$

This transformaton forms Figure 5.

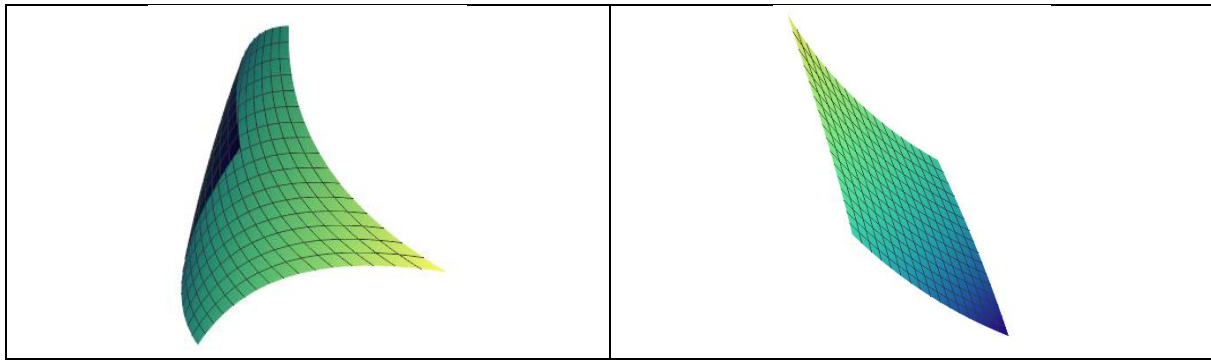


Figure 4: Lines on leaf surfaces of sphere

Remark. Figure 4 and Figure 5 gives us a clue about that not only translations forms family of parallel of lines in plane but also it forms family of parallel circular arcs on the sphere, under the inverse Lambert azimuthal equal-area projection.

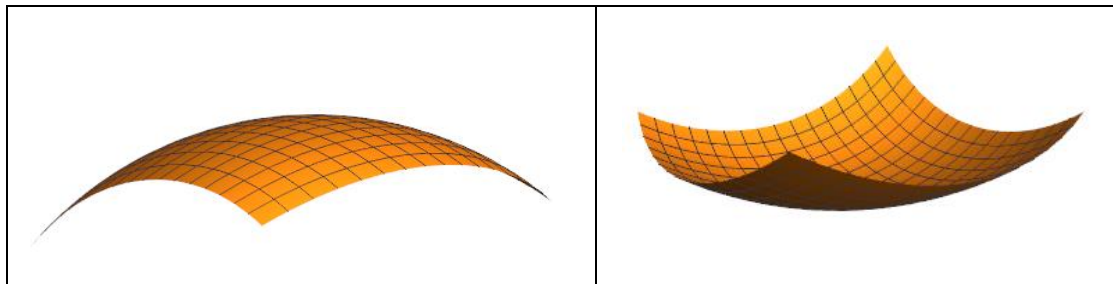


Figure 5: Arcs on fluffy patches

Example 4.2 $\Omega = 0$, and $|\omega| = 1$. Then, $\mathcal{M}(z) = e^{i\theta} z$ or explicitly $\mathcal{M}(z) = r e^{i(\theta_1 + \theta_2)}$ where $\theta = \theta_1$, $z = r e^{i\theta_2}$. Thus, inverse Lambert projection maps points $(X, Y) \in \mathcal{M}(z)$ to the following points:

$$(r, \phi) = \left(r \sqrt{1 - \frac{r^2}{4}} \cos \phi, r \sqrt{1 - \frac{r^2}{4}} \sin \phi, -1 + \frac{r^2}{2} \right), \quad (3.14)$$

where $\phi = \theta_1 + \theta_2$. Depend on (r, ϕ) , Eq. (3.14) represents the parts of sphere.

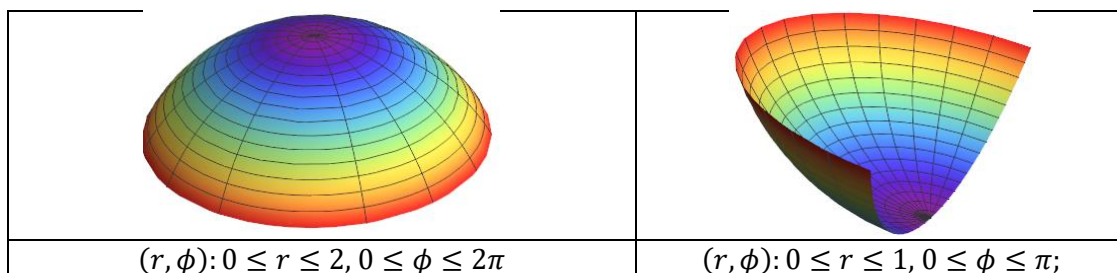


Figure 6: Hemisphere and quarter part

Remark. Figure 6 gives us a clue such that the rotations in the plane corresponds to circles on the sphere \mathbb{S}^2 , under the inverse Lambert azimuthal equal-area projection.

Example 4.3 Let us consider the points $P_1(\frac{2}{7}, \frac{3}{7}, \frac{6}{7})$ and $P_2(-\frac{3}{\sqrt{17}}, -\frac{2}{\sqrt{17}}, \frac{2}{\sqrt{17}})$ on unit sphere. It is easily seen that $OP_1 \cdot OP_2 = 0$ where \cdot is inner product of Euclidean space. Thus, $OP_1 \perp OP_2$. Lambert projection sends points P_1 and P_2 to

$$P_1'(\frac{2\sqrt{14}}{7}, \frac{3\sqrt{14}}{7}) \text{ and } P_2'(-3\sqrt{\frac{2}{221}(17+2\sqrt{17})}, -2\sqrt{\frac{2}{221}(17+2\sqrt{17})})$$

respectively. It is obvious that P_1' is not orthogonal to P_2' . That is, Lambert projection is not conformal.

5. CONCLUSION

In the recent literature, there is not enough paper about Lambert azimuthal equal-area projection. However, a few papers in cartography, especially in [7] and [8] some basic theorems about the projection are given. In this study, we give elementary and differential geometric proofs of theorems related with the projection. We discuss the projection by using south pole projection. Moreover, the fundamental properties of the projection are examined. On the other hand, by using Möbius transformation and the Lambert azimuthal equal-area projection, some patterns on the sphere are given. We hope that this paper will be useful for further studies about the projection. Also, it will fill a void in the literature.

CONFLICT OF INTEREST

The author(s) stated that there are no conflicts of interest regarding the publication of this article.

CRedit AUTHOR STATEMENT

Emre Öztürk: Formal analysis, Writing - original draft, Conceptualization, Investigation, Supervision, Visualization.

REFERENCES

- [1] Marić M. A toolbox for visualizing Möbius transformations. IV Nordic GeoGebra Conference, Copenhagen, 2013.
- [2] Wilson P. Curved Spaces: From Classical Geometries to Elementary Differential Geometry. Cambridge University Press, New York-United States of America, 2008. pp. 39-44.
- [3] Marsland S, McLachlan RI. Möbius invariants of shapes and images. Symmetry, Integrability and Geometry: Methods and Applications 2016; 12: 1-29.
- [4] Mork LK, Ulness DJ. Visualization of Mandelbrot and Julia sets of Möbius transformations. Fractal and Fractional 2021; 5-73.
- [5] Osborne P. The Mercator projections: The normal and transverse Mercator projections on the sphere and the ellipsoid with full derivations of all formulae. Edinburg Zenodo. <https://doi.org/10.5281/zenodo.35392>
- [6] Fong C. An Indoor Alternative to Stereographic Spherical Panoramas. Proceedings of Bridges 2014: Mathematics, Music, Art, Architecture, Culture. pp. 103-110.

- [7] Borradaile G. Statistics of Earth Science Data. Springer-Verlag Berlin Heidelberg New York, 2003.
- [8] Snyder JP. Map Projections-A Working Manual. United States Government Printing Office, Washington, 1987.
- [9] Pressley A. Elementary Differential Geometry, Springer Undergraduate Mathematics Series, London-England, 2010. pp. 391-398.



RESEARCH ARTICLE

DETERMINATION OF DEEP RED REMOVAL POTENTIAL OF ACTIVATED CARBON
PRODUCED FROM WHEAT BRAN

Ilknur DEMIRAL¹, Canan SAMDAN^{2,*}, Fatma Betül KUS³

¹ Eskişehir Osmangazi University, Faculty of Engineering and Architecture, Department of Chemical Engineering, 26480 Eskişehir, Turkey
idemiral@ogu.edu.tr - [0000-0003-2867-5205](https://orcid.org/0000-0003-2867-5205)

² Eskişehir Osmangazi University, Faculty of Engineering and Architecture, Department of Chemical Engineering, 26480 Eskişehir, Turkey
caydin@ogu.edu.tr - [0000-0001-8755-0790](https://orcid.org/0000-0001-8755-0790)

³ Eskişehir Osmangazi University, Faculty of Engineering and Architecture, Department of Chemical Engineering, 26480 Eskişehir, Turkey
fmbtl341016@hotmail.com - [0000-0003-4223-4596](https://orcid.org/0000-0003-4223-4596)

Abstract

In this study, the production of activated carbon from wheat bran was carried out using the chemical activation method. $ZnCl_2$ was used as the chemical agent in the chemical activation. The impregnation ratio was used as 2:1, and the activation temperature was set to 500 °C. The activated carbon (WB-500) was used to remove the deep red dye substance from aqueous solutions. The outcome of the adsorption studies revealed that the highest adsorption capacity was attained when the adsorbent was exposed for 24 hours, maintained at a temperature of 45°C, and a pH of 2.17. The adsorption process effectively removed 95.238 mg with 1 g WB-500. Adsorption study was determined to follow the pseudo-second-order kinetic model and Langmuir isotherm. According to the second order, the adsorption rate increased from $1.22 \cdot 10^{-4}$ to $3.43 \cdot 10^{-4}$ with the increase in temperature from 25 °C to 45 °C. According to adsorption thermodynamics, adsorption is endothermic (ΔH^0 , 41.08 kJ mol⁻¹) and occurs physically and chemically forces. Activated carbon produced from wheat bran can effectively remove the Deep red dye substance from wastewater.

Keywords

Activated carbon,
Deep red,
Adsorption

Time Scale of Article

Received :07 February 2024
Accepted : 16 July 2024
Online date : 30 September 2024

1. INTRODUCTION

The dyes used in the textile industry's colouring fabrics, produced synthetically in different chemical structures and compositions, can reach the environment with wastewater and, from there, to living things [1]. The dyes used in the textile industry differ according to the type of fabric such as cotton dyes, dyes used for denim fabrics, fluorescent-coloured dyes, dyes used to dye linen and leather. Deep red (DR) (CAS:3564-22-5) belongs to the category of azo dyes, it is a synthetic organic compound that includes one or more azo groups ($-N=N-$). The structure of the DR is given in Figure 1. The presence of the azo group also plays a crucial role in the dyeing process, as it allows the dye to form strong covalent bonds with the substrate. The IUPAC name, Color Index (CI), molecular formula and molecular weight is (4Z)-4-[(4-methyl-2-nitrophenyl)hydrozolinidin]-N-(3-nitrophenyl)-3-oxynaphthalene-2-carboxamide, 12350, $C_{24}H_{17}N_5O_6$, 471.42 g/mol, respectively [2]. Around 10,000 different textile colours are introduced to the market annually, and these dyes' wastewater is partially treated and discharged into the receiving waters. Therefore, dyes cause toxic, mutagenic and carcinogenic effects on aquatic animals

*Corresponding Author: caydin@ogu.edu.tr

and humans. Textile products are the product group that has the most relationship with the human body after foodstuffs. Paint residues and chemicals on our clothes penetrate our bodies through sweat and respiration and affect our health at least as much as the chemicals in foodstuffs. According to some studies, some of these chemicals cause allergies and carry a risk of cancer [3]. The limits of the amount of paint that can be found in wastewater in Turkey are determined by environmental legislation. The central legislations in Turkey include the Environmental Law [4], a regulation ensuring the prevention of water pollution to protect the potential of the country's underground and surface water resources and ensure their best use [5], the Wastewater Treatment Regulation and the Wastewater Discharge Regulation. According to these regulations, the amount of paint found in wastewater is determined depending on the type of paint and the area of use.

Single or hybrid processes are used to remove pollutants in water. There are various methods to purify water, such as reverse osmosis. This method operates by removing large molecules like dissolved salts and bacteria. Another method is Ion Exchange, which attracts different water ions to a solid surface with a charged structure. Beneficial ions are then released into the water [6,7]. Chemical precipitation is another water purification method [8]. Ultrafiltration and nanofiltration are used to purify water [9,10]. Flocculation, which is the process of forming aggregates of particles, is another method [11]. These methods have drawbacks, including high cost, maintenance, energy requirements, and management difficulties.

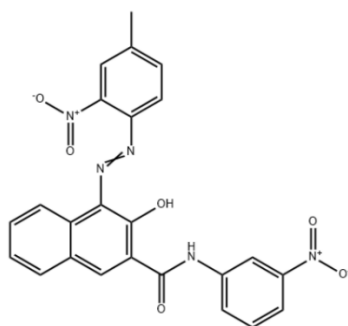


Figure 1. Molecular structure of deep red

Process; the equipment can be set up easily, and the hybrid systems can be easily adjusted to integrate with other treatment techniques. This method requires adsorbent material with a high affinity for contaminants. Adsorption is a technique known for its high effectiveness in removing pollutants from wastewater and ease of use. This approach has been widely utilized and has consistently yielded successful results [12]. Additionally, the adsorbent material can be regenerated through an appropriate desorption process, allowing it to be reused without losing its exceptional pollutant removal capabilities [13–15].

Activated carbon can retain various pollutants thanks to its porous structure with a surface area of 1800-2000 m² per gram. Due to its structure, it can selectively act as a sieve with different pore sizes and keep a wide variety of oxygenated functional groups bound on its surface. It can bind foreign substances on its surface and remove them from water. However, researchers continue to focus on the search for cheap raw materials to reduce production costs [16,17].

The consumption of naturally occurring biomass resources is a green method that has significant implications in many areas when used to derive functional porous carbons that are considered environmentally friendly, economical and sustainable [18]. Biomass is a renewable source of bio-organic-inorganic energy produced by natural and human-induced processes. The benefits of using biomass include easy processability, economic benefit and recyclability. The advantages of biomass over other carbon precursors are that it is naturally abundant, renewable, environmentally friendly and sustainable.

Examples of commonly used biomass include coconut shells [19], palm kernel shells [20], lotus stones [21], palm kernels [22], rice husk [23] leaves [24], sugarcane waste [25], rice husk [26], algae [27]. Renewable carbon sources such as glucose [28], chitin [29], chitosan [30], gelatin [31] and starch [32] can also be used as biopolymers. The characteristics of a carbon-based material, such as pore sizes, surface area, and grain size, can differ based on the raw biomass source. Additionally, the biomass source used can impact the quantity and variety of active sites on the material's surface. These active spots can capture a range of different types of molecules. The preparation of activated carbon from biomass consists of two main steps; first, the biomass is treated with a chemical agent. It is then carbonised in an oxygen-free environment and simultaneously improved by activating the microstructural properties of the carbon [33]. In this study, wheat bran was chosen as the starting material for synthesising the carbon-based adsorbent and the chemical activation method was used in the production process.

2. EXPERIMENTAL

2.1. Chemicals

Wheat bran (WB) was utilized as a carbon source, and Zinc chloride ($ZnCl_2$ - reagent grade, $\geq 98\%$) served as the chemical activation agent in the chemical activation of WB. Sodium chloride (NaCl- ACS reagent, $\geq 99.0\%$) is employed in studies to determine the point of zero charge of active carbon. Hydrochloric acid (HCl- ACS reagent, 37%) and sodium hydroxide (NaOH- pellets for analysis EMSURE®) were employed to adjust the solutions to the desired pH.

2.2 Carbonisation Of Wheat Bran

In the synthesis of carbon-based adsorbents, chemicals are used to obtain a porous structure. Pre-treatment is carried out by impregnating the raw material in various proportions. For this purpose, wheat bran and $ZnCl_2$ were mixed. In a ratio of 2:1 by mass ($ZnCl_2$ g/raw material g), the chemical agent was mixed under a back cooler in a heated magnetic stirrer at 80 °C for 6 hours with 20 g of wheat bran. After the wheat bran absorbed the chemical, the filtration process was performed, and the soft and wet sample with cake structure was taken into drying containers and dried at 85 °C for 24 hours. The sample that had absorbed $ZnCl_2$ was then subjected to carbonisation. Remove some structures from the impregnated sample in Carbolite brand TZF 12/75/700 tube furnace at 500 °C for 1 hour in nitrogen atmosphere ($100\text{ cm}^3\text{ min}^{-1}$ flow rate), starting from the laboratory temperature. After the sample was cooled, it was weighed and first washed in a 0.5 M hydrochloric acid (HCl), then filtered, and the sample, which was brought into contact with hot water repeatedly, was purified from the excess $ZnCl_2$ contained in it. The prepared sample was named WB-500.

2.3. Studies Of Deep Red Adsorption With WB-500

In the adsorption studies, the Thermo Electron AquaMate brand UV-vis spectrophotometer (UV-vis) device was used to determine the amount of deep red at 621 nm. A measure of the effectiveness of adsorbents is the magnitude of adsorption per gram of porous material. This is expressed in q_t (mg g^{-1}) and calculated using Eq.1. The percentage expression of the amount of deep red removed from the solution by adsorbing by the WB-500 was calculated by Eq.2.

$$q_t = \frac{(C_0 - C_t) \cdot V}{W} \quad (1)$$

$$\text{Removal \%} = \frac{(C_0 - C_e)}{C_0} \cdot 100 \quad (2)$$

C_0 (mg L^{-1}) is the amount of deep red contained in 1 litre of water before treatment; C_e (mg L^{-1}) is the amount of deep red in 1 litre of water after treatment. The concentration of deep red in the water during treatment is represented by C_t (mg L^{-1}); V is the volume of deep red solution used during treatment (L); W is the mass (g) of WB-500 brought into contact with contaminated water.

2.4. Determination of the Effect of the pH Value of Deep Red Solution

The pH_{PZC} value of the WB-500 sample was determined using the acid-base titration method. 0.1 g WB-500 and 50 ml of 0.02 M NaCl solution were placed in the conical flask and solutions were prepared with different pH values (pH_i). After 24 hours of agitation, the final pH values of the solutions were measured (pH_f). The $\Delta\text{H}=\text{pH}_f-\text{pH}_i$ value was graphed and the pH_{PZC} value was determined.

Necessary amounts of 0.1 M hydrochloric acid (HCl) or 0.1 M sodium hydroxide (NaOH) were added to the solutions to adjust the pH value of the deep red solution before treatment. For each experiment, 0.1 g of WB-500, 50 mL, 100 mg L^{-1} deep red solution were combined and placed in the flasks. The pH values of the solutions were adjusted with a pH meter to 2.14, 3.12, 4.06 (original), 5.04, 5.92, 7.14, 8.03 and 9.12. For 0.1 g of WB-500 remove the deep red in the solution by adsorption, the flasks were shaken in a water bath at 25°C for 24 hours.

2.5. Determination Of The Effect Of The Amount Of WB-500

For kinetics and isotherm studies, 50 mL of deep red water at 100 mg L^{-1} was used to determine the optimum amount of activated carbon. 0.025 g, 0.05 g, 0.1 g and 0.15 g WB-500 were contacted with polluted water at 25 °C in a shaking water bath heated at both initial pH (4.06) and pH 2.14 for 24 hours.

2.6. Kinetics And Equilibrium Experiments

In kinetic and equilibrium studies, 0.15 g WB-500 was brought into contact with 50 mL of deep red solution containing 100 mg L^{-1} deep red at a pH of 2.14. During the treatment process, kinetic studies were carried out at three different temperatures: 25, 35 and 45 °C. Non-adsorbed concentrations were measured by UV-vis, taking samples at regular intervals.

Equilibrium studies were conducted with solution containing different amounts of deep red (100, 150, 200, 250, 300, 350, 400 and 450 mg L^{-1}). In equilibrium studies, the initial pH of the solutions was adjusted to 2.14 and 0.15 g of WB-500 was used. The data obtained from equilibrium and kinetic studies were applied to the kinetic and isotherm models to understand the nature and mechanism of adsorption. All results were evaluated with an error of 5%. The results of the experiment were expressed in graphs using values calculated with 5% error. ($Y_j=Y_i\pm(Y_i*0.05)$ where Y_i is experimental results.) For the result obtained experimentally, two values are derived, taking 1.05 times and 0.95 times the experimental value. Using these two values, the error bar is plotted. This is done for each experimental outcome.

3. RESULTS

3.1. pH Effect

Activated carbon is an amphoteric solid because of the positive and negative groups that form the adsorption points attached to its surface. The zero point charge (pH_{PZC}) refers to the pH value where the net loads on the inner and outer surfaces of the porous material are zero. When the pH is bigger than pH_{PZC} , the activated carbon surface is negatively charged and suitable for adsorbing cations. When the pH is smaller than pH_{PZC} , the surface is positively charged and suitable for adsorbing anions [34]. Figure 2 shows the pH_{PZC} graph of deep red.

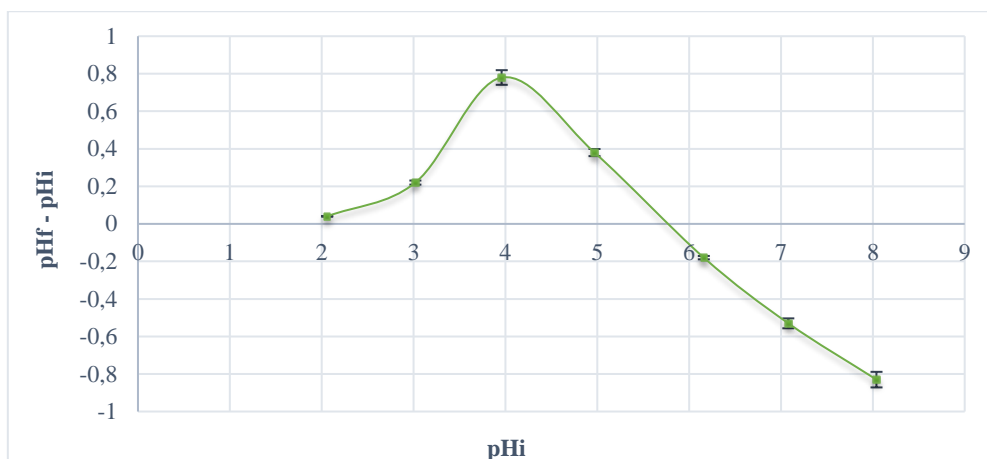


Figure 2. pH_{PZC} graph (WB-500: 0.1 g, V: 50 mL, C₀: 100 mg L⁻¹, T:25 °C, Time:24 h)

The value of the pH_{PZC} point is 5.9. The original pH of the deep red solution is about 4.06. In this case, when the pH value of the deep red solution is not changed without using any chemicals, the pH_{PZC} value is bigger than the pH value of the deep red solution. In water containing deep red, the surface of WB-500 is positively charged and tends to adsorb anions. In most adsorption studies, pH has been found to affect the adsorption process significantly [35]. Figure 3 shows the graph showing the effect of solution pH.

As a result of the studies carried out with deep red solutions with different pH values, WB-500 adsorbed 94% of the deep red in the solution at pH 2.14. As the pH value rises towards 9, the removal seems to decrease. This shows us that the adsorption capacity decreases at increasing pH values. It is observed that the removal does not change much between pH 4-6. Deep red dyestuff is a reactive dyestuff. The reactive end of the deep red dyestuff is negatively charged. Derici explained the high dark red removal at low pH values by replacing the hydrogen ions on the surface of the porous material with anionic dye molecules in the solution [36]. For this reason, the pH value was continued in the following studies by setting it to about 2.0. Derici et al. conducted studies on the adsorption of the Deep red dyestuff of activated carbon produced with kidney bean shells and reached the highest removal at pH 2 [36].

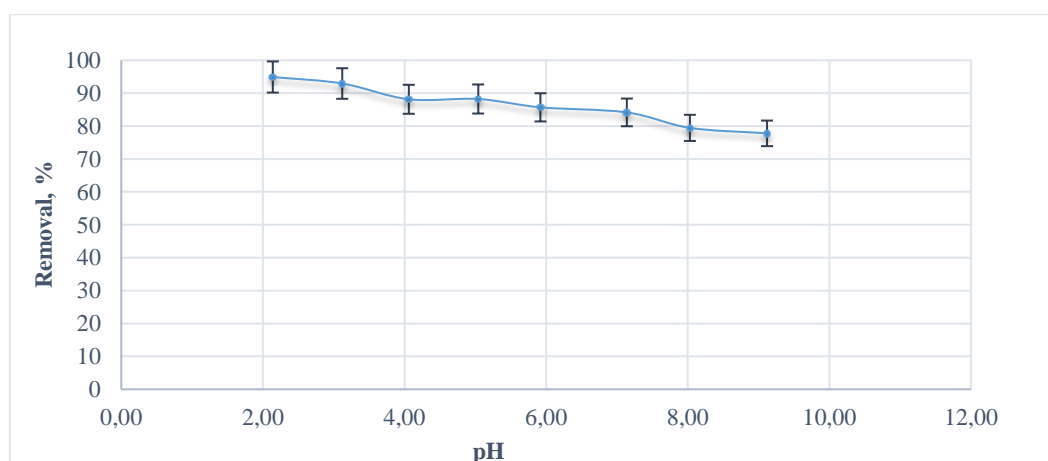


Figure 3. The effect of pH on deep red adsorption on WB-500 (WB-500: 0.1 g, V: 50 mL, C₀: 100 mg L⁻¹, T:25 °C, Time:24 h)

3.2. Effect of The Amount of WB-500

The increased amount of adsorbent leads to increased adsorption as it provides more adsorption centres, allowing more paint to be adsorbed to the surface [35]. In Figure 4, the % deep red adsorbed by different amounts of WB-500 at pH 2.14 and 4.06 and the amount of deep red removed per unit adsorbent are graphically expressed.

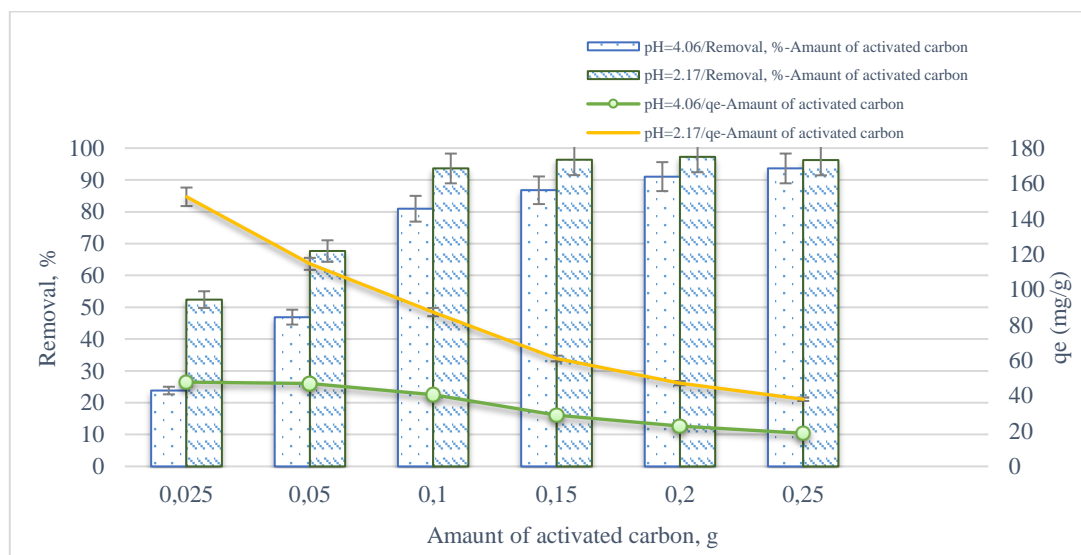


Figure 4. Amount of adsorbed Deep red per unit adsorbent in equilibrium against varying amounts of adsorbent and % amount of adsorption in equilibrium (V: 50 mL, C_0 : 100 mg L⁻¹, T:25 °C, Time:24 h)

During dark red adsorption at pH 2.14, 0.05 g of WB-500 removed 67.65% of the dark red in the solution, while 0.15 g of WB-500 removed 96.33%. While the amount of WB-500 in contact with deep red increased to 0.20 g, WB-500 adsorbed 97.27% of the deep red in the solution. A similar change was observed at pH 4.06, and 0.15 g of WB-500 removed 86.76% of the deep red, and 0.20 g of WB-500 removed 91.05% of the deep red from the solution. As the amount of WB-500 in the solution increases, the probability of the adsorption active sites coming into contact with the deep red molecules increases. Thus, it is possible to remove more pollutants from the water. Using 0.15 g of WB-500 was appropriate in kinetic and balance studies. A slight increase in removal was observed when WB-500 increased from 0.15 g to 0.20 g at both pHs. In addition, since the increase in the amount of WB-500 is greater than the increase in the amount of adsorbed deep red, the q_e value decreases. This shows that the increased amount of WB-500 will not be reflected in the amount of pollution removal from the water at the same rate.

3.3. Interaction Time

For this purpose, Figure 5 shows the change over time in the amount of deep red adsorbed by WB-500. Additionally, Figure 6 shows the graph showing the removal (%) amounts of deep red according to contact time. During the first 8 hours at all studied temperatures, deep red adsorption occurred rapidly, and the amount of adsorption increased continuously. At the end of 8 hours, 78.28% of deep red at 25 °C, 81.86% at 35 °C and 88.76% at 45 °C were removed from the aqueous solution. Since active sites of WB-500 in the solution were covered mainly with deep red molecules at the end of 8 hours, the increase in the amount of deep red adhered to the surface slowed down as the contact time increased. At all temperatures, adsorption reached equilibrium at 19 hours. After 19 hours, the active sites in the WB-500 adsorbed 93.33 % of the dark red at 45°C.

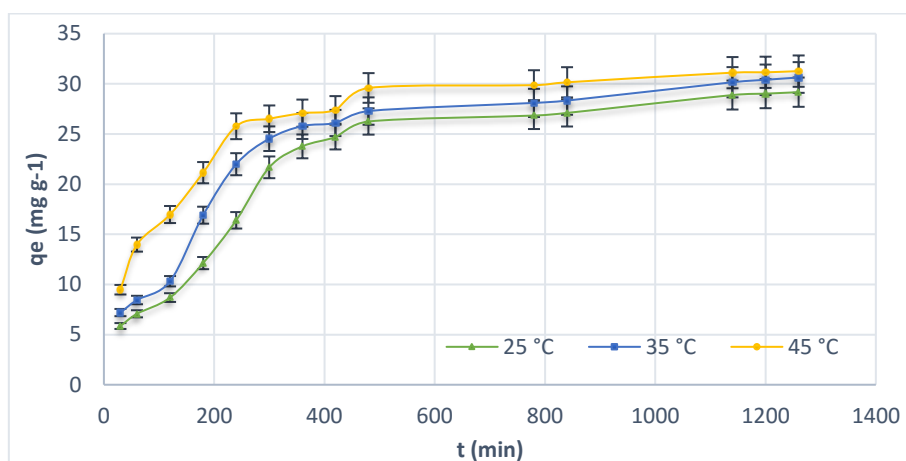


Figure 5. q_e (mg g^{-1}) values against contact time (WB-500: 0.15 g, V: 50 mL, C_0 : 100 mg L^{-1} , T: 25, 35 and 45 $^{\circ}\text{C}$, pH: 2)

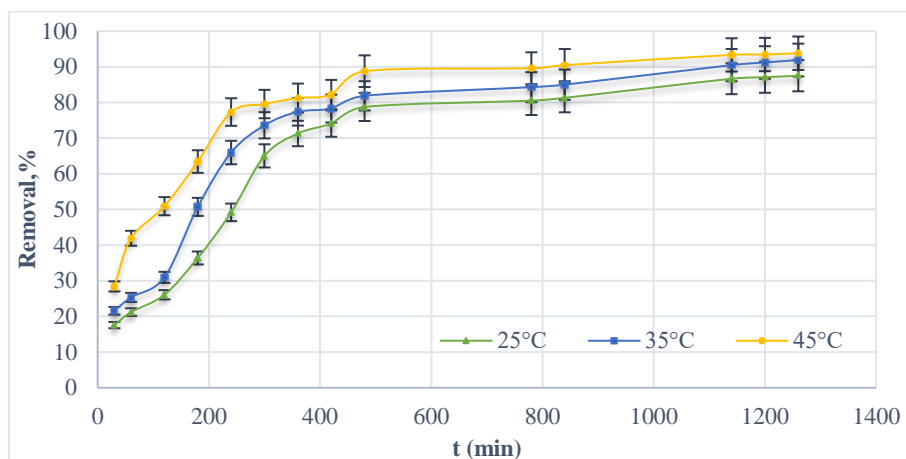


Figure 6. Deep red removal (%) values against contact time (WB-500: 0.15 g, V: 50 mL, C_0 : 100 mg L^{-1} , T: 25, 35 and 45 $^{\circ}\text{C}$, pH: 2)

The kinetic data obtained by using the amounts of dyes removed from the deep red property over time to examine the adsorption mechanism were applied to the Pseudo-First-Order (Pse. Fst. Or.) (Eq. (3) and Figure 7), Pseudo-Second-Order ((Pse. Sec. Or.)) (Eq. (4) and Figure 8) and Intra-Particle Diffusion kinetic models (Eq. (5) and Figure 9.). Table 1 gives the kinetic model parameters of deep red adsorption.

The pseudo-first-order :

$$\log(q_e - q_t) = \log q_{e,1} - \frac{k_1 t}{2.303} \quad (3)$$

The pseudo-second-order:

$$\frac{t}{q_t} = \frac{1}{k_2 q_{e,2}^2} + \frac{t}{q_{e,2}} \quad (4)$$

Intra-particle diffusion model

$$q_t = k_i t^{0.5} + C \quad (5)$$

Where $q_{e,1}$ and $q_{e,2}$ are the maximum magnitude of the amount of adsorption per gram of WB-500 based on the pseudo-first-order kinetic model and pseudo-second-order kinetic model, respectively. k_1 is the first-order rate constant in units of min^{-1} , and k_i is the intraparticle diffusion constant in units of $\text{mg g}^{-1} \text{min}^{-0.5}$. C is proportional to the boundary layer thickness, and k_2 is the pseudo-second-order rate constant in units of $\text{g mg}^{-1} \text{min}^{-1}$ [37, 38].

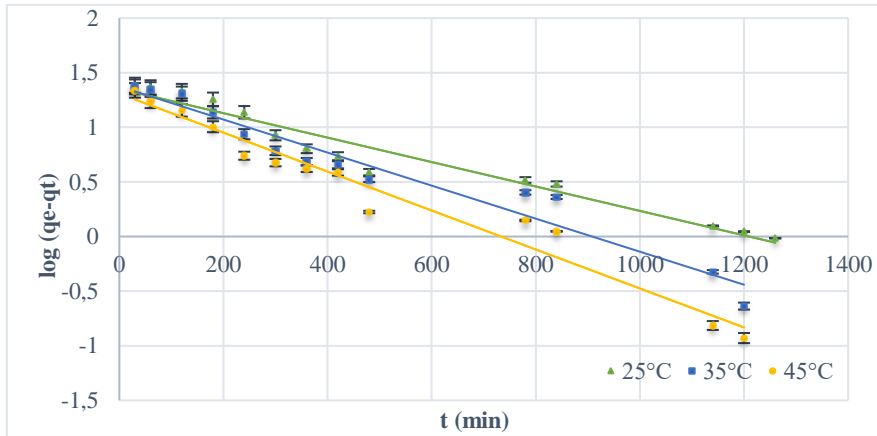


Figure 7. The PFO kinetic model of deep red adsorption.

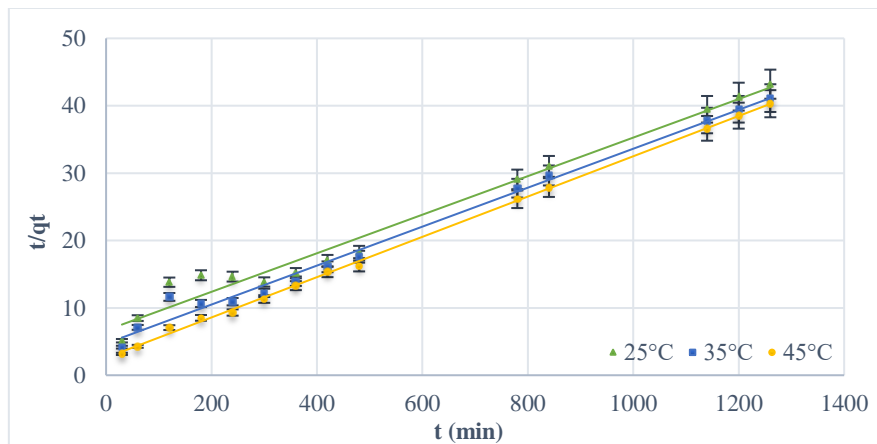


Figure 8. PSO kinetic model of deep red adsorption.

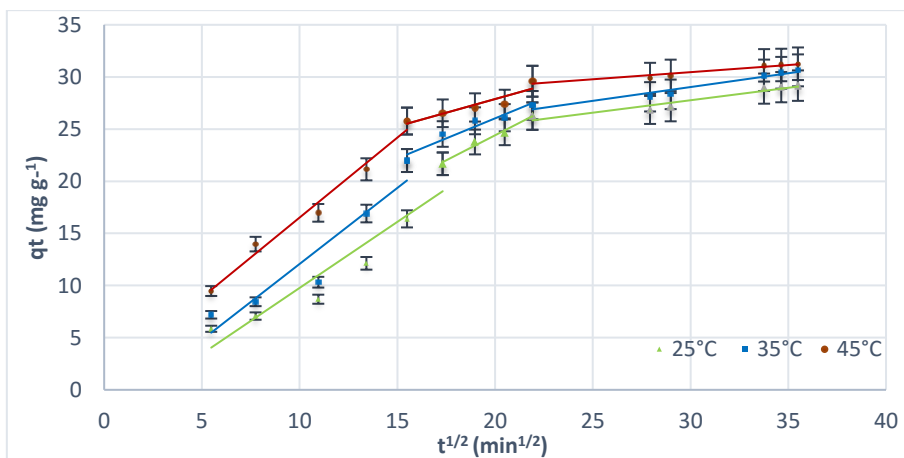


Figure 9. Intra-particle diffusion model of deep red adsorption.

Table 1. Kinetic model parameters of deep red adsorption.

First-order kinetic model			
	25 °C	35 °C	45 °C
q_{e,1} (mg g ⁻¹)	22.53	23.64	20.33
k₁ (min ⁻¹)	2.53.10 ⁻³	3.45.10 ⁻³	4.14.10 ⁻³
R²	0.95	0.94	0.96
Second-order kinetic model			
	25 °C	35 °C	45 °C
q_{e,2} (mg g ⁻¹)	34.96	34.60	33.44
k₂ (g mg ⁻¹ .min ⁻¹)	1.22.10 ⁻⁴	1.77.10 ⁻⁴	3.43.10 ⁻⁴
R²	0.97	0.99	0.99
Intra-particle diffusion model			
	25 °C	35 °C	45 °C
k_{id} (mg g ⁻¹ min ^{-0.5})	0.96	0.77	0.52
C	5.21	10.66	17.39
R²	0.98	0.93	0.85

They were comparing the Pse. Sec. Or. kinetic and Pse. Ft. Or. kinetic models, the Pse. Sec. Or. kinetic model better represents the kinetic data based on the time that WB-500 removes deep red by adsorption in all three temperatures. The rate constants of the Pse. Sec. Or. kinetic model shows that the reaction occurs slowly and that the adsorption rate increases with the increase in temperature. The experimental value of q_e is 30.12 mg g⁻¹.

The shape of the graph of the intraparticle diffusion model can give information about the adsorption mechanism. Suppose the deep red molecules attached to the WB-500 surface reach the pores or the surface by film diffusion due to the water covering the WB-500 surface. In that case, the graph consists of 3 parts, and the graph does not pass through the origin and has a C value. The graph's second part is formed if the deep red molecules reach the adsorption points by intraparticle diffusion and advance in the activated carbon's pores. The third part of the graph represents the adsorption step. [39]. The intraparticle diffusion pattern appears to occur in three phases. This shows us that the adsorption process takes place gradually. The k_{id} value is decreased from 0.96 mg g⁻¹ min^{-0.5} to 0.52 mg g⁻¹ min^{-0.5}. As the temperature increased, the effect of film diffusion on adsorption increased, while the effect of intraparticle diffusion decreased. The temperature increase increased the C value from 5.21 to 17.39. This shows us that the temperature increase causes the film layer thickness, where film diffusion occurs, to increase.

3.4. Equilibrium Experiments

How molecules or ions interact with the solid surface can be explained by adsorption isotherms that provide information about the equilibrium states of an adsorption system. The main objective in expressing the data obtained during the adsorption process of the dye molecules of different initial concentrations with isotherms is to show the equilibrium conditions of the porous material and porous material relationship and to reveal the deposition mechanism of the substances on the surface [40]. Equilibrium data of the adsorption of deep red were obtained by performing experiments in deep red solutions at 3 different temperatures and different initial concentrations, and the data are presented in Figure 10. The conformity of the obtained data to four different isotherms was examined. Linear forms of isotherms are given in Eq. (6-9). The Langmuir isotherm model describes adsorbed molecules on a homogeneous surface containing adsorption points with similar attractive forces and in which the molecules are adsorbed in a single layer. At the same time, according to the Langmuir model, all active sites are considered to have the same energy and equal interest in the molecules to be adsorbed. The

isotherm plots and constants of deep red adsorption are given in Figure 11 and Table 2, respectively. [35,41].

$$\text{Langmuir} \quad q_e = \frac{q_L K_L C_e}{1 + K_L C_e} \quad \frac{C_e}{q_e} = \frac{1}{q_L K_L} + \frac{C_e}{q_L} \quad (6)$$

$$\text{Freundlich} \quad q_e = K_F C_e^{1/n} \quad \log(q_e) = \log K_F + \frac{1}{n} \log C_e \quad (7)$$

$$\text{Temkin} \quad q_e = \frac{RT}{b_T} \ln(K_T C_e) \quad q_e = B_1 \ln K_T + B_1 \ln C_e \quad (8)$$

$$\text{Dubinin–Radushkevich (D–R)} \quad \ln q_e = \ln q_m - \beta \varepsilon^2 \quad (9)$$

- q_L : Langmuir adsorption capacity of the WB-500 (mg g^{-1})
- K_L : Langmuir adsorption constant ($\text{dm}^3 \text{mg}^{-1}$)
- K_F and n are Freundlich constants
- b_T : Temkin constant (J mol^{-1})
- K_T : The equilibrium binding constant (L g^{-1})
- q_m : Theoretical monolayer saturation capacity (mg g^{-1})
- ε , The Polanyi potential, $\varepsilon = RT \ln(1 - 1/C_e)$
- T : Temperature (K)
- R : The universal gas constant ($8,314 \text{ J mol}^{-1} \text{K}^{-1}$)
- β : Dubinin–Radushkevich constant ($\text{mol}^2 \text{J}^{-2}$)
- E : The average free energy of adsorption (kJ mol^{-1}), $E = \frac{1}{(2\beta)^{1/2}}$

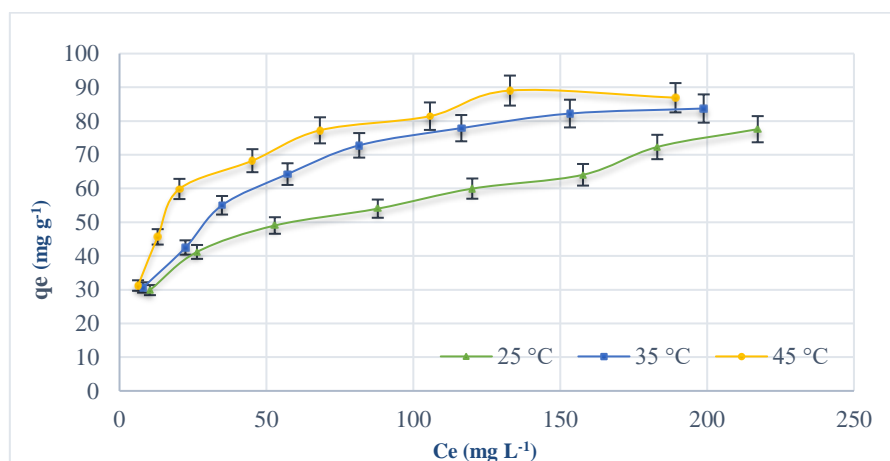


Figure 10. The effect of temperature on deep red adsorption. (WB-500: 0.15 g, V: 50 mL, T: 25, 35 and 45 °C, Time: 24 h, pH: 2)

There is a relationship of $q_e (45 \text{ }^\circ\text{C}) > q_e (35 \text{ }^\circ\text{C}) > q_e (25 \text{ }^\circ\text{C})$ between the q_e values obtained in all studies performed in deep red solutions with different initial concentrations. The temperature increase positively affected the adsorption capacity of WB-500 under equilibrium conditions. The adsorption nature of deep red is thermodynamically endothermic.

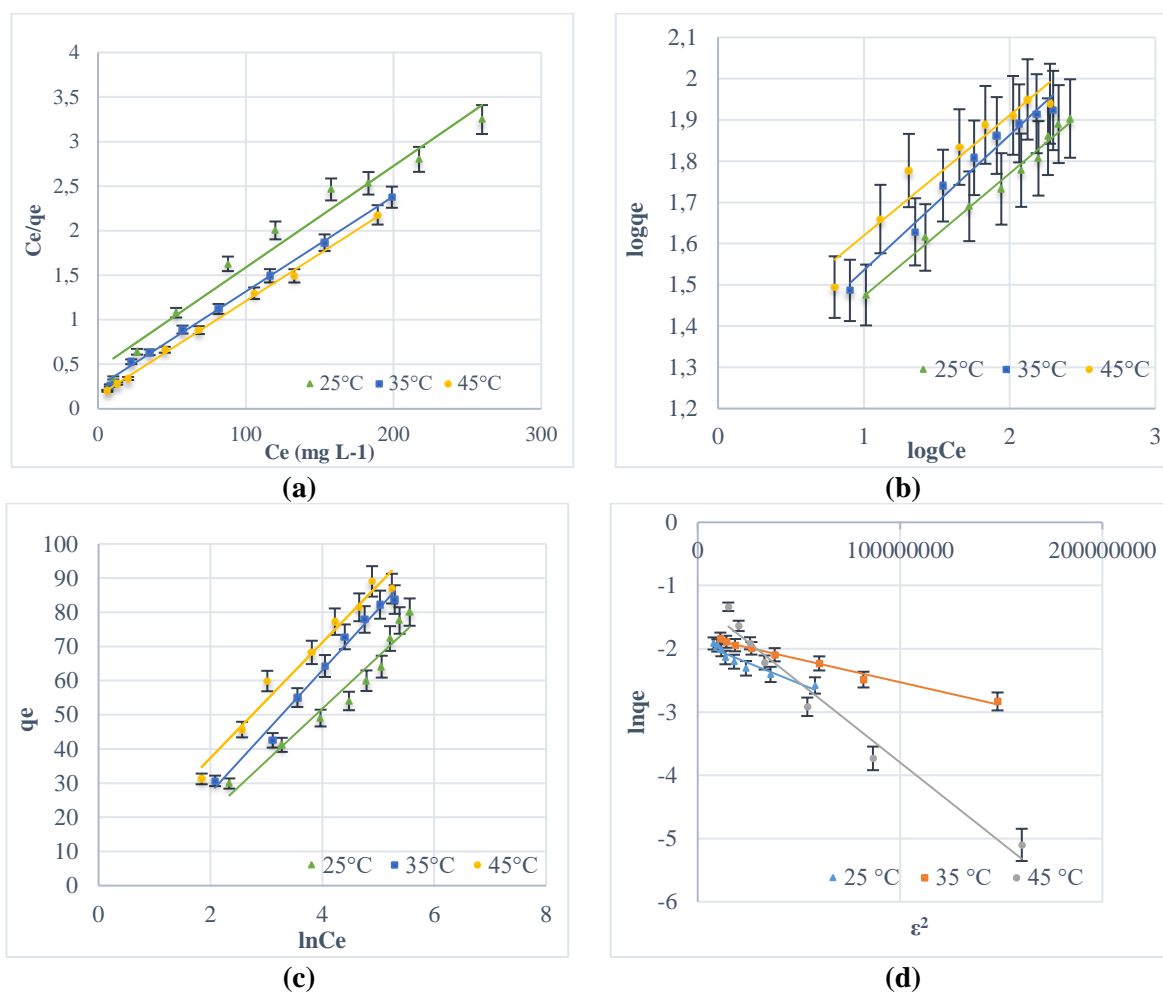


Figure 11. Isotherm models' graphs Langmuir (a), Freundlich (b), Temkin (c) and The Dubinin–Radushkevich (D–R) (d)

When the isotherm graphs drawn using data obtained from studies conducted at different temperatures were compared, the experimental data in the Freundlich model deviated from the model line. Due to the homogeneity of WB-500 produced from wheat bran, the adsorbing behaviour of deep red is suitable for the Langmuir type. The $1/n$ values are close to zero, and the surface of the activated carbon is homogeneous.

Deep red's maximum monolayer adsorption capacities were calculated according to the Langmuir model in Table 2. The q_L values for 25, 35 and 45 °C are 87.71, 93.45 and 95.23 mg g⁻¹, respectively. As can be seen, the Langmuir adsorption capacities increased as the temperature increased. The Temkin model is the adsorption isotherm, which considers the interactions between adsorbed substances. The Temkin equation states that as the adsorbed molecules adhere to the surface of the porous material, the active adsorption points decrease, and a linear decrease in the adsorption energy occurs [42]. According to the Temkin isotherm equation, the heat of adsorption at 25 °C is obtained as 162.12 j mol⁻¹, while for 45 °C, it is obtained as 156.7 j mol⁻¹. As the temperature increased, the amount of coating of the adsorbed increased, and therefore the adsorption heat decreased.

The Dubinin–Radushkevich model is more general than the Langmuir model. The Dubinin–Radushkevich model does not assume that adsorption occurs on a homogeneous surface. The E value explains whether the adsorption mechanism occurs by the ion exchange mechanism or by the effect of

van der Waals forces [39]. According to the D-R model, one mole of deep red is adsorbed to the active points of WB-500 at 25, 35 and 45 °C with an adsorption energy of 7.07, 8.45 and 4.08 kJ, respectively. Since these values are close to 8 kJ and less than 8 kJ, the deep red molecules may have been held onto the surface by van der Waals forces.

Table 2. Isotherm model parameters of deep red adsorption.

Langmuir Isotherm model			
	q_L (mg g ⁻¹)	K_L (L mg ⁻¹)	R^2
25 °C	87.71	0.025	0.97
35 °C	93.45	0.043	0.99
45 °C	95.23	0.072	0.99
Freundlich Isotherm model			
	1/n	K_f	R^2
25 °C	0.30	3.23	0.98
35 °C	0.33	3.34	0.97
45 °C	0.29	3.77	0.92
Temkin Isotherm model			
	b_T	K_T	R^2
25 °C	162.12	0.54	0.94
35 °C	143.2	0.61	0.98
45 °C	156.7	1.23	0.97
The Dubinin–Radushkevich (D–R) Isotherm model			
	E (kJ mol ⁻¹)	q_m (mg g ⁻¹)	R^2
25 °C	7.07	81.19	0.89
35 °C	8.45	89.85	0.98
45 °C	4.08	153.74	0.96

3.5. Adsorption Thermodynamics

Gibbs free energy (Eq.10), entropy and enthalpy parameters were examined to examine the thermodynamics of studies with deep red adsorption. Using the K_L values obtained from the Langmuir equation, the $\ln K_L$ values against $1/T$ were graphed and given in Figure 12 The thermodynamic values of ΔH° and ΔS° were calculated by Eq. 11.

$$\Delta G^\circ = -RT \ln K_L \quad (10)$$

$$\Delta G^\circ = \Delta H^\circ - T\Delta S^\circ \quad (11)$$

The free energy change (ΔG°) in the adsorption of dark red was calculated to be approximately -23.28, -25.43 and -27.59 kJ mol⁻¹ at 25, 35 and 45 °C. Generally, the change of free energy for physisorption is between -20 and 0 kJ mol⁻¹, the physisorption together with chemisorption is at the range of -20 to -80 kJ mol⁻¹ and chemisorption is at a range of -80 to -400 kJ mol⁻¹ [43]. According to the free energy exchange results, the adsorption process occurred under the influence of physical and chemical forces [44]. ΔH° value of 41.08 kJ mol⁻¹ indicates the system must receive heat for adsorption. The ΔS° value was calculated as 215.86 j mol⁻¹ K⁻¹, and the positive value of entropy indicates an increase in randomness and irregularity at the solid/solution interface. This indicates that adsorption occurs with increased entropy [45,46].

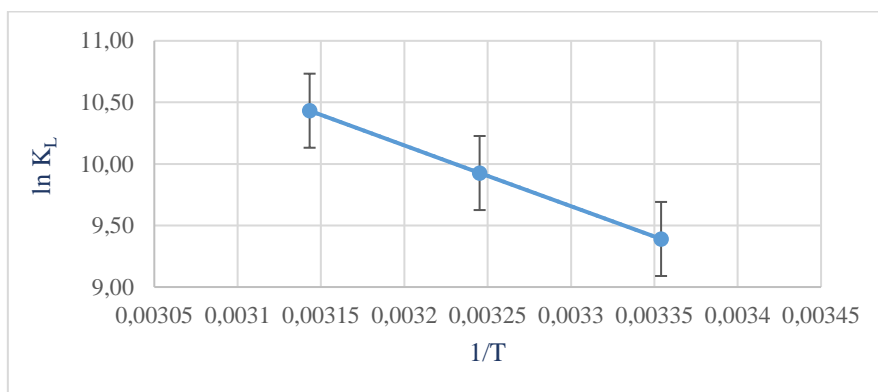


Figure 12. 1/T versus lnK_L exchange of deep red adsorption.

4. CONCLUSIONS

In this study, wheat bran was recycled, and activated carbon production with economic value was realised. The deep red adsorption capacity of the activated carbon produced was determined. The nature of adsorption was determined by performing kinetic and equilibrium studies. Deep red's maximum monolayer adsorption capacities were calculated according to the Langmuir model as are 87.71, 93.45 and 95.23 mg g⁻¹ for 25, 35 and 45 °C, respectively. Based on the Temkin isotherm, as temperature increased, the quantity of adsorbed coating rose, leading to a decrease in the heat of adsorption 162.12 j mol⁻¹ to 156.7 j mol⁻¹. According to the results of the kinetic study, deep red adsorption on WB-500 increased from 1.22.10⁻⁴ to 3.43.10⁻⁴ g mg⁻¹.min⁻¹ as the temperature dropped from 25 °C to 45 °C. The adsorption process takes place gradually according to the intra-particle diffusion modal. The k_{id} value is decreased from 0.96 mg g⁻¹ min^{-0.5} to 0.52 mg g⁻¹ min^{-0.5}. The Langmuir model has a better correlation coefficient than other mathematical models at all temperatures examined in the current study. The resulting single-layer adsorption capacity value was obtained at 95.23 mg g⁻¹ 45 °C. In conclusion, the results show that activated carbon produced from wheat bran can be effectively applied to remove deep red from wastewater.

CONFLICT OF INTEREST

The authors declare that they have no conflict of interest regarding the publication of this article.

ACKNOWLEDGMENTS: This study was prepared within the scope of the Master's Thesis studies conducted by Fatma Betül Kuş, a student of Eskişehir Osmangazi University, Institute of Natural and Applied Sciences, Department of Chemical Engineering.

CRedit AUTHOR STATEMENT:

Ilknur Demiral: Conceptualization, Data curation, Formal Analysis, Investigation, Methodology, Resources, Supervision, Review and editing. **Canan Samdan:** Conceptualization, Data curation, Formal Analysis, Investigation, Methodology, Supervision, Visualization, Writing – original draft & editing, **Fatma Betül Kus:** Conceptualization, Data Curation, Formal Analysis, Methodology, Validation, Writing

REFERENCES

- [1] Schneider K, Hafner C, Jäger I. Mutagenicity of textile dye products. *J Appl Toxicol.* 2004; 24 (2), 83-91.
- [2] Deep Red Cas#: 3564-22-5. ChemicalBook. https://m.chemicalbook.com/ProductChemicalProperties/CB8356989_EN.htm. Accessed May 29, 2024.
- [3] Sulistina DR, Martini S. The Effect of Rhodamine B on the Cerebellum and Brainstem Tissue of Rattus Norvegicus. *J Public Health Res.* 2020; 9 (2).
- [4] Environmental Law. 1983. <https://www.mevzuat.gov.tr/MevzuatMetin/1.5.2872.pdf>. Accessed June 22, 2023.
- [5] Water Pollution Control Regulation.; 2004:25687. <https://www.mevzuat.gov.tr/mevzuat?MevzuatNo=7221&MevzuatTur=7&MevzuatTertip=5>. Accessed June 22, 2023.
- [6] Inamuddin. Applications of Adsorption and Ion Exchange Chromatography in Waste Water Treatment. Materials Research Forum LLC, 2017.
- [7] Wong CW, Barford JP, Chen G, McKay G. Kinetics and equilibrium studies for the removal of cadmium ions by ion exchange resin. *J Environ Chem Eng.* 2014; 2 (1), 698-707.
- [8] Zamora-Ledezma C, Negrete-Bolagay D, Figueroa F, Zamora-Ledezma E, Ni M, Alexis F, et al. Heavy metal water pollution: A fresh look about hazards, novel and conventional remediation methods. *Environ Technol Innov.* 2021; 22, 101504.
- [9] Secondes MFN, Naddeo V, Belgiorno V, Ballesteros F. Removal of emerging contaminants by simultaneous application of membrane ultrafiltration, activated carbon adsorption, and ultrasound irradiation. *J Hazard Mater.* 2014; 264, 342-349.
- [10] Abdel-Fatah MA. Nanofiltration systems and applications in wastewater treatment: Review article. *Ain Shams Eng J.* 2018;9 (4), 3077-3092.
- [11] Teh CY, Budiman PM, Shak KPY, Wu TY. Recent Advancement of Coagulation–Flocculation and Its Application in Wastewater Treatment. *Ind Eng Chem Res.* 2016; 55 (16), 4363-4389.
- [12] Savci S, Donmez S, Mazmanci MA. Performance And Mechanisms Of Malachite Green Dye Adsorption Using Industrial Solid Waste As Adsorbent. *Environ Eng Manag J.* 2023; 22 (1), 97-104.
- [13] Simsek R, Ciftci BN, Uysal Y. An Experimental Study On The Efficiency Of Chromium (VI) Removal With Starch-Magnetite Nanocomposite (Starch@Mnps). *Anadolu Univ J Sci Technol- Appl Sci Eng.* 2020; 21 (2), 322-334.
- [14] Dikmen S, Ersoy B, Dikmen Z. Adsorption Behaviour Of Ionic And Non-Ionic Surfactants Onto Talc A Naturally Hydrophobic Mineral-A Comparative Study. *Eskişehir Tech Univ J Sci Technol - Appl Sci Eng.* 2020; 21 (1), 139-152.
- [15] Savci S, Uysal MM. Adsorption of Methylene Blue and Methyl Orange By Using Waste Ash. *Süleyman Demirel Üniversitesi Fen Bilim Enstitüsü Derg.* 2017; 21 (3), 831.

- [16] Neolaka YAB, Riwu AAP, Aigbe UO, Ukhurebor KE, Onyancha RB, Darmokoesoemo H, et al. Potential of activated carbon from various sources as a low-cost adsorbent to remove heavy metals and synthetic dyes. *Results Chem.* 2023; 5, 100711.
- [17] Başar B, Şayan E. Optimization Of Selective Cu^{2+} Adsorption Within The Multi-Ion System By Using Activated Carbon Prepared By Ultrasound. *Anadolu Univ J Sci Technol- Appl Sci Eng.* 2018; 19 (4), 893-906.
- [18] Manasa P, Sambasivam S, Ran F. Recent progress on biomass waste derived activated carbon electrode materials for supercapacitors applications—A review. *J Energy Storage.* 2022; 54, 105290.
- [19] Yağmur HK, Kaya İ. Synthesis and characterization of magnetic ZnCl_2 -activated carbon produced from coconut shell for the adsorption of methylene blue. *J Mol Struct.* 2021; 1232, 130071.
- [20] Syed-Hassan SSA, Zaini MSM. Optimization of the preparation of activated carbon from palm kernel shell for methane adsorption using Taguchi orthogonal array design. *Korean J Chem Eng.* 2016; 33 (8), 2502-2512.
- [21] Boudechiche N, Fares M, Ouyahia S, Yazid H, Trari M, Sadaoui Z. Comparative study on removal of two basic dyes in aqueous medium by adsorption using activated carbon from *Ziziphus lotus* stones. *Microchem J.* 2019; 146, 1010-1018.
- [22] Kundu A, Sen Gupta B, Hashim MA, Redzwan G. Taguchi optimization approach for production of activated carbon from phosphoric acid impregnated palm kernel shell by microwave heating. *J Clean Prod.* 2015; 105, 420-427.
- [23] Metin N, Savci S. Adsorption of Malachite Green by An Agricultural Waste: Rice Husk. *Türk Tarım Ve Doğa Bilim Derg.* 2021; 8 (1), 23-29.
- [24] Mosoarca G, Vancea C, Popa S, Gheju M, Boran S. *Syringa vulgaris* leaves powder a novel low-cost adsorbent for methylene blue removal: isotherms, kinetics, thermodynamic and optimization by Taguchi method. *Sci Rep.* 2020; 10 (1), 17676.
- [25] Srenscek-Nazzal J, Kamińska W, Michalkiewicz B, Koren ZC. Production, characterization and methane storage potential of KOH-activated carbon from sugarcane molasses. *Ind Crops Prod.* 2013; 47, 153-159.
- [26] Luo Y, Li D, Chen Y, Sun X, Cao Q, Liu X. The performance of phosphoric acid in the preparation of activated carbon-containing phosphorus species from rice husk residue. *J Mater Sci.* 2019; 54 (6), 5008-5021.
- [27] Aravindhana R, Raghava Rao J, Unni Nair B. Preparation and characterization of activated carbon from marine macro-algal biomass. *J Hazard Mater.* 2009; 162 (2-3), 688-694.
- [28] Eshghi A, kheirmand M. Graphene/Ni–Fe layered double hydroxide nano composites as advanced electrode materials for glucose electro oxidation. *Int J Hydrog Energy.* 2017; 42 (22), 15064-15072.
- [29] Das MP. Removal of Methylene Blue by Adsorption Using Fish Scale Chitin. *Nat Environ Pollut Technol.* 2018; 17 (3), 7.

- [30] Wong KT, Wong VL, Lim SS. Bio-sorptive Removal of Methyl Orange by Micro-Grooved Chitosan (GCS) Beads: Optimization of Process Variables Using Taguchi L9 Orthogonal Array. *J Polym Environ*. 2021; 29 (1), 271-290.
- [31] Mahmoud ME. Water treatment of hexavalent chromium by gelatin-impregnated-yeast (Gel-Yst) biosorbent. *J Environ Manage*. 2015; 147, 264-270.
- [32] Chen L, Zhu Y, Cui Y, Dai R, Shan Z, Chen H. Fabrication of starch-based high-performance adsorptive hydrogels using a novel effective pretreatment and adsorption for cationic methylene blue dye: Behavior and mechanism. *Chem Eng J*. 2021; 405, 126953.
- [33] Malini K, Selvakumar D, Kumar NS. Activated carbon from biomass: Preparation, factors improving basicity and surface properties for enhanced CO₂ capture capacity – A review. *J CO₂ Util*. 2023; 67, 102318.
- [34] Zhang Y, Song X, Xu Y, Shen H, Kong X, Xu H. Utilization of wheat bran for producing activated carbon with high specific surface area via NaOH activation using industrial furnace. *J Clean Prod*. 2019; 210, 366-375.
- [35] Alomar T, Qiblawey H, Almomani F, Al-Raoush RI, Han DS, Ahmad NM. Recent advances on humic acid removal from wastewater using adsorption process. *J Water Process Eng*. 2023; 53, 103679.
- [36] Derici C. Production of Activated Carbon from Kidney Bean Shells and Its Use in Dyestuff Removal. Master Thesis. Eskişehir Osmangazi University Institute of Science and Technology, 2021.
- [37] Khaled A, El Nemr A, El-Sikaily A, Abdelwahab O. Treatment of artificial textile dye effluent containing Direct Yellow 12 by orange peel carbon. *Desalination*. 2009; 238 (1), 210-232.
- [38] Torres-Perez J, Gerente C, Andres Y. Conversion of agricultural residues into activated carbons for water purification: Application to arsenate removal. *J Environ Sci Health Part A*. 2012; 47 (8), 1173-1185.
- [39] Hydari S, Sharififard H, Nabavinia M, Parvizi MR. A comparative investigation on removal performances of commercial activated carbon, chitosan biosorbent and chitosan/activated carbon composite for cadmium. *Chem Eng J*. 2012; 193-194.
- [40] Garg V. Basic dye (methylene blue) removal from simulated wastewater by adsorption using Indian Rosewood sawdust: a timber industry waste. *Dyes Pigments*. 2004; 63 (3), 243-250.
- [41] Naghizadeh A, Momeni F, Kamani H. Study of Ultrasonic Regeneration and Adsorption of Humic Acid on Activated Carbon. *Health Scope*. 2018; 7 (2).
- [42] Danish M, Ahmad T, Majeed S, Ahmad M, Ziyang L, Pin Z, et al. Use of banana trunk waste as activated carbon in scavenging methylene blue dye: Kinetic, thermodynamic, and isotherm studies. *Bioresour Technol Rep*. 2018; 3, 127-137.
- [43] Gerçel Ö, Özcan A, Özcan AS, Gerçel HF. Preparation of activated carbon from a renewable bio-plant of *Euphorbia rigida* by H₂SO₄ activation and its adsorption behavior in aqueous solutions. *Appl Surf Sci*. 2007; 253 (11), 4843-4852.

- [44] Mei D, Liu L, Yan B. Adsorption of uranium (VI) by metal-organic frameworks and covalent-organic frameworks from water. *Coord Chem Rev.* 2023; 475, 214917.
- [45] Benjelloun M, Miyah Y, Akdemir Evrendilek G, Zerrouq F, Lairini S. Recent Advances in Adsorption Kinetic Models: Their Application to Dye Types. *Arab J Chem.* 2021; 14 (4), 103031.
- [46] Chen S, Qin C, Wang T, Chen F, Li X, Hou H, et al. Study on the adsorption of dyestuffs with different properties by sludge-rice husk biochar: Adsorption capacity, isotherm, kinetic, thermodynamics and mechanism. *J Mol Liq.* 2019; 285, 62-74.



RESEARCH ARTICLE

FIBONACCI AND LUCAS NUMBERS AS PRODUCTS OF THEIR ARBITRARY TERMS

Ahmet DAŞDEMİR ¹, Ahmet EMİN ^{2,*}

¹ Department of Mathematics, Faculty of Science, Kastamonu University, Kastamonu, Türkiye

ahmetdasdemir37@gmail.com - [0000-0001-8352-2020](https://orcid.org/0000-0001-8352-2020)

² Department of Mathematics, Faculty of Science, Karabük University, Karabük, Türkiye

ahmetemin@karabuk.edu.tr - [0000-0001-7791-7181](https://orcid.org/0000-0001-7791-7181)

Abstract

This study presents all solutions to the Diophantine equations $F_k = L_m L_n$ and $L_k = F_m F_n$. To be clear, the Fibonacci numbers that are the product of two arbitrary Lucas numbers and the Lucas numbers that are the product of two arbitrary Fibonacci numbers are determined herein. The results under consideration are proven by using the Dujella-Pethő lemma in coordination with Matveev's theorem. All common terms of the Fibonacci and Lucas numbers are determined. Further, the Lucas-square Fibonacci and Fibonacci-square Lucas numbers are given.

Keywords

Fibonacci and Lucas numbers,
Logarithmic height in
logarithms,
Matveev theorem,
Dujella - Pethő lemma

Time Scale of Article

Received :07 February 2024
Accepted : 16 July 2024
Online date :30 September 2024

1. INTRODUCTION

Let $(F_n)_{n \geq 0}$ and $(L_n)_{n \geq 0}$ be the n^{th} terms of the Fibonacci and Lucas numbers, which can be produced by utilizing the recurrence relation $F_{n+1} = F_n + F_{n-1}$ and $L_{n+1} = L_n + L_{n-1}$ for all integers $n \geq 1$ with the initial conditions $(F_0, F_1) = (0, 1)$ and $(L_0, L_1) = (2, 1)$, respectively. It can be observed that the Fibonacci and Lucas numbers are a second-order integer sequence that satisfies the algebraic equation $x^2 - x - 1 = 0$. By considering this algebraic equation with the mentioned initial conditions, one can develop their Binet's formulae for all $n \in \mathbb{N}$:

$$F_n = \frac{\alpha^n - \beta^n}{\alpha - \beta} \text{ and } L_n = \alpha^n + \beta^n \tag{1}$$

where $\alpha = \frac{1+\sqrt{5}}{2}$ and $\beta = \frac{1-\sqrt{5}}{2}$. More detail can be referenced to [1-3].

It can be stated immediately that the above integer sequences are the most beloved subject of mathematics and are paid great attention by almost all branches of modern sciences. Today, the respective results and discussions are expanding to an exciting aspect: finding all possible solutions to Diophantine equations, including special integer sequences, i.e., Fibonacci, Lucas, Pell, or Jacobsthal numbers, etc. In [4], Marques investigated the Fibonacci numbers that can be expressible in terms of the generalized Cullen and Woodall numbers. In [5], Chaves and Marques determined all terms of generalized Fibonacci numbers, which are the sum of the powers of the consecutive generalized

*Corresponding Author: ahmetemin@karabuk.edu.tr

Fibonacci sequence. In [6], Bravo and Gómez considered k -generalized Fibonacci numbers that are the Mersenne numbers. In [7], Pongsriiam found all the Fibonacci and Lucas numbers, which are one away from the product of an arbitrary number of the Fibonacci or Lucas numbers. In [8], Ddamulira et al. solved the Pillai-type problem with k -generalized Fibonacci numbers and powers of 2 for $k > 3$. In [9], Kafle et al. dealt with finding all solutions to the Pell equations related to the product of two Fibonacci numbers. In [10], Qu and Zeng investigated all Lucas numbers that are concatenations of two repdigits. In [11], Şiar et al. found all Fibonacci or Lucas numbers that are products of two repdigits in base b . In [12], Alan and Alan discovered the Mersenne numbers that can be written in terms of the products of two Pell numbers. In [13], Rihane and Togbé obtained terms of k -Fibonacci numbers in the arrays of the Padovan or Perrin numbers.

In the open literature, there are a few more specific papers that study the Diophantine-type equations concerning the Fibonacci numbers or other integer sequences. However, both the above brief literature survey and other source works show that integer sequences in the right-hand side and the left-hand side of problems under consideration are of different characteristic algebraic equations. For example, Fibonacci or Lucas number vs. Pell number by Alekseyev [14], Fibonacci number vs. Pell number by Ddamulira et al. [15], generalized Fibonacci number vs. generalized Pell number by Bravo et al. [16], Fibonacci number vs. Jacobsthal number by Erduvan and Keskin [17], and Leonardo number vs. Jacobsthal number by Bensella and Behloul [18]. Motivated by the results of the current literature, in this paper, we address finding problem of all possible solutions to the following Diophantine equations for positive integers k , m , and n according to the famous Matveev's theorem and the Dujella-Pethő lemma:

$$F_k = L_m L_n \tag{2}$$

and

$$L_k = F_m F_n \tag{3}$$

Here, due to multiplicative symmetry, it is sufficient that the case where $k \geq 1$ and $1 \leq m \leq n$ is considered. However, our equations consist of the Fibonacci and Lucas numbers that have the same characteristic equation. This makes the application of the Dujella-Pethő lemma impossible because some parameters disappear unlike the solution processes in the current literature. One of the novelties of the paper is to display a new approach to this issue.

It should be noted that in [19], Carlitz considered the same problems the first time by employing divisibility properties and some elementary identities. However, the author's results are either incorrect or incomplete. More precisely, the author asserted that while the unique solution of equation (2) is $(k, m, n) = (8, 4, 2)$ for $1 < n \leq m$, Equation (3) has no solution for $2 < n \leq m$. Further, in [20], based on the elementary properties and inequalities, Wang et al. stated that while Equation (3) has no solution, the triple $(k, m, n) = (4, 2, 1)$ is one solution to Equation (2). As can be seen, the results of both studies are also contradictory to each other. The results of our paper will both eliminate this deficiency and will end this debate.

2. BASIC TOOLS

This section introduces essential tools and definitions, lemmas, and theorems required in the rest of the paper. Our proof process is based on the Matveev's theorem, which uses the linear forms in logarithms to limit the variables of the problem, and the Dujella-Pethő lemma, which allows us to reduce the bounds.

Let η be an algebraic number of degree d with the minimal polynomial

$$f(x) := \sum_{j=0}^d a_j x^{d-j} = a_0 x^d + a_1 x^{d-1} + \dots + a_d = a_0 \prod_{i=1}^d (x - \eta^{(i)}) \in \mathbb{Z}[x]$$

where $a_0 > 0$ is the leading coefficient, a_j 's are integers, and $\eta^{(i)}$ is the i^{th} conjugate of η . The logarithmic height, denoted by $h(\eta)$ of η is defined by

$$h(\eta) = \frac{1}{d} \left(\log a_0 + \sum_{i=1}^d \log(\max\{|\eta^{(i)}|, 1\}) \right).$$

Let $\eta_1, \eta_2, \dots, \eta_s$ be positive algebraic numbers in the real number field \mathcal{F} of degree D and let b_1, b_2, \dots, b_s be nonzero rational numbers. Introduce the notations

$$\Lambda := \eta_1^{b_1} \eta_2^{b_2} \dots \eta_s^{b_s} - 1 \text{ and } B := \max\{|b_1|, |b_2|, \dots, |b_s|\}.$$

Let A_1, A_2, \dots, A_s be the positive real numbers such as

$$A_j \geq \max\{Dh(\eta_j), |\log \eta_j|, 0.16\} \text{ for all } j = 1, 2, \dots, s.$$

In this case, we can give the famous Matveev's theorem [21] and the Dujella-Pethő lemma [22].

Theorem 1 (Matveev [21]) *The following inequality holds for non-zero Λ over real field \mathcal{F} :*

$$\log \Lambda > -1.4 \times 30^{s+3} \times D^2 \times (1 + \log D) \times (1 + \log B) \times A_1 \times A_2 \times \dots \times A_s.$$

Lemma 2 (Dujella and Pethő [22]) *Let M be a positive integer, $\frac{p}{q}$ be a convergent of the continued fraction of the irrational τ such that $q > 6M$, and let A, B, μ be some real numbers with $A > 0$ and $B > 1$. Let $\varepsilon := \|\mu q\| - M \|\tau q\|$, where $\|\cdot\|$ is the distance from the nearest integer. If $\varepsilon > 0$, then there is no integer solution (x, y, z) of inequality*

$$0 < x\tau - y + \mu < AB^{-z}$$

with

$$x \leq M \text{ and } z \geq \frac{\log(Aq/\varepsilon)}{\log B}.$$

The following lemmas will be used later.

Lemma 3 Let n be a positive integer. Then,

$$\alpha^{n-2} \leq F_n \leq \alpha^{n-1}, \tag{4}$$

$$\alpha^{n-1} \leq L_n \leq 2\alpha^n, \tag{5}$$

$$|\beta|^{-(n-2)} \leq F_n \leq |\beta|^{-(n-1)}, \tag{6}$$

and

$$|\beta|^{-(n-1)} \leq L_n \leq |\beta|^{-(n+1)}. \tag{7}$$

Proof. The proof can be made by using the induction method on n .

Lemma 4 (Ddamulira et al. [15]) For all $x \in \left(-\frac{1}{2}, \frac{1}{2}\right)$, $|x| < 2|e^x - 1|$ is satisfied.

3. MAIN RESULTS

In this section, we will present all solutions to Equations (2) and (3) and will prove our results.

Theorem 5 Let k, m , and n be a positive integer. Then,

- Equation (2) is satisfied only for the triples of

$$(k, m, n) \in \{(1,1,1), (2,1,1), (4,1,2), (8,2,4)\}. \tag{8}$$

- Equation (3) holds only for the triples of

$$(k, m, n) \in \{(1,1,1), (1,1,2), (1,2,2), (2,1,4), (2,2,4), (3,3,3)\}. \tag{9}$$

Proof. Here, to reduce the size of the paper, we will only share a detailed proof for Equation (2), neglecting that of Equation (3).

From Equation (2) and Lemma 3, we can write

$$\alpha^{k-2} \leq F_k = L_m L_n \leq |\beta|^{-n-m-2}$$

and naturally

$$(k - 2)\log\alpha \leq -(n + m + 2)\log|\beta| \Rightarrow 2 - (n + m + 2) \frac{\log|\beta|}{\log\alpha} \Rightarrow k < 4n.$$

Considering Binet's formulas in Equation (1) and the fact that $\alpha = -\beta^{-1}$, we can arrange Equation (2) as follows:

$$\Lambda_1 := |\alpha^{-k} \beta|^{n+m} \sqrt{5} - 1| < \frac{8}{\alpha^{2m}}. \tag{10}$$

In this case, we can consider the case $s = 3, \eta_1 = \alpha, \eta_2 = |\beta|, \eta_3 = \sqrt{5}, b_1 = -k, b_2 = n + m$ and $b_3 = 1$ in Theorem 1. To be clear, $\eta_1, \eta_2, \eta_3 \in \mathbb{Q}(\sqrt{5})$ and $\mathcal{F} = \mathbb{Q}(\sqrt{5})$ of degree $D = 2$. Here, since $\alpha^k |\beta|^{-n-m} = \sqrt{5}$ is not satisfied when computing the square of its both sides, $\Lambda_1 \neq 0$. In addition,

$$h(\eta_1) = h(\eta_2) = \frac{1}{2} \log\alpha, h(\eta_3) = \log\sqrt{5}, A_1 = A_2 = \log\alpha, \text{ and } A_3 = 2\log\sqrt{5}.$$

Further, for $B = 4n, B \geq \max\{-k, n + m, 1\}$. Then, with these values, Theorem 1 implies that

$$\log(\Lambda_1) > -3.62 \times 10^{11} \times (1 + \log 4n). \tag{11}$$

Also, with Equation (10), we obtain

$$\log(\Lambda_1) < \log 8 - 2m \log\alpha. \tag{12}$$

As a result, we get

$$m < 3.77 \times 10^{11} \times (1 + \log 4n) . \tag{13}$$

Further, coming back to Equation (2), after some mathematical arrangements, we can write

$$\Lambda_2 := |\alpha^{-k}|\beta|^n(\sqrt{5}L_m) - 1| < \frac{33}{\alpha^n} \tag{14}$$

which implies that $s = 3, \eta_1 = \alpha, \eta_2 = |\beta|, \eta_3 = \sqrt{5}L_m, b_1 = -k, b_2 = n$ and $b_3 = 1$. Here, $\eta_1, \eta_2, \eta_3 \in \mathbb{Q}(\sqrt{5})$ and $\mathcal{F} = \mathbb{Q}(\sqrt{5})$ of degree $D = 2$. On the other hand, one can prove that $\Lambda_2 \neq 0$ by applying the same procedure above. As a result,

$$h(\eta_1) = h(\eta_2) = \frac{1}{2} \log \alpha, \text{ and } A_1 = A_2 = \log \alpha.$$

Further, since η_3 is the root of the polynomial $x^2 - 5L_m^2$, $h(\eta_3) = \log(\sqrt{5}L_m)$ and $A_3 = 6m \log \alpha$. In addition, $B \geq \max\{|-k|, n, 1\}$ for $B = 4n$. From Theorem 1, we can write

$$\log(\Lambda_2) > -6.49 \times 10^{11} \times m \times (1 + \log 4n) . \tag{15}$$

Solving Equations (13) and (15) together, we get

$$\log(\Lambda_2) > -2.45 \times 10^{23} \times m \times (1 + \log 4n)^2 . \tag{16}$$

Also, from Equation (14), we obtain

$$\log(\Lambda_2) < \log 33 - n \log \alpha . \tag{17}$$

Considering Equations (13), (16) and (17), we find

$$n < 2.18 \times 10^{27} . \tag{18}$$

After applying a similar process into Equation (3), we determine the bounds

$$m < 7.52 \times 10^{11} \times (1 + \log 4n) \text{ and } n < 2.25 \times 10^{27} . \tag{19}$$

Summing up, it is sufficient that we consider the following lemma in order to complete the proof.

Lemma 6 *Both Equations (2) and (3) are satisfied for all the ordered triples of (k, m, n) over the ranges $k < 4n, 1 \leq m \leq n$, and $n < 2.25 \times 10^{27}$.*

According to Lemma 6, there is a finite number of solutions. But, the bounds are huge, and thereby, we must obtain a more favorable condition. To do this, we will use Dujella-Pethó lemma for two different cases.

Case I: Introducing the notation

$$\Gamma_1 := -k \log \alpha + (n + m) \log |\beta| + \log \sqrt{5}.$$

we can write

$$\Lambda_1 = |\exp(\Gamma_1) - 1| < \frac{8}{\alpha^{2m}}.$$

From Lemma 4, we obtain

$$0 < \left| k \frac{\log \alpha}{\log |\beta|} - (n + m) + \frac{\log(1/\sqrt{5})}{\log |\beta|} \right| < \left| \frac{16}{\alpha^{2m} \log |\beta|} \right| < \frac{34}{\alpha^{2m}}.$$

When applying Dujella-Pethő lemma into the last inequality by considering $M = 9.1 \times 10^{27}$ ($M > 4n > k$) and $\tau = \frac{\log \alpha}{\log |\beta|}$, computing the continued fraction expansions of τ yields.

$$\frac{p_{47}}{q_{47}} = \frac{13949911361108065346183311454}{92134223612043233793615516979}.$$

This means that $6M < q_{47} = 92134223612043233793615516979$. As a result, we obtain

$$\varepsilon := \|\mu q_{47}\| - M \|\tau q_{47}\|, \varepsilon > 0.486, \text{ and } \mu = \frac{\log(1/\sqrt{5})}{\log |\beta|}.$$

In this case, taking $A := 34$, $B := \alpha^2$, and $z := m$ in Lemma 2, we conclude that $m \leq 73$.

Case II: Assume that $5 < m \leq 73$. Considering

$$\Gamma_2 := -k \log \alpha + n \log |\beta| - \log \left(\frac{1}{\sqrt{5} L_m} \right),$$

we have

$$\Lambda_2 = |\exp(\Gamma_2) - 1| < \frac{33}{\alpha^n}.$$

From Lemma 4, we can write

$$0 < \left| k \frac{\log \alpha}{\log |\beta|} - n + \frac{\log(\sqrt{5} L_m)}{\log |\beta|} \right| < \left| \frac{66}{\alpha^n \log |\beta|} \right| < \frac{138}{\alpha^n}.$$

For the case where $M = 9.1 \times 10^{27}$ ($M > 4n > k$) and $\tau = \frac{\log \alpha}{\log |\beta|}$, computing the continued fraction expansions of τ gives.

$$\frac{p_{47}}{q_{47}} = \frac{13949911361108065346183311454}{92134223612043233793615516979}.$$

This means that $6M < q_{47} = 92134223612043233793615516979$. In this case

$$\varepsilon_m := \|\mu_m q_{47}\| - M \|\tau_m q_{47}\|, \varepsilon > 0.034, \text{ and } \mu_m = \frac{\log(\sqrt{5} L_m)}{\log |\beta|},$$

As a result, taking where $A := 138$, $B := \alpha$, and $z := n$ in Lemma 2, we obtain that $n \leq 156$.

It should be noted that applying a similar investigation into Equation (3), we obtain the bounds in which $m \leq 75$ and $n \leq 153$. Then, we can compose a unique looping in Mathematica[®] over the range $m \leq 75$ and $n \leq 156$ to determine all possible solutions to both Equations (2) and (3). So, running our Pc algorithm validates Theorem 5. This exhausts the proof.

A simple observation of the outcomes of Theorem 5 reveals the following inferences.

Corollary 7 *All common terms of the Fibonacci and Lucas numbers are 1 and 3.*

Proof. For the case where $m = 1$, Equation (2) is reduced to $F_k = L_n$. In this case, the result follows from Theorem 5.

Corollary 8 *The only Lucas-square Fibonacci numbers are $F_1 = L_1^2 = 1$ and $F_2 = L_1^2 = 1$.*

Proof. When $m = n$, Equation (2) is reduced to $F_k = L_n^2$. From Theorem 2, the result can be drawn.

Corollary 9 *The only Fibonacci-square Lucas numbers are $L_1 = F_1^2 = 1$, $L_1 = F_2^2 = 1$ and $L_3 = F_3^2 = 4$.*

Proof. Taking $m = n$ in Equation (3) into account, the proof is easily obtained.

ACKNOWLEDGEMENTS

We would like to thank the referees for their important suggestions and comments that improve the study.

CONFLICT OF INTEREST

The authors stated that there are no conflicts of interest regarding the publication of this article.

CRedit AUTHOR STATEMENT

Ahmet Daşdemir: Formal analysis, Writing - original draft, Investigation, Conceptualization, Software.
Ahmet Emin: Formal analysis, Writing – Review & Editing, Investigation, Conceptualization, Software.

REFERENCES

- [1] Koshy T. Fibonacci and Lucas numbers with applications. New York, USA: Wiley, 2019.
- [2] Vajda S. Fibonacci and Lucas numbers, and the golden section: theory and applications. New York, USA: Courier Corporation, 2008.
- [3] Vorobiev NN. Fibonacci numbers. Berlin, Germany: Springer Science & Business Media, 2002.
- [4] Marques D. On generalized Cullen and Woodall numbers that are also Fibonacci numbers. Journal of Integer Sequences 2014; 17(9): 14-9.
- [5] Chaves AP, Marques D. A Diophantine equation related to the sum of powers of two consecutive generalized Fibonacci numbers. Journal of Number Theory 2015; 156: 1-14.

- [6] Bravo JJ, Gómez CA. Mersenne k -Fibonacci numbers. *Glasnik Matematički* 2016; 51(2): 307-319.
- [7] Pongsriiam P. Fibonacci and Lucas numbers which are one away from their products. *Fibonacci Quarterly* 2017; 55(1): 29-40.
- [8] Ddamulira M, Gómez CA, Luca F. On a problem of Pillai with k -generalized Fibonacci numbers and powers of 2. *Monatshefte für Mathematik* 2018; 187: 635-664.
- [9] Kafle B, Luca F, Montejano A, Szalay L, Togbé A. On the x -coordinates of Pell equations which are products of two Fibonacci numbers. *Journal of Number Theory* 2019; 203: 310-333.
- [10] Qu Y, Zeng J. Lucas numbers which are concatenations of two repdigits. *Mathematics* 2020; 8(8): 1360.
- [11] Şiar Z, Keskin R, Erduvan F. Fibonacci or Lucas numbers which are products of two repdigits in base b . *Bulletin of the Brazilian Mathematical Society, New Series* 2021; 52: 1025–1040.
- [12] Alan M, Alan KS. Mersenne numbers which are products of two Pell numbers. *Boletín de la Sociedad Matemática Mexicana* 2022; 28(2): 38.
- [13] Rihane SE, Togbé A. k -Fibonacci numbers which are Padovan or Perrin numbers. *Indian Journal of Pure and Applied Mathematics* 2023; 54(2): 568-582.
- [14] Alekseyev MA. On the intersections of Fibonacci, Pell, and Lucas numbers. *Integers* 2011; 11(3): 239-259.
- [15] Ddamulira M, Luca F, Rakotomalala M. Fibonacci Numbers which are products of two Pell Numbers. *Fibonacci Quarterly* 2016; 54(1): 11-18.
- [16] Bravo JJ, Herrera JL, Luca F. Common values of generalized Fibonacci and Pell sequences. *Journal of Number Theory* 2021; 226: 51-71.
- [17] Erduvan F, Keskin R. Fibonacci numbers which are products of two Jacobsthal numbers. *Tbilisi Mathematical Journal* 2021; 14(2): 105-116.
- [18] Bensella H, Behloul D. Common terms of Leonardo and Jacobsthal numbers. *Rendiconti del Circolo Matematico di Palermo Series* 2023; 2: 1-7.
- [19] Carlitz L. A note on Fibonacci numbers. *Fibonacci Quarterly* 1964; 2(1): 15–28.
- [20] Wang M, Yang P, Yang Y. Carlitz's equations on generalized Fibonacci numbers. *Symmetry* 2022; 14(4): 764.
- [21] Matveev EM. An explicit lower bound for a homogeneous rational linear form in the logarithms of algebraic numbers. II. *Izvestiya Mathematics* 2000; 64(6): 1217–1269.
- [22] Dujella A, Pethő A. A generalization of a theorem of Baker and Davenport, *The Quarterly Journal of Mathematics* 1998; 49(195): 291–30.



RESEARCH ARTICLE

PRODUCTIVITY, EFFICIENCY AND ENTREPRENEURIAL - INNOVATIVE UNIVERSITY INDEX: AN ANALYSIS FOR UNIVERSITIES IN TÜRKİYE

İsmail YENİLMEZ^{1,*}

¹ Department of Statistics, Science Faculty, Eskişehir Technical University, Eskişehir, Türkiye

ismailyenilmez@eskisehir.edu.tr -  [0000-0002-3357-3898](https://orcid.org/0000-0002-3357-3898)

Abstract

The productivity and efficiency of universities were analysed in this study. The data and results of the Entrepreneurial and Innovative University Index-EIUI, which is calculated by TÜBİTAK every year by considering various information for universities, were used. The study aimed to discuss the index, productivity, and efficiency results comparatively. Four-year data (2019-2022) and the index values were used. Balanced panel data analysis was performed on universities consistently included in the list each year. In the calculation of the index, a weighted sum of values standardized by the min-max method was taken into account. This is available in the calculation methodology of the index. Total factor productivity and stochastic frontier model methods were used for the analysis of productivity and efficiency, respectively. Universities that enter the index list every year and are at the top are effective, but they could not increase their productivity in the previous years. Universities established before 1992 may have approached the saturation level in terms of the input-output relationship, but it can be said that they can maintain their effectiveness. Some public and private universities that were established in 1992 and later have raised their productivity and efficiency. Although the index value and efficiency values overlapped to a certain extent, the significant differences in productivity were remarkable. While the studies in the literature focused on the meta-analysis of the index and the efficiency analysis of universities with various methods, this study presented an inclusive and comparative analysis in terms of index, productivity, and efficiency with panel data analysis.

Keywords

Total Factor Productivity,
Stochastic Frontier Model,
Triple Helix Model of Innovation,
Innovation Helix Framework,
Balanced Panel Data

Time Scale of Article

Received :20 March 2024
Accepted : 29 July 2024
Online date :30 September 2024

1. INTRODUCTION

Efficiency and productivity are often used interchangeably and confused in literature. Although they overlap, they have different meanings. Productivity is referred to as the ratio of outputs to inputs of a production process; efficiency represents the comparison between observed and optimal inputs - outputs [1]. For the measurement of productivity and efficiency, detailed research was carried out and the process related to the analysis was associated with three criteria. The basic criteria are macro/micro; frontier/non-frontier and deterministic/econometric [2]. These criteria are also presented as frontier/non-frontier, parametric/nonparametric (and semi-parametric), and stochastic/deterministic [3]. For a detailed reading, an introduction to efficiency and productivity analysis can be examined [4].

The activities of institutions and organizations can be examined, but the efficiency and productivity of higher education can be considered one of the most critical issues. The efficiency of higher education units has been investigated with multilevel frontier analysis. [5]. The 2018 performance of the top 10

*Corresponding Author: ismailyenilmez@eskisehir.edu.tr

Entrepreneurial and Innovative Turkish universities has been examined through multiple-criteria decision making methods [6]. Data envelopment analysis and Malmquist total factor productivity index have been used for the efficiency analysis of Turkish universities [7]. The productivity and efficiency of 43 state universities in Türkiye for the 2014–2015 academic year using data envelopment analysis and super efficiency models have been evaluated and followed by Tobit and beta regression analysis to identify factors affecting efficiency [8]. The efficiency of ten research universities and five candidate research universities in Türkiye, established in 2017 have been investigated using 2017 input and output data. The findings indicated that the number of scientific research projects negatively impacts efficiency, while citation rates per publication and the rate of PhD graduates per PhD program positively influence efficiency [9]. A two-stage DEA model to measure the efficiency of Turkish state universities has been employed focusing on graduate education and scientific research competency, confirming efficiency rankings aligned with criteria set by the Council of Higher Education [10].

In a similar but broader perspective, this study aims to draw attention to and analysis the terms productivity and efficiency for innovation in universities. The productivity and efficiency of universities directly affect the innovation process. In addition to efficiency and productivity, the emphasis on innovation, another important term, is on the world agenda. The impact of higher education has been examined for entrepreneurship and innovation [11]. In this case, a different perspective can be presented to the industry-technology-university-innovation quartet with productivity and efficiency measures. When the context expressed is examined, it overlaps with a term in the literature. The triple helix model of innovation concept is the interaction between academia, industry, and government to promote economic and social development in the system where concepts such as knowledge economy and knowledge society are defined [12]. The triple helix model of innovation is a conceptualization that is used as a basis for innovation and is frequently used in the literature. However, this situation has not been addressed for universities in Türkiye in the literature. The efficiency of regional innovation ecosystems was examined within the framework of the Triple-Helix Model for 81 provinces in Türkiye and the period 2011-2015, and it was concluded that the contribution of universities and public supports differ at the regional level [13]. According to the Triple Helix model, Türkiye's capacity to create innovation has been examined. It has been seen that the Triple Helix approach is not valid for Türkiye within the scope of the examined period [14]. As can be seen from the literature, the concepts of efficiency, productivity, and innovation index have not been discussed cumulatively for universities, which are the source of innovation, and these concepts have not been examined separately in depth.

In this context, the general motivation of this study is to analyze the productivity and efficiency of universities with a different approach to the triple helix model of innovation. When the literature is examined, efficiency analyses on this subject are grouped under certain methods. The special motivation is to evaluate the efficiency and productivity from the perspective of Türkiye by using data from Turkish universities. Because universities are one of the sources of innovation in Türkiye, as well as all over the world. Moreover, the existence of a system that supports the triple helix model of innovation for Türkiye can be seen. For instance, it is seen that the Ministry of Industry and Technology of the Republic of Türkiye follows The Scientific and Technological Research Council of Türkiye - TÜBİTAK's study, closely¹. There are also important collaborations between the Ministry of Industry and Technology of the Republic of Türkiye and TÜBİTAK.

From another perspective, the literature-based theoretical comparison for the criteria of the TÜBİTAK Entrepreneurial and Innovative University Index (EIUI) has been carried out in terms of the prominent operational areas of the entrepreneurial university in higher education journals [15]. In this context, it aims to comparatively discuss the index, productivity, and efficiency using EIUI data in this study. In

¹ <https://www.sanayi.gov.tr/medya/haber/deneme2>

other words, the study aims to deal with the index, productivity, and efficiency analysis cumulatively with the help of EIUI data regularly shared by TÜBİTAK.

The study is designed as follows: In the second part of this study, the theoretical and computational methods used in the study were presented. In the third part, the results of the analysis were shared. In the last section, all the findings were discussed.

2. DATA

The data and results of the EIUI were used. The EIUI is announced annually by the TUBİTAK, and fifty universities are listed. The EIUI has been calculated by TÜBİTAK every year by considering various information for universities. Although the index was calculated with five components for the first time in 2012, it has been calculated by reducing it to four components since 2018. The four relevant components are economic and social contribution / cooperation and interaction / intellectual property pool / scientific and technological research competence. Twenty-three sub-components are quantitatively measured values that constitute the relevant four main components. All of the sub-components in EIUI are as follows: i) Number of Scientific Publications, Number of Citations, Number of Projects, Amount of Funds Obtained from Projects Number of National and International Science Awards, Number of PhD Graduates. ii) National Patent Document Number, Number of National Utility Model Certificates, Number of International Patent Applications, Number of International Patent Documents. iii) Number of Projects Done with Industry Cooperation, Amount of Funds Obtained from Projects Done with Industrial Cooperation, Number of Projects Done with International Cooperation, Amount of Funds Obtained from Projects Done with International Cooperation, Number of Teaching Staff / Students in Circulation, Number of Students Registered in the Industrial Doctorate Program. iv) Number of Academician Companies, Number of Student / Graduate Companies, Net Sales Income of Academic Companies, Net Sales Revenue of Student/Graduate Companies, Number of Licensed Patents / Utility Models / Industrial Designs, Number of Bigg Companies, 4004-4005 Number of Projects. In this study, analysis was conducted only for the first component: scientific and technological research competence [16]. In other components, the abundance of empty cells and the fact that the imputation rate would be very high if filled was seen as an obstacle. Using the balanced panel data analysis methodological framework within the scope of the study can be considered as another important reason for conducting analyses through the first component.

4-year data (2019-2022) and index values were used. The 4-component index offered by TUBİTAK was used, the 5-component index presented before 2019 was not taken into account. The weights of the sub-dimensions of the index considered have changed as of 2019. This is the reason why 2018 and earlier was not included in the analysis. The 2023 data has not been released yet. As a result, a data for 4 years was compiled. The top 50 universities are listed in the index result document. Universities included in the relevant list each year were included in the analysis. Thus, balanced panel data analysis was performed.

In calculation of the EIUI, weighted sum of values standardized by min-max method was considered. It is available in the calculation methodology of the relevant index. This information was last presented as a footnote in the 2020 data announced in 2021 [17]. 4-year data and index values were accessed from TÜBİTAK (for 2019, 2021, and 2022 years) and Yeditepe University (for 2020 year) websites as public data². Ratio data, one of the data types, was conducted in this analysis. Since TUBİTAK data were prepared by considering the weighted sum of the values standardized with the min-max method, these

² https://www.tubitak.gov.tr/sites/default/files/gostergebazliveri_tablo.pdf

<https://tubitak.gov.tr/sites/default/files/gyue2021.pdf>

<https://tubitak.gov.tr/sites/default/files/18842/2020-gyue-2020-print.pdf>

https://tto.yeditepe.edu.tr/sites/default/files/2019_gyue.pdf

data were used for analysis without the need for any other transformation. This introduces phenomena such as categories, rank order, true zero, and equal intervals between data. It can be clearly stated that ratio data is superior to nominal, ordinal, and interval data according to the characteristics of the values.

In addition, the year 1992 was taken as the border in the study. In this context, the type (the abbreviations *pu* and *pr* represent public and private universities, respectively.) and establishment years of the universities used in the study are presented in Table 1. 20 of the 38 universities were founded before 1992, and only 1 of them is a private university. The number of universities established in 1992 and later is 18, and 11 of them are private universities.

Table 1. Type and Establishment of Universities Used in the Study

<i>Universities</i>	<i>Year</i>	<i>Public/State-Private</i>	<i>Universities</i>	<i>Year</i>	<i>Public/State-Private</i>
ISTANBUL U.	1933	PU	IZM. INST OF TECH	1992	PU
ISTANBUL TECH U.	1944	PU	GEBZE TECH U.	1992	PU
ANKARA U.	1946	PU	KOCAELİ U.	1992	PU
EGE U.	1955	PU	SAKARYA U.	1992	PU
KARADENİZ TECH U.	1955	PU	PAMUKKALE U.	1992	PU
ATATURK U.	1957	PU	S. DEMIREL U.	1992	PU
MIDD EAST TECH U.	1959	PU	KOC U.	1993	PR
HACETTEPE U.	1967	PU	SABANCI U.	1996	PR
BOGAZICI U.	1971	PU	YEDİTEPE U.	1996	PR
CUKUROVA U.	1973	PU	ATILIM U.	1997	PR
BURSA ULUDAG U.	1975	PU	BAHCESEHIR U.	1998	PR
SELCUK U.	1975	PU	IST. OKAN U.	1999	PR
FIRAT U.	1975	PU	YAŞAR U.	2001	PR
ERCIYES U.	1978	PU	TOBB ETU	2003	PR
YILDIZ TECH U.	1982	PU	ÖZYEGİN U.	2007	PR
GAZI U.	1982	PU	H. KALYONCU U.	2008	PR
DOKUZ EYLÜL U.	1982	PU	IST. MEDİPOL U.	2009	PR
AKDENİZ U.	1982	PU	A. GUL U.	2010	PU
MARMARA U.	1982	PU			
İ.D. BILKENT U.	1984	PR			

3. METHODS

3.1. Total Factor Productivity

The total factor productivity (TFP) model was used to analysis productivity in this study. Based on the basic definition, TFP can be written as:

$$TFP_{nt} = \frac{Y_{nt}}{X_{nt}} \tag{1}$$

where X_{nt} and Y_{nt} are the aggregate input – output of the n^{th} firm in period t , respectively. TFP changes are specified as being the ratio of the index (output quantity index/input quantity index) [18]. Such index numbers can be represented as multiplicatively complete [19]. Among the multiplicatively complete indices, the Hicks-Moorsteen TFP index is one of the multiplicatively complete indices and it can be estimated without requiring price data (Arjomandi et al., 2015). Hicks-Moorsteen TFP index is represented as:

$$TFP_{HM}^{t,t+1} = \sqrt{\left[\left(\frac{D_o^{t+1}(x^{t+1},y^{t+1})D_o^t(x^t,y^{t+1})}{D_o^{t+1}(x^{t+1},y^t)D_o^t(x^t,y^t)} \right) \left(\frac{D_f^{t+1}(x^t,y^{t+1})D_f^t(x^t,y^t)}{D_f^{t+1}(x^{t+1},y^{t+1})D_f^t(x^{t+1},y^t)} \right) \right]} \tag{2}$$

where $D_I(x, y)$ and $D_O(x, y)$ are input – output distance functions, respectively.

3.2. Stochastic Frontier Model

The stochastic frontier model (SFM) was used for the analysis of efficiency. In fact, the SFM is obtained by adding statistical information to the deterministic model which is:

$$y_i = f(x_i; \beta)TE \quad (3)$$

y_i and x_i are the observed scalar output of the producer and the vector of N inputs used by the producer, respectively. $f(x_i; \beta)$ is the frontier production function. TE denotes the technical efficiency and is defined as the ratio of observed output to maximum feasible output. The maximum producible output expressed as technical inefficiency cannot be obtained from Eq. 3. An alternative models including shocks [one-sided [20] and modification for one-sided [21] are presented in Eq. 4-5 as the model included statistical information.

$$y_i = f(x_i; \beta) + \varepsilon_i \quad (4)$$

$$y_i = f(x_i; \beta) + v_i + u_i \quad (5)$$

In fact, the error term (ε_i) in Eq. 4 is accepted as $\varepsilon_i = v_i + u_i$. In this way, Eq.5 is obtained. v_i and u_i represent random effects (statistical noise, measurement errors, random factors outside the firm's control and random variables that are not included in the production function) and technical efficiency (non-negative random variable representing inefficiency), respectively.

4. RESULTS

The sub-components of Component-1 (scientific and technological research competency - STRCI) have been focused on the analysis of the activities of the universities in the index list. The first of the four components was represented with STRCI, and it was the main component discussed in the research. Balanced panel data analysis was performed and the universities that were included in the list each year for the 4 years examined in the research were obtained with the help of a pivot table.

Thirty-eight universities were included in the analysis, and the universities were presented in Table 2. In calculating the Total Index, the weighted sum of the values of each sub-component standardized by the min-max method has been considered. STRCI is obtained from the first component's sub-components. The ranking has been based on the ranking averages on the list for 4-year data. In addition, the index averages of the universities included in the list for 4-year data have been presented in Table 2.

The first column (*Universities*) was created by taking into account the general ranking numbers of the universities in the EIUI for every year. It can be considered as a general ranking. The second column (*Total Index*) shows the average of the index values. The third column (STRCI) presents the averages according to the Component-1. The ranking presented in parentheses represents the order to be created according to these column values for both.

Depending on the number of personnel and the high occupancy rate of the cells for each university, productivity and efficiency have been examined in this context. The number of academic staff and 5 sub-components of the STRCI have been accepted as input and output, respectively. TFP and SFM were used to analysis productivity and efficiency. Productivity and efficiency values for thirty-eight universities have been presented in Table 3 as *Pro* and *Eff*. All results have been shown in Table 3.

Table 2. General Ranking and EIUI- STRCI average Values and Rankings (in parenthesis) of Universities

<i>Universities</i>	<i>Total Index</i>	<i>STRCI</i>
MIDDLE EAST TECHNICAL U.	83,0775 (1)	12,4725 (1)
SABANCI U.	76,9275 (2)	10,3150 (6)
ISTANBUL TECHNICAL U.	73,9425 (3)	11,3075 (5)
İHSAN DOĞRAMACI BILKENT U.	72,3000 (4)	11,4950 (3)
YILDIZ TECHNICAL U.	68,0375 (5)	9,2950 (10)
BOGAZICI U.	67,5925 (6)	9,5775 (9)
KOC U.	65,8850 (7)	11,6850 (2)
GEBZE TECHNICAL U.	63,0150 (8)	8,8425 (14)
ÖZYEĞİN U.	61,5150 (9)	6,1100 (28)
IZMIR INSTITUTE OF TECHNOLOGY	61,2150 (10)	9,2675 (11)
HACETTEPE U.	60,0450 (11)	11,4675 (4)
EGE U.	58,5575 (12)	9,1500 (13)
ERCIYES U.	56,3925 (13)	8,1050 (16)
ANKARA U.	54,7850 (14)	9,9525 (8)
ISTANBUL U.	54,4100 (15)	10,0550 (6)
GAZI U.	53,8725 (16)	9,2000 (12)
TOBB ETU	52,1975 (17)	5,9125 (29)
DOKUZ EYLÜL U.	51,2800 (18)	8,1850 (15)
BURSA ULUDAG U.	48,5425 (19)	6,4600 (25)
KOCAELİ U.	45,8175 (21)	5,5800 (33)
AKDENİZ U.	46,0425 (20)	6,9075 (22)
MARMARA U.	44,4825 (24)	7,4550 (18)
SAKARYA U.	45,2075 (22)	6,4750 (24)
SELCUK U.	44,6675 (23)	7,1350 (21)
ATILIM U.	44,4125 (26)	5,7200 (31)
YEDITEPE U.	44,4150 (25)	5,7775 (30)
ISTANBUL MEDIPOL U.	42,6725 (27)	5,6700 (32)
CUKUROVA U.	41,9775 (28)	6,4425 (26)
BAHCESEHIR U.	40,0525 (32)	5,0800 (35)
KARADENİZ TECHNICAL U.	41,6800 (29)	7,2925 (19)
HASAN KALYONCU U.	40,4550 (30)	3,8500 (37)
ATATURK U.	39,5200 (34)	7,4650 (17)
ABDULLAH GUL U.	39,7275 (33)	7,1825 (20)
FIRAT U.	39,4625 (35)	6,8925 (23)
YAŞAR U.	40,4275 (31)	4,6250 (36)
PAMUKKALE U.	38,1550 (37)	5,1175 (34)
SULEYMAN DEMIREL U.	38,7350 (36)	6,1875 (27)
ISTANBUL OKAN U.	35,9975 (38)	3,4350 (38)

Table 3. Productivity and Efficiency Results and Rankings of Universities

<i>Ranking</i>	<i>Universities</i>	<i>Pro.</i>	<i>Universities</i>	<i>Eff.</i>
1	AJ Uni, Pr, 92 or Post-92	1,2711	G Uni, Pu, Pre-92	0,9988
2	AF Uni, Pr, 92 or Post-92	1,1755	AA Uni, Pr, 92 or Post-92	0,9368
3	M Uni, Pu, Pre-92	1,1448	U Uni, Pr, Pre-92	0,9216
4	AG Uni, Pr, 92 or Post-92	1,1285	H Uni, Pu, Pre-92	0,9194
5	AE Uni, Pr, 92 or Post-92	1,1172	B Uni, Pu, Pre-92	0,9065
6	J Uni, Pu, Pre-92	1,1020	AB Uni, Pr, 92 or Post-92	0,8270
7	Y Uni, Pu, 92 or Post-92	1,0867	A Uni, Pu, Pre-92	0,8061
8	T Uni, Pu, Pre-92	1,0854	C Uni, Pu, Pre-92	0,7979
9	X Uni, Pu, 92 or Post-92	1,0851	I Uni, Pu, Pre-92	0,7678
10	Z Uni, Pu, 92 or Post-92	1,0756	O Uni, Pu, Pre-92	0,7452
11	AK Uni, Pr, 92 or Post-92	1,0640	V Uni, Pu, 92 or Post-92	0,7430
12	F Uni, Pu, Pre-92	1,0575	P Uni, Pu, Pre-92	0,7376
13	AI Uni, Pr, 92 or Post-92	1,0563	D Uni, Pu, Pre-92	0,7336
14	AB Uni, Pr, 92 or Post-92	1,0558	AL Uni, Pr, 92 or Post-92	0,7089
15	N Uni, Pu, Pre-92	1,0544	R Uni, Pu, Pre-92	0,6562
16	S Uni, Pu, Pre-92	1,0454	N Uni, Pu, Pre-92	0,6498
17	K Uni, Pu, Pre-92	1,0452	F Uni, Pu, Pre-92	0,5985
18	W Uni, Pu, 92 or Post-92	1,0422	T Uni, Pu, Pre-92	0,5977
19	AL Uni, Pr, 92 or Post-92	1,0325	E Uni, Pu, Pre-92	0,5846
20	C Uni, Pu, Pre-92	1,0306	W Uni, Pu, 92 or Post-92	0,5758
21	L Uni, Pu, Pre-92	1,0281	L Uni, Pu, Pre-92	0,5720
22	O Uni, Pu, Pre-92	1,0271	S Uni, Pu, Pre-92	0,5538
23	E Uni, Pu, Pre-92	1,0262	M Uni, Pu, Pre-92	0,5526
24	AH Uni, Pr, 92 or Post-92	1,0261	Y Uni, Pu, 92 or Post-92	0,5191
25	Q Uni, Pu, 92 or Post-92	1,0233	K Uni, Pu, Pre-92	0,5179
26	D Uni, Pu, Pre-92	1,0205	J Uni, Pu, Pre-92	0,5165
27	AA Uni, Pr, 92 or Post-92	1,0201	Q Uni, Pu, 92 or Post-92	0,4960
28	P Uni, Pu, Pre-92	1,0200	AI Uni, Pr, 92 or Post-92	0,4898
29	AC Uni, Pr, 92 or Post-92	1,0185	AH Uni, Pr, 92 or Post-92	0,4740
30	AD Uni, Pr, 92 or Post-92	1,0096	AC Uni, Pr, 92 or Post-92	0,4632
31	V Uni, Pu, 92 or Post-92	1,0032	AD Uni, Pr, 92 or Post-92	0,4586
32	R Uni, Pu, Pre-92	1,0013	AK Uni, Pr, 92 or Post-92	0,4546
33	B Uni, Pu, Pre-92	0,9938	X Uni, Pu, 92 or Post-92	0,4473
34	H Uni, Pu, Pre-92	0,9856	Z Uni, Pu, 92 or Post-92	0,4103
35	I Uni, Pu, Pre-92	0,9827	AE Uni, Pr, 92 or Post-92	0,4072
36	G Uni, Pu, Pre-92	0,9807	AG Uni, Pr, 92 or Post-92	0,3708
37	U Uni, Pr, Pre-92	0,9788	AJ Uni, Pr, 92 or Post-92	0,3086
38	A Uni, Pu, Pre-92	0,9730	AF Uni, Pr, 92 or Post-92	0,2754

5. DISCUSSION

The harmony between the General Ranking (Column 1 in Table 2) and the Total Index Ranging (Column 2 in Table 2) deteriorates at certain intervals after the twentieth university. STRCI Ranking (Column 3 in Table 2) differ significantly from the Total Index Ranking. The top 10 universities for the Total Index

Ranking are as follows: Middle East Technical University, Sabancı University, Istanbul Technical University, İhsan Doğramacı Bilkent University, Yıldız Technical University, Boğaziçi University, Koç University, Gebze Technical University, Özyeğin University, İzmir High Technology Institute. According to the STRCI Ranking, the top 10 universities are listed as follows: Middle East Technical University, Koç University, İhsan Doğramacı Bilkent University, Istanbul Technical University, Sabancı University, Boğaziçi. University, Yıldız Technical University. The universities in the top 10 in both rankings are as follows: Middle East Technical University, Sabancı University, Istanbul Technical University, İhsan Doğramacı Bilkent University, Yıldız Technical University, Boğaziçi University, Koç University.

Three universities (Hacettepe University, Istanbul University, Ankara University) are not in the top 10 according to STRCI ranking. Three Universities established in 1992 and later (Gebze Technical University, Özyeğin University, İzmir High Technology Institute) are not in the top 10 according to the Total Index, but they are in the STRCI top 10 rankings.

In the efficiency analysis, the top 10 universities are listed as follows: G Uni, Pu, Pre-92 - AA Uni, Pr, 92 or Post-92 - U Uni, Pr, Pre-92 - H Uni, Pu, Pre-92 - B Uni, Pu, Pre-92 - AB Uni, Pr, 92 or Post-92 - A Uni, Pu, Pre-92 - C Uni, Pu, Pre-92 - I Uni, Pu, Pre-92 - O Uni, Pu, Pre-92. On the other hand, considering the productivity ranking, the top 10 universities are listed as follows: AJ Uni, Pr, 92 or Post-92 - AF Uni, Pr, 92 or Post-92 - M Uni, Pu, Pre-92 - AG Uni, Pr, 92 or Post-92 - AE Uni, Pr, 92 or Post-92 - J Uni, Pu, Pre-92 - Y Uni, Pu, 92 or Post-92 - T Uni, Pu, Pre-92 - X Uni, Pu, 92 or Post-92 - Z Uni, Pu, 92 or Post-92.

The remarkable result is that there is no university in the top 10 on either list. When the lists are examined in detail, it is seen that the productivity values of universities with high-efficiency values are low, and vice versa.

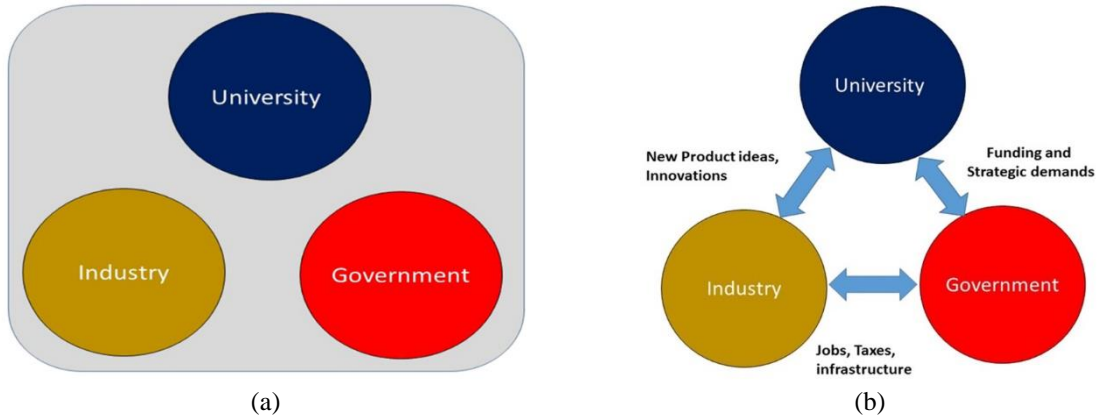


Figure 1. (a) Triple Helix Interactions in a Developing Country (Silo Confinement); (b) Beginning of Triple Helix Strategic Interactions in a Middle Income Country (Push-Pull) (Kimatu, J.N., 2016) [22]

There are three basic components in the triple helix model of innovation. Although a mathematical Venn diagram representation is very common in the literature (as shown in Figure 1a for LMICs), the representation in Figure 1b for DCs offers a more transitional structure with borders not separated by red lines. While the terms low- and middle-income countries (LMICs) and developing countries (DCs) can be used interchangeably, this study does not delve into their terminological differences. However, Türkiye's situation appears more suitable for Figure 1b. The primary reason for preferring Figure 1b in this research is the existence of notable points specific to Türkiye in the triangle of academia, industry, and government. For example, TUBITAK is an organization of the Ministry of Industry and Technology

and has strong cooperation with universities. Assigning it to a specific cluster in a Venn diagram might overlook its multifaceted roles. Similarly, the Union of Chambers and Commodity Exchanges of Türkiye (abbreviated in Turkish as TOBB) is a professional organization with a legal personality and the nature of a public institution, which might not fit neatly into an industrial cluster alone. The last but not-to-be-forgotten example is that Technology Transfer offices (TTO) are a formation derived from in the triple helix model of innovation. This organization, which is often located within universities, is a bridge in collaboration with the industry. It may be insufficient to belong only to the academy cluster.

Considering all these analyses, the literature, and Türkiye's dynamics, the adaptation of the Triple Helix Model and interactions for Türkiye is proposed within the scope of this study in Figure 2.

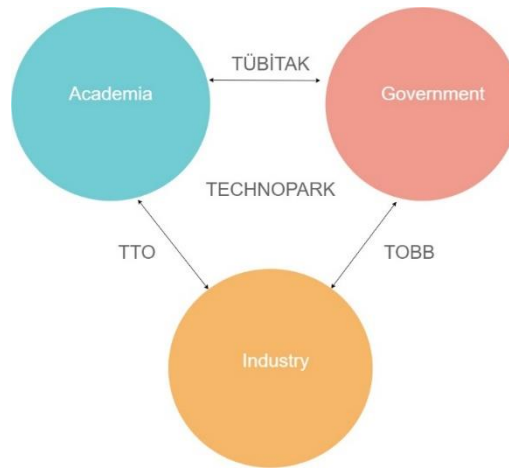


Figure 2. Triple Helix Model and interactions for Türkiye

The visual relationship presented in Figure 2 can be schematized as *the 4T's for Innovation in Türkiye*. Due to the lack of sharp lines, the Venn diagram is not given in an intersecting manner. This can be considered as an advantage rather than a disadvantage. However, according to [22], there are intersections in the developed country innovation diagram, in addition to those presented in Figure 1. Considering Türkiye as a developing country and considering that the interaction between relevant institutions and organizations will relate to protocols in the future, this scheme can be revised and a more comprehensive scheme in the context of the Quadruple and Quintuple Innovation Helix Framework can be presented in the future.

Study limitations and their explanations can be summarized as follows: i) Focusing only on the sub-components of Component-1 (scientific and technological research competency) of the components. The main cause is presented in the *Data*. ii) Although the use of panel data analysis, which contains more information and variability compared to time series and cross-sectional data, is an advantage, the use of short panels with many individuals and few time periods can be considered a limitation. This is because the date of disclosure of the data by TÜBİTAK is not very old and the calculation method has changed. iii) Since there were 4 observations for each university and relatively close values, the average was used. In case there are more observations and values that are far from each other, that is, values with high deviation, more robust statistics can be used against outliers such as median. iv) Analyses were conducted for twenty-three sub-components for thirty-eight universities. In addition, it is a constraint to evaluate universities' only outputs in terms of their innovation roles as "scientific and technological research competence". It may be possible to consider other variables in the EIUI as innovation indicators. For this, a data set with data collected for a longer period and fewer missing cells is needed. v) In the literature, the total budget used to measure the efficiency and effectiveness of universities is the number of staff, number of students, number of programs/departments, purchase of

goods and services, education expenses, research expenses, etc. inputs are available. In future studies, a more comprehensive analysis will be conducted if the relevant data is available for all universities.

6. CONCLUSION

It aimed to discuss the index, productivity, and efficiency results comparatively. Balanced panel data analysis was conducted with thirty-eight universities included in this list for 4-year data. Total factor productivity and stochastic frontier model methods were used for the analysis of productivity and efficiency, respectively. While the studies in literature focused on the meta-analysis of the index and the efficiency analysis of universities with various methods, this study presented an inclusive and comparative analysis in terms of index, productivity, and efficiency with panel data analysis. Data envelopment analysis (DEA) was used for Hicks Moorsteen type TFP in this study. DEA-based Hicks Moorsteen TFP was used due to various calculation conveniences and assumption structures. The reasons for using this method in the productivity analysis of universities have been discussed in detail, and DEA-based Hicks Moorsteen TFP has been applied to Malaysian public universities to measure productivity change in higher education [18]. On the other hand, the SFM, a parametric method based on various assumptions and used in different disciplines [23], has been applied to higher education data in the context of efficiency analysis [16]. Since 1992, a significant milestone in Turkish university history, notable developments and the establishment of numerous universities have marked a transformative period. This pivotal year serves as a reference point in research, particularly evident in studies directly focusing on this period. For instance, a comparative analysis of the strategic plans of 23 state universities established in Türkiye in 1992 has been conducted following the implementation of performance-based budgeting under the 2006 Public Financial Management and Control Law, examining their missions, visions, goals, and objectives [24].

The findings from this study can be summarized as follows:

- Universities established before 1992 that enter the index list every year and rank at the top are efficient, but their productivity has not improved in the same direction.
- Some public and private universities have been able to increase their productivity and efficiency. Although the index value and efficiency values overlap to a certain extent for certain universities, serious differences in productivity in general are striking.
- Compared to previous years, productivity appears to be upward for new (established in 1992 and later) and private universities. On the contrary, effective universities established before 1992 cannot increase their productivity rapidly compared to previous years. This may be because the relevant universities are close to saturation. It can be associated with the level of relevant inputs and outputs.
- The index points in a similar direction to efficiency. However, productivity can proceed in a different direction from efficiency and the index.

The fact that universities established before 1992 may have approached the saturation level (in the context of the input-output relationship) may prevent them from making serious progress in efficiency every year, but it can be said that they can maintain their effectiveness. Although the efficiency of private and new universities (established in 1992 and later) is not high, their productivity may show positive development compared to previous years.

The innovation term, which fundamentally affects the world and is accelerated by universities, can be perceived as self-evaluation and self-criticism by evaluating universities in the context of the innovation term. With the results obtained from here, more productive and effective universities will be the source of more innovative universities.

DISCLAIMER STATEMENT

The analysis results of this study have been presented with labels, excluding information that is publicly accessible to everyone. Comments are provided with general statements based on two groups: post-1992 (1992 and later) and pre-1992 (before 1992). The analyses in this study were conducted using publicly available data related to universities. However, it has been noted by the peer reviewer that some universities may prefer their names to remain confidential for the results of the analyses. Therefore, the names of universities in this study have been labeled, and these labels do not contain any specific judgment or evaluation towards any university. No ethical approval was required for this study because publicly available data were used, and university names were labeled in the analyses presented.

CONFLICT OF INTEREST

The author stated that there are no conflicts of interest regarding the publication of this article.

CRedit AUTHOR STATEMENT

İsmail Yenilmez: Conceptualization, Methodology, Software, Validation, Formal analysis, Investigation, Resources, Data Curation, Writing – Original Draft, Writing – Review & Editing, Visualization, Supervision, Project administration, Funding acquisition.

REFERENCES

- [1] Fried HO, Lovell CAK, Schmidt SS. Efficiency and productivity. In: Fried HO, Lovell CAK, Schmidt SS, eds. *The Measurement of Productive Efficiency and Productivity Change*. Oxford University Press; 2008:1-106.
- [2] Del Gatto M, Di Liberto A, Petraglia C. Measuring productivity. Working Paper CRENoS 200818, Centre for North South Economic Research, University of Cagliari and Sassari, Sardinia; 2008.
- [3] Pieri F. *Essays on Productivity and Efficiency Analysis* [PhD dissertation]. University of Trento; 2010.
- [4] Coelli TJ, Rao DSP, O'Donnell CJ, Battese GE. *An Introduction to Efficiency and Productivity Analysis*. 2nd ed. Springer; 2005.
- [5] Naderi A. Efficiency measurement of higher education units using multilevel frontier analysis. *J Prod Anal*. 2022;57:79-92.
- [6] Oğuz S. Evaluation of the entrepreneurial and innovative universities in Turkey through multiple-criteria decision making methods. *Kastamonu Eğitim Dergisi*. 2022;30(2):353-361.
- [7] Saygın Karagöz Ö, Deveci Kocakoç İ, Üçdoğruk Ş. Girişimcilik ve yenilikçilik faaliyetleri odağında Türkiye'deki üniversitelerin etkinlik analizi. *İzmir İktisat Dergisi*. 2020;35(4):713-723.
- [8] Türkan S, Özel G. Efficiency of state universities in Turkey during the 2014–2015 academic year and determination of factors affecting efficiency. *Educ Sci*. 2017;42(191):307-322.
- [9] Mammadov R, Aypay A. Efficiency analysis of research universities in Turkey. *Int J Educ Dev*. 2020;75:102176.

- [10] Kocak E, Orkcü HH. Measuring the efficiency of Turkish state universities based on a two-stage DEA model. *Gazi Univ J Sci*. 2021;34(4):1210-1220.
- [11] Portuguese Castro M, Ross Scheede C, Gómez Zermeño MG. The impact of higher education on entrepreneurship and the innovation ecosystem: A case study in Mexico. *Sustainability*. 2019;11(20):5597.
- [12] Etzkowitz H. Innovation in innovation: The triple helix of university-industry-government relations. *Soc Sci Inf*. 2003;42(3):293-337.
- [13] Erkul A, Kırankabeş MC. Türkiye’de bölgesel inovasyon ekosistemi: Üçlü-sarmal modeli çerçevesinde bir değerlendirme. *Verimlilik Dergisi*. 2020;(1):55-81.
- [14] Mert N, Cengiz S. Üçlü sarmal yaklaşımına göre Türkiye’nin yenilik yaratma kapasitesi. *Bus Econ Res J*. 2020;11(4):1001-1012.
- [15] Uslu B, Çalıköğlü A, Seggie FN, Seggie SH. TÜBİTAK girişimci ve yenilikçi üniversite endeksi kriterlerinin girişimci üniversitelerde öne çıkan faaliyetler açısından değerlendirilmesi. *Yükseköğretim Dergisi*. 2020;10(1):1-11.
- [16] Yenilmez İ, Mert Kantar Y, Arık İ. Efficiency measurement of Turkish universities using the stochastic frontier model. In: EGE 7th International Conference on Applied Sciences; December 24-25, 2022; İzmir, Türkiye. Proceedings. p. 1017-1023. ISBN: 978-605-72197-9-4.
- [17] TÜBİTAK. 2020 yılı girişimci ve yenilikçi üniversite endeksi sonuçları (2020 entrepreneurial and innovative university index results). Available from: <https://tubitak.gov.tr/sites/default/files/18842/2020-gyue-2020-print.pdf>. Accessed August 7, 2023.
- [18] Arjomandi A, Salleh MI, Mohammadzadeh A. Measuring productivity change in higher education: An application of Hicks–Moorsteen total factor productivity index to Malaysian public universities. *J Asia Pac Econ*. 2015;20(4):630-643.
- [19] O'Donnell CJ. An aggregate quantity framework for measuring and decomposing productivity change. *J Prod Anal*. 2012;38(3):255-272.
- [20] Schmidt P. On the statistical estimation of parametric frontier production functions. *Rev Econ Stat*. 1976;58:238-239.
- [21] Aigner D, Lovell C, Schmidt P. Formulation and estimation of stochastic frontier production function models. *J Econom*. 1977;6(1):21-37.
- [22] Kimatu JN. Evolution of strategic interactions from the triple to quad helix innovation models for sustainable development in the era of globalization. *J Innov Entrep*. 2016;5:16. doi:10.1186/s13731-016-0056-8.
- [23] Kantar M, Yenilmez I. Technical efficiency assessment of Turkish banks using stochastic frontier method. In: Proceeding Book of the I. International Symposium on Economics, Finance, and Econometrics; Istanbul, Türkiye.
- [24] Günay A, Dulupçu MA. Türkiye’de 1992 yılında kurulan devlet üniversitelerinin stratejik planlarının karşılaştırmalı bir analizi. *Yükseköğretim ve Bilim Dergisi*. 2015;14(1):236-254.



RESEARCH ARTICLE

MULTI-LEVEL CLASSIFICATION BASED ON DEEP LEARNING FOR ACCURATE RISK STRATIFICATION OF ARRHYTHMIAS

Evin ŞAHİN SADIK^{1,*},

¹ Kütahya Dumlupınar University, Electrical and Electronics Engineering Department, Kütahya, Turkey

evin.sahin@dpu.edu.tr -  [0000-0002-2212-4210](https://orcid.org/0000-0002-2212-4210)

Abstract

Arrhythmias, also known as irregular heartbeats, are important health problems that must be accurately identified to diagnose and treat cardiovascular disease. Within the scope of this study, a network for classifying arrhythmias, which are important in the diagnosis and treatment of cardiovascular diseases, was proposed by using one-dimensional convolutional neural network (1D CNN), one of the deep learning techniques. With the proposed 1D-CNN architecture, arrhythmia types and normal rhythm ECGs were subjected to a more detailed examination from general to specific according to urgency situations. In the classifications made, first of all, a binary classification was made and an evaluation was made as whether there was a life risk or not. In triple, quadruple and six-fold classification, the detection of arrhythmia status is detailed. More complex classifications have helped to define different types of arrhythmias in more detail. This study proposes a deep learning network for automatic identification and classification of arrhythmias and shows that different arrhythmia conditions can be diagnosed with a single network model by applying the proposed network structure to multi-class arrhythmia disorders.

Keywords

Cardiac Arrhythmias,
CNN,
Classification,
ECG

Time Scale of Article

Received :07 April 2024
Accepted : 20 August 2024
Online date : 30 September 2024

1. INTRODUCTION

The heart is the most vital organ for humans, and diseases that affect the heart and blood vessels are called cardiovascular diseases [1]. The term cardiovascular disease refers to a wide range of conditions that affect the heart and blood vessels [2]. According to the World Health Organization, 17.9 million deaths occurred from cardiovascular diseases in 2016. This number is expected to increase to 23.6 million in 2030 [3]. The heart's continuous electrical activity is essential for assessing its health and function. A medical procedure called an electrocardiogram (ECG) is used to observe and record the electrical activity of the heart. ECG is very important for diagnosing and following up heart diseases as it quickly evaluates the electrical rhythm and structure of the heart non-invasively.

Additionally, using ECG, diseases such as arrhythmia [4], coronary artery [5], myocardial infarction [6], pericarditis [7], cardiomyopathy [8], hypertrophic cardiomyopathy [9] and pulmonary embolism [10] can be diagnosed. Arrhythmia, being among these ailments, manifests in various forms, including AF, atrial flutter, ventricular tachycardia, bradycardia, supraventricular tachycardia (SVT), ventricular fibrillation, and premature atrial or ventricular contractions. Occasionally, arrhythmias cannot be diagnosed immediately using ECG alone [11]. Additionally, 20% of atrial fibrillation cases occur without any symptoms [12]. In such cases, doctors resort to additional methods such as Diagnostic Holter monitor, event monitor, stress test, electrophysiological test or echocardiogram [13]. When arrhythmias are not diagnosed and treated early, they can lead to serious health problems such as heart failure, stroke, cardiac arrest or cause symptoms that reduce the quality of life such as dizziness, fainting,

*Corresponding Author: evin.sahin@dpu.edu.tr

shortness of breath, chest pain and depression [14]. Early diagnosis and appropriate treatment can reduce the risk of complications from arrhythmia and significantly improve a patient's quality of life [15].

Nowadays, detecting arrhythmia from ECG signals using artificial intelligence techniques is a Machine Learning (ML) and Deep Learning (DL) techniques are employed to detect arrhythmias. A review of these research studies, focusing on work from the past twelve years, reveals that out of 40 studies, 29 (or 72.5%) utilized DL methods, nine (22.5%) applied ML methods, and two studies integrated both approaches for arrhythmia prediction [16]. Traditional methods for diagnosing arrhythmias with computer assistance rely on established medical rules but exploring artificial intelligence approaches can provide doctors with highly precise tools for diagnosing arrhythmias. Artificial intelligence algorithms could be embedded in smart ECG devices to help more people screen for arrhythmias early [17]. In classifications made using ML algorithms, the feature extraction part usually varies significantly in the success of the study, so different approaches are used for feature extraction [18]. One of the most essential features extracted is peak detection [19], [20]. Some of the other methods used are empirical mode decomposition, Pan Tompkins Algorithm, Hilbert and Wavelet Transform [21]–[23].

Literature reviews on the efficacy of deep learning (DL) algorithms versus traditional ML in diagnosing arrhythmias from electrocardiograms (ECGs) indicate that DL algorithms demonstrate enhanced performance in detecting and classifying ECG arrhythmias, surpassing the capabilities of conventional ML techniques. Deep learning methods offer superior performance with automatic feature selections without requiring manual feature selection and extraction [24]. DL algorithms are known to be effective in detecting conditions such as AF and Premature Ventricular Contraction (PVC), which rely on single heartbeats and require the identification of patterns between multiple beats [25]. Studies have been conducted in the literature using different DL methods to detect arrhythmia from ECGs [26], [27]. Studies have shown that artificial intelligence and DL techniques are increasingly used in ECG-based arrhythmia detection and that the use of DL algorithms in the healthcare sector is developing. Increasing success in the methods significantly reduces the pressure on doctors to analyze ECGs, resulting in significant advances in arrhythmia diagnosis.

Evaluation of existing methods does not show any significant difference in arrhythmia classification based on ECG signals. Most existing methods use multilayered and complex deep learning models. This leads to overfitting on limited and unbalanced data sets. Additionally, models trained on specific datasets have difficulty generalizing across different patient populations and varying ECG signal characteristics. The high computational requirements and long processing time of deep models limit timely decision making in clinical environments. Traditional methods often rely on manual feature extraction. Since it is not known which features perform best on the model, it can be time-consuming and may not effectively capture all relevant signal features. This study aims to address these gaps and proposes a simplified CNN architecture with two convolutional layers. The architecture is restricted to two convolutional layers, achieving a balance between model complexity and performance and reducing the risk of overfitting. When the simpler model structure is combined with regularization techniques such as batch normalization and dropout, the model's generalization ability across different datasets is enhanced. The reduced computational burden of the model makes it more suitable for real-time applications in clinical settings. By leveraging the automatic feature extraction capabilities of CNN, our approach eliminates manual intervention and is able to capture signal features more comprehensively.

Within the scope of this study, the data were subjected to four different classifications. In the first classification, arrhythmia types were classified as life-threatening arrhythmias and less dangerous conditions. These two categories differ markedly in terms of potential health risks and the need for immediate intervention. In addition, the data were examined in three and four classes to examine it more thoroughly. Finally, the performance metrics of the model were examined by classification for six different situations.

The proposed study aims to offer a layered approach according to the severity or urgency of arrhythmias and develop an auxiliary artificial intelligence system to help manage situations requiring rapid intervention more effectively.

It is aimed to prevent the development of a new model for each problem by applying the same network structure to different classification types. In this part of the study, a controversial analysis of the literature was made. In the remaining sections, information about the dataset in the material and method is given, the proposed method is mentioned, arrhythmia classification is mentioned and evaluation metrics are explained. The classification results were examined with graphs and tables in the evaluation results section. In the Conclusion section, a general evaluation of the study was made.

2. MATERIALS AND METHODS

In this study, a series of processing steps were applied to classify ECG signals. First, the raw ECG signal was divided into 2-second segments. The segmented data transformed into the frequency domain using the Fast Fourier Transform (FFT) method. The frequency spectra obtained from FFT were processed with a 1D Convolutional Neural Network (1D CNN), a DL based classification model. Figure 1 gives the implementation steps of the proposed model. Starting from the segmentation of the ECG signal, FFT application, processing with the CNN model and finally the classification results steps are visualized in the figure. This process shows how the model distinguishes different types of rhythms and how results are obtained for each classification group.

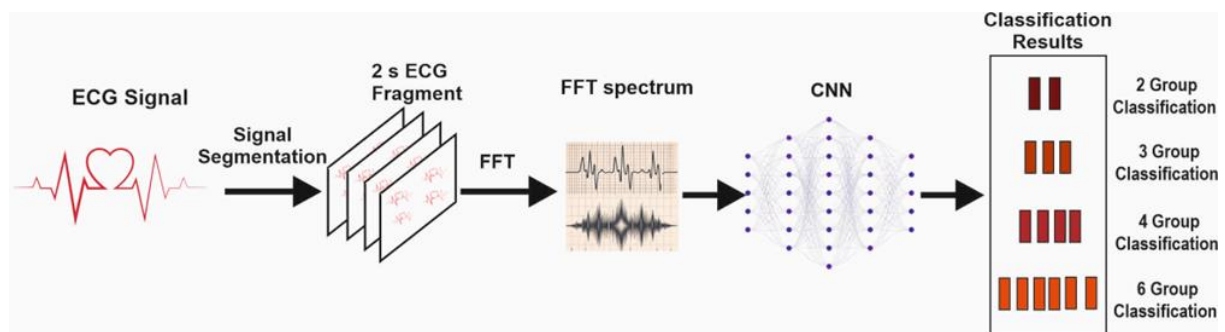


Figure 1. Application steps of the proposed model.

The classification process was performed in different scenarios based on clinical significance. The visual showing the classification scenarios and the data in these groups is given in Figure 2. The first of these classification scenarios is to divide the data into two groups: life-threatening arrhythmias and less dangerous or normal rhythms. Secondly, the data were divided into three groups. These are ventricular arrhythmias (more dangerous), potentially dangerous arrhythmias, supraventricular and normal rhythms. In another classification, the data is divided into four groups. In this classification, very dangerous ventricular arrhythmias, threatening ventricular arrhythmias, potentially dangerous arrhythmias, low-risk ventricular arrhythmias, and supraventricular and normal rhythms are discussed separately. In the final classification scenario, six groups were classified. Here, the entire ECG data set is divided into six separate groups and each group is classified within itself. Metrics like recall, specificity, F1 score, accuracy and the ROC curve were utilized to assess the performance of each classification scenario. These metrics were used to measure the potential effectiveness and reliability of our model in clinical practice. The model used in our study is CNN. In this model, the hyperparameters of the model were adjusted for each classification scenario and the model was classified into four different scenarios to provide the highest validation set performance.

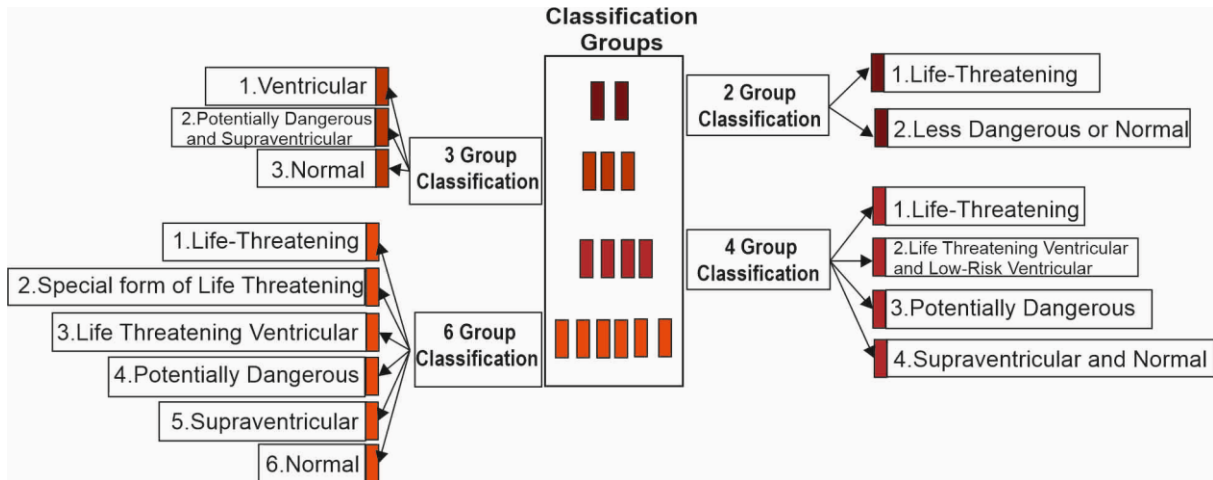


Figure 2. Diagram showing classification groups.

The figure shows how the classification scenarios are separated in our study. Binary classification aims to distinguish between life-threatening arrhythmias and less dangerous or normal rhythms. This distinction is critical to prioritizing emergency medical attention in clinical settings. Binary classification ensures that the model can accurately distinguish between critical categories. This allows patients requiring urgent treatment to be quickly identified.

The three-class classification scenario, in contrast to the two-class classification, categorizes ECG signals into normal rhythms, potentially dangerous and supraventricular arrhythmias, and ventricular arrhythmias. It helps prioritize patients according to the severity of their condition. Unlike binary classification, triple classification also classifies potentially dangerous arrhythmias.

Four-class and six-class classification scenarios aim to provide more detailed information for diagnosis and treatment by simultaneously classifying different arrhythmia types, capturing the entire spectrum of arrhythmia diversity.

2.1. Dataset

The first version of the arrhythmia dataset used in the study was the MIT-BIH Malignant Ventricular Ectopia Database (MVED) [28]. This database collected 48 half-hourly 2-channel ECG recordings from 47 people. The data in the MVED dataset was divided into 2-second segments and labeled according to arrhythmia types by expert cardiologists. It became the High-Risk Labeled ECG Fragment dataset in PhysioNet [29], [30].

The data contains ECG signals consisting of 6 different classes, one class containing normal and the other arrhythmia types. There are a total of 1016 ECG records in the data set presented in PhysioNet. Each recording is presented in 4 different ways. The first of these is recorded as 2-second fragments, while the second, the version used in this study, is the full spectrum of the 2-second signal containing the range 0-180 Hz in 0.5 Hz steps. The third signal is the smoothed spectrum signal called 15_2, from which 15 features are extracted in 1 Hz steps in the 0-15 Hz range. The fourth and last recording method is the signal containing 10 features extracted in 1.5 Hz steps from 0-15 Hz. Since the process was carried out with a deep learning model within the scope of the study, the entire spectrum of the 2-second signal was used. Since there was an unbalanced distribution between classes in the data set, the SMOTE algorithm was used to balance the data set.

2.2. Arrhythmia Classification

In this study, (1) Dangerous Arrhythmia, (2) The Early Form of Life-Threatening Arrhythmia, (3) Life-Threatening Ventricular Arrhythmia, (4) Potentially Dangerous Ventricular Arrhythmia, (5) Supraventricular Arrhythmia and (6) Normal Rhythm classification has been made. It is as given in Figure 3.

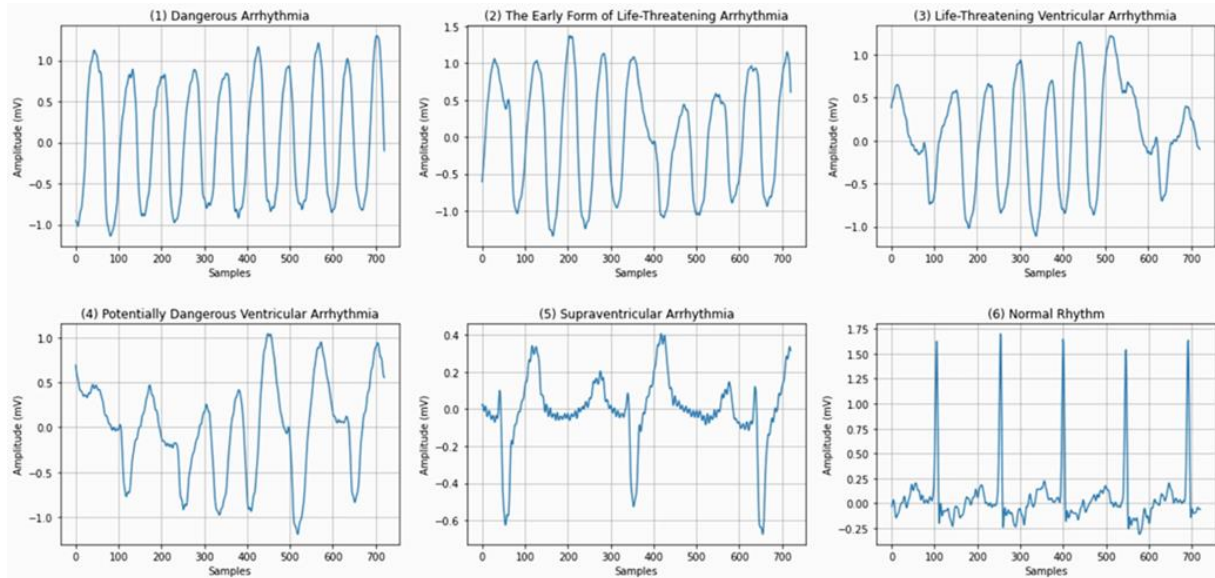


Figure 3. Types of ECG waves used for classification

The heart rhythm of healthy people is a regular ECG, known as normal sinus rhythm. Dangerous Arrhythmias are Arrhythmias that are Dangerous and Require Urgent Intervention. These arrhythmias have two subsections: Ventricular Flutter (VFL) and Ventricular Fibrillation (VF). In VFL, the lower chambers of the heart (ventricles) beat too fast and irregularly, resulting in the heart's inability to pump blood effectively. VF is an emergency condition in which the ventricles contract irregularly and ineffectively, requiring cardiopulmonary resuscitation (CPR) and defibrillation. (2) The Early Form of Life-Threatening Arrhythmia (TdP) is a special type of ventricular tachycardia. It is associated with prolongation of the QT interval and is potentially dangerous. (3) Life-Threatening Ventricular Arrhythmia (VT), Ventricular tachycardia, is the ventricles beating in an abnormal and rapid rhythm. Fast heartbeats can lead to the inability to pump blood effectively. (4) Potentially Dangerous Ventricular Arrhythmia, these rhythms are divided into Ventricular Bigeminy (B), High Grade Ventricular Ectopic Activity (HGEA) and Ventricular Escape Rhythm (VER). B: It is the occurrence of a premature ventricular contraction (PVC) after each normal beat. This creates a regular pattern. HGEA is a high degree of abnormal ventricular activity, such as frequent ventricular extrasystoles or consecutive PVCs. VER, A condition in which the ventricles beat in an abnormally slow rhythm. It usually occurs when the sinus node or AV node cannot produce a rhythm fast enough. (5) Supraventricular Arrhythmia is divided into these rhythms as Atrial Fibrillation (AFIB), Supraventricular Tachyarrhythmia (SVTA), Sinus Bradycardia (SBR), First Degree Heart Block (BI) and Nodal Rhythm (NOD). AFIB is irregular and rapid beating of the atria (upper chambers of the heart). It may increase the risk of blood clots and stroke. SVTA is a fast heart rhythm originating from the atrium or AV node. SBR is a slower-than-normal heart rate originating from the sinus node. BI is when each beat is delayed in passing through the AV node, but no beats are missed. NOD is the rhythm originating from the AV node and is usually slow. (6) These are divided into two in Normal Rhythm. Normal Sinus Rhythm (N) and Normal Rhythm with Extrasystole (Ne). N are heartbeats originating from the sinus node and occurring at normal

intervals. The Ne is the normal rhythm but with occasional extra beats (extrasystoles). Table 1 shows the classes in the ECG Database and the number of records in the classes.

Table 1. Classes in the ECG Database and the number of records in the classes.

Type	Record
Class 1 (VFL, VF)	337
Class 2 (VTTdP)	72
Class 3 (VTHR)	169
Class 4 (VTLR, B, HGEA, VER)	132
Class 5 (AFIB, SVTA SBR, BI, NOD)	106
Class 6 (BBB, N, Ne)	200
Total	1016

2.3. Proposed Model

In our study, the CNN architecture used to classify ECG data is shown in detail in Figure 4. In the first step, ECG signals were given as input to the CNN. The convolution layer contains two consecutive convolution layers to extract features from ECG data. Each convolution layer performs feature extraction on the data using 5x5 filters. The purpose of this process is to detect important signal patterns in the ECG data. Regularization Layers, following convolution layers, a dropout layer is implemented to prevent overlearning and increase model generalization ability. The dropout rate was set to 0.5, meaning half of the neurons were randomly disabled at each training step. After the pooling layer, the size of the feature maps was reduced using a max pooling layer. Using a 2x2 window, it selects the maximum values from each feature map, thus reducing the data size. The outputs of the flattening and fully connection pooling layer were flattened and then transferred to a fully connected layer containing 200 neurons. This layer takes the flattened features and creates the final feature vector for classification.



Figure 4. Structure of the proposed 1D-CNN Network.

The model was trained and evaluated for different classification scenarios. Each classification scenario corresponds to ECG signal classes that represent specific medical conditions. Model performance was evaluated using various metrics such as precision, recall, accuracy F1 score and Matthews Correlation Coefficient (MCC).

For the task at hand, which involves classifying ECG signals, we found that a simpler architecture with fewer layers was sufficient to achieve high accuracy. Adding more convolutional layers can lead to increased computational complexity and longer training times without significantly improving performance for such data. With limited training data, deeper networks are more prone to overfitting. While designing the CNN architecture chosen within the scope of the study, this architecture was preferred because a good balance between performance and calculation was not achieved in multi-layer networks. Using only two convolution layers, we aimed to balance model complexity and generalization ability. In our study, the hyperparameters used in the CNN architecture to classify arrhythmias from ECG data are learning rate, batch size, epoch size, dropout rate and optimizer. 0.001 was chosen as the learning rate. This value was found by performing a grid search to find the optimal value that effectively minimizes the loss function. 32 was used as a batch size. By balancing the batch size used, batch size, training speed and model performance, it was ensured that the gradient descent steps were neither too large nor too small. The model was trained with 150 epochs. This number is determined by where the training and validation losses meet. Thus, the data in the model was learned sufficiently and did not show overfitting. Additionally, a 50% dropout rate was applied to prevent overfitting. This value was chosen based on standard practices. RMSprop optimizer was used as the optimizer. This optimizer was

chosen for its efficient handling of sparse gradients and adaptive learning rate features, which helped in faster convergence. These hyperparameters were selected by a combination of grid search and manual tuning, considering the model's computational efficiency and generalization ability. In classifying ECG signals, we found that a simpler architecture with fewer layers was sufficient to achieve high accuracy. Adding more convolution layers can increase computational complexity and training times without significantly improving performance for this type of data.

Since ECG signals are time series, the 1D-CNN method was chosen to process these signals in this study. Compared to other machine learning methods, 1D-CNN automatically extracts the features for classification. The model provides high accuracy with its simplicity and high performance, and it prevents overfitting. Thus, it stands out as a suitable network model for clinical studies.

2.4. Performance Evaluation Metrics

In our study, seven basic metrics were used to evaluate the performance of the CNN model used in classifying ECG signals. These are, respectively, confusion matrix [31], accuracy, precision, recall, F1 Score, MCC, and ROC Curve. Accuracy is calculated is given in Equation (1). Here, TP represents the number of true positives, that is, those that are positive and predicted as positive by the classifier, and FP represents the number of positives that are positive but not predicted as positive by the classifier. FN refers to the number of false negatives, that is, it shows the number of those that were not predicted as negative by the classifier when they were negative. It shows the situations that are negative in the classification given by FP but are predicted as positive by the classifier. The precision metric measures how many of the cases classified as positive are actually positive. This indicates the accuracy of the positive predictions produced by our model and is calculated by the formula given in Equation (2). Recall indicates how much of all true positive cases are correctly classified. It is calculated as given in Equation (3). F1 score is the harmonic mean of precision and recall and combines both metrics in a balanced manner. How it is calculated is given in Equation (4). It evaluates how well the model performs overall. MCC is a metric that measures the quality of a classification performance by considering all four confusion matrix values. Both binary and multiple classifications can be used. How it is calculated is given in Equation (5).

$$Accuracy = \frac{TP + TN}{TN + TN + FP + FN} \quad (1)$$

$$Precision = \frac{TP}{TP + FP} \quad (2)$$

$$Recall = \frac{TP}{TP + FN} \quad (3)$$

$$F1 \text{ Score} = 2 \times \frac{Precision + Recall}{Precision \times Recall} \quad (4)$$

$$MCC = \frac{(TP \times TN) - (FP \times FN)}{\sqrt{(TP + FP) \times (TP + FN) \times (TN + FP) \times (TN + FN)}} \quad (5)$$

3. FINDINGS AND DISCUSSION

Four different classifications were made within the scope of the study. With the help of CNN network, arrhythmias were classified according to different conditions. Figure 5 shows the training process and losses of classification models with different numbers of groupings. Figure 5 a) shows the training and loss graph for binary classification. While the accuracy of the model increased over time, the loss value

decreased. It is seen that the model showed a steady improvement during the training process and reached a high accuracy rate without overfitting at the end of approximately 150 epochs. Figure 5 b) shows the training and loss graph for classifying ECG signals belonging to 3 different groups with the CNN network. In this graph, accuracy increased and loss decreased as the number of epochs increased. However, fluctuations in the loss graph may indicate that the model is starting to overfit the training data at specific points. Training and loss for 4 Group Classification in 5 c) the accuracy rate fluctuates slightly but generally increases. The loss rate is in a downward trend but decreasing more slowly. Given in Figure 5 d) Training and Loss for 6 Group Classification. This model has a lower accuracy rate and a higher loss value than others. This suggests that the model faces a more complex classification task and may need more training epochs or model tuning. Each graph tracks both accuracy and loss values throughout training to measure the model's performance. Such graphs are an important tool in understanding the training process of the model and adjusting the hyperparameters.

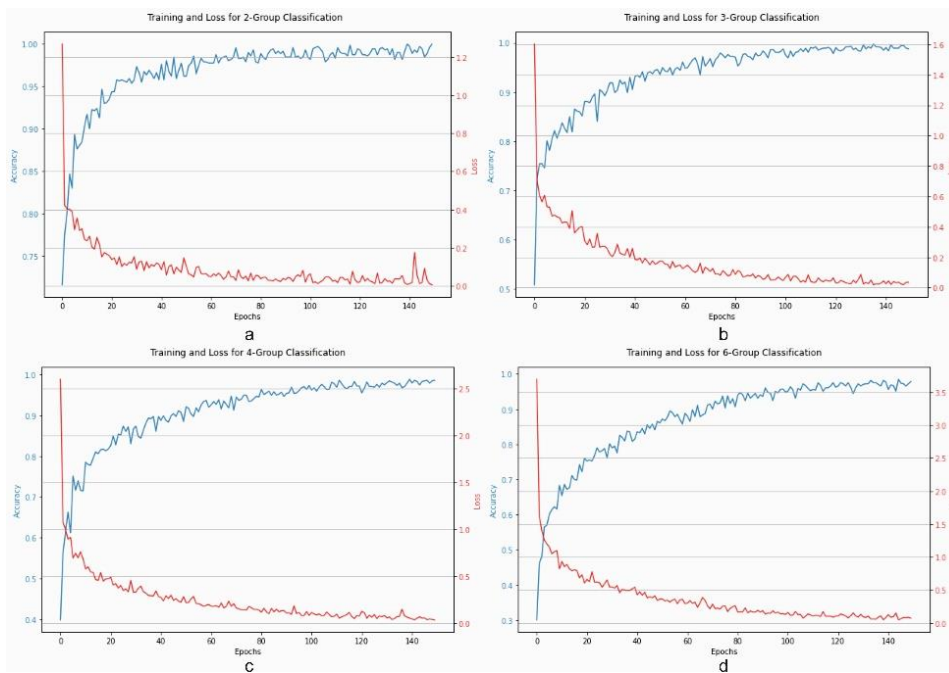


Figure 5. Training and loss graphs a) For 2-class classification b) For 3-class classification c) For 4-class classification d) For 6-class classification.

Separate confusion matrices were calculated for four different situations with different class numbers and are given in Figure 6. Figure 6 shows the confusion matrices that visualize the performance of the model for classification tasks with 2 classes in (a), 3 classes in (b), 4 classes in (c) and 6 classes in (d). Each matrix shows how well the model predicts for each class. In figure 6 (a), the predictions for Class 0 and Class 1 are largely correct. For Class 0, there are 161 correct predictions and 8 false negatives, and for Class 1, there are 173 correct predictions and 5 false positives. This indicates high accuracy and recall rates. In figure 6 (b), Class 0 showed high accuracy with 162 correct and 4 incorrect predictions. Class 1 demonstrated very good performance with 183 correct predictions and minimal confusion (1 false positive and 1 false negative). Class 2 also performed well with 151 correct predictions, but some confusion is seen with 12 false negatives and 4 false positives. In figure 6 (c), the model performs relatively well for Class 0 and Class 3, with 87 and 84 correct predictions, respectively. However, it experiences more confusion (false positives and false negatives) for Class 1 and Class 2. Specifically, Class 0 has 23 false positives, and Class 1 has 4 false negatives. In figure 6 (d), high accuracy is observed in Class 0 and Class 5, with 87 and 81 correct predictions, respectively. However, significant confusion exists among other classes. For example, Class 0 has 16 false negatives, and Class 1 has 10 false

negatives, while Class 4 has 7 false negatives and 5 false positives. The number of false positives and false negatives, especially in Classes 2, 3, and 4, is notable.

It has been observed that there is a general decrease in the performance of the model as the number of classes in the confusion matrices increases. This shows that the difficulty of the classification task increases as the number of classes increases and the model finds it difficult to manage the complexity. High rates of false positives and false negatives indicate that the model may confuse certain classes with other classes, which may indicate that the boundaries between classes are unclear or have insufficient representation in the training data set. Since the data distribution in this dataset is unbalanced, it is thought that it does not show high success in multiple classification.

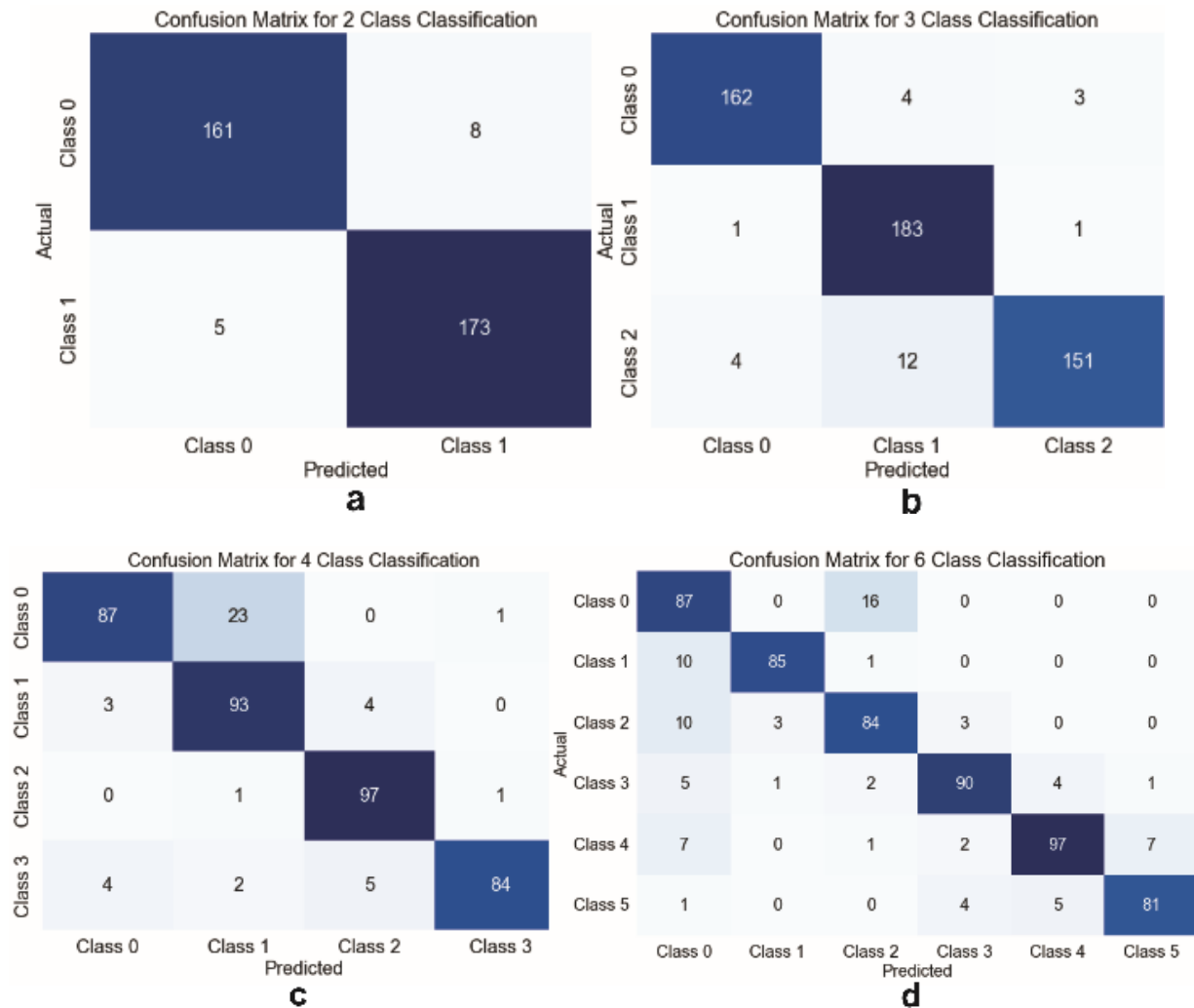


Figure 6. Confusion matrices for four different classification results: a) For 2-class classification b) For 3-class classification c) For 4-class classification d) For 6-class classification.

We also assess our model's performance using the ROC curve, which illustrates the correlation between the true positive rate (TPR) and the false positive rate (FPR) across various possible threshold settings of the model. The area under the curve (AUC) numerically expresses how well the model performs. In Figure 7, separate ROC curves are drawn for the 4 different classification cases performed in this study. When the graphs are examined, Figure 7 shows the ROC curve of the model for a classification task. The AUC value is 0.99 and the model showed very high performance. Figure 7 b) contains the ROC curves for a three-class task. There is a separate curve for each class, and each has high AUC values, meaning that the model appears to discriminate all classes well. Figure 7c shows AUC values for four

classes and shows high-performance curves for each class. Figure 7 d) shows ROC curves and AUC values for six different classes. This task is more complex and models generally perform less well with more classes, but the model shown here has quite high AUC values.

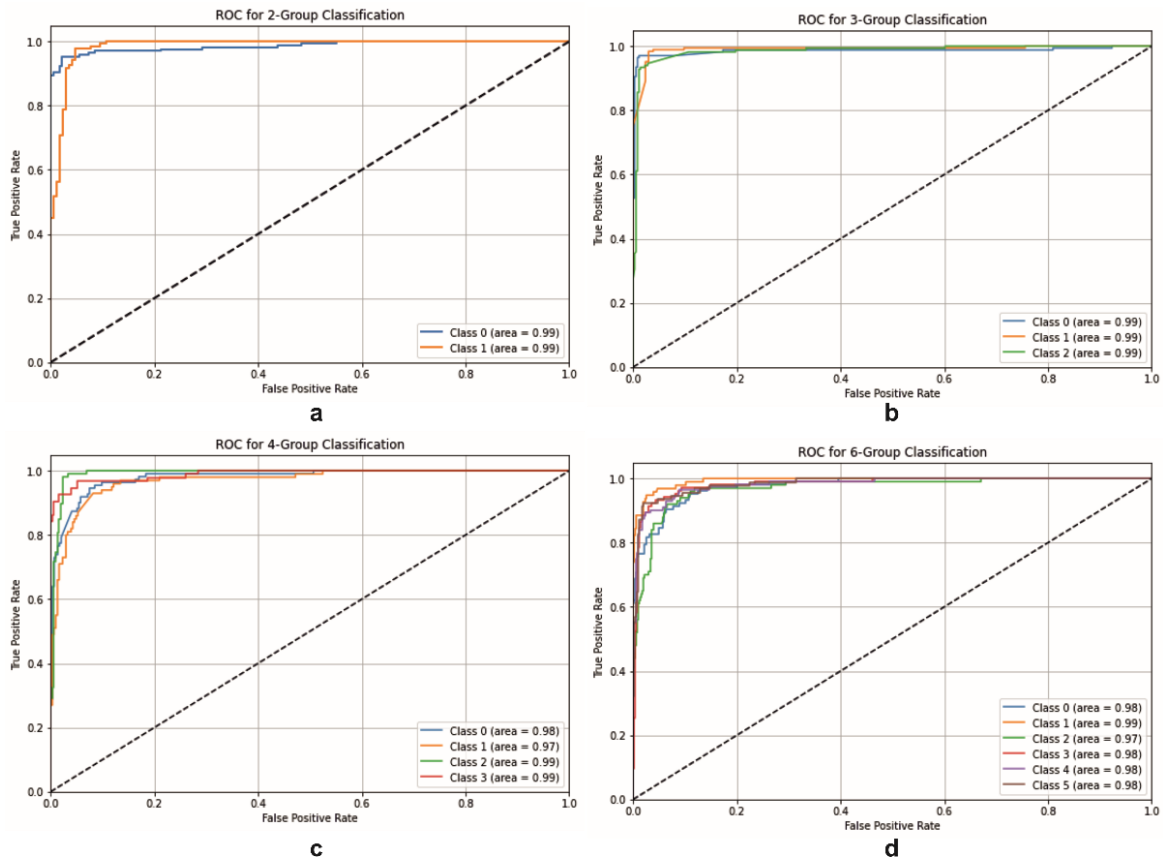


Figure 7. ROC curves for different classifications. a) For 2-class classification b) For 3-class classification c) For 4-class classification and d) 6-class classification.

When the metrics of each classification results are evaluated, the results of the two-class classification are given in Table 2. When the results are evaluated, it clearly shows that the model has high performance. Precision, Recall, F1-score, AUC, Accuracy and MCC values are all quite high, showing that the model works successfully for both classes. These results show that the model detects true positives well and the false positive rate is low. Overall, the performance of the model is near perfect and can be used safely in classification tasks.

Table 2. Classification metrics for two-class classification

Classes	Precision	Recall	F1-score	AUC	Accuracy	MCC
Class0	0.97	0.95	0.96	0.99	0.96	0.93
Class1	0.96	0.97	0.96	0.99	0.96	0.93

Both classes in the binary classification exhibit equally high F1-scores, demonstrating the model's balanced and effective performance in distinguishing between the two classes. Three-class classification results are given in Table 3. When the table is examined, it is clearly seen that the model has high performance. Precision, Recall, F1-score, AUC, Accuracy and MCC values are all quite high, showing that the model works successfully for all three classes. Especially high recall and F1-score values for Class 1 show that the model is quite effective in this class. Overall, the performance of the model is close to perfect and it can be used safely in classification tasks.

Table 3. Classification metrics for three-class classification.

Classes	Precision	Recall	F1-score	AUC	Accuracy	MCC
Class0	0.97	0.96	0.96	0.99	0.95	0.93
Class1	0.92	0.99	0.95	0.99		
Class2	0.97	0.90	0.94	0.99		

The high F1-scores across all classes in the three-class classification indicate that the model is well-calibrated and performs consistently across different classes, with minimal performance degradation. The four-class classification results are given in Table 4. The overall performance of the model is quite high. Precision, Recall, F1-score, AUC, Accuracy and MCC values are high, showing that the model works successfully for all four classes. However, some metrics for Class 0 and Class 1 appear to be slightly lower than other classes. Especially the recall value for Class 0 being 0.78 shows that there are more false negatives in this class. These results show that the overall performance of the model is quite good, but it may need improvement in some classes.

Table 4. Classification metrics for four-class classification

Classes	Precision	Recall	F1-score	AUC	Accuracy	MCC
Class0	0.93	0.78	0.85	0.98	0.89	0.86
Class1	0.78	0.93	0.85	0.97		
Class2	0.92	0.98	0.95	0.99		
Class3	0.98	0.88	0.93	0.99		

The six-class classification results are given in table 5. When the model results are examined, it can be seen that it generally performs well. This model, where most of the Precision, Recall, F1-score, AUC, Accuracy and MCC values are high, shows that it works successfully in all six classes. It can be seen that some metrics for Class 0 and Class 2 are slightly lower than other classes. Especially the low precision and F1-score values for Class 0 indicate that there are more false positives in this class. These results show that the overall functioning of the model is good, but it may need improvement in some classes.

Table 5. Classification metrics for six-class classification

Classes	Precision	Recall	F1-score	AUC	Accuracy	MCC
Class0	0.72	0.84	0.78	0.98	0.87	0.84
Class1	0.96	0.89	0.92	0.99		
Class2	0.81	0.84	0.82	0.97		
Class3	0.91	0.87	0.89	0.98		
Class4	0.92	0.87	0.89	0.98		
Class5	0.91	0.87	0.89	0.98		

A detailed evaluation of the average key metrics for each classification group is provided in Table 6. It is clearly seen that the performance of the model in classification tasks decreases as the number of classes increases. In two- and three-class classifications, the model exhibits near-perfect performance with high accuracy, precision, sensitivity, F1-Score and MCC values. However, these metrics drop slightly in four- and six-class classifications. This shows that as the number of classes increases, the model's ability to distinguish classes becomes more difficult and the complexity increases. Nevertheless, the overall performance of the model across all classification groups is satisfactory, indicating that the model is reliable and consistent. These results show that the model performs reasonably even on more complex classification tasks.

Table 6. Comparative table showing average metrics for all classification groups.

	Accuracy	Precision	Recall	F1-Score	MCC
For 2 Class	0.96	0.96	0.96	0.96	0.93
For 3 Class	0.95	0.95	0.95	0.95	0.93
For 4 Class	0.89	0.90	0.89	0.89	0.86
For 6 Class	0.87	0.87	0.86	0.87	0.84

When the results obtained in the study were compared with other studies in the literature, the results in Table 7 were obtained. When the table is examined, studies compare the results obtained using different databases and methods for classifying ECG signals. The results show that the proposed methodology provides high accuracy rates compared to existing methods. The high accuracy rates obtained especially in two-class and three-class classification reveal that this approach is a potentially effective classification method.

Table 7. Comparison table with other existing methods.

Study	Database	Class	Method	Accuracy(%)
Acharya et al. (2013) [37]	MIT-BIH arrhythmia database, MIT-BIH malignant ventricular arrhythmia database, Creighton University ventricular tachyarrhythmia database	2	CNN	93.18
Mathews et al. (2018) [32]	MIT-BIH Arrhythmia Database	2	RBM & DBN	93.78
Yao et al.,(2018) [34]	China Physiological Signal Challenge	9	TI-CNN	77.3
Tripaty et al., (2018) [36]	Creighton university ventricular tachy-arrhythmia database (CUIDB) and MIT-BIH malignant ventricular arrhythmia database	2	LS-SVM	89.81
Ebrahimzadeh et al. (2019) [38]	MIT-BIH Sudden Cardiac Death Holter and Sudden Cardiac Death Holter	2	Mixture of Experts (ME)	82.85
Yao et al., (2020) [35]	China Physiological Signal Challenge	9	ATI-CNN	81.2
Prabhakararao et al. (2021) [33]	PhysioNet/CinC-2017	3	DMSCE	88
	PTBXL-2020	5		85.65
Popadina et al. (2023) [39]	MIT-BIH Malignant Ventricular Ectopy Database (MVED)	2	1D CNN	95
This Study	MIT-BIH Malignant Ventricular Ectopy Database (MVED)	6	1D CNN	87
		4	1D CNN	89
		3	1D CNN	95
		2	1D CNN	96

4. CONCLUSIONS AND RECOMMENDATIONS

Within the scope of this study, we focused on proposing a CNN architecture and classifying different arrhythmia types according to their risk level. The effectiveness of the CNN architecture in the study in classifying cardiac arrhythmias was examined in detail. Our results show that CNN-based models

provide significant accuracy in identifying and classifying cardiac arrhythmias. Accuracy rates of 96% in binary classification, 95% in triple classification, 89% in quadruple classification and 87% in six-fold classification were achieved. These results show that overall accuracy decreases as the complexity of the model increases, but high levels of accuracy are still maintained.

The high performance at the binary classification level reveals that the CNN can effectively distinguish basic arrhythmia types. On the other hand, more detailed levels of classification allow specific types of arrhythmias to be recognized in more detail. Study results highlight the potential of CNN-based DL models in automatic identification and classification of cardiac arrhythmias and encourage the use of these technologies in the field of cardiology.

In conclusion, this study demonstrates the feasibility and effectiveness of deep learning techniques in cardiac arrhythmia classification. These approaches may play an important role in the diagnosis and treatment of cardiovascular diseases in the future and may support clinical decision-making processes. However, additional studies on larger and more diverse data sets will help further develop these models and find broader applications in clinical settings.

CONFLICT OF INTEREST

The author stated that there are no conflicts of interest regarding the publication of this article.

CRedit AUTHOR STATEMENT

Evin Şahin Sadık: Writing - original draft, Writing – Review & Editing, Visualization, Conceptualization, Methodology, Software.

REFERENCES

- [1] Tada H, Fujino N, Nomura A, et al. Personalized medicine for cardiovascular diseases. *J Hum Genet.* 2021;66(1):67-74.
- [2] Gaidai O, Cao Y, Loginov S. Global cardiovascular diseases death rate prediction. *Curr Probl Cardiol.* Published online 2023:101622.
- [3] Zheng Q, Tang Q, Wang ZL, Li Z. Self-powered cardiovascular electronic devices and systems. *Nat Rev Cardiol.* 2021;18(1):7-21.
- [4] Zheng Q, Tang Q, Wang ZL, Li Z. Self-powered cardiovascular electronic devices and systems. *Nat Rev Cardiol.* 2021;18(1):7-21.
- [5] Buja LM, Willerson JT. The role of coronary artery lesions in ischemic heart disease: insights from recent clinicopathologic, coronary arteriographic, and experimental studies. *Hum Pathol.* 1987;18(5):451-461.
- [6] Reed GW, Rossi JE, Cannon CP. Acute myocardial infarction. *Lancet.* 2017;389(10065):197-210.
- [7] LeWinter MM. Acute pericarditis. *N Engl J Med.* 2014;371(25):2410-2416.
- [8] Wexler R, Elton T, Pleister A, Feldman D. Cardiomyopathy: an overview. *Am Fam Physician.* 2009;79(9):778.

- [9] Maron BJ, Maron MS. Hypertrophic cardiomyopathy. *Lancet*. 2013;381(9862):242-255.
- [10] Agnelli G, Becattini C. Acute pulmonary embolism. *N Engl J Med*. 2010;363(3):266-274.
- [11] Gawałko M, Balsam P, Lodziński P, et al. Cardiac arrhythmias in autoimmune diseases. *Circ J*. 2020;84(5):685-694.
- [12] Yusupova NI, Bogdanov MR. Assessment of the Risk of Sudden Cardiac Death Using Machine Learning Methods. *Pattern Recognit Image Anal*. 2023;33(3):536-543.
- [13] Galli A, Ambrosini F, Lombardi F. Holter monitoring and loop recorders: from research to clinical practice. *Arrhythmia Electrophysiol Rev*. 2016;5(2):136.
- [14] Mikhaylov AY, Yumashev A V, Kolpak E. Quality of life, anxiety and depressive disorders in patients with extrasystolic arrhythmia. *Arch Med Sci AMS*. 2022;18(2):328.
- [15] Nie L-Y, Wang X-D, Zhang T, Xue J. Cardiac complications in systemic sclerosis: early diagnosis and treatment. *Chin Med J (Engl)*. 2019;132(23):2865-2871.
- [16] Boulif A, Ananou B, Ouladsine M, Delliaux S. A Literature Review: ECG-Based Models for Arrhythmia Diagnosis Using Artificial Intelligence Techniques. *Bioinform Biol Insights*. 2023;17:11779322221149600.
- [17] Liu J, Li Z, Jin Y, et al. A review of arrhythmia detection based on electrocardiogram with artificial intelligence. *Expert Rev Med Devices*. 2022;19(7):549-560.
- [18] Aziz S, Ahmed S, Alouini M-S. ECG-based machine-learning algorithms for heartbeat classification. *Sci Rep*. 2021;11(1):18738.
- [19] Sahoo S, Dash M, Behera S, Sabut S. Machine learning approach to detect cardiac arrhythmias in ECG signals: A survey. *Irbm*. 2020;41(4):185-194.
- [20] Mohanty M, Sahoo S, Biswal P, Sabut S. Efficient classification of ventricular arrhythmias using feature selection and C4. 5 classifier. *Biomed Signal Process Control*. 2018;44:200-208.
- [21] Rodríguez R, Mexicano A, Bila J, Ponce R, Cervantes S, Martinez A. Hilbert transform and neural networks for identification and modeling of ECG complex. In: *Third International Conference on Innovative Computing Technology (INTECH 2013)*. IEEE; 2013:327-332.
- [22] Martis RJ, Krishnan MMR, Chakraborty C, et al. Automated screening of arrhythmia using wavelet based machine learning techniques. *J Med Syst*. 2012;36:677-688.
- [23] Devi RL, Kalaivani V. Machine learning and IoT-based cardiac arrhythmia diagnosis using statistical and dynamic features of ECG. *J Supercomput*. 2020;76(9):6533-6544.
- [24] Şahin Sadık E, Saraoğlu HM, Canbaz Kabay S, Kesinkılıç C. Deep Learning-Based Approach for Classification Of Mental Tasks From Electroencephalogram Signals. *Avicenna J Neuro Psycho Physiol*. 2023;10(1):15-21.
- [25] Ansari Y, Mourad O, Qaraqe K, Serpedin E. Deep learning for ECG Arrhythmia detection and classification: an overview of progress for period 2017–2023. *Front Physiol*. 2023;14.

- [26] Essa E, Xie X. An ensemble of deep learning-based multi-model for ECG heartbeats arrhythmia classification. *iee access*. 2021;9:103452-103464.
- [27] Parvaneh S, Rubin J, Babaeizadeh S, Xu-Wilson M. Cardiac arrhythmia detection using deep learning: A review. *J Electrocardiol*. 2019;57:S70-S74.
- [28] Greenwald SD. The development and analysis of a ventricular fibrillation detector. Published online 1986.
- [29] Manilo LA, Nemirko AP, Evdakova EG, Tatarinova AA. ECG Database for Evaluating the Efficiency of Recognizing Dangerous Arrhythmias. In: 2021 IEEE Ural-Siberian Conference on Computational Technologies in Cognitive Science, Genomics and Biomedicine (CSGB). IEEE; 2021:120-123.
- [30] Nemirko A, Manilo L, Tatarinova A, Alekseev B, Evdakova E. ECG fragment database for the exploration of dangerous arrhythmia. Published online 2022.
- [31] Heydarian M, Doyle TE, Samavi R. MLCM: Multi-label confusion matrix. *IEEE Access*. 2022;10:19083-19095.
- [32] Mathews SM, Kambhamettu C, Barner KE. A novel application of deep learning for single-lead ECG classification. *Comput Biol Med*. 2018;99:53-62.
- [33] Prabhakararao E, Dandapat S. Multi-scale convolutional neural network ensemble for multi-class arrhythmia classification. *IEEE J Biomed Heal Informatics*. 2021;26(8):3802-3812.
- [34] Yao Q, Fan X, Cai Y, Wang R, Yin L, Li Y. Time-incremental convolutional neural network for arrhythmia detection in varied-length electrocardiogram. In: 2018 IEEE 16th Intl Conf on Dependable, Autonomic and Secure Computing, 16th Intl Conf on Pervasive Intelligence and Computing, 4th Intl Conf on Big Data Intelligence and Computing and Cyber Science and Technology Congress (DASC/PiCom/DataCom/CyberSciTech. IEEE; 2018:754-761.
- [35] Yao Q, Wang R, Fan X, Liu J, Li Y. Multi-class arrhythmia detection from 12-lead varied-length ECG using attention-based time-incremental convolutional neural network. *Inf Fusion*. 2020;53:174-182.
- [36] Tripathy RK, Zamora-Mendez A, De la O Serna JA, Paternina MRA, Arrieta JG, Naik GR. Detection of life threatening ventricular arrhythmia using digital taylor fourier transform. *Front Physiol*. 2018;9:722.
- [37] Acharya UR, Oh SL, Hagiwara Y, Tan JH, Adeli H. Deep convolutional neural network for the automated detection and diagnosis of seizure using EEG signals. *Comput Biol Med*. 2018;100:270-278.
- [38] Ebrahimzadeh E, Foroutan A, Shams M, et al. An optimal strategy for prediction of sudden cardiac death through a pioneering feature-selection approach from HRV signal. *Comput Methods Programs Biomed*. 2019;169:19-36.
- [39] Popadina AO, Nemirko AP. Detection of Dangerous Arrhythmias Using a 1D Convolutional Neural Network Trained on the Full Spectrum of a Short ECG Signal. In: 2023 Seminar on Digital Medical and Environmental Systems and Tools (DMEST). IEEE; 2023:109-112.




RESEARCH ARTICLE

END-TO-END AUTOMATIC MUSIC TRANSCRIPTION OF POLYPHONIC QANUN AND
OUD MUSIC USING DEEP NEURAL NETWORK

Emin GERMEN^{1*}, Can KARADOĞAN²

¹ Electrical & Electronics Engineering Dept. Engineering Faculty Eskişehir Technical University, Eskişehir, Turkey
egermen@eskisehir.edu.tr -  [0000-0003-1301-3786](https://orcid.org/0000-0003-1301-3786)

² MIAM Center of Advanced Studies in Music, State Conservatory, Istanbul Technical University, İstanbul, Turkey
karadoganc@itu.edu.tr -  [0000-0003-3611-6980](https://orcid.org/0000-0003-3611-6980)

Abstract

This paper introduces an automatic music transcription model using Deep Neural Networks (DNNs), focusing on simulating the "trained ear" in music. It advances the field of signal processing and music technology, particularly in multi-instrument transcription involving traditional Turkish instruments, Qanun and Oud. Those instruments have unique timbral characteristics with early decay periods. The study involves generating basic combinations of multi-pitch datasets, training the DNN model on this data, and demonstrating its effectiveness in transcribing two-part compositions with high accuracy and F1 measures. The model's training involves understanding the fundamental characteristics of individual instruments, enabling it to identify and isolate complex patterns in mixed compositions. The primary goal is to empower the model to distinguish and analyze individual musical components, thereby enhancing applications in music production, audio engineering, and education.

Keywords

Music transcription,
Signal processing,
Deep learning,
Constant Q transform

Time Scale of Article

Received :11 April 2024
Accepted : 18 Septembert 2024
Online date :30 September 2024

1. INTRODUCTION

End-to-end music transcription is a highly challenging subject, captivating those in signal processing research, musicians, and the people involved in music technology[1]. This field initially took shape with advancements in multi-instrument music transcription, rooted in Blind Source Separation (BSS) [2], [3] regarding signal processing and linear system methods like Non-Negative Matrix Factorization[4]. However, the landscape evolved[5] significantly with the advent of accessible processing capabilities and breakthroughs in Deep Neural Networks (DNN)[6]–[8]. These developments have expanded the interest in BSS to researchers focused on Data Learning. Beyond mere source separation, the domain has diversified to include various methodologies, such as extracting instruments from music compositions[5], segregating music and voices through 2D Fourier Transform techniques[9], and isolating monaural speech[10] further enriching the research literature.

The human auditory system can discern distinct patterns and separate acoustic sources, such as different musical instruments or vocals. However, a crucial aspect of this capability is that it often requires some degree of familiarization or training[11]. Individuals lacking exposure to a particular musical genre or

*Corresponding Author: egermen@eskisehir.edu.tr

unfamiliar with specific types of instruments may find it challenging to isolate and recognize distinct components within the music.

For instance, someone with no background in classical Indian music might struggle to identify patterns in Indian Raga or Sargam music. These compositions, rich in their unique structure and rhythm, could seem intricate and elusive to an untrained ear. Similarly, Western classical music, known for its complex harmonies and arrangements, might appear as a series of perplexing patterns to an adolescent unfamiliar with this style. In another scenario, a person who has spent considerable time immersed in Western Classical music might find metal music overwhelming or even disturbing. Often characterized by its intense and heavily distorted guitar riffs, metal music starkly contrasts Western Classical music's more structured and melodic nature. This divergence can make it difficult for someone accustomed to the latter to comprehend and appreciate the former's musical themes, nuances, and even instruments.

Overall, the ease with which a person can recognize and separate elements within a musical piece significantly depends on their prior exposure and understanding of the specific musical style. This highlights the importance of cultural and experiential factors in shaping our auditory perception and appreciation of music. The main focus in this context is the trained ear and how this phenomenon is modeled.

The concept of a "trained ear" in music pertains to the ability to discern and identify specific instruments and the music played by them. This skill, often developed over time through exposure and practice, involves a deep understanding of the distinct characteristics of various instruments[12]. The process of acquiring such a nuanced auditory ability is both elaborate and complex, reflecting the intricate nature of musical perception and appreciation[13]. The concept of "training," particularly in the context of music separation, represents a significant milestone in the field of music analysis. This training refers to the process of developing systems that can identify specific patterns within a mixed musical piece, which is effectively treated as a signal in this context. Various methodologies have been explored to achieve this, as noted in the works of [14], [15]

In the context of using models, such as Deep Neural Networks (DNNs)[16], to replicate or assist in this process of music separation and identification, the starting point often involves understanding the basic characteristics of individual instruments. By training the model with these fundamental traits, it can begin to recognize and isolate the complex patterns specific to each instrument. This approach involves feeding the model with data that encapsulates the unique acoustic signatures of different instruments. As the model learns these characteristics, it becomes increasingly adept at identifying these instruments within a mixed musical composition.

The goal is to enable the model to not only recognize an instrument but also to isolate the music played by that instrument from a composition featuring multiple instruments. This ability to discriminate and analyze individual components of a musical piece is valuable for various applications, including music production, audio engineering, and even in enhancing music education and research. It is a testament to how combining human auditory skills and advanced technological models can lead to a deeper and more precise understanding of music.

This study aims to explore the differentiation of instruments and their music within composite audio data, focusing on recognizing distinct, well-defined signatures of individual instruments. Specifically, the Turkish plucked instruments, Qanun and Oud, have been selected for analysis in this model. A DNN model has been developed and trained to utilize the fundamental characteristics of the amalgamated sounds from these instruments. The trained model is then employed to distinguish polyphonic music compositions involving these instruments. The outcomes of this approach have been notably satisfactory.

One of the most significant contributions of this study is the development of a system that enables the separation of complex musical data consisting of two or more sounds, using only the fundamental composite data characteristics of the acoustic instruments to be separated, independently of the instrument databases used in previously trained models. Moreover, it is noteworthy that this study successfully applies such a separation to Turkish music instruments, which have not been studied in the world literature before. The successful results obtained demonstrate that this approach can also be applied to Turkish music.

The paper’s organization is structured as follows: Chapter Two presents a comprehensive description of the model utilized for transcribing two-part music. This chapter will detail the preparation of the dataset used for training, as well as the features involved. Chapter Three is devoted to an in-depth discussion of the results derived from this study. Conclusively, Chapter Four offers a summation and final thoughts of the paper.

2. AUTOMATIC MUSIC TRANSCRIPTION MODEL

In this detailed section, we delve into the complexities of the model architecture, the generation of training data, and the signal processing techniques employed for feature extraction, all of which are integral to our research study. The framework is given in Figure 1.

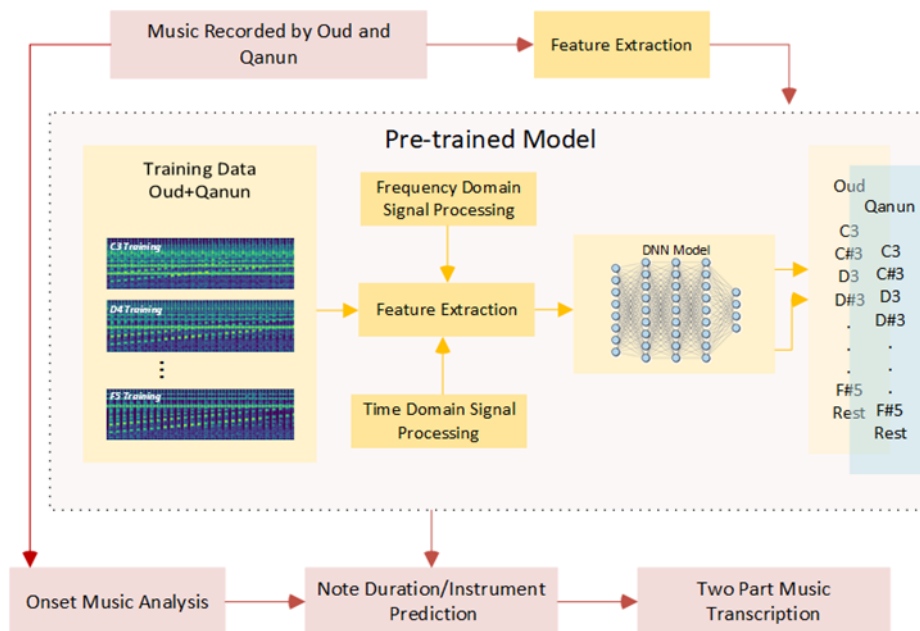


Figure 1. The framework of the two-part music transcription

Training Data Generation:

The primary objective of constructing this model is to facilitate the understanding of the mechanism behind the ear training phenomena by scrutinizing the fundamental instrumental combinations in music creation. This research employs a blend of music incorporating Turkish Qanun and Oud instruments, aiming to generate a multi-instrument, multi-pitch dataset. A critical step in this process is the disentanglement of the musical pieces, which necessitates capturing the distinct multi-timbral characteristics of these two instruments playing concurrently.

The concept of a "well-trained ear" in this context signifies proficiency in precisely discerning, identifying, and interpreting sounds, especially within music. This ability is greatly esteemed among musicians, audio engineers, and music lovers. The most crucial element of such a trained ear is the

recognition of pitches in polyphonic music. This study investigates whether such training can be mimicked through the note combinations of two simultaneously played instruments. The methodology adopted is straightforward: while the Oud plays a single note (e.g., C3), the Qanun explores various notes spanning three octaves, and all possible combinations are systematically recorded.

Figure 2 exemplifies the training data for the A4 note on the Qanun. In this illustration, the Qanun plays the A4 note while the Oud progresses in chromatic from C3 to A5. Notably, this method also can accommodate training for microtonal intervals. In this work, they are omitted. For each note, a 56-second sample of mixed music is captured for training purposes. The predicted output of 56 seconds data truly considered as A4. In total, thirty-seven distinct datasets were compiled for the Qanun, covering chromatic notes from C3 to A5. Therefore, the corpus for Qanun consists of total 2072 seconds long data with 37 different predicted outputs to span the notes C3 to A5. An additional dataset was added to the Qanun corpus to represent musical pauses, where only the Oud is audible or there is silence. This resulted in 37 diverse datasets dedicated to identifying Qanun phrases within the mixed music. Here 37 different outputs are C3, C3#, D3, D3#, ... A5, and Rest for Qanun, which are equally probably distributed. The same methodology was replicated for compiling the Oud data. This systematic approach ensures a thorough coverage of the musical spectrum, enabling the study to capture the intricacies of pitch variation and harmonic relationships between the two instruments. By focusing on the combination of notes from two distinct instruments, the study paves the way for advanced understanding and modeling of complex musical interactions.

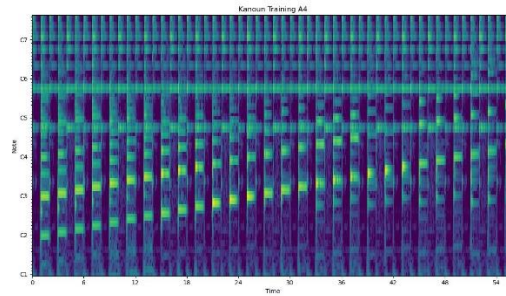


Figure 2. A4 training data for Qanun with Oud spanning the scale in 3 octaves.

Feature Extraction

The features are generated using Short Time Fourier Transform (STFT), Constant Q Transform (CQT), Spectral Centroid (ST) and Band Energy Ratio (BER) combinations of music signal. In music analysis, the STFT [17] is a key tool for tasks like pitch detection, note mapping, and timing. It is effective because it analyzes music in both time and frequency, providing a detailed view of musical pieces. STFT helps break down complex polyphonic compositions into simpler parts, making it easier to understand the structure of the music. However, it is important to mention that while the STFT is good for understanding the sound qualities of instruments, it is not the best at picking up the finer details of musical notes, especially in the 64 Hz to 1.5 kHz frequency range. The CQT [18] is a better tool for this purpose. Its bins are arranged in line with musical notes, especially useful in Western music where an octave is divided into 12 semitones, as denoted in Equation (1).

$$f_m = f_{min} 2^{\frac{m}{12 \cdot b}} \quad (1)$$

Here f_{min} is the minimal frequency in analysis, and b is the number of bins per semi-tone. The CQT can be derived with a quality factor $Q = \frac{f_m}{f_{m+1} - f_m} = 1 / (2^{\frac{1}{12b}} - 1)$

$$F_{CQT}[m, \Lambda] = \frac{1}{N_m} \sum_{k=0}^{N_m-1} x[k + \Lambda R] w_m[k] e^{-i \frac{2\pi Q k}{N_m}} \quad (2)$$

To accurately identify both the exact frequencies of musical notes and the unique sound qualities of instruments, a feature set combining the STFT and the CQT has been developed. For the STFT, a 2048-point Fast Fourier Transform (FFT) is used, focusing on the first 500 frequency components from 0 Hz to 9 kHz. At the same time, the CQT uses 80 bins to cover the range of musical notes from the C in the first octave to the C in the eighth octave, between 32.7 Hz and 4186 Hz. This combined use of STFT and CQT provides a thorough and detailed representation of the music, capturing both the frequencies of notes and the distinct sound characteristics of various instruments across a wide frequency range.

The Spectral Centroid [19] shown in Equation (3) is a pivotal feature in music analysis, serving as a quantitative measure that denotes the 'center of gravity' of the spectrum for each analyzed bin. This metric is crucial in discerning the musical texture and timbral qualities of different instruments within a composition. It effectively indicates the concentration of energy across the spectrum, providing insights into the brightness or dullness of the sounds.

$$SC_k = \frac{\sum_{n=1}^N m_k(n)n}{\sum_{n=1}^N m_k(n)} \quad (3)$$

Like the Spectral Centroid, the BER is another critical audio feature that can be extracted for in-depth music analysis. This parameter is calculated for each window of the audio signal, as detailed in Equation (4). The BER quantifies the energy distribution within specific frequency bands of the audio spectrum, thereby providing a nuanced understanding of the spectral characteristics of the sound. This measurement is essential for tasks such as identifying the dominant frequency bands in a piece of music, understanding the textural components of sound, and distinguishing between different types of sounds or instruments based on their energy distribution across the spectrum.

$$BER_k = \frac{\sum_{n=1}^{F-1} m_k(n)^2}{\sum_{n=F}^N m_k(n)^2} = \frac{\text{mean square of lower frequency components}}{\text{mean square of higher frequency components}} \quad (4)$$

Training the DNN Model

The study employs a comprehensive dataset derived from the multipitch characteristics of the Qanun and Oud instruments, covering octaves ranging from C3 to B5. From this dataset, the features are extracted and utilized as the foundational data for training a sophisticated 7-layer Deep Neural Network (DNN). The architecture of this DNN is thoughtfully designed, with the input layer comprising 586 nodes for the FFT components, CQT bins, Spectral Centroids, and BER features to identify the mixture components of two instruments.

The model is a deep neural network built using the Keras Sequential API, designed for multi-class classification. It consists of five hidden layers with 586, 400, 200, 400, and 200 neurons, each utilizing the ReLU activation function to introduce non-linearity and enhance the network's ability to learn complex patterns. The output layer comprises 37 neurons with softmax activation, producing a probability distribution across 37 different musical notes that span the 3 octaves. Compiled with the categorical cross-entropy loss function and the Adam optimizer, the model is optimized for efficient training and effective convergence. The accuracy metric evaluates performance throughout the training and testing phases, ensuring the model's effectiveness in classifying data into multiple categories. The model is trained using 67% of the data and tested on the remaining 33%, providing a more thorough evaluation of its classification capabilities.

Transient Detection and Onset Analysis

Music transcription fundamentally involves recognizing temporal changes within a musical piece, such as variations in notes played by instruments or their intermittent silences. These fluctuations, termed as transients, are particularly pronounced during the attack phase of an instrument's note. In the context of

this study, which focuses on plucked instruments like the Oud and Qanun, these transients are distinctly identifiable. To accurately track these transients and thereby detect structural shifts within the time series of the music, both the energy envelope and zero crossings are utilized. Concurrently, frequency-domain features, including the spectral centroid, spectral skewness, and spectral kurtosis, are employed to provide a more granular understanding of potential onset points. Figure 3 exemplifies this process, showcasing onset detection in a recording featuring both the Oud and Qanun, with illustrations in both time and frequency domains. This comprehensive approach allows for a precise music transcription, capturing the dynamic and nuanced interplay of these instruments.

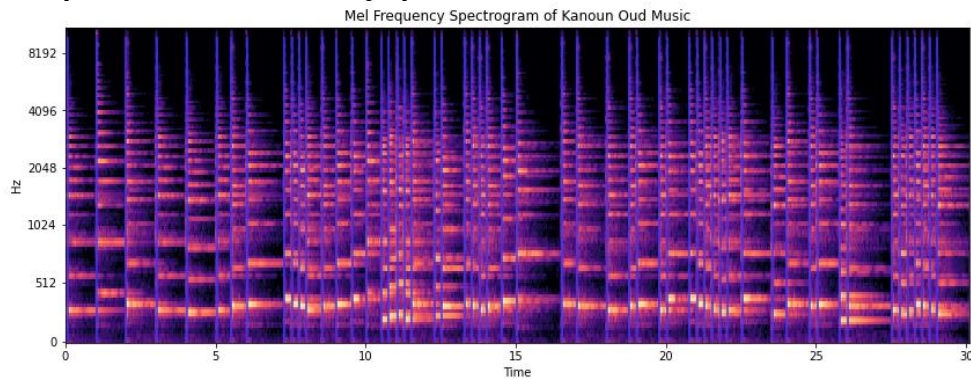


Figure 3. Onset times of music played by Qanun and Oud

The Music Transcription

After completing the model's training process, a two-part musical composition is processed through the trained DNN. The output from this DNN comprises potential notes that form the basis of the musical piece. Concurrently, onset analysis is employed to identify and track the potential transients of notes and the intervals of silence (rests) within the music.

In conducting a comparative analysis of original melodies and their transcriptions, a methodology was utilized to reduce them into smaller constituent elements. This was achieved by transforming the duration of each note and rest within the compositions into an equivalent duration represented by sixteenth notes. The decomposition of these melodies into increments of sixteenth notes allowed for a uniform and exact measure of temporal divisions. This standardization was crucial in representing rhythmic patterns consistently, and it facilitated an accurate examination of nuanced differences, including syncopations and articulations, within the musical pieces.

3. RESULTS

The trained model with data of simple combinations of Oud and Qanun is used to separate and transcribe two-part music. We evaluated the model's efficiency using an originally composed piece, as detailed in Figure 4. This composition, featuring both instruments, was recorded in a CD-quality at a tempo of 60 beats per minute (bpm) and endured 1 minute and 38 seconds.

Composition 1 for Qanun and Oud



Figure 4. The Composition 1 for Qanun and Oud Music

To evaluate the model's performance, the entire musical composition was segmented into precise segments, each corresponding to a duration of sixteenth notes. This structured division allowed for a detailed analysis of the model's accuracy and F1 measure in recognizing and transcribing each note segment. The F1 measure is a special metric that combines precision (how often we were right when we thought we were) and recall (how many of the right things we caught) into one score. Those are calculated as :

$$Precision = \sum_{n=1}^N \frac{True\ Positive[n]}{True\ Positive[n] + False\ Positive[n]} \quad (5)$$

$$Recall = \sum_{n=1}^N \frac{True\ Positive[n]}{True\ Positive[n] + False\ Negative[n]} \quad (6)$$

$$Accuracy = \sum_{n=1}^N \frac{True\ Positive[n]}{True\ Positive[n] + False\ Positive[n] + False\ Negative[n]} \quad (7)$$

$$F1\ measure = \frac{2 * Precision * Recall}{Precision + Recall} \quad (8)$$

The Qanun Transcription of the music is given in Figure 5. Figure 6 shows the Confusion Matrix corresponding to Qanun's transcription. Here, it is noted that NO represents the rest.

Comparison of Original and Transcribed Qanun Part of Composition 1

Figure 5. Transcription of Extracted Qanun from Composition 1

In this confusion matrix of Qanun of Composition 1:

The Accuracy: 0.6538461538461539, F1 Score: 0.6636862141708085 are calculated.

Confusion Matrix of Actual and Transcribed in 16'th Notes

Actual Notes	A#4	A#5	A4	A5	B4	B5	C#4	C#5	C4	C5	D#4	D#5	D4	D5	E4	E5	F#4	F#5	F4	F5	G#4	G#5	G4	ND
A#4	2	0	0	0	0	0	0	0	0	0	0	0	0	0	0	0	0	0	0	0	0	0	0	0
A#5	0	9	0	0	0	0	0	0	0	0	0	0	0	0	0	0	0	0	0	0	0	0	0	1
A4	0	0	18	0	0	0	0	0	0	0	0	0	0	0	0	0	0	0	0	0	0	0	0	6
A5	0	0	0	7	0	0	0	0	0	0	0	0	0	0	0	0	0	0	0	0	0	0	0	13
B4	0	0	0	0	6	0	0	0	0	0	0	0	0	0	0	0	0	0	0	0	0	0	0	7
B5	0	0	0	0	0	11	0	0	0	0	0	0	0	0	0	0	0	0	0	0	0	0	0	12
C#4	0	0	0	0	0	0	8	0	0	0	0	0	0	0	0	0	0	0	0	0	0	0	0	8
C#5	0	0	0	0	0	0	0	10	0	0	0	0	0	0	0	0	0	0	0	0	0	0	0	8
C4	0	0	0	0	0	0	0	0	6	0	0	0	0	0	0	0	0	0	0	0	0	0	0	2
C5	0	0	0	0	0	0	0	0	0	8	0	0	0	0	0	0	0	0	0	0	0	0	0	0
C6	0	0	0	0	0	0	0	0	0	0	0	0	0	0	0	0	0	0	0	0	0	0	0	0
D#4	0	0	0	0	0	0	0	0	0	0	1	0	0	0	0	0	0	0	0	0	0	0	0	4
D#5	0	0	0	0	0	0	0	0	0	0	0	14	0	0	0	0	0	0	0	0	0	0	0	1
D4	0	0	0	0	0	0	0	0	0	0	0	0	8	0	0	0	0	0	0	0	0	0	0	0
D5	0	0	0	0	0	0	0	0	0	0	0	0	0	1	0	0	0	0	0	0	0	0	0	0
E4	0	0	0	0	0	0	0	0	0	0	0	0	0	0	7	0	0	0	0	0	0	0	0	8
E5	0	0	0	0	0	0	0	0	0	0	0	0	0	0	0	6	0	0	0	0	0	0	0	7
F#4	0	0	0	0	0	0	0	0	0	0	0	0	0	0	0	0	15	0	0	0	0	1	0	6
F#5	0	0	0	0	0	0	0	0	0	0	0	0	0	0	0	0	0	8	0	0	0	0	0	2
F4	0	0	0	0	0	0	0	0	0	0	0	0	0	0	0	0	0	0	3	0	0	0	0	7
F5	0	0	0	0	0	0	0	0	0	0	0	0	0	2	0	0	0	0	0	0	0	10	0	4
G#4	0	0	0	0	0	0	0	0	0	0	0	0	0	0	0	0	0	0	0	0	0	5	0	0
G#5	0	0	0	0	0	0	0	0	0	0	0	0	0	0	0	0	0	0	0	0	0	0	4	1
G4	0	0	0	0	0	0	0	0	0	0	0	0	0	0	0	0	0	0	0	0	0	0	0	3
ND	0	1	0	0	0	0	0	0	0	0	0	0	0	0	0	0	0	0	0	0	0	0	0	85

Figure 6. Confusion matrix of Transcribed Qanun part

The experiment conducted to transcribe qanun music yielded an accuracy of approximately 0.65, and the F1 score is 0.66, which, upon examination of the confusion matrix and results, was found to be implausible. Notably, a significant number of rests were transcribed instead of notes, primarily due to

the distinctive pitch characteristics of the qanun instrument. The limited sustain inherent to the qanun often renders the related sound imperceptible, leading to its transcription as a rest. Nevertheless, it is crucial to highlight that despite this limitation, the qanun music's transcribed sections successfully capture the melody's progression, which remains the most critical aspect in this context. The transcriptions effectively preserve the descriptive elements associated with the melody's development and trajectory. However, it is essential to acknowledge that the accuracy metric of 0.65 may not fully encompass the transcription's overall quality, particularly when a specific instrument or music-specific attributes have not been adequately accounted for.

The primary objective of the transcription process is to accurately track the progression of the melody and capture the temporal changes in notes. Figure 7 illustrates that, despite successfully identifying the overall melody progression in both measure 1 and measure 2, there are discrepancies in specific note durations.



Figure 7. Extract from the Qanun music.

In measure 1, for instance, the sustained C#4, which lasts for 16 sixteenth notes, is transcribed as 8 sixteenth notes followed by 8 rests. This transcription fails to represent the continuous nature of the note's duration accurately. Similarly, at the beginning of the second measure, the sustained Eb5, which endures 8 sixteenth notes, is transcribed in the correct time position. It is shown in the second box in Figure 7. However, it is represented as 3 sixteenth notes instead of the intended 8. This discrepancy disregards the sustained quality of the note and fails to capture its full duration.

As mentioned before, in the case of qanun music, the characteristic pitch of the instrument may lead to the transcriptions incorrectly identifying rests due to the lack of sustain in the instrument. Since the sustain is insufficient to sustain the sound, it is transcribed as a rest.

The primary focus of melody transcription lies in accurately capturing the progression of the melody. The events presented in Figure 7, while not impacting the recognition of the melody itself, significantly affect metrics such as the confusion matrix, as well as satisfaction measures like Accuracy and F1 scores. A specialized heuristic has been developed to solve this issue. At the core of this heuristic is a decision-making process based on probability metrics, particularly when determining the musical notes at the output layer in DNN. Here, the algorithm meticulously evaluates the likelihood of each possible note. The one with the highest probability score is typically selected as the most appropriate note value. However, the heuristic introduces a nuanced twist in scenarios where the output indicates a rest, which, in musical terms, means a pause or silence. Instead of automatically accepting this rest, the algorithm delves deeper, examining the probability value associated with the note immediately preceding the supposed rest. If this preceding note's probability value is found to be higher than that of any other outputs except the rest, the heuristic dynamically adjusts its decision. In this case, it opts to consider the preceding note as being more representative of the intended musical expression rather than the rest. The example illustrated in Figure 7 within the red box shows a probability value of 0.82 at the end of the duration of the quarter note for C3. Subsequently, the rest probabilities are 0.47, 0.52, 0.57, and 0.48, which are higher than all other note possibilities. Meanwhile, C3 exhibits probability values of 0.26, 0.26, 0.21, and 0.20 during this time, making them the second-highest probabilistic values identified by

the algorithm. Since the previous note value aligns with these second most probable notes over time, the algorithm decides to continue the note instead of replacing it with a rest value.

This heuristic evaluates whether rests are present in the music, considering the rapid decay attributes of the qanun instrument. This assessment is done without compromising the transcription accuracy of individual notes. After implementing this heuristic, the transcribed music played on the qanun has been regenerated and is displayed in Figure 8. Although the musical characteristics remain unchanged, there has been a notable improvement in both the F1 score and overall accuracy.

Comparison of Original and Transcribed Qanun of Composition 1



Figure 8. Transcription of Extracted Qanun from Composition 1

In this transcription:

The Accuracy : 0.9846153846153847 F1 Score : 0.9873858802696013 are calculated.

The confusion matrix is given in Figure 9

		Confusion Matrix of Actual and Transcribed in 16 th Notes																									
		A#4	A#5	A4	A5	B4	B5	C#4	C#5	C4	C5	C6	D#4	D#5	D4	D5	E4	E5	F#4	F#5	F4	F5	G#4	G#5	G4	N0	
Actual Notes	A#4	2	0	0	0	0	0	0	0	0	0	0	0	0	0	0	0	0	0	0	0	0	0	0	0	0	
	A#5	0	10	0	0	0	0	0	0	0	0	0	0	0	0	0	0	0	0	0	0	0	0	0	0	0	0
	A4	0	0	24	0	0	0	0	0	0	0	0	0	0	0	0	0	0	0	0	0	0	0	0	0	0	0
	A5	0	0	0	20	0	0	0	0	0	0	0	0	0	0	0	0	0	0	0	0	0	0	0	0	0	0
	B4	0	0	0	0	13	0	0	0	0	0	0	0	0	0	0	0	0	0	0	0	0	0	0	0	0	0
	B5	0	0	0	0	0	23	0	0	0	0	0	0	0	0	0	0	0	0	0	0	0	0	0	0	0	0
	C#4	0	0	0	0	0	0	16	0	0	0	0	0	0	0	0	0	0	0	0	0	0	0	0	0	0	0
	C#5	0	0	0	0	0	0	0	18	0	0	0	0	0	0	0	0	0	0	0	0	0	0	0	0	0	0
	C4	0	0	0	0	0	0	0	0	17	0	0	0	0	0	0	0	0	0	0	0	0	0	0	0	0	2
	C5	0	0	0	0	0	0	0	0	0	8	0	0	0	0	0	0	0	0	0	0	0	0	0	0	0	0
	C6	0	0	0	0	0	0	0	0	0	0	0	0	0	0	0	0	0	0	0	0	0	0	0	0	0	0
	D#4	0	0	0	0	0	0	0	0	0	0	0	5	0	0	0	0	0	0	0	0	0	0	0	0	0	0
	D#5	0	0	0	0	0	0	0	0	0	0	0	0	22	0	0	0	0	0	0	0	0	0	0	0	0	1
	D4	0	0	0	0	0	0	0	0	0	0	0	0	0	8	0	0	0	0	0	0	0	0	0	0	0	0
	D5	0	0	0	0	0	0	0	0	0	0	0	0	0	1	0	0	0	0	0	0	0	0	0	0	0	0
	E4	0	0	0	0	0	0	0	0	0	0	0	0	0	0	15	0	0	0	0	0	0	0	0	0	0	0
	E5	0	0	0	0	0	0	0	0	0	0	0	0	0	0	0	13	0	0	0	0	0	0	0	0	0	0
	F#4	0	0	0	0	0	0	0	0	0	0	0	0	0	0	0	0	21	0	0	0	0	1	0	0	0	0
	F#5	0	0	0	0	0	0	0	0	0	0	0	0	0	0	0	0	0	10	0	0	0	0	0	0	0	0
	F4	0	0	0	0	0	0	0	0	0	0	0	0	0	0	0	0	0	10	0	0	0	0	0	0	0	0
	F5	0	0	0	0	0	0	0	0	0	2	0	0	0	0	0	0	0	0	0	14	0	0	0	0	0	0
	G#4	0	0	0	0	0	0	0	0	0	0	0	0	0	0	0	0	0	0	0	0	5	0	0	0	0	0
	G#5	0	0	0	0	0	0	0	0	0	0	0	0	0	0	0	0	0	0	0	0	0	5	0	0	0	0
	G4	0	0	0	0	0	0	0	0	0	0	0	0	0	0	0	0	0	0	0	0	0	0	0	11	0	0
	N0	0	0	0	0	0	0	0	0	0	0	0	0	0	0	0	0	0	0	0	0	0	0	0	0	0	93

Figure 9. The Confusion matrix recalculated using heuristics.

The Oud part's transcription results exhibit a similar quality level as depicted in Figure 10. The evaluation of these results includes the calculation of Accuracy and F1 score metrics, which are considered impressive for assessing the performance of the transcription model. In this transcription: The Accuracy : 0.9894736842105263 F1 Score : 0.9918660287081339 are calculated.

The same experiments have been repeated randomly generated compositions and the results are shown in Table 1

Table 1. Quality Metrics of Transcription of Qanun and Oud in different compositions

	Qanun		Oud	
	Accuracy	F1 Measure	Accuracy	F1 Measure
Composition 1	0.984	0.987	0.989	0.991
Composition 2	0.991	0.990	0.987	0.989
Composition 3	0.989	0.991	0.994	0.997

Comparision of Original and Transcribed Oud of Composition 1



Figure 10. Comparison of Original and Transcribed Oud of Melody 1

To evaluate the effectiveness of the proposed model, we examined and trained the current state-of-the-art automatic music transcription models. One of the most significant challenges is that these models heavily rely on corpora based on Western music and Western instruments. For example, the commercially available Automatic Music Transcription software, AnthemScore 5 [20] attempted to transcribe the music shown in Figure 4, resulting in a highly inaccurate transcription, as depicted in Figure 11. In this software, the guitar is the closest instrument to the qanun and oud.

Composition 1 For Qanun And Oud



Figure 11. AnthemScore 5 output of Composition 1 For Qanun and Oud

Another well-known Automatic Music Transcription model, based on probabilistic latent component analysis using matrix factorization, developed by [21], was tested on the music shown in Figure 4. The output was a time series of probabilities for 80 different notes in matrix form. This matrix was then resolved, and the notes were configured. However, the model failed to separate the two instruments, and for each time sample, the most probable two note signatures were considered. The accuracy of this approach for the qanun was calculated as 0.342, and the F1 measure was calculated as 0.57, both of which are significantly lower than the proposed model.

4. CONCLUSION

In this research, an end-to-end automatic music transcription solution based on learning basic trained patterns has been formulated. The underlying motivation is to simulate the trained ear on specific instruments or combinations of instruments. Here, the test bench has been developed using the traditional Turkish instruments Qanun and Oud. The DNN has been trained by the basic combinations of those two instruments. Those multipitched and plucked instruments are highly susceptible to the early decay periods; however, an algorithm has also been devised to grasp the true melodic formations.

Recent developments in machine learning-based algorithms for automatic music transcription predominantly involve models trained on specific data structures. These models have been effectively applied to the analysis of Western music and the separation of Western instruments. However, the literature lacks a comprehensive corpus for authentic instruments such as the Qanun, Oud, Tambour, etc, The proposed work aims to address this gap by creating a dedicated corpus for these instruments and utilizing it for music transcription. Nonetheless, a notable limitation of the model is its dependency on the corpus for introducing and separating the instruments. Consequently, a model trained on a corpus created for instruments like the Qanun and Oud would not be applicable to the separation of other instruments.

In this research, different compositions with very complicated combinations of those instruments have been generated in polyphonic scope, and the transcription of two-part music related to two instruments has been obtained in a very satisfactory manner. Here, this approach is the fundamental step to identify a much more complex pattern regarding the Maqam, which depends on microtonal structures. In Maqam music, the whole interval has been separated into 5 to 9 microtones, and a half interval is divided into 4 microtonal intervals. This proposed approach will be improved to transcribe classical Turkish music.

The proposed approach, currently successful in transcribing complex Western music patterns, is expected to evolve and become capable of handling the sophisticated structures of classical Turkish music. This progression is not just a technical achievement but also an important cultural one. By improving the transcription of Maqam and other traditional Turkish music forms, this technology plays a vital role in preserving and promoting the understanding of Turkey's rich musical heritage. The ability to accurately transcribe and study these complex musical forms could open new avenues for musicological research and appreciation, bridging the gap between traditional musical art forms and modern technological advancements.

CONFLICT OF INTEREST

The authors declare that they have no conflict of interest regarding the publication of this article.

CRedit AUTHOR STATEMENT:

Emin Germen: Conceptualization, Methodology, Software, Formal Analyses, Writing, Validation, Investigation. **Can Karadoğan:** Conceptualization, Validation, Supervision, Resources.

REFERENCES

- [1] Benetos E, Dixon S, Duan Z, Ewert S. Automatic Music Transcription: An Overview. *IEEE Signal Process Mag.* 2019;36(1):20-30. doi:10.1109/MSP.2018.2869928
- [2] Bertin N, Badeau R, Richard G. Blind Signal Decompositions for Automatic Transcription of Polyphonic Music: NMF and K-SVD on the Benchmark. In: 2007 IEEE International Conference on Acoustics, Speech and Signal Processing - ICASSP '07. IEEE; 2007:I-65-I-68. doi:10.1109/ICASSP.2007.366617
- [3] Ansari S, Alatrany AS, Alnajjar KA, et al. A survey of artificial intelligence approaches in blind source separation. *Neurocomputing.* 2023;561:126895. doi:https://doi.org/10.1016/j.neucom.2023.126895
- [4] Munoz-Montoro AJ, Carabias-Orti JJ, Cabanas-Molero P, Canadas-Quesada FJ, Ruiz-Reyes N. Multichannel Blind Music Source Separation Using Directivity-Aware MNMF With Harmonicity Constraints. *IEEE Access.* 2022;10:17781-17795. doi:10.1109/ACCESS.2022.3150248
- [5] Uhlich S, Giron F, Mitsufuji Y. Deep neural network based instrument extraction from music. In: ICASSP, IEEE International Conference on Acoustics, Speech and Signal Processing - Proceedings. ; 2015. doi:10.1109/ICASSP.2015.7178348
- [6] Nishikimi R, Nakamura E, Goto M, Yoshii K. Audio-to-score singing transcription based on a CRNN-HSMM hybrid model. *APSIPA Trans Signal Inf Process.* 2021;10(1):e7. doi:10.1017/ATSIP.2021.4
- [7] Sigtia S, Benetos E, Boulanger-Lewandowski N, Weyde T, d'Avila Garcez AS, Dixon S. A hybrid recurrent neural network for music transcription. In: 2015 IEEE International Conference on Acoustics, Speech and Signal Processing (ICASSP). IEEE; 2015:2061-2065. doi:10.1109/ICASSP.2015.7178333

- [8] Sigtia S, Benetos E, Dixon S. An end-to-end neural network for polyphonic piano music transcription. *IEEE/ACM Trans Audio Speech Lang Process.* 2016;24(5):927-939. doi:10.1109/TASLP.2016.2533858
- [9] Seetharaman P, Pishdadian F, Pardo B. Music/Voice separation using the 2D fourier transform. In: *IEEE Workshop on Applications of Signal Processing to Audio and Acoustics.* ; 2017. doi:10.1109/WASPAA.2017.8169990
- [10] Huang P Sen, Chen SD, Smaragdis P, Hasegawa-Johnson M. Singing-voice separation from monaural recordings using robust principal component analysis. In: *ICASSP, IEEE International Conference on Acoustics, Speech and Signal Processing - Proceedings.* ; 2012. doi:10.1109/ICASSP.2012.6287816
- [11] Tervaniemi M. Musicians - Same or different. In: *Annals of the New York Academy of Sciences.* Vol 1169. ; 2009. doi:10.1111/j.1749-6632.2009.04591.x
- [12] Andrianopoulou M. *Aural Education: Reconceptualising Ear Training in Higher Music Learning.* Taylor & Francis; 2019. https://books.google.com.tr/books?id=p_S2DwAAQBAJ
- [13] Corey J. Technical ear training: Tools and practical methods. In: *Proceedings of Meetings on Acoustics.* Vol 19. AIP Publishing; 2013:025016-025016. doi:10.1121/1.4795853
- [14] Chabriel G, Kleinstuber M, Moreau E, Shen H, Tichavsky P, Yeredor A. Joint Matrices Decompositions and Blind Source Separation. *A Survey of Methods, Identification and Applications.* *Signal Processing Magazine, IEEE.* 2014;31:34-43. doi:10.1109/MSP.2014.2298045
- [15] Luo Z, Li C, Zhu L. A comprehensive survey on blind source separation for wireless adaptive processing: Principles, perspectives, challenges and new research directions. *IEEE Access.* Published online 2018. doi:10.1109/ACCESS.2018.2879380
- [16] LeCun Y, Bengio Y, Hinton G. Deep learning. *Nature.* 2015;521(7553):436-444. doi:10.1038/nature14539
- [17] Sigtia S, Benetos E, Boulanger-Lewandowski N, Weyde T, D'Avila Garcez AS, Dixon S. A hybrid recurrent neural network for music transcription. In: *ICASSP, IEEE International Conference on Acoustics, Speech and Signal Processing - Proceedings.* Vol 2015-August. *Institute of Electrical and Electronics Engineers Inc.;* 2015:2061-2065. doi:10.1109/ICASSP.2015.7178333
- [18] Brown J. Calculation of a Constant Q Spectral Transform. *Journal of the Acoustical Society of America.* 1991;89:425. doi:10.1121/1.400476
- [19] Giannakopoulos T, Pikrakis A. *Introduction to Audio Analysis: A MATLAB Approach.* Published online 2014:1-266. doi:10.1016/C2012-0-03524-7
- [20] AnthemScore 5 Music AI 2024. <https://www.lunaverus.com/>
- [21] Benetos E, Cherla S, Weyde T. An Efficient Shift-Invariant Model for Polyphonic Music Transcription. https://code.soundsoftware.ac.uk/projects/amt_mssiplca_fast



RESEARCH ARTICLE

IMPACT OF THE OBJECTIVE ATTRIBUTE WEIGHTING ON FIVE POPULAR MULTI-CRITERIA DECISION-MAKING METHODS: AN EMPIRICAL STUDY

Hamiyet MERKEPÇİ¹

¹ Department of Mathematics, Gaziantep University, Gaziantep, Turkey

hamiyetmerkepci@hotmail.com -  [0000-0003-4302-1162](https://orcid.org/0000-0003-4302-1162)

Abstract

In a Multi Criteria Decision Making (MCDM) problem, it is rarely possible to optimize all objectives simultaneously, since they can be contradictory, ambiguous or may involve other types of inconsistencies or uncertainties. Therefore, when trying to choose from a number of available alternatives, a decision maker is expected to assign weights to attributes whose values are utilized to evaluate the alternative under consideration for ranking. Attributes can be qualitative or quantitative, and their weights can be assigned by the decision maker in a somewhat subjective manner or algorithmically. In this paper, the impact of attribute weighting approaches on the ranking results across a number of widely used MCDM methods are discussed. That is, it examines how different weighting methods affect the results on the same multi-criteria decision-making methods when making a rating. In doing so, consider five MCDM methods, namely, Evamix, Aras, Topsis, Vikor, Waspas, under three different objective attribute weight assignment procedures, namely, Critic, Entropy, and Standart Deviation (SD). Results indicate that, in some cases, the employed attribute weight-assignment mechanism influences the rating results more heavily than the MCDM method itself. In other words, different MCDM methods tend to yield similar results under the same weight assignment method whereas, the same method produces more distinguishable results under different weighting schemes.

Keywords

Multi-Criteria Decision Making (Mcdm),
Critic,
Entropy,
Evamix,
Topsis,

Time Scale of Article

Received : 14 May 2024
Accepted : 18 September 2024
Online date : 30 September 2024

1. INTRODUCTION

Decision making has been becoming an increasingly more complex process in today's social and business environments where information and technology keep changing rapidly, thus, giving rise to more challenging problems across many diverse fields of study. Decision makers (DMs) who want to find the most effective option among a number of available alternatives need to consider multiple criteria that characterize an alternative for evaluation against the others. In doing so, a DM usually employs the following basic steps of decision analysis; defining the problem, listing all possible options, constructing the decision table showing the results of each option for each event, choosing a decision model, applying the model, and finally, choosing an option [47]. A decisive step in this process is the determination of the degree of importance of each criterion, since the ranking of the alternatives is heavily influenced by them. For this reason, a DM first should look at the nature of the problem in order to specify the most appropriate criteria and then determine the importance levels of the criteria by assigning weights to them. Basically, there are two ways to assign weights to criteria (also called attributes); the DM either assigns them drawing upon his personal experience and preferences, or uses an algorithm for the task. The first type of approaches is called subjective methods for obvious reasons. In contrast, the second

*Corresponding Author: hamiyetmerkepci@hotmail.com

type of so-called objective methods does not need any direct input from the DM, assuming that the required information to assign weights already exists in the decision matrix.

In this paper, when making a rating, it is examined how different weighting methods affect the results in the same multi-criteria decision-making methods. As the weight ratios and ranking methodology change, changes to the rankings are discussed. Three well-known objective weighting methods are used to assign weights to the selection criteria, namely CRITIC, Entropy and standard deviation (SD) methods. Then, using these weights, EVAMIX, ARAS, TOPSIS, VIKOR, and WASPAS methods are utilized for ranking the available alternatives. The data in the article are taken from Raymond Bissdorf's study titled "The Euro 2004 Best Poster Award (EBPA): Choosing The Best Poster in a Scientific Conference" [8]. This article is structured as follows: Section 2 and Section 3 briefly introduce the methods used in the study. Section 4 presents the Case study. Finally, Section 5 includes a discussion of the results and conclusions.

2. OBJECTIVE WEIGHT ASSIGNMENT METHODS

Before going into the details of the methods, first discuss what makes a criterion more important compared to the others. Intuitively, a criterion is more valuable to the DM if it helps her to remove a larger uncertainty towards a solution and, this happens only when the attribute values are well dispersed. Let us give an example to illustrate this point better. Suppose that you want to buy a house and your real-estate agent presents you with five alternatives, with price tags (all expressed in thousands of dollars) given as $A = (900, 700, 500, 300, 100)$. Depending on your budget, this set of values helps you a great deal (removes a lot uncertainty) in your analysis towards a decision. Now, assume that the price tags are presented as $B = (900, 895, 905, 910, 890)$. Since the values are not so much different, you obviously want to have a closer look at the values of the other attributes (number of rooms, number of bathrooms, distance to your work, distance to city center, quality of the district, etc.) before making a decision. In other words, the price attribute values of B do not remove as much uncertainty as the price attribute values of A. In general, all the objective weight assignment methods addressed in this paper, and most others, uses the capacity of the attribute to remove uncertainty (measured one way or the other) to assign weights; the higher the uncertainty removal capacity, the higher the weight. Note that, in the following we always use the normalized attribute values, so that commensurability holds to an acceptable degree across different value ranges.

Standard Deviation (SD) is a simple method that tries to measure the uncertainty removal capacity of a given attribute using standard deviation of the values, the expectation is being that a set of values with higher standard deviation values have a wider spread. Consequently, it assigns smaller weights to attributes with smaller standard deviation values. However, this expectation is not always justified and, its violation may lead to unexpected consequences, as we will demonstrate shortly.

Entropy was first defined by Rudolf Clausius in 1965 as a measure of disorder and uncertainty in a system [57]. Entropy is used to measure the amount of useful information provided by existing data [53]. The main feature of the entropy method is that it can make an objective weighting that can be acted upon directly on the data without the need for the judgments of the decision makers. However, it may not be as robust as expected.

CRITIC (The Criteria Importance Through Intercriteria Correlation) method was first introduced in [24]. It calculates weights by scaling the standard deviation of the attributes with the linear correlation coefficient between the alternatives in a multiplicative aggregation formulation. Despite its popularity, it is not a silver-bullet solution for all cases either. We will not discuss this subject here any further, but simply indicate that it extends the weight assignment problem beyond the sole domain of a single attribute to a more holistic level where correlation is involved.

Going back to our house-buying example, let us discuss further cases to demonstrate certain weaknesses in SD and Entropy methods. Note that, the formulation of entropy, as stated in the communication theory, uses only the probability of occurrences, not the actual values themselves, and, since in both cases there are five distinct values, their entropy will be the same. The dispersion characteristics of the actual values simply cannot be captured by this definition the entropy. For this reason, MCDM methods use normalized attribute values, instead of probability of occurrences. Consequently,

$$\begin{aligned} Entropy(A) &= Entropy ([0.36 \ 0.28 \ 0.20 \ 0.12 \ 0.04]) \\ &= -\frac{1}{\ln 5} (0.36 \times \ln 0.36 + 0.28 \times \ln 0.28 + 0.20 \times \ln 0.20 + 0.12 \times \ln 0.12 + 0.04 \times \ln 0.04) \\ &= 0.88807 \end{aligned}$$

In the same manner, we calculate Entropy(B)= 0.99998. Since weights are calculated according to (1 – Entropy) values, the highest weight goes to case A, as expected. Using the SD method, we calculate std(A)=0.11314 and std(B)= 0.0015713, indicating that the case A deserves much more weight; a result which complies with our expectations.

However, consider another case C = (900, 905, 500, 110, 100). A human quickly recognizes three groups in the data, which offers actually three choices; two homes approximately at 900, one home at 500 and two homes around 100 price range. Therefore, she can easily surmise that the case C is more helpful than case B but less so than case A. Consequently, we expect that the highest weight to be assigned to the attribute at case A, a lesser weight at case C and even lesser weight at case B. However, since the standard deviation of case C is std(C)= 0.14182, the highest weight goes to the case C. On the other hand, it is not a completely unexpected result if you are aware of the following fact from statistics: for bimodal distributions with two peaks, the standard deviation will increase as the spacing between peaks increases and, this is exactly what we did in case C. Similarly, Entropy(C) = 0.82066, again assigning the highest weight to the case C. Both results simply contradict the basic premise of understanding of the uncertainty removal capacity; the higher the weight, the better the dispersion.

The point of this discussion is to re-emphasize the fact that weighting is a difficult problem, which involves controversy and uncertainty [15]. So far, no overarching solution method has been proposed that can deliver optimum results in all possible cases. To address this issue, some authors have proposed hybrid or integrated approaches that combine the preferences of DMs with a decision matrix for obtaining the criteria weights, in order to take advantage of both method types. Others advocated solving MCDM scenarios initially without weights, and employing them only when the DM reckons that they are necessary in some criteria [38]. In any case, they seem to be claiming that the intervention of a DM is compulsory since the weight assignment process is an overly complex task, which cannot be fully automated.

3. MCDM METHODS

In this section, the five MCDM methods used in this article will be briefly introduced. Some references are provided to their various applications and refer the interested reader to Alinezhad's book where their mathematical formulations and numerical examples are conveniently provided in a single source [1].

EVAMIX (The EVAluation of MIXed data) method, introduced in 1982 by Voogd, has been applied to a diverse set of MCDM problems ever since [52]. Qureshi et al. [41] established a model for environmental and natural resource management using weighted total, expected value and EVAMIX methods. [34], Hajkovicz and Higgins [27] and Chung and Lee [20] analyzed water resources management projects with the EVAMIX method. Andalecio [2] evaluated seven different fishing strategies proposed by the municipality in the Philippines using Regime and EVAMIX methods. Chatterjee et al. [11] used COPRAS and EVAMIX methods in the complex material selection problem.

Dosal et al. [25] used EVAMIX, weighted total, ELECTRE II and Regime methods in site selection for recycling businesses. Chatterjee and Chakraborty [13] applied the EVAMIX method to select the non-traditional manufacturing process. Darji and Rao [21] used AHP and EVAMIX methods for appropriate material selection. Darji and Rao [22] solved the material selection problem in the sugar industry with the improved TODIM, ARAS, OCRA and EVAMIX methods. Chatterjee and Chakraborty [14] selected the best flexible manufacturing system for a manufacturing company with six MCDM methods, including EVAMIX.

ARAS (The Additive Ratio ASsessment) introduced by Zavadskas et al. [54] who modeled location selection problem for ports using Analytical Hierarchy Process (AHP) and Fuzzy ARAS methods. Medineckiene et al. [37] evaluated the sustainability of the buildings with ARAS. Stanujkic et al. [45] conducted studies with TOPSIS, VIKOR, MOORA, SAW, Gray Relational Analysis, COPRAS and ARAS methods. Turskis and Zavadskas [49] extended the ARAS method with Gray System Theory. Chatterjee and Chakraborty [12] handled the material selection decision problem using COPRAS and ARAS methods in their study. Reza and Majid [42] evaluated the use of Reliable Online Banking at the scale of financial institutions, using ARAS and Analytical Network Process (ANP) methods. Bakshi and Sarkar [6] used AHP and ARAS methods in their project selection performance evaluation decision problem. Ghadikolaie and Esbouei [26] used Fuzzy AHP and Fuzzy ARAS methods together for financial performance evaluation in their studies. Baležentis et al. [3] evaluated the sectors in the Lithuanian economy on the scale of financial ratios by using Fuzzy VIKOR, Fuzzy TOPSIS and Fuzzy ARAS methods. Sliogerience et al. [44] dealt with the problem of analysis and selection of energy production alternatives using AHP and ARAS methods. Shariati et al. [43] modeled the ARAS method for waste dump site selection in their study. They solved the decision problem by integrating fuzzy logic into a model named GARAS. Baležentis and Streimikienė [5] used TOPSIS and ARAS methods to determine the priorities of sustainable growth strategies for Lithuania. Kaklauskas et al. [29] developed a knowledge-based model for a standard home renovation and used the ARAS method to select the most ideal renovation project. Keršulienė and Turskis [30] used the Fuzzy ARAS method in the accounting department chief selection process for a business. Balezentiene and Kusta [4] determine the fuel type that will provide the most ideal gas emission for green houses by using the ARAS method. Stanujkic and Jovanovic [46] used the ARAS method for faculty web page quality measurement and evaluation.

TOPSIS (Technique of Order Preference by Similarity to the Ideal Solution) method is one of the most common methods among the MCDM, which has been applied for; evaluating the organizational performance of banks in capital management [16], multi-purpose inventory planning [17], evaluating the performance of insurance companies [28], the evaluation of the service quality of the banking sector [35], evaluating the service quality of hotel businesses [7], data mining [23] and, determining the facility location selection [18].

VIKOR (VlseKriterijuska Optimizacija I Komoromisno Resenje) method was first proposed by Opricovic and Tzeng [39] for multi-criteria optimization of complex systems. Tzeng et al. [51] used TOPSIS and VIKOR methods to evaluate bus fuels to be used in public transportation in Taiwan. Chu et al. [19] compared three methods: simple weighted average method (SAW), TOPSIS and VIKOR and discussed the applicability of these methods in group decision analysis in information societies. Opricovic and Tzeng [40] compared the extended VIKOR method with the TOPSIS, PROMETHEE and ELECTRE methods. Tong et al. [48] proposed the VIKOR method, which can take into account the variation in quality losses, for the optimization of multi-response processes. Liu and Yan [32] consider the VIKOR method to evaluate construction project proposals.

WASPAS (The Weighted Aggregates Sum Product Assessment) method has been applied in the solution of many decision-making problems due to its convenience. Zolfani et al. [58] proposed an integrated method based on SWARA and WASPAS methods for shopping mall location evaluation. Zavadskas et al. [56] evaluated the facade alternatives of four public and commercial buildings with

WASPAS and ratio method, reference point method and MOORA (Multi-Objective Optimization on the basis of Ratio Analysis) method based on multiplicative system. Madic et al. [33] made a multi-criteria economic analysis of various machine processes with WASPAS. Lashgari et al. [31] listed the outsourcing strategies in health care and selected the best of these strategies with the Quantitative Strategic Planning Matrix and WASPAS methods. Chakraborty and Zavadskas [10] have solved eight real selection problems that arise in production with the WASPAS method. Turskis et al. [50] combined fuzzy set theory with WASPAS. Chakraborty et al. [9] solved the parameter selection problems of non-traditional machine processes with the WASPAS method. Zavadskas et al. [55] solved the site selection problem for the waste incineration plant with a method called WASPAS-SVNS. Mathew et al. [36] used the WASPAS method in the selection of industrial robots

4. CASE STUDY

In this section, the effect of weighting methods in MCDM methods is discussed. The problem definition and relevant input data are taken from a study where 13 posters {P1, P2, P3, ..., P12, P13} are evaluated against four criteria {Scientific Quality (SQ), Contribution to OR Theory and/or Practice (TP), Originality (OR), Presentation Quality (PQ)} by five jury members {J1, J2, J3, J4, J5} for choosing the best poster in a scientific conference [8]. The scores given by the jury members are presented in Table 1. Note that, some scores are unevaluated by the jury members, which are denoted by a dash in the table

Table 1. The evaluation sheet used by the jury members.

Poster ID	Scientific Quality (SQ)					Contribution to Theory and/or Practice (TP)					Originality (OR)					Presentation Quality (PQ)				
	j ₁	j ₂	j ₃	j ₄	j ₅	j ₁	j ₂	j ₃	j ₄	j ₅	j ₁	j ₂	j ₃	j ₄	j ₅	j ₁	j ₂	j ₃	j ₄	j ₅
P1	4	7	5	5	3	4	7	6	5	3	4	6	6	7	3	4	7	5	6	2
P2	-	1	6	2	-	-	1	7	3	-	-	1	8	3	-	-	3	9	7	-
P3	6	6	7	6	2	8	9	7	6	4	6	7	7	7	5	6	6	9	7	5
P4	8	9	9	8	6	7	8	6	7	4	8	8	7	7	4	8	6	7	7	6
P5	8	6	8	7	2	8	7	9	7	0	8	5	7	7	2	8	8	8	6	5
P6	5	5	5	6	2	5	7	5	5	0	5	5	5	6	2	5	7	6	5	5
P7	6	5	6	6	-	7	8	7	6	-	6	5	5	6	-	8	8	5	3	-
P8	4	-	5	6	2	4	-	5	6	0	4	-	7	5	2	7	-	10	5	4
P9	-	-	5	3	-	-	-	5	3	-	-	-	7	3	-	-	-	10	3	-
P10	9	9	8	8	4	9	9	9	7	6	9	9	9	7	7	9	10	10	8	7
P11	6	9	8	7	5	6	8	6	6	5	6	9	7	8	5	8	9	8	7	3
P12	4	5	7	5	-	4	5	7	5	-	4	3	7	5	-	4	5	3	3	-
P13	4	8	8	8	8	4	8	8	7	10	4	6	7	7	8	4	9	9	8	10

Based on the evaluation sheet by the jury members, the author creates the decision matrix given in Table 2. An order of importance of the criteria was taken into consideration (SQ=0.4. TP=0.3. OR=0.2. PQ=0.1) and the score given by each jury member to each criterion is multiplied by these numbers. For the unevaluated values in Table 1, the arithmetic average of the scores given to each criterion by the other jury members is taken. Note that, this a decision matrix in which scores are already weighted. After an elaborate evaluation process, the author presents the ranking result as a partially ordered set (poset) in which p10 is the best , p9 is the worst and, the posters in the same equivalence class are denoted in curly braces: (p10, {p3, p4, p5, p12, p13}, p7, {p1, p6, p8, p11}, p2, p9).

Table 2. Decision Matrix

Poster ID	Scientific Quality					Contribution to Theory or Practice of OR					Originality					Presentation Quality				
	j ₁	j ₂	j ₃	j ₄	j ₅	j ₁	j ₂	j ₃	j ₄	j ₅	j ₁	j ₂	j ₃	j ₄	j ₅	j ₁	j ₂	j ₃	j ₄	j ₅
P1	1,6	2,8	2	2	1,2	1,2	2,1	1,8	1,5	0,9	0,8	1,2	1,2	1,4	0,6	0,4	0,7	0,5	0,6	0,2
P2	0,72	0,4	2,4	0,8	0,72	0,66	0,3	2,1	0,9	0,66	0,48	0,2	1,6	0,6	0,48	0,24	0,3	0,9	0,7	0,24
P3	2,4	2,4	2,8	2,4	0,8	2,4	2,7	2,1	1,8	1,2	1,2	1,4	1,4	1,4	1	0,6	0,6	0,9	0,7	0,5
P4	3,2	3,6	3,6	3,2	2,4	2,1	2,4	1,8	2,1	1,2	1,6	1,6	1,4	1,4	0,8	0,8	0,6	0,7	0,7	0,6
P5	3,2	2,4	3,2	2,8	0,8	2,4	2,1	2,7	2,1	0	1,6	1	1,4	1,4	0,4	0,8	0,8	0,8	0,6	0,5
P6	2	2	2	2,4	0,8	1,5	2,1	1,5	1,5	0	1	1	1	1,2	0,4	0,5	0,7	0,6	0,5	0,5
P7	2,4	2	2,4	2,4	1,84	2,1	2,4	2,1	1,8	1,68	1,2	1	1	1,2	0,88	0,8	0,8	0,5	0,3	0,42
P8	1,6	1,36	2	2,4	0,8	1,2	0,9	1,5	1,8	0	0,8	0,72	1,4	1	0,4	0,7	0,5	1	0,5	0,4
P9	0,64	0,64	2	1,2	0,64	0,48	0,48	1,5	0,9	0,48	0,4	0,4	1,4	0,6	0,4	0,2	0,2	1	0,3	0,2
P10	3,6	3,6	3,2	3,2	1,6	2,7	2,7	2,7	2,1	1,8	1,8	1,8	1,8	1,4	1,4	0,9	1	1	0,8	0,7
P11	2,4	3,6	3,2	2,8	2	1,8	2,4	1,8	1,8	1,5	1,2	1,8	1,4	1,6	1	0,8	0,9	0,8	0,7	0,3
P12	1,6	2	2,8	2	1,68	1,2	1,5	2,1	1,5	1,26	0,8	0,6	1,4	1	0,76	0,4	0,5	0,3	0,3	0,24
P13	1,6	3,2	3,2	3,2	3,2	1,2	2,4	2,4	2,1	3	0,8	1,2	1,4	1,4	1,6	0,4	0,9	0,9	0,8	1

At this stage, the ready weighted decision matrix is taken and the importance weights of the criteria for each jury member are calculated using Standard Deviation (SD), Entropy and Critic methods (Table 3).

Table 2. Decision Matrix

	j1	j2	j3	j4	j5	
SD	SQ	0,91182	1,06725	0,57467	0,73867	0,78665
	TP	0,69621	0,82323	0,41324	0,41602	0,85928
	OR	0,43155	0,50442	0,21363	0,31622	0,39416
	PQ	0,23706	0,23669	0,22560	0,18327	0,22983
Entropy	SQ	0,27135	0,28248	0,22080	0,30439	0,18288
	TP	0,2631	0,27351	0,19886	0,18331	0,50303
	OR	0,22672	0,27885	0,11777	0,21219	0,15524
	PQ	0,23881	0,16515	0,46255	0,30010	0,15883
CRITIC	SQ	0,16316	0,22459	0,27536	0,16951	0,25211
	TP	0,25408	0,2525	0,26064	0,19844	0,19686
	OR	0,17441	0,23028	0,16456	0,19165	0,20837
	PQ	0,40835	0,29263	0,29944	0,4404	0,34266

Table 3. Importance weights of criteria by objective methods.

At this point, recall the basic operating principle of all objective weight assignment methods; objective methods are utilized to prevent human-made instabilities and obtain results that are more realistic. The objective methods use mathematical models and only data within the decision matrix assuming that all the required information to assign weights properly already exists in the decision matrix, thus without needing to consider the preferences of decision makers. While the decision matrix is constructed, an order of importance of the criteria is imposed upon the alternatives. Therefore, when weights are assigned to attributes using the Standard Deviation, Entropy and Critic methods, one would expect the already imposed importance pattern (SQ > TP > OR > PQ) to emerge more clearly in the result. Table 4 which summarizes the results in Table 3, shows that this is not always the case.

Table 4. Order of importance according to the three objective weighting methods

	j1	j2	j3	j4	j5
SD	SQ > TP > OR > PQ	SQ > TP > OR > PQ	SQ > TP > OR > PQ	SQ > TP > OR > PQ	TP > SQ > OR > PQ
Entropy	SQ > TP > PQ > OR	SQ > OR > TP > PQ	PQ > SQ > TP > OR	SQ > PQ > OR > TP	TP > SQ > PQ > OR
CRITIC	PQ > TP > OR > SQ	PQ > TP > OR > SQ	PQ > SQ > TP > OR	PQ > TP > OR > SQ	PQ > SQ > OR > TP

The Standard Deviation, Entropy and Critic methods have quite different indicators about the relative importance of the four criteria. Whatever importance information already present in the raw data or imposed by the multiplication operation seemed to be caught only by the SD method in a consistent manner. The minor discrepancy observed for J5 (TP and SQ switched places) can be attributed to the fact J5 did not specify any scores for many attributes and those are replaced by the averages. For Entropy method, three of the four criteria are indicated by the scores of different jurors as the most important one, with the exception of OR. Critic method has the greatest consistency, regarding the most important criterion, which is indicated as PQ by all five jurors. Since multiplication coefficient for PQ was the smallest (0.1), It is suspected that there must be a strong correlation between the alternatives for such a result to occur. Now apply the five MCDM methods, for a discussion of the magnitude of possible effects of weighting on them. First starts with no weighting condition (in fact, all four criteria are assigned a weight of 0.25 equally to avoid duplicating the code).

Table 5. Ranking of alternatives with no weights

Order Method	1st	2nd	3rd	4th	5th	6th	7th	8th	9th	10th	11th	12th	13th
EVAMIX	P8	P2	P10	P9	P6	P11	P3	P5	P1	P13	P4	P7	P12
ARAS	P10	P13	P4	P11	P3	P5	P7	P1	P6	P12	P8	P2	P9
TOPSIS	P10	P13	P4	P11	P5	P3	P7	P1	P6	P8	P12	P2	P9
WIKOR	P10	P13	P4	P11	P5	P3	P7	P1	P6	P8	P12	P2	P9
WASPAS	P10	P13	P4	P11	P3	P5	P7	P1	P6	P12	P8	P2	P9

In this case, all methods seem to be in complete agreement, with the exception Evamix method. In fact, they are exactly the same if allow only two of them to switch the places of the 5th and 6th posters, and places of the 10th and 11th posters. Recall the ranking poset that was produced by Bisdorff, which was (p10, {p3, p4, p5, p12, p13}, p7, {p1, p6, p8, p11}, p2, p9). Reordering the posters in the equivalence classes as (p10, {p13, p4, p5, p12, p3}, p7, {p1, p6, p8, p11}, p2, p9). You see that the first three and last two posters are the same. At this point It can be state that four out of five MCDM methods give very close results, and any inconsistencies that may arise later can be attributed to the feature weighting method used, which will be discussed in the next section.

First, apply the SD method (Table 6).

Table 6. Ranking of alternatives by SD method

Order Method	1st	2nd	3rd	4th	5th	6th	7th	8th	9th	10th	11th	12th	13th
EVAMIX	P13	P10	P1	P4	P3	P11	P5	P2	P7	P12	P6	P8	P9
ARAS	P10	P13	P4	P11	P5	P3	P7	P1	P12	P6	P8	P2	P9
TOPSIS	P10	P13	P4	P11	P5	P3	P7	P12	P1	P6	P8	P2	P9
WIKOR	P10	P13	P4	P11	P5	P3	P7	P12	P1	P6	P8	P2	P9
WASPAS	P10	P13	P4	P11	P5	P3	P7	P1	P6	P12	P8	P2	P9

The SD method increased the uniformity among the results of the four methods even further. Now we have a complete match in 10 places out of 13. Even the Evamix agrees about last place. In short, SD method served to diminish the differences between methods.

Next, apply the Entropy method (Table 7).

Table 7. Ranking of alternatives by the Entropy method

Order Method	1 st	2 nd	3 rd	4 th	5 th	6 th	7 th	8 th	9 th	10 th	11 th	12 th	13 th
EVAMIX	P10	P13	P4	P11	P5	P3	P7	P1	P8	P6	P12	P2	P9
ARAS	P10	P13	P4	P11	P3	P5	P7	P1	P6	P8	P12	P2	P9
TOPSIS	P10	P13	P11	P4	P3	P5	P7	P1	P6	P8	P12	P2	P9
WIKOR	P10	P13	P11	P4	P3	P5	P7	P1	P6	P8	P12	P2	P9
WASPAS	P10	P13	P4	P11	P3	P5	P7	P1	P6	P8	P12	P2	P9

The overall agreement between the results becomes even more pronounced. Aras-Waspas and Topsis-Vikor pairs exhibit a complete match between themselves. The most striking difference is observed in the behavior of Evamix that matches the rankings of the other four methods in 7 out of 13 places. Allowing four pair wise switching of places in three methods, the consensus among the methods will be complete. In other words, the methods will deliver the most similar rankings using the weights produces by the Entropy method.

Lastly, apply the Critic method (Table 8).

Table 8. Ranking of alternatives by the CRITIC method

Order Method	1 st	2 nd	3 rd	4 th	5 th	6 th	7 th	8 th	9 th	10 th	11 th	12 th	13 th
EVAMIX	P10	P13	P4	P5	P11	P3	P7	P8	P6	P1	P2	P12	P9
ARAS	P10	P13	P4	P11	P5	P3	P7	P1	P6	P8	P12	P2	P9
TOPSIS	P10	P13	P4	P11	P5	P3	P7	P6	P8	P1	P12	P2	P9
WIKOR	P10	P13	P4	P11	P3	P5	P7	P1	P6	P8	P12	P2	P9
WASPAS	P10	P13	P4	P11	P3	P5	P7	P1	P6	P8	P12	P2	P9

The weights calculated by the Critic method allow all methods, without exception, to deliver equal rankings in the top three places. This implies the existence of some underlying correlation between the alternatives, which only the Critic method is able to extract from the decision matrix.

So far, some changes in the behavior of MCDM methods resulting from the use of different weighting methods have been observed. It will now be discussed how their significance compares with the significance of the differences that may arise in the rankings of a particular MCDM method under SD, Entropy and Critical method. (Table 9, Table 10, Table 11, Table 12, Table 13).

Table 9. EVAMIX

Order Method	1 st	2 nd	3 rd	4 th	5 th	6 th	7 th	8 th	9 th	10 th	11 th	12 th	13 th
CRITIC	P10	P13	P4	P5	P11	P3	P7	P8	P6	P1	P2	P12	P9
ENTROPY	P10	P13	P4	P11	P5	P3	P7	P1	P8	P6	P12	P2	P9
SD	P13	P10	P1	P4	P3	P11	P5	P2	P7	P12	P6	P8	P9

Table 10. ARAS

ARAS	Order	1st	2nd	3rd	4th	5th	6th	7th	8th	9th	10th	11th	12th	13th
	Method													
	CRITIC	P10	P13	P4	P11	P5	P3	P7	P1	P6	P8	P12	P2	P9
	ENTROPY	P10	P13	P4	P11	P3	P5	P7	P1	P6	P8	P12	P2	P9
	SD	P10	P13	P4	P11	P5	P3	P7	P1	P12	P6	P8	P2	P9

Table 11. TOPSIS

TOPSIS	Order	1st	2nd	3rd	4th	5th	6th	7th	8th	9th	10th	11th	12th	13th
	Method													
	CRITIC	P10	P13	P4	P11	P5	P3	P7	P6	P8	P1	P12	P2	P9
	ENTROPY	P10	P13	P11	P4	P3	P5	P7	P1	P6	P8	P12	P2	P9
	SD	P10	P13	P4	P11	P5	P3	P7	P12	P1	P6	P8	P2	P9

Table 12. VIKOR

VIKOR	Order	1st	2nd	3rd	4th	5th	6th	7th	8th	9th	10th	11th	12th	13th
	Method													
	CRITIC	P10	P13	P4	P11	P3	P5	P7	P1	P6	P8	P12	P2	P9
	ENTROPY	P10	P13	P11	P4	P3	P5	P7	P1	P6	P8	P12	P2	P9
	SD	P10	P13	P4	P11	P5	P3	P7	P12	P1	P6	P8	P2	P9

Table 13. WASPAS

WASPAS	Order	1st	2nd	3rd	4th	5th	6th	7th	8th	9th	10th	11th	12th	13th
	Method													
	CRITIC	P10	P13	P4	P11	P3	P5	P7	P1	P6	P8	P12	P2	P9
	ENTROPY	P10	P13	P4	P11	P3	P5	P7	P1	P6	P8	P12	P2	P9
	SD	P10	P13	P4	P11	P5	P3	P7	P1	P6	P12	P8	P2	P9

Examination of Tables 9-13 reveals the following observations:

- Evamix has only one match across its own rankings under three weighting methods (Table 9). Thus, it is the most sensitive method to the selected weighting assignment mechanism.
- Aras and Waspas exhibit no significant changes in rankings under three weighting methods (Table 10 and Table 13). Its rankings are more similar to each other under the Entropy and Critic methods, while SD ranking differs from these to a greater extent.
- The agreement between the rankings of Aras and Vikor are less than those of Aras and Waspas (5 places vs. 8 and 9). Interestingly, the Critic ranking of Topsis agrees with its SD ranking at four more places, as opposed to Entropy. This behavior is unique among the cases considered here.

5. CONCLUSION

This article considers five potential preference ranking-based methods and compares ranking performances and the effect of criterion weights on preferences for ranking posters at a scientific conference. The performance tests conducted for ranking performance comparison and to measure the degree of concordance between the rankings in a quantitative manner are provided in the Appendix. Based on these test results, it can be stated that objective attribute weighting methods have a strong impact on the rankings produced by different MCDM methods, albeit some are more sensitive than the others are. In almost all cases (with a single exception), all MCDM-weighting method combinations agree on that P10 is the best poster, and (without any exception) P9 is the worst one. If one is only interested in finding the best or worst alternative, there is no difference between combinations. However, if whole ranking is important, we propose that DM should construct the Table 4 for its own data and inspect the order of importance implied therein to choose those MCDM-weighting method combinations that matches best to the order of importance that she has in mind. Such an approach produces more rational and justified rankings.

ACKNOWLEDGEMENTS

The author expresses his gratitude to the editor for providing valuable assistance throughout the publication process.

CONFLICT OF INTEREST

The author stated that there are no conflicts of interest regarding the publication of this article.

CRedit AUTHOR STATEMENT

Hamiyet Merkepci: Formal analysis, Visualization, Writing, Original Draft, Review & Editing, Conceptualization.

REFERENCES

- [1] Alinezhad A, Khalili J. *New Methods and Applications in Multiple Attribute Decision Making (MADM)*, Springer, 2019.
- [2] Andalecio MN. Multi-criteria decision models for management of tropical coastal fisheries. A review. *Agronomy for Sustainable Development*, 2010; 30, 557–580.
- [3] Baležentis A, Baležentis T, Misiunas A. An integrated assessment of Lithuanian economic sectors based on financial ratios and fuzzy MCDM methods. *Technological and Economic Development of Economy*, 2012; 18(1), 34-53.
- [4] Baležentienė L, Kusta A. Reducing greenhouse gas emissions in grassland ecosystems of the central Lithuania: multi-criteria evaluation on a basis of the ARAS method. *The Scientific World Journal*, 2012.
- [5] Baležentis A, Štreimikienė D. Integrated Sustainability Index: the Case Study of Lithuania. *Intelektinė ekonomika*, 2013; 7 (3), 289-303.

- [6] Bakshi T, Sarkar B. MCA based performance evaluation of project selection. arXiv preprint arXiv:1105.0390, 2011.
- [7] Benitez JM, Martin JC, Roman C. Using Fuzzy Number For Measuring Quality Of Service In The Hotel Industry. *Tourism Management*, 2007; 28(2), 544–555.
- [8] Bisdorff R., et al. Evaluation and decision models with multiple criteria. Berlin: Springer, 2015.
- [9] Chakraborty S, Bhattacharyya O, Zavadskas EK, Antucheviciene J. Application of WASPAS method as an optimization tool in non-traditional machining processes. *Information Technology and Control*, 2015; 44(1), 77-88.
- [10] Chakraborty S, Zavadskas EK. Applications of WASPAS method in manufacturing decision making. *Informatica*, 2014; 25(1), 1–20.
- [11] Chatterjee P, Athawale VM., Chakraborty S. Materials selection using complex proportional assessment and evaluation of mixed data methods. *Materials and Design*, 2011; 32, 851–860.
- [12] Chatterjee P, Chakraborty S. Gear Material Selection using Complex Proportional Assessment and Additive Ratio Assessment-based Approaches: A Comparative Study. *International Journal of Materials Science and Engineering*, 2013; 1(2), 104-111.
- [13] Chatterjee P, Chakraborty S. Nontraditional machining processes selection using evaluation of mixed data method. *International Journal Advanced Manufacturing Technology*, 2013; 68, 1613–1626.
- [14] Chatterjee P, Chakraborty S. Flexible manufacturing system selection using preference ranking methods: A comparative study. *International Journal of Industrial Engineering Computations*, 2014; 5, 315–338.
- [15] Chen YC, Shi Y, et al. Fuzzy MCDM technique for planning the environment watershed, In *Cutting-edge research topics on multiple criteria decision making*, Berlin, Heidelberg: Springer, 2009; 744–752.
- [16] Cheng RW, Tsai LC., TSAI Pei Hsuan. Financial Service of Wealth Management Banking: Balanced Scorecard Approach. *Journal of Social Sciences*, 2008; 4 (4), 255-263.
- [17] Tsou CS. Multi-Objective Inventory Planning Using MOPSO And TOPSIS. *Expert Systems With Applications*, 2008; 35, 136-142.
- [18] Chu TC. Facility Location Selection Using Fuzzy TOPSIS Under Group Decisions. *International Journal Of Uncertainty. Fuzziness and Knowledge Based Systems*, 2002; 10 (6) 687–701.
- [19] Chu MT, Shyu J, Tzeng GH, Khosla R. Comparison Among Three Analytical Methods for Knowledge Communities Group-Decision Analysis. *Expert Systems with Applications*, 2007; 33, 1011–1024.
- [20] Chung ES, Lee KS. Identification of spatial ranking of hydrological vulnerability using multi-criteria decision making techniques: case study of Korea. *Water Resour Manage*, 2009; 23, 2395–2416.

- [21] Darji VP, Rao RV. Application of AHP/EVAMIX method for decision making in the industrial environment. *American Journal of Operations Research*, 2013; 3, 542-569.
- [22] Darji VP, Rao RV. Intelligent Multi Criteria Decision Making Methods for Material Selection in Sugar Industry. *Procedia Materials Science*, 2014; 5, 2585 –2594.
- [23] Dashti Z, Pedram MM., Shanbehzadeh J. A Multi-Criteria Decision Making Based Method For Ranking Sequential Patterns. *International MultiConference Of Engineers And Computers Scientists March 17-19, 2010*; I, 611-614.
- [24] Diakoulaki D., Mavrotas G., Papayannakis L. Determining objective weights in multiple criteria problems: the CRITIC method. *Computers & Operations Research*, 1995; 22(7), 763–770.
- [25] Dosal E, Coronado M, Muñoz I, Viguri R, Andrés A, Application of multi-criteria decision-making tool to locate construction and demolition waste (C&DW) recycling facilities in a Northern Spanish Region. *Environmental Engineering and Management Journal*, 2012; 11(3), 545-556.
- [26] Ghadikolaei AS, Esbouei SK. Integrating Fuzzy AHP and Fuzzy ARAS for evaluating financial performance. *Boletim da Sociedade Paranaense de Matemática*, 2014; 32(2), 163-174.
- [27] Hajkowicz S, Higgins A, A comparison of multiple criteria analysis techniques for water resource management. *Euro J Oper Res*, 2008; 184, 255–265.
- [28] Hui Yin, Bao-Huey, Wang Huang, An Siou. Combining ANP And TOPSIS Concepts For Evaluation The Performance Of Property-Liability Insurance Companies. *Journal Of Social Sciences*, 2008; 4 (1), 56-61.
- [29] Kaklauskas A. Tupenaite L, Kanapeckiene L, Naimaviciene J. Knowledge-based model for standard housing renovation. *Procedia Engineering*, 2013; 57, 497-503.
- [30] Keršulienė V, Turskis Z. An integrated multi-criteria group decision making process: selection of the chief accountant. *Procedia-Social and Behavioral Sciences*, 2014; 110, 897-904.
- [31] Lashgari S, Antuchevičienė J, Delavari A, Kheirkhah O. Using QSPM and WASPAS methods for determining outsourcing strategies. *Journal of Business Economics and Management*, 2014; 15(4), 729-743.
- [32] Liu H, Yan T. Bidding-Evaluation of Construction Projects Based on VIKOR Method. *Proceedings of the IEEE International Conference on Automation and Logistics*. Jinan, China, 2007.
- [33] Madić M, Gecevska V, Radovanović M, Petković D. Multi-criteria economic analysis of machining processes using the WASPAS method. *Journal of Production Engineering*, 2014; 17(2), 79-82.
- [34] Maimone M. Multi-criteria evaluation techniques in water resource planning. *Universities Council on Water Resources in American Water Resources Association Technical Publication Series*. 2001; 227-232.

- [35] Manabendra N, Choudhury PK. Exploring The Dimensionality Of Service Quality: An Application Of TOPSIS In The Indian Banking Industry. *Asia-Pacific Journal of Operational Research*, 2009; 26(1), 115- 133.
- [36] Mathew M, Sahu S, Upadhyay AK. Effect of normalization techniques in robot selection using weighted aggregated sum product assessment. *International Journal of Innovative Research and Advanced Studies (IJIRAS)*, 2017; 4(2), 59-63.
- [37] Medineckiene M, Zavadskas EK, Björk F, Turskis Z. Multi-criteria decision-making system for sustainable building assessment/certification. *Archives of Civil and Mechanical Engineering*, 2015; 15(1), 11-18.
- [38] Nolberto M, et al. *Strategic Approach in Multi-Criteria Decision Making : A Practical Guide for Complex Scenarios*, Springer, 2019: ProQuest Ebook Central, <http://ebookcentral.proquest.com/lib/polije-ebooks/detail.action?docID=5654954>.
- [39] Opricovic S, Tzeng GH., Compromise Solution by MCDM Methods: a Comparative Analysis of VIKOR and TOPSIS. *European Journal of Operational Research*, 2004; 156, 445-455.
- [40] Opricovic S, Tzeng GH. Extended VIKOR Method in Comparison with Other Outranking Methods. *European Journal of Operational Research*, 2007; 178, 514-529.
- [41] Qureshi ME, Harrison SR, Wegener MK. Validation of multicriteria analysis model. *Agriculture Systems*, 1999; 62, 105-116.
- [42] Reza S, Majid A. Ranking Financial Institutions Based on of Trust in online banking Using ARAS and ANP Method. *International Research Journal of Applied and Basic Sciences*. 2013; 6 (4), 415-423.
- [43] Shariati S, Yazdani-Chamzini A, Salsani A, Tamošaitienė J. Proposing a New Model for Waste Dump Site Selection: Case Study of Ayerma Phosphate Mine. *Engineering Economics*, 2014; 25(4). 410-419.
- [44] Sliogeriene J, Turskis Z, Streimikiene D. Analysis and choice of energy generation technologies: the multiple criteria assessment on the case study of Lithuania. *Energy Procedia*, 2013; 32, 11-20.
- [45] Stanujkic D, Djordjevic B, Djordjevic M. Comparative analysis of some prominent MCDM methods: A case of ranking Serbian banks. *Serbian Journal of Management*, 2013; 8(2), 213-241.
- [46] Stanujkic D, Jovanovic R. Measuring a Quality of Faculty Website Using ARAS Method. *Contemporary Issues In Business. Management And Education* 2012 ISSN 2029-7963/ISBN 978-609-457-323-1 doi:10.3846/cibme, 2012; 45.
- [47] Tekin M. *Üretim Yönetimi. Artı Ofset*, Konya, 1996; 1-16.
- [48] Tong LI, Chen CC, Wang CH. Optimization of Multi-Response Processes Using the VIKOR Method. *International Journal of Advanced Manufacturing Technology*, 2007; 31, 1049–1057.
- [49] Turskis Z, Zavadskas EK. A novel method for multiple criteria analysis: grey additive ratio assessment (ARAS-G) method. *Informatika*, 2010; 21(4), 597-610.

- [50] Turskis Z, Zavadskas EK, Antucheviciene J, Kosareva N. A hybrid model based on fuzzy AHP and fuzzy WASPAS for construction site selection. *International Journal of Computers Communications & Control*, 2015; 10(6), 873-888.
- [51] Tzeng GH, Lin CW, Opricovic S. Multi Criteria Analysis of Alternative-Fuel Buses for Public Transportation. *Energy Policy*, 2005; 33, 1373-1383.
- [52] Voogd H. Multicriteria evaluation with mixed qualitative and quantitative data. *Environment and Planning B: Planning and Design*, 1982; 9(2), 221–236.
- [53] Wu Z, Sun J, Liang L, Zha Y. Determination of weights for ultimate cross efficiency using Shannon entropy. *Expert Systems with Applications*, 2011; 38, 5162-5165.
- [54] Zavadskas EK, Antucheviciene J, Šaparauskas J, Zenonas Turskis Z. Multicriteria assessment of facades' alternatives: peculiarities of ranking methodology. *Procedia Engineering*, 2013; 57, 107 – 112.
- [55] Zavadskas EK, Baušys R, Lazauskas M. Sustainable assessment of alternative sites for the construction of a waste incineration plant by applying WASPAS method with single-valued neutrosophic set. *Sustainability*, 2015; 7, 15923–15936.
- [56] Zavadskas EK, Turskis Z, Vilutiene T. Multiple criteria analysis of foundation instalment alternatives by applying Additive Ratio Assessment (ARAS) method. *Archives of civil and mechanical engineering*, 2010; 10(3), 123-141.
- [57] Zhang H, Gu CL, Gu LW, Zhang Y The evaluation of tourism destination competitiveness by TOPSIS & information ENTROPY - A case in the Yangtze River Delta of China. *Tourism Management*, 2011; 32, 443-451.
- [58] Zolfani SH, Aghdaie MH, Derakhti A, Zavadskas EK, Varzandeh MHM. Decision making on business issues with foresight perspective; an application of new hybrid MCDM model in shopping mall locating. *Expert systems with applications*, 2013; 40(17), 7111-7121.

APPENDIX: Performance tests conducted for ranking performance comparison and for measuring the degree of concordance between the rankings.

Tests are conducted using the methodology described in [14]. The test results are provided in the form of value tuples where

- (a) Spearman's rank correlation coefficient: Using Spearman's rank correlation coefficient (r_s) value, the similarity between two sets of rankings can be measured. Usually, its value lies between -1 and $+1$, where the value of $+1$ denotes a perfect match between two rank orderings.
- (b) Agreement between the top three ranked alternatives: Here, a result of (1,2,3) means the first, second and third ranks match; (1,2,#) means the first and second ranks match; (1,#,#) means only the first ranks match; and (#,#,#) means no match.
- (c) The last test is performed with respect to the number of ranks matched, expressed as the percentage of the number of alternatives considered.

Test 1: (For Table 6)

Method	Aras	Topsis	Vikor	Waspas
Evamix	0.96704, (1,2,3),53.8	0.98352, (1,2,3),53.8	0.98352, (1,2,3), 76.9	0.95605, (1,2,3), 46.2
Aras		0.98352, (1,2,3), 76.9	0.98352, (1,2,3), 53.8	0.99451,(1,2,3), 84.6
Topsis			0.98352, (1,2,3), 53.8	0.97528,(1,2,3), 61.5
Vikor				0.97253,(1,2,3), 46.2

Test 2: (For Table 7)

Method	Aras	Topsis	Vikor	Waspas
Evamix	0.98902, (1,2,3), 69.2	0.98352, (1,2,#), 53.8	0.98352, (1,2,#), 53.8	0.98902, (1,2,3), 69.2
Aras		0.99451, (1,2,#), 84.6	0.99451, (1,2,#), 84.6	1,(1,2,3), 100
Topsis			1, (1,2,3), 100	0.99451,(1,2,#), 84.6
Vikor				0.99451,(1,2,#), 84.6

Test 3: (For Table 8)

Method	Aras	Topsis	Vikor	Waspas
Evamix	0.83517, (##,##), 7.69	0.79671, (##,##), 7.69	0.79671, (##,##), 7.69	0.82968, (##,##), 15.3
Aras		0.99451, (1,2,3), 84.6	0.99451, (1,2,3), 84.6	0.99451,(1,2,3), 84.6
Topsis			1, (1,2,3), 100	0.98352,(1,2,3), 76.9
Vikor				0.98352,(1,2,3), 76.9

Test 4: (For Table 9)

Method	Entropy	SD
Critic	0.97252, (1,2,3), 46,15	0.72527, (##,##), 7,69
Entropy		0.81318,(##,##), 7,69

Test 5: (For Table 10)

Method	Entropy	SD
Critic	0.99746, (1,2,3), 84,61	0.98351, (1,2,3), 76,92
Entropy		0.97802,(1,2,3), 61,53

Test 6: (For Table 11)

Method	Entropy	SD
Critic	0.97252, (1,2,#), 46,15	0.95054, (1,2,3), 69,23
Entropy		0.95604,(1,2,#), 38,46

Test 7: (For Table 12)

Method	Entropy	SD
Critic	0.99450, (1,2,#), 84,61	0.96153, (1,2,3), 53,84
Entropy		0.95604,(1,2,#), 38,46

Test 8: (For Table 13)

Method	Entropy	SD
Critic	1 (1,2,3), 100	0.98901, (1,2,3), 69,23
Entropy		0.98901,(1,2,3), 69,23



RESEARCH ARTICLE

NUMERICAL SOLUTIONS OF BOUSSINESQ TYPE EQUATIONS BY MESHLESS METHODS

Murat ARI^{1,*}, Yılmaz DERELİ²

¹ Department of Mathematics, Kamil Özdağ Science Faculty, Karamanoğlu Mehmetbey University, Karaman, Turkey
muratari@kmu.edu.tr - [0000-0002-4039-5970](https://orcid.org/0000-0002-4039-5970)

² Department of Mathematics, Faculty of Science, Eskişehir Technical University, Eskişehir, Türkiye
ydereli@eskisehir.edu.tr - [0000-0003-0149-0542](https://orcid.org/0000-0003-0149-0542)

Abstract

In this paper, two different meshfree method with radial basis functions (RBFs) is proposed to solve Boussinesq-type (Bq) equations. The basic conservative properties of the equation are investigated by computing the numerical values of the motion's invariants. The accuracy of the method is tested using computational tests to simulate solitary waves in terms of L_∞ error norm. The outcomes are contrasted with analytical solution and a few other earlier studies in the literature. The results show that meshless methods are very effective and accurate.

Keywords

Radial basis function,
Collocation method,
Method of lines,
Soliton,
Boussinesq equation

Time Scale of Article

Received :19 May 2024
Accepted : 15 Ağustos 2024
Online date :30 September 2024

1. INTRODUCTION

The Boussinesq equation is a well-known partial differential equation used in fluid mechanics to model the behavior of shallow water waves. It was first introduced by the French mathematician Joseph Boussinesq in the late 19th century [1]. The equation is a simplified version of the Navier-Stokes equations, and it is often used as an approximation for modeling wave propagation in a wide range of applications. The Boussinesq equation:

$$u_{tt} = u_{xx} + (u^2)_{xx} + qu_{xxxx} \quad (1.1)$$

where $u = u(x, t)$ is a sufficiently differentiable function and q is a real constant. When $q = -1$ Boussinesq equation (Bq) is called "good" or "well-posed" (GBq) and when $q = 1$ is called "bad" or "ill-posed" (BBq). An improved version of Boussinesq equation (Bq) is Improved Boussinesq (IBq) equation given as follows:

$$u_{tt} = u_{xx} + (u^2)_{xx} + u_{xxtt} \quad (1.2)$$

The Boussinesq type equations has been solved by using a variety of numerical methods. In [2], Manoranjan et al. used Petrov-Galerkin method to get numerical solution of (GBqE). Then, Manoranjan et al. [3] examined the interaction of solitary waves and underlined three essential characteristics of

*Corresponding Author: muratari@kmu.edu.tr

solitary waves. Bratsos [4] used method of lines approach to get solution of Bq equation. Pani and Saranga [5] employed the finite element Galerkin method, while Ortega and Serna [6] developed the finite difference method to solve the (GBqE). The Boussinesq equation was solved numerically by El-Zoheiry [7] using an implicit finite difference scheme, and Wazwaz [8] suggested the Adomian decomposition method. Ismail and Bratsos [9] predictor-corrector scheme to obtain numerical solutions to the (GBq) and (BBq) equations. Additionally, the third order implicit finite difference method has been used to solve the (GBqE) by Bratsos [10, 11]. He used modified Predictor-Corrector and Predictor-Corrector techniques to solve the equation. For the numerical solution of the Boussinesq equation, Dehghan and Salehi [12] combined the boundary knot method and meshless analog equation approach. In addition, Ucar et al. [13] applied Galerkin FEM to the (BqE) using cubic B-spline basis, and Ismail and Mosally [14] created a fourth-order FDM for approximating solutions to the (GBqE). Kırılı and Irk [15] gave numerical solutions of (GBqE) by using the quartic B-spline Galerkin method. Zhijian [16] investigated the existence and uniqueness of solutions, and non-existence of global solutions to the initial-boundary value problem of a generalized IBq equation both locally and globally in time. In order to discretize the nonlinear partial differential equation in space, Lin et al. [17] used the finite element method with linear B-spline basis functions. They then developed a second-order system using only ordinary derivatives to solve a class of initial-boundary value problems for the improved Boussinesq equation. Iskandar and Jain [18] used numerical analysis to examine the dynamical behavior of the IBq equation. Irk and Dag [19] used two finite difference schemes and two finite element approaches, based on the second- and third-order temporal discretization, to achieve numerical simulations of the improved Boussinesq equation.

The objective of the current work is to use meshless radial basis functions collocation method and meshless kernel based method of lines to obtain the numerical solution of Boussinesq type equations. Thus, to obtain the numerical solution of the Boussinesq type equations, radial basis functions in the mesh free approach will be employed. Different types of radial basis functions can be found in literature. We'll employ the widely used radial basis functions.

2. THE MESHLESS RBF COLLOCATION METHOD

First, let us introduce the Meshless RBF Collocation Method that we will use in this section. This method is a meshless method (MRBFCM) and was first used by Kansa [20, 21]. To apply the method, let us approximate the function $u(x, t)$ in equations (1.1) and (1.2) by a linear combination of radial basis functions:

$$u(x) = \sum_{j=1}^N \lambda_j \phi_j(r_j), \quad i = 1, 2, \dots, N \tag{2.1}$$

In equation (2.1) $\{\lambda_j\}_j^N$ are the unknown coefficients to be determined and the $\phi_i(r_j)$ are radial basis functions. The formulas of the used basis functions are defined as follows:

Multiquadric (MQ)	$\phi(r_j) = \sqrt{(\epsilon r_j)^2 + 1}$
Gaussian (GA)	$\phi(r_j) = \exp(-r_j^2 / \epsilon^2)$

where ε is a shape parameter that the method automatically calculates for each kernel matrix that is used and $r_j = |x - x_j|$ represents the Euclidean norm between x and x_j . Wendland's functions [22] are a class of compactly supported radial basis function and have the following general form:

$$\phi_{l,k}(r) = (1 - r)_+^n p_{l,k}(r)$$

with following conditions:

$$(1 - r)_+^n = \begin{cases} (1 - r)^n, & \text{if } 0 \leq r < 1 \\ 0, & \text{if } r \geq 1 \end{cases}$$

where p is a prescribed polynomial for $k \geq 1$ and l is the dimension number. In our calculations, following form of Wendland's function is used:

$$\phi_{7,5}(r) = (1 - r)_+^{12} (9 + 108r + 566r^2 + 1644r^3 + 2697r^4 + 2048r^5)$$

For ease of notation in tables $\phi_{l,k}(r)$ will be used as W .

We write meshless methods the following form equation (1.1) by using $u_t = v$ then we get

$$\begin{aligned} u_t &= v, \\ v_t &= u_{xx} + 2((u_x)^2 + u_{xx}u) + qu_{xxxx}. \end{aligned} \tag{2.2}$$

System (2.2) is discretized by using a forward difference rule for u_t and a Crank–Nicolson scheme for u between successive time levels as follows

$$\begin{aligned} \frac{u^{n+1} - u^n}{\Delta t} &= \frac{v^{n+1} + v^n}{2}, \\ \frac{v^{n+1} - v^n}{\Delta t} &= \frac{u_{xx}^{n+1} + u_{xx}^n}{2} + 2 \frac{[(u_x^2)^{n+1} + (u_x^2)^n]}{2} + 2 \frac{[(uu_{xx})^{n+1} + (uu_{xx})^n]}{2} + q \frac{u_{xxxx}^{n+1} + u_{xxxx}^n}{2} \end{aligned}$$

where u_x^2 and uu_{xx} are nonlinear terms and by using Taylor's formula we obtain their linear forms [23],

$$(u_x u_x)^{n+1} = u_x^n u_x^{n+1} + u_x^n u_x^{n+1} - u_x^n u_x^n$$

and

$$(uu_{xx})^{n+1} = u_{xx}^n u^{n+1} + u^n u_{xx}^{n+1} - u^n u_{xx}^n.$$

Thus, we get following linearized difference equation by substituting these linear forms:

$$\begin{aligned} u^{n+1} - \frac{\Delta t}{2} v^{n+1} &= u^n + \frac{\Delta t}{2} v^n, \\ v^{n+1} - \frac{\Delta t}{2} u_{xx}^{n+1} - 2\Delta t u_x^{n+1} u_x^n - \Delta t u^n u_{xx}^{n+1} - \Delta t u^{n+1} u_{xx}^n - \frac{q\Delta t}{2} u_{xxxx}^{n+1} &= v^n + \\ \frac{\Delta t}{2} u_{xx}^n + \frac{q\Delta t}{2} u_{xxxx}^n \end{aligned}$$

For each time iteration, by substituting

$$u(x) = \sum_{j=1}^N \lambda_j \phi_i(r_j), \quad i = 1, 2, \dots, N \tag{2.3}$$

and

$$v(x) = \sum_{j=1}^N \gamma_j \phi_i(r_j), \quad i = 1, 2, \dots, N \tag{2.4}$$

following form of linear equations system is obtained:

$$\begin{aligned} & \sum_{j=1}^N \lambda_j^{n+1} \phi_i(r_j) - \frac{\Delta t}{2} \sum_{j=1}^N \gamma_j^{n+1} \phi_i(r_j) = \sum_{j=1}^N \lambda_j^n \phi_i(r_j) + \frac{\Delta t}{2} \sum_{j=1}^N \gamma_j^n \phi_i(r_j), \\ & \sum_{j=1}^N \gamma_j^{n+1} \phi_i(r_j) - \frac{\Delta t}{2} \sum_{j=1}^N \lambda_j^{n+1} \phi_i''(r_j) - 2\Delta t \sum_{j=1}^N \lambda_j^{n+1} \phi_i'(r_j) \sum_{j=1}^N \lambda_j^n \phi_i'(r_j) \\ & - \Delta t \sum_{j=1}^N \lambda_j^{n+1} \phi_i''(r_j) \sum_{j=1}^N \lambda_j^n \phi_i(r_j) - \Delta t \sum_{j=1}^N \lambda_j^n \phi_i''(r_j) \sum_{j=1}^N \lambda_j^{n+1} \phi_i(r_j) - \frac{q\Delta t}{2} \sum_{j=1}^N \lambda_j^{n+1} \phi_i''''(r_j) \\ & = \sum_{j=1}^N \gamma_j^n \phi_i(r_j) + \frac{\Delta t}{2} \sum_{j=1}^N \lambda_j^n \phi_i''(r_j) + \frac{q\Delta t}{2} \sum_{j=1}^N \lambda_j^n \phi_i''''(r_j) \end{aligned} \tag{2.5}$$

When similar steps are applied for equation (1.2) we get

$$\begin{aligned} & \sum_{j=1}^N \lambda_j^{n+1} \phi_i(r_j) - \frac{\Delta t}{2} \sum_{j=1}^N \gamma_j^{n+1} \phi_i(r_j) = \sum_{j=1}^N \lambda_j^n \phi_i(r_j) + \frac{\Delta t}{2} \sum_{j=1}^N \gamma_j^n \phi_i(r_j), \\ & \sum_{j=1}^N \gamma_j^{n+1} \phi_i(r_j) - \frac{\Delta t}{2} \sum_{j=1}^N \lambda_j^{n+1} \phi_i''(r_j) - 2\Delta t \sum_{j=1}^N \lambda_j^{n+1} \phi_i'(r_j) \sum_{j=1}^N \lambda_j^n \phi_i'(r_j) \\ & - \Delta t \sum_{j=1}^N \lambda_j^{n+1} \phi_i''(r_j) \sum_{j=1}^N \lambda_j^n \phi_i(r_j) - \Delta t \sum_{j=1}^N \lambda_j^n \phi_i''(r_j) \sum_{j=1}^N \lambda_j^{n+1} \phi_i(r_j) + \sum_{j=1}^N \gamma_j^{n+1} \phi_i''(r_j) \\ & = \sum_{j=1}^N \gamma_j^n \phi_i(r_j) + \frac{\Delta t}{2} \sum_{j=1}^N \lambda_j^n \phi_i''(r_j) + \sum_{j=1}^N \gamma_j^n \phi_i''(r_j). \end{aligned} \tag{2.6}$$

By solving these systems at each time step values of λ and γ are obtained. Substituting computed values of λ_j and γ_j in (2.3) and (2.4) numerical values of $u(x, t)$ and $v(x, t)$ are evaluated.

3. THE MESHLESS KERNEL BASED METHOD OF LINES

The meshless kernel based method of lines (MKBMOL), a second numerical method, will be utilized to find the numerical solution to the Boussinesq type equations. Since this meshless approach generates ordinary differential equations, temporal discretization is not required, and the nonlinear partial differential equation will not be artificially linearized as in the first method. where the kernel function is a radial basis function.

$$u(x, t) = \sum_{j=1}^N \alpha_j(t) \phi_i(x), \quad v(x, t) = \sum_{j=1}^N \beta_j(t) \phi_i(x)$$

where $\alpha_j(t), \beta_j(t)$ are unknown time-dependent functions to be determined each time level as column vectors and $\phi_i(x)$ are defined by any well-known radial basis functions. Derivatives in Equation (1.1) with respect to time and space variables can be described as:

$$\begin{aligned} u_t(x, t) &= \sum_{j=1}^N \alpha_j'(t) \phi_i(x), \quad v_t(x, t) = \sum_{j=1}^N \beta_j'(t) \phi_i(x) \\ u_x(x, t) &= \sum_{j=1}^N \alpha_j(t) \phi_i'(x), \quad u_{xx}(x, t) = \sum_{j=1}^N \alpha_j(t) \phi_i''(x) \\ u_{xxxx}(x, t) &= \sum_{j=1}^N \alpha_j(t) \phi_i''''(x) \end{aligned} \tag{3.1}$$

By substituting (3.1) and its derivatives in the main (1.1) we get:

$$\begin{aligned} \sum_{j=1}^N \alpha_j'(t)\phi_i(x) &= \sum_{j=1}^N \beta_j(t)\phi_i(x), \\ \sum_{j=1}^N \beta_j'(t)\phi_i(x) &= \sum_{j=1}^N \alpha_j(t)\phi_i''(x) + 2\left(\sum_{j=1}^N \alpha_j(t)\phi_i'(x)\right)^2 + 2\sum_{j=1}^N \alpha_j(t)\phi_i''(x) \sum_{j=1}^N \alpha_j(t)\phi_i(x) \\ &+ q \sum_{j=1}^N \alpha_j(t)\phi_i''''(x) \end{aligned} \tag{3.2}$$

The system (3.2) can be written with matlab notations

$$\begin{aligned} V * \alpha'(t) &= V * \beta(t), \\ V * \beta'(t) &= V'' * \alpha(t) + 2(V' * \alpha(t))^2 + 2(V'' * \alpha(t))(V * \alpha(t)) + qV'''' * \alpha(t) \end{aligned} \tag{3.3}$$

where the * is the pointwise product. Since matrice V is invertible we get:

$$\begin{aligned} \alpha'(t) &= V^{-1} * (V * \beta(t)), \\ \beta'(t) &= V^{-1} * (V'' * \alpha(t) + 2(V' * \alpha(t))^2 + 2(V'' * \alpha(t))(V * \alpha(t)) + qV'''' * \alpha(t)) \end{aligned} \tag{3.4}$$

When similar steps are applied for equation (1.2) we get

$$\begin{aligned} \alpha'(t) &= V^{-1} * (V * \beta(t)), \\ \beta'(t) &= (V - V'')^{-1} * (V'' * \alpha(t) + 2(V' * \alpha(t))^2 + 2(V'' * \alpha(t))(V * \alpha(t))) \end{aligned} \tag{3.5}$$

where V is defined as follows:

$$V = \phi_i(x_j).$$

The MATLAB ode solver can be used to solve system 3.4 and 3.5 which are first-order differential equations. We utilized the Adams-Bashforth-Moulton approach i.e ode113 for our computations.

4. NUMERICAL EXAMPLES

In this section, we give solutions of Boussinesq type equations for proposed methods. The accuracy of the solutions are tested by maximum error L_∞

$$L_\infty = \|u - U_N\|_\infty = \max_j |u_j - U_j|$$

The order of convergence is calculated by following formula:

$$\text{order} = \frac{\log \left| \frac{(L_\infty)_{\Delta t_i}}{(L_\infty)_{\Delta t_{i+1}}} \right|}{\log \left| \frac{\Delta t_i}{\Delta t_{i+1}} \right|}$$

Here $(L_\infty)_{\Delta t_i}$ is the error norm L_∞ for the time step Δt_i .

Since the difference between the figures for both methods is indistinguishable, we have given a single graph for each method.

4.1. Numerical Results For GBqE

We consider the GBqE which is Eq. (1.1) with $q = -1$.

4.1.1. The Single Soliton Wave

The initial conditions from the analytic solution for GBqE is as given:

$$u(x, 0) = -A \operatorname{sech}^2 \left(\sqrt{\frac{A}{6}} (x - \bar{x}_0) \right)$$

$$u_t(x, 0) = -2Ac \sqrt{\frac{A}{6}} \operatorname{sech}^2 \left(\sqrt{\frac{A}{6}} (x - \bar{x}_0) \right) \tanh \left(\sqrt{\frac{A}{6}} (x - \bar{x}_0) \right).$$

The exact solution of this test problem is given by

$$u(x, t) = -A \operatorname{sech}^2 \left(\sqrt{\frac{A}{6}} (x - ct - \bar{x}_0) \right) - (b + 1/2)$$

and boundary conditions can be found with the help of exact solutions. In the exact solution, $c = \sqrt{1 - 2A/3}$ is the speed of the soliton wave and A is the amplitude of the soliton wave.

We worked over the solution domain $-80 \leq x \leq 100$ and the time interval $0 \leq t \leq 30$ for $A = 0.369, b = \frac{-1}{2}, h = 0.5$ and $0.3, \bar{x}_0 = 0$ and $\Delta t = 0.002$. Table 1. lists the results of meshless approaches employing Multiquadric, Gaussian and Wendland functions. Meshless approaches are thought to offer superior precision. The calculated numerical results are excellent. Figure 1. shows the trajectory of a single solitary wave for GBqE. The error norm L_∞ and rate of convergence for both proposed methods are listed in Table 2. for $[-40,40]$ space interval and $A = 0.5, \bar{x}_0 = 0$, space step $h = 0.1$, and various time steps $\Delta t = 5,2,1,0.5,0.2,0.1$ at time $t = 10$. The results in Tables 1 and 2, shows proposed methods are considerable good in comparison with other methods. It is observed from Table 2 that the orders of the proposed methods converge to 2 for MRBFCM and 0.52 for MKBMOL.

Table 1. The error norm L_∞ of numerical solutions of GBqE.

h	RBF-MQ	RBF-G	RBF-W	MOL-MQ	MOL-G	MOL-W	[15]
0.5	4.2136e-04	9.0293e-08	2.1516e-04	8.0420e-04	7.4523e-10	7.5896e-05	8.4650e-08
0.3	4.3005e-04	9.0397e-08	2.5410e-04	5.3194e-04	1.6384e-09	5.6709e-04	3.6130e-09

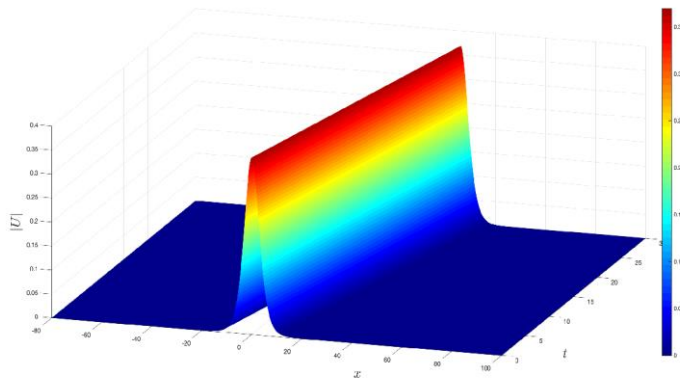


Figure 1. Motion of the single solitary wave for GBqE.

Table 2. The error norm and order of convergence.

Δt	MRBFCM		MKBMOL	
	L_∞	Order	L_∞	Order
5	1.36×10^{-1}	1.21	2.46×10^{-7}	0.40
2	4.49×10^{-2}	1.76	2.46×10^{-7}	0.52
1	1.32×10^{-2}	2.06	2.46×10^{-7}	0.52
0.5	3.17×10^{-3}	2.01	2.46×10^{-7}	0.52
0.2	5.01×10^{-4}	2.00	2.46×10^{-7}	0.52
0.1	1.25×10^{-4}		2.46×10^{-7}	

4.1.2. Interaction of Two Soliton Waves

The following initial conditions are used to study the problem of two soliton waves interaction for GBqE

$$u(x, 0) = u_1(x, 0) + u_2(x, 0),$$

$$v(x, 0) = v_1(x, 0) + v_2(x, 0),$$

where

$$u_i(x, 0) = -A_i \operatorname{sech}^2 \left[\sqrt{\frac{A_i}{6}} (x - x_i^0) \right],$$

$$v_i(x, 0) = -2A_i c_i \sqrt{\frac{A_i}{6}} \operatorname{sech}^2 \left[\sqrt{\frac{A_i}{6}} (x - x_i^0) \right] \tanh \left[\sqrt{\frac{A_i}{6}} (x - x_i^0) \right],$$

$$c_i = \pm \left(1 - \frac{2A_i}{3} \right)^{\frac{1}{2}}, \quad i = 1, 2.$$

By selecting the parameters $x_1^0 = -x_2^0 = -50, A_1 = A_2 = 0.369, c_1 = -c_2 = \sqrt{1 - 2A/3}, h = 0.1,$ and $\Delta t = 0.01$ the computations are performed. These parameters produce two separate soliton waves located at $x_1^0 = -50$ and $x_2^0 = 50$, respectively. The program runs over the range $x \in [-100, 100]$ up until time $t = 120$. Figure 1 shows the interaction of two soliton waves. The figure illustrates how the waves collide and appear as a single wave around $t = 60$.

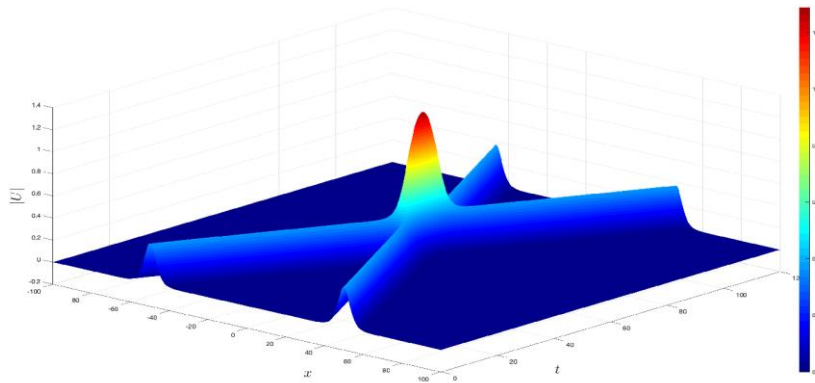


Figure 2. Interaction of two solitons for GBqE.

4.2. Numerical Results For BBqE

We consider the BBqE which is Eq. (1.1) with $q = 1$.

4.2.1. The Single Soliton Wave

The initial conditions from the analytic solution for BBqE is as given:

$$u(x, 0) = A \operatorname{sech}^2 \left(\sqrt{\frac{A}{6}} (x - \bar{x}_0) \right)$$

$$u_t(x, 0) = 2Ac \sqrt{\frac{A}{6}} \operatorname{sech}^2 \left(\sqrt{\frac{A}{6}} (x - \bar{x}_0) \right) \tanh \left(\sqrt{\frac{A}{6}} (x - \bar{x}_0) \right)$$

For various space and time steps, numerical solutions of the single wave with amplitude $A = 0.369$ are obtained. The error norms L_∞ is computed for $A = 0.369, h = 4$ and $x \in [-80, 100]$. The obtained results with the MQ, G, and Wendland's functions are compared with the Ref. [13] and presented in Table 2. We run the program till $t = 72$ to demonstrate the motion of a single wave. As can be observed

from the Figure 2, there are secondary waves whose amplitudes increase and fluctuating with each time step.

Table 3. The error norm L_∞ of numerical solutions of BBqE.

Δt	t	RBF-MQ	RBF-G	RBF-W	MOL-MQ	MOL-G	MOL-W	[13]
0.1	36	0.041749	0.038566	0.044717	0.041761	0.038649	0.045754	0.0118
	72	0.059383	0.061030	0.065906	0.064723	0.062128	0.066795	0.0207
0.01	36	0.041454	0.038890	0.045719	0.042825	0.038649	0.045684	0.0118
	72	0.058355	0.061452	0.066536	0.060705	0.071248	0.066795	0.0207

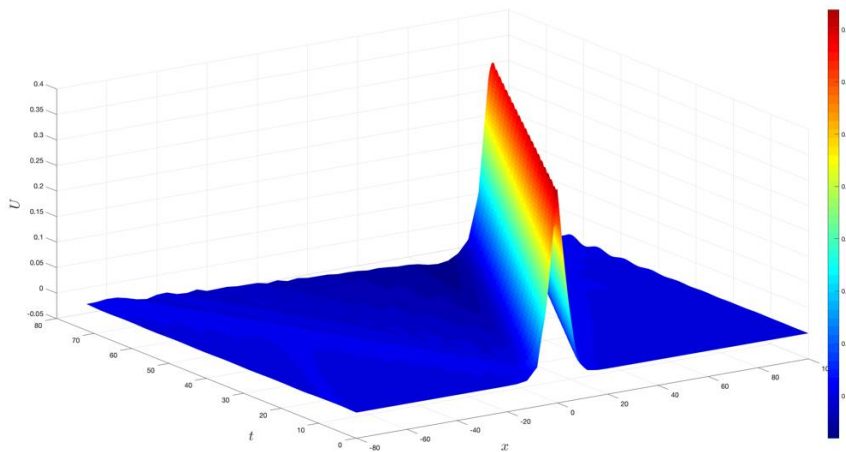


Figure 3. Motion of the single solitary wave for BBqE.

4.2.2. Interaction of Two Soliton Waves

The following initial conditions are used to study the problem of two soliton waves interaction for BBqE

$$\begin{aligned}
 u(x, 0) &= u_1(x, 0) + u_2(x, 0), \\
 v(x, 0) &= v_1(x, 0) + v_2(x, 0),
 \end{aligned}$$

where

$$u_i(x, 0) = A_i \operatorname{sech}^2 \left[\sqrt{\frac{A_i}{6}} (x - x_i^0) \right],$$

$$v_i(x, 0) = 2A_i c_i \sqrt{\frac{A_i}{6}} \operatorname{sech}^2 \left[\sqrt{\frac{A_i}{6}} (x - x_i^0) \right] \tanh \left[\sqrt{\frac{A_i}{6}} (x - x_i^0) \right],$$

$$c_i = \pm \left(1 - \frac{2A_i}{3} \right)^{\frac{1}{2}}, \quad i = 1, 2.$$

We examine the interaction of two waves travelling toward each other by using A_i as the wave amplitudes, x_i^0 as the beginning locations, and c_i ($c_1 = c_2$) as the wave speeds. The waves are situated at $x_1^0 = -40$ and $x_2^0 = 40$, with the interval being taken as $x \in [-150, 150]$. Figure 9 shows the results for waves with same amplitudes $A_1 = A_2 = 0.369$ and $h = 4$, $\Delta t = 0.1$, $t = 72$. We can infer that the waves interact and combine to generate a single wave whose amplitude is greater than the sum of its components.

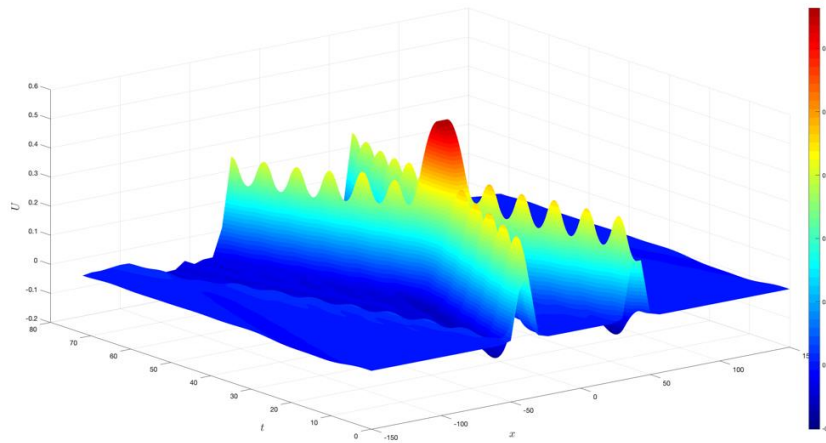


Figure 4. Motion of the two solitary wave interaction for BBqE.

4.3. Numerical Results For IBqE

We consider the IBqE which is Eq. (1.2).

4.3.1. The Single Soliton Wave

The initial conditions for IBqE is as given:

$$u(x, 0) = A \operatorname{sech}^2 \left(\frac{1}{c} \sqrt{\frac{A}{6}} (x - \bar{x}_0) \right)$$

$$u_t(x, 0) = 2Ac \sqrt{\frac{A}{6}} \operatorname{sech}^2 \left(\frac{1}{c} \sqrt{\frac{A}{6}} (x - \bar{x}_0) \right) \tanh \left(\frac{1}{c} \sqrt{\frac{A}{6}} (x - \bar{x}_0) \right)$$

The exact solution of this test problem is given by

$$u(x, t) = A \operatorname{sech}^2 \left(\frac{1}{c} \sqrt{\frac{A}{6}} (x - ct - \bar{x}_0) \right); \quad c = \pm \left(1 + \frac{2A}{3} \right)^{\frac{1}{2}}$$

and boundary conditions can be found from the exact solutions. In the exact solution, c is the speed and A is the amplitude of the soliton wave. Table 3 shows error norm L_∞ with mesh size $h = 0.25$ for amplitudes $A = 0.25$ and $A = 0.5$. Table 4 shows comparison of error norm L_∞ with [24] for mesh size $h = 0.5$ and amplitudes $A = 0.25$ and $A = 0.5$. Figure 4 demonstrates the solutions of the solitary wave for $h = 0.5$, $\Delta t = 0.01$ and $A = 0.5$ at different time levels. The graphic makes it clear that, as time goes on, the single wave advances steadily to the right while maintaining a nearly constant amplitude.

Table 4. The error norm L_∞ of numerical solutions of IBqE with $h = 0.25$.

A	Δt	RBF-MQ	RBF-G	RBF-W	MOL-MQ	MOL-G	MOL-W	[24]
0.25	0.025	2.0333e-05	4.1073e-05	2.0896e-05	1.7517e-04	3.7115e-05	5.1494e-04	5.5570e-06
	0.05	8.3072e-05	8.7266e-05	8.8111e-05	1.7517e-04	3.7115e-05	5.1494e-04	2.2962e-05
0.5	0.025	8.5668e-05	1.5781e-04	9.6307e-05	4.0970e-04	8.9967e-06	2.3852e-05	4.1959e-05
	0.05	3.6089e-04	3.6788e-04	3.6753e-04	4.0970e-04	8.9967e-06	2.3852e-05	1.6799e-04

Table 5. The error norm L_∞ of numerical solutions of IBqE with $h = 0.5$.

A	Δt	RBF-MQ	RBF-G	RBF-W	MOL-MQ	MOL-G	MOL-W	[24]
0.25	0.025	6.7022e-05	2.1038e-05	5.1600e-05	9.2647e-06	2.1765e-05	6.5628e-06	4.1670e-06
	0.05	9.0387e-05	8.4104e-05	8.6177e-05	9.2647e-06	2.1765e-05	6.5628e-06	2.1512e-05
0.5	0.025	1.0382e-04	9.1404e-05	1.0049e-04	2.9753e-05	5.1133e-06	9.2057e-08	3.4386e-04
	0.05	3.2376e-04	3.6552e-04	3.7008e-04	2.9753e-05	5.1133e-06	9.2057e-08	1.6019e-04

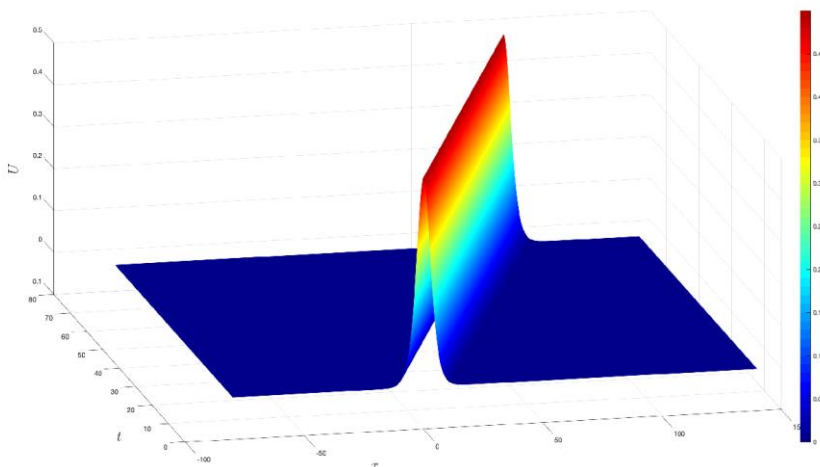


Figure 5. Motion of the single solitary wave for IBqE.

4.3.2. Interaction of Two Soliton Waves

The following initial conditions are used to study the problem of two soliton waves interaction for IBqE

$$\begin{aligned} u(x, 0) &= u_1(x, 0) + u_2(x, 0), \\ v(x, 0) &= v_1(x, 0) + v_2(x, 0), \end{aligned}$$

where

$$\begin{aligned} u_i(x, 0) &= A_i \operatorname{sech}^2 \left[\frac{1}{c_i} \sqrt{\frac{A_i}{6}} (x - x_i^0) \right], \\ v_i(x, 0) &= 2A_i \sqrt{\frac{A_i}{6}} \operatorname{sech}^2 \left[\frac{1}{c_i} \sqrt{\frac{A_i}{6}} (x - x_i^0) \right] \tanh \left[\frac{1}{c_i} \sqrt{\frac{A_i}{6}} (x - x_i^0) \right], \\ c_i &= \pm \left(1 + \frac{2A_i}{3} \right)^{\frac{1}{2}}, \quad i = 1, 2. \end{aligned}$$

In this example we study the interaction of two waves travelling toward each other by using A_i as the wave amplitudes, x_i^0 as the beginning locations, and c_i ($c_1 = c_2$) as the wave speeds. The waves are situated at $x_1^0 = -20$ and $x_2^0 = 30$, with the interval being taken as $x \in [-80, 150]$. Figure 9 shows the results for waves with same amplitudes $A_1 = A_2 = 2$ and $h = 0.25$, $\Delta t = 0.001$, $t = 72$. We can infer that the waves interact and combine to generate a single wave whose amplitude is greater than the sum of its components.

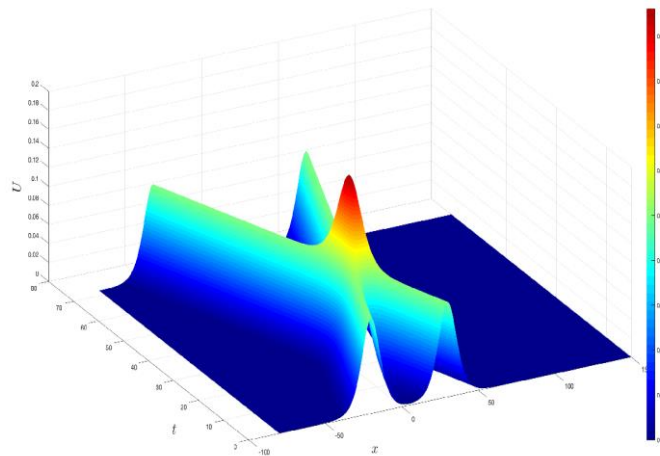


Figure 6. Motion of the two solitary wave interaction for IBqE.

5. ACKNOWLEDGEMENTS

The authors are grateful to Eskişehir Technical University Scientific Research Council (BAP No: 23ADP113).

CONFLICT OF INTEREST

The author(s) stated that there are no conflicts of interest regarding the publication of this article.

CRedit AUTHOR STATEMENT

Murat Ari: Formal analysis, Writing - original draft, Visualization, Software.

Yilmaz Dereli: Supervision, Visualization, Conceptualization, Project administration.

REFERENCES

- [1] Boussinesq J. Theorie des ondes et des remous qui se propagent le long d'un canal rectangulaire horizontal, en communiquant au liquide contenu dans un canal des vitesses sensiblement pareilles de la surface au fond. *J. Math. Pures Appl.* 1872; 7: 55–108.
- [2] Manoranjan VS, Mitchell AR, Morris JL. Numerical solutions of the good Boussinesq equation. *SIAM Journal on Scientific and Statistical Computing* 1984; 5(4): 946-957.
- [3] Manoranjan VS, Ortega T, Sanz-Serna JM. Soliton and antisoliton interactions in the “good” Boussinesq equation. *J. Math. Phys.* 1988; 29: 1964–1968.
- [4] Bratsos AG. The solution of the Boussinesq equation using the method of lines. *Comput. Methods Appl. Mech. Engrg.* 1998; 157: 33–44.
- [5] Pani AK, Saranga H. Finite element Galerkin method for the “good” Boussinesq equation. *Nonlinear Analysis: Theory, Methods and Applications*, 1997; 29: 937-956.
- [6] Ortega T, Sanz-Serna JM. Nonlinear stability and convergence of finite difference methods for the “good” Boussinesq equation. *Numerische Mathematik*, 1990; 58: 215-229. doi: 10.1007/BF01385620
- [7] El-Zoheiry H. Numerical investigation for the solitary waves interaction of the “good” Boussinesq equation. *Applied Numerical Mathematics*, 2003; 45: 161-173.
- [8] Wazwaz AM. Construction of soliton solutions and periodic solutions of the Boussinesq equation by the modified decomposition method. *Chaos, Solitons and Fractals*, 2001; 12: 549-1556.
- [9] Ismail MS, Bratsos AG. A predictor-corrector scheme for the numerical solutions of the Boussinesq equation. *Journal of Applied Mathematics and Computing*, 2003; 13: 11-27.
- [10] Bratsos AG, A second-order numerical scheme for the solution of the one-dimensional Boussinesq equation. *Numer. Algorithms* 46, 2007; 45–58.
- [11] Bratsos AG. Solitary-wave propagation and interactions for the ‘good’ Boussinesq equation. *Int. J. Comput. Math.* 85, 2008; 1431–1440.
- [12] Dehghan M, Salehi RA. Meshless based numerical technique for traveling solitary wave solution of Boussinesq equation. *Applied Mathematical Modelling*, 2012; 36(5): 1939-1956.
- [13] Ucar Y, Esen A, Karaagac B. Numerical solutions of Boussinesq equation using Galerkin finite element method. *Numerical Methods for Partial Differential Equations*, 2020; 3782: 1612-1630.

- [14] Ismail MS, Mosally F. A fourth order finite difference method for the good Boussinesq equation. *Abstract and Applied Analysis*, 2014; 323260: 10 pages.
- [15] Kirli E, Irk D. A Fourth Order One Step Method for Numerical Solution of Good Boussinesq Equation. *Turkish Journal of Mathematics*, 2021; 45(5): 2693-2703.
- [16] Zhijian Y. Existence and non-existence of global solutions to a generalized modification of the improved Boussinesq equation. *Math. Methods Appl. Sci.* 1998; 21: 1467.
- [17] Lin Q, Wu YH, Loxton R. Linear B-Spline Finite Element Method for the Improved Boussinesq Equation. *J. Comput. Appl. Math.* 2009; 224: 658.
- [18] Iskandar L, Jain PC, *Proc. Indian Acad. Sci. Math. Sci.* 89, 1980, 171.
- [19] Irk D, Dağ I, *Numer. Methods Partial Differential Equations*, 2009, doi:10.1002/num.20492.
- [20] Kansa EJ. Multiquadrics–A scattered data approximation scheme with applications to computational fluid dynamics. I., *Comput. Math. Appl.* 1990; 19: 127–145.
- [21] Kansa EJ. Multiquadrics– A scattered data approximation scheme with applications to computational fluid dynamics. II., *Comput. Math. Appl.* 1990; 19: 147–161.
- [22] Wendland H. *Scattered Data Approximation*. Cambridge Monographs on Applied and Computational Mathematics, Cambridge: Cambridge University Press, 17, 2005.
- [23] Rubin SG, Graves RA. *A Cubic Spline Approximation for Problems in Fluid Mechanics* (NASA TR R-436, Washington, DC, 1975).
- [24] Karaagac B, Ucar Y, Esen A. Numerical Solutions of the Improved Boussinesq Equation by the Galerkin Quadratic B-Spline Finite Element Method. *Filomat* 2018; 32:16: 5573–5583.



RESEARCH ARTICLE

GEOMETRIC PATTERN OF POWERS OF THREE VIA SIERPINSKI TRIANGULAR NUMBERS

Temel ERMiŞ^{1,*}

¹ Department of Mathematics and Computer Sciences, Faculty of Science, Eskişehir Osmangazi University, Türkiye.

termis@ogu.edu.tr -  [0000-0003-4430-5271](https://orcid.org/0000-0003-4430-5271)

Abstract

In this study, we describe a new number sequence based on integers arranged in a fractal like structure to visualize powers of three. Moreover, we associate these new numbers with triangular numbers.

Keywords

Triangular number,
Sierpinski triangular number,
Sierpinski triangle,
Diophantine equation

Time Scale of Article

Received :28 May 2024
Accepted :30 July 2024
Online date :30 September 2024

1. INTRODUCTION

Following the belief that “everything is number”, Pythagoreans regarded any positive integer as a set of points on the plane. In this sense, Pythagoreans of the 6th century BC introduced figurate numbers which started a very rich history of efforts to associate geometry and arithmetic with each other. In general, a figurate number is a number that can be represented by a regular geometrical arrangement of equally spaced points. If the arrangement forms a regular polygon, a regular polyhedron or a regular polytope, the number is called a polygonal, polyhedral or polytopical number, respectively.

In general, Fermat–Euler theorem, Gauss–Legendre theorem, and Lagrange theorem, which are related to expressing natural numbers as the sum of squares, are some well-known classical results in number theory. As a continuation of these famous theorems, P. Fermat’s claim in 1638 that every natural number can be written as the sum of three triangular numbers was proved by C.F. Gauss in 1796. After proving that any natural number can be written as the sum of two triangular numbers and a square in the 1870s, there are many studies that have survived to the present day on the use of triangular numbers in obtaining a natural number. After such studies, triangular numbers became very popular among polygonal numbers in number theory.

The triangular number counts the number of dots in an equilateral triangle array. The first five triangular numbers are 1, 3, 6, 10, 15 as shown in Figure 1. n^{th} triangular number T_n (Sloane’s A000217, <https://oeis.org/A000217>) is given by the following formula

$$T_n = 1 + 2 + 3 + \dots + n = \frac{n(n + 1)}{2}.$$

*Corresponding Author: termis@ogu.edu.tr

That is, the triangular number T_n is equal to the sum of the natural numbers from 1 to n (we refer the reader to for [1]-[18] a wider treatment).

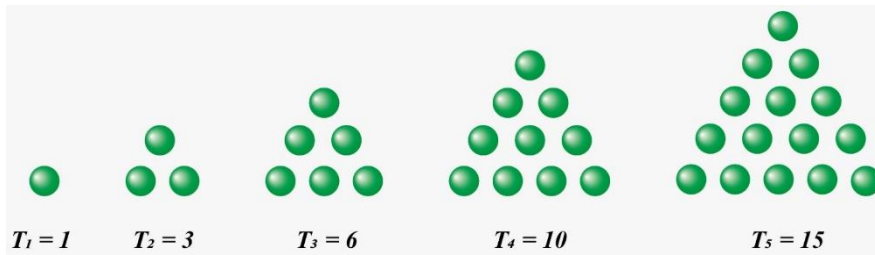


Figure 1. The first five triangular numbers

2. MAIN RESULT

The main motivation for this article is to answer the question “Can powers of three be associated with a geometric model?” In 2000, the equation (I)

$$\sum_{k=0}^{n-1} 3^k = \frac{3^n - 1}{2}$$

for $n \in \mathbb{N} = \{0,1,2, \dots\}$ given by David Sher [14] in his proof without words about the sums of powers of three can be considered as an answer to this question. In 2016, Charles David Leach [11] gave the relationship between triangular numbers and powers of three with the equation (II)

$$T_{2^k} = 3^n + \sum_{k=1}^{n-1} (3^{n-k-1})(T_{2^{k-1}}),$$

after his observations in Sher’s visual proof. These two equations are identities, which are obtained using the graphical and combinatorial properties of triangular numbers. The main idea that distinguishes our results from the two results above is that we use a new set of numbers to construct powers of three, namely Sierpinski triangular numbers. In many studies in recent years, it seems that powers of three play an important role in the solution of diophantine equations associated with Fibonacci, Pell and Lucas numbers. [3], [4] and [18] are examples of these studies. Therefore, associating the powers of three with a geometric model will effectively contribute to giving visual, understandable and easy proofs in such studies in number theory. Frankly, this situation has been a source of motivation for us to carry out this study.

The Sierpinski triangle, one of the basic and also popular examples of self-similar sets, is a fractal defined by Polish mathematician Waław Sierpiński in 1915. It is known that the Sierpinski triangle is created using the following steps; in the first step, any triangle is considered. In the second step, the new triangle formed by considering the midpoints of each side of the first triangle is removed from the original. Thus, three triangles within the original triangle are obtained. Then, the first and second steps are applied again to these three triangles, and the third step is realized. The set of points obtained in this process, which continues by iterating to infinity, is the Sierpinski triangle. By enumerating the total number of vertices of the triangles (Sloane’s A000217, <https://oeis.org/A067771>) that occur in each iteration of the construction of a Sierpinski triangle, we obtain a sequence of numbers which we call “*the sequence of Sierpinski triangular numbers*”, or simply “*the Sierpinski triangular numbers*”. Let ST_n denote the Sierpinski triangular number n^{th} , then the equalities

Consequently, in the section up to this point, besides characterizing the powers of three with Sierpinski triangular numbers, the relationship between triangular numbers and Sierpinski triangular numbers has been given. By using the combinatorial properties of the Sierpinski triangle, many theorems can be given within the scope of elementary number theory. One such theorem is proved below. But, since it will be out of purpose of our article, we will be content with the following theorem. We should emphasize that this theorem and many others making use of the Sierpinski triangular numbers have an important place in number theory.

Theorem 1: Positive integer solutions of the quadratic Diophantine equation $(x - y)^2 = (2y - 3)^2$ for $x > y$ are consecutive Sierpinski triangular numbers.

Proof. Let x and y be consecutive Sierpinski triangular numbers such that $x = ST_{n+1}$ and $y = ST_n$. Then, using the equality (III), we have that

$$(x - y)^2 = (ST_{n+1} - ST_n)^2 = \left(\frac{3 + 3^{n+1}}{2} - \frac{3 + 3^n}{2} \right)^2 = (3^n)^2 = (2y - 3)^2.$$

Conversely, we assume that $(x - y)^2 = (2y - 3)^2$ for $x > y$. In here, if we make the substitution $x - y = 3^u$ and $2y - 3 = 3^v$, then it is obtained the equalities

$$3^u = 3^v, \quad x = \frac{2 \cdot 3^u + 3^v + 3}{2} \quad \text{and} \quad y = \frac{3^v + 3}{2}.$$

Using last three equalities, we get that

$$x = \frac{2 \cdot 3^u + 3^v + 3}{2} = \frac{2 \cdot 3^u + 3^u + 3}{2} = ST_{u+1} \quad \text{and} \quad y = \frac{3^v + 3}{2} = \frac{3^u + 3}{2} = ST_u.$$

Thus, x and y are consecutive Sierpinski triangular numbers.

CONFLICT OF INTEREST

The author stated that there are no conflicts of interest regarding the publication of this article.

CRedit AUTHOR STATEMENT

Temel Ermış: Methodology, Investigation, Formal analysis, Validation, Visualization, Writing – original draft, Writing – review & editing.

REFERENCES

- [1] Bruckman P, Dence JB, Dence TP, Young J. Series of reciprocal triangular numbers. The College Math J 2013; 44(3): 177-184.
- [2] Caglayan G. Covering a triangular number with pentagonal numbers. Math Intelligencer 2020; 42: 55.
- [3] Cagman A. Explicit solutions of powers of three as sums of three Pell numbers based on Baker's type inequalities. Turkish Journal of Inequalities 2021; 5(1): 93-103.

- [4] Coons M, Winning HH. Powers of two modulo powers of three. *Journal of Integer Sequences* 2015; 18: article 15.6.1.
- [5] Charles FM. Proof without words: Square triangular sums. *Mathematics Magazine* 2019; 92(4): 269.
- [6] Edgar T. Proof without words: A recursion for triangular numbers and more. *Mathematics Magazine* 2017; 90(2): 124-125.
- [7] Edgar T. Visual triangular number identities from positional number systems. *The College Math J* 2021; 52(2): 133-136.
- [8] Hopkins B. Proof without words: Products of odd squares and triangular numbers. *Mathematics Magazine* 2018; 91(1): 42.
- [9] Jones MA. Proof without words: The square of a balancing number is a triangular number. *The College Math J* 2012; 43(3): 212.
- [10] Leach CD. Proof without words: Powers of three and triangular numbers. *The College Math J* 2016; 47: 120.
- [11] Matthew JH, Jones MA. Proof without words: Nonnegative integer solutions and triangular numbers. *Mathematics Magazine* 2002; 75(5): 388.
- [12] Nelsen RB. Proof without words: Squares of triangular numbers. *Mathematics Magazine* 1990; 63(3): 178.
- [13] Nelsen RB. Proofs without words II. *Classroom Resource Materials*. Mathematical Association of America, pp 108, 2000.
- [14] Plaza Á. Proof without words: Sum of triangular numbers. *Mathematics Magazine* 2016; 89(1): 36-37.
- [15] Stephen LS. Proof without words: Alternating sum of squares = triangular number. *Mathematics Magazine* 1992; 65(2): 90.
- [16] Tiebekabe P, Diouf I. Powers of three as difference of two Fibonacci numbers. *JP Journal of Algebra, Number Theory and Applications* 2021; 49(2): 185-196.
- [17] Unal H. A visual proof for the sum of the first n triangular numbers. *Math Intelligencer* 2010; 32: 6-7.
- [18] Zerger MJ. Proof without words: Sums of triangular numbers. *Mathematics Magazine* 1990; 63(5): 314.



RESEARCH ARTICLE

AN ANALYSIS ON THE USE OF MODIFIED EXPANDED PERLITE AND PUMICE IN
INORGANIC BONDED FIBROUS COMPOSITE BOARDS

Lütfullah GÜNDÜZ¹, Şevket Onur KALKAN^{2,*}

¹ Department of Civil Engineering, Faculty of Engineering and Architecture, İzmir Katip Çelebi University, İzmir, Türkiye.
lutfullah.gunduz@ikcu.edu.tr - [0000-0003-2487-467X](https://orcid.org/0000-0003-2487-467X)

² Department of Civil Engineering, Faculty of Engineering and Architecture, İzmir Katip Çelebi University, İzmir, Türkiye.
sevketonur.kalkan@ikcu.edu.tr - [0000-0003-0250-8134](https://orcid.org/0000-0003-0250-8134)

Abstract

It is often stated that there is an energy efficiency difference between optimum energy use and actual energy use in the world. In the construction industry, various building materials are produced and used to optimize energy efficiency in buildings. Among these building materials, inorganic bonded fibrous composite boards, whose energy efficiency criteria have begun to be improved, are widely used both in Türkiye and in the world. This article presents an experimental analysis of the utilization of modified expanded perlite and pumice as key constituents in the development of inorganic bonded fibrous composite boards. The study investigates the influence of these modified porous materials on the physical, mechanical, and thermal properties of the composite boards. For this purpose; composite mortars were produced using micronized quartz sand, a hybrid fiber consisting of cellulose and glass fiber, modified expanded perlite (MEP) with stearic acid (1, 2, 3, 4, 5, 6, 7, 8, 9 wt.%) and modified pumice (MPU) with stearic acid (1, 2, 3, 4, 5, 6, 7, 8, 9 wt.%). In order to make a comparison, a control mortar that did not contain modified expanded perlite and modified pumice was produced. Through a series of experiments, it is concluded that the density values of all other mixture designs with MEP and MPU aggregate additives under equivalent conditions are lower than the control sample. The water absorption values of the samples always remained below the control sample, and with the increase in the MPU ratio and decrease in the MEP ratio, the water absorption values of the samples also decreased. The average modulus of rupture (MOR) value of control sample in the analysis made after 14 days of curing under ambient conditions is 3.73 MPa. The highest MOR value of the test samples is 3.51 MPa, which is the mixture using the highest MPU. The thermal conductivity value of the control mixture is 0.352 W/mK. The thermal conductivity value of test mixtures with MEP and MPU aggregates varies between 0.175 W/mK and 0.287 W/mK.

Keywords

Coating for water resistance,
Cemented composite board,
Modulus of rupture,
Thermal properties,
Energy saving

Time Scale of Article

Received :04 March 2024
Accepted : 28 September 2024
Online date : 30 September 2024

1. INTRODUCTION

One of the most basic human needs is the need for shelter. Over time, human beings have begun to attach more importance to the security, durability, convenience, aesthetics and comfort of the structure. Additionally, the construction of buildings with sustainable materials that are easy to install and apply has increasingly gained importance. This has rapidly led humanity to research, development activities and applications of innovative and sustainable material production. Building designers and building users insist on developing healthy living and working environments to achieve a high degree of efficiency for the protection, health, and comfort of the residents and to satisfy sustainable development

*Corresponding Author: sevketonur.kalkan@ikcu.edu.tr

commitments [1]. While the increasing growth in the construction sector and the need to benefit from innovative technology in the construction sector continues, it is of vital importance to deteriorate the ecological balance due to the use of natural resources and energy consumption. In the construction industry, creative methods are needed in the selection of building materials to ensure the best use of available resources in building material production. In particular, 40% of the energy and 25% of the water consumed worldwide are spent in building construction or use [2, 3, 4, 5]. As the building system and culture change, the materials used in the building and the production styles also differ and develop to adapt to this change [6]. The construction of different building systems, within the context of processes and social/cultural structures in different physical environments, is shaped by cultural differences in human enculturation, through socialization, and intergenerational sharing of culturally worked content [7–10]. One of the most effective materials of this process has been the use of cement-bonded fiber reinforced boards products in building sections. These plate products are not only a facade cladding material, thanks to their flexible structure that can be used in all kinds of structures, but also have features that can be easily adapted to different project applications [11, 12, 13]. In addition, cement-bonded fiber reinforced boards, which can be used in different climatic conditions and change the appearance of buildings due to the material components used in their production, take their place among the environmentally and human-friendly materials [14, 15].

These boards contain one or more types of organic or inorganic fibers as reinforcing elements and cement as the binding element [16, 17]. However, different minerals, commonly containing quartz or similar high amounts of silica, can be used as other elements forming the structure as the main and/or filling material. Depending on the intended use of the boards, various additives can be added to the formulation to improve properties such as heat insulation, electrical resistance and fire resistance. The production of cement-bonded fiber reinforced sheets can be carried out by two different methods: air curing or autoclaving [17, 18, 19]. Regardless of the fiber used or the production method, all products within the scope of fiber reinforced cement board are evaluated within the scope of Standard EN 12467 [20]. These sheet products, according to their technical specifications, can be used for exterior and interior wall coverings of all kinds of prefabricated or reinforced concrete buildings, sandwich panel-shaped partition walls and separators, all kinds of ceiling and mezzanine floor chassis coverings, under-roof coverings, all kinds of prefabricated buildings and steel construction [21, 22, 23]. It can be used in the application of building elements.

Cement-bound fiber reinforced sheets can be produced in different density values ranging from 1200 to 1600 kg/m³, depending on the place and purpose of use [23, 24]. It is known that the increase in density value and the type and amount of fiber reinforcement it contains have positive effects on the development of the mechanical strength of the plate. However, as a result of the rapid development of global and climate changes observed today, ensuring thermal comfort in building sections and the use of more energy efficient building material components gain special importance [25-27].

The development of energy efficiency in building sections in buildings directly depends on the components that make up the building section to be made of materials that provide high resistance to heat transfer. The use of plate products with low thermal conductivity and high thermal insulation performance in building sections is on the agenda as a new research topic. In order to achieve this, the use of aggregate derivatives with low density, high porosity, natural origin, and long-lasting durability [28-32] in plate production is an issue that needs to be investigated in detail. For this purpose, the use of expanded perlite and natural pumice rock of volcanic origin as fine-grained aggregate components in the production of cement-bonded fiber reinforced sheets [33-39] can be seen as an approach that can shed light on this issue. When the literature is examined, it can be observed that the studies in which expanded perlite or pumice aggregate used in the production of cement-based lightweight boards are directly added to the mixture after sizing are very limited. Also, these types of aggregates are quite porous and have a high water absorption capacity. It has been observed that there are not enough studies on the effect of using these types of aggregates in cementitious lightweight boards on the board products

after coating. In an ongoing experimental research study, detailed technical analyzes are carried out on the use of coated expanded perlite and coated pumice aggregate components in the production of cement-bonded fiber reinforced boards and their effects on the physical, mechanical and thermal properties of the board, and the findings obtained are discussed comparatively in this article.

2. MATERIALS AND METHODS

2.1. Materials

2.1.1. Cement

CEM I 42.5R ordinary Portland cement (OPC), which is similar to ASTM Type I cement, was used in the mix design of ten different Inorganic Bonded Fiber Composite Board (IBFCB) samples. The specific gravity of cement is 3.15. In the entire study, OPC was used as the main inorganic binder material. Chemical composition of the cement is given in Table 1.

2.1.2. Micronized quartz sand

In the preparation of IBFCB test samples, classified micronized quartz sand (MQS) with a maximum size of 250 microns, obtained from market conditions, was used as the main aggregate material. The average bulk density of ground quartz sand is $1500 \pm 180 \text{ kg/m}^3$. Chemical composition of the micronized quartz sand is given in Table 1.

2.1.3. Mixed fiber

In the preparation of IBFCB test specimens, a mixture of fiber materials of two different origins was used as fiber reinforcement in order to provide reinforcement elements in the matrix structure. These fiber materials are cellulose and glass fiber. The cellulose material in the mixture was first subjected to an opening process and fibrillized, and was transformed into pulp with water in the thinnest fibrous form possible. However, other fiber additive material was used as textile type glass fiber obtained in different sizes by physical recycling of uncontaminated fabric waste/residues generated in the production of wind turbine blades. The nominal length of the glass fiber material is 6 mm on average. Specific gravity weight of glass fiber is 2.58 g/cm^3 , fiber diameters are 13-15 ($\pm 15\%$) microns, tensile strength is $>3200 \text{ MPa}$, Elasticity Modulus is $\geq 70 \text{ GPa}$, moisture content is $<0.15\%$, yarn ratio is $<0\%$, 20 and application temperature is between -60°C and 650°C . In order to prepare the test samples, a mixed fiber additive (FIB) consisting of 40% cellulose fiber by weight and 60% textile type glass fiber material by weight was prepared and used in the production of all test samples.

2.1.4. Modified expanded perlite

In the preparation of IBFCB test samples, in order to reduce the unit volume weight of the mortar and create a lighter mortar design, 0-1 mm expanded perlite, obtained from market conditions, was first coated with the help of heat treatment using 3% stearic acid under laboratory conditions. With this process, expanded perlite aggregates are given a water-impermeable feature. However, it was also observed that after the coating process, the grain strength of the perlite aggregate increased, and it became more resistant to crumbling. Throughout the study, the lightweight aggregate obtained as a result of this process was named as modified expanded perlite (MEP) material. The average bulk density of MEP material after the coating process was 145 kg/m^3 and it is off-white in color. Chemical composition of the modified expanded perlite is given in Table 1.

2.1.5. Modified pumice

In order to reduce the unit volume weight of the mortar and create a more porous matrix structure in the preparation of IBFCB test samples, 750 μm size classified pumice aggregate was obtained from the Nevşehir region in Turkey under market conditions. As with the MEP material, pumice aggregates were also coated with the help of heat treatment using 4% stearic acid under laboratory conditions. With this process, fine-grained pumice aggregates are given a water-impermeable feature. Throughout the study, the pumice obtained as a result of this process was used as lightweight aggregate, modified pumice (MPU) material. The bulk density of the MPU material after the coating process is 640 kg/m^3 on average and it is light grayish in color. Chemical composition of the modified pumice is given in Table 1.

General view of all ingredients of IBFCBs are shown in Figure 1. Sieve analysis of MQS, MPE and MPU are represented in Figure 2.

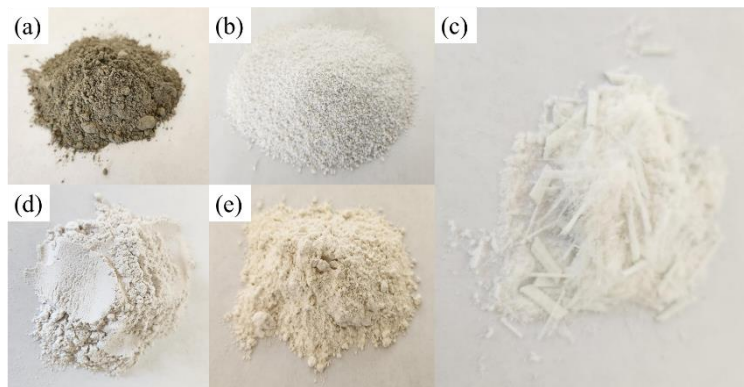


Figure 1. (a) OPC; (b) MEP; (c) FIB; (d) MPU; (e) MQS

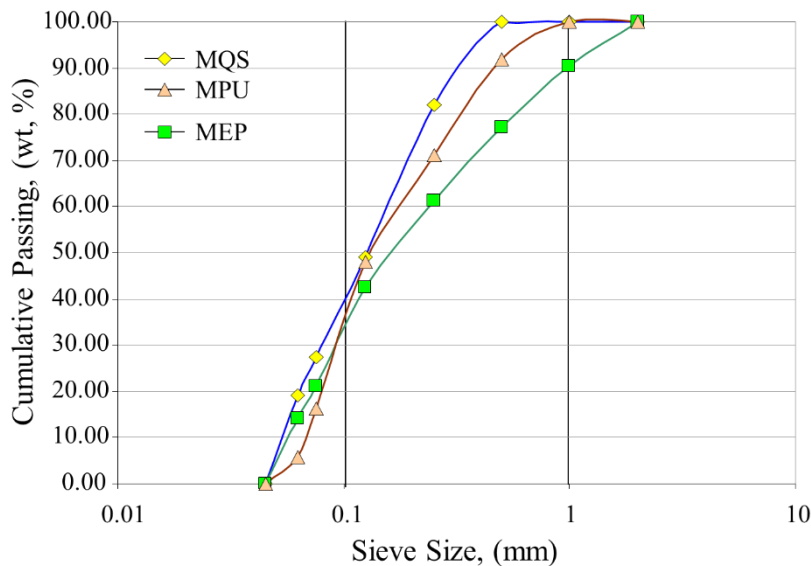


Figure 2. Sieve analysis of MQS, MEP and MPU

Table 1. Proportions of trial mixtures (% by weight)

Chemical composition (%)	Cement	MQS	MEP	MPU
SiO ₂	19.22	98.32	72.20	74.10
Al ₂ O ₃	4.84	0.33	11.40	13.45
Fe ₂ O ₃	3.69	0.24	0.53	1.40
MgO	0.91	0.01	0.33	0.35
CaO	64.72	0.02	0.63	1.17
Na ₂ O	0.45	0.47	3.30	3.70
K ₂ O	0.67	0.20	4.20	4.10
SO ₃	2.48	-	1.87	-
LOI (%)	3.01	0.40	0.56	1.34

2.2. Methods

2.1.1. IBFCB production

In this experimental study, nine different proportions of composite mortar mixtures were designed to investigate the extent to which modified expanded perlite and pumice aggregates affect the technical properties of inorganic bonded fiber composite boards (IBFCB). In order to represent board samples in these mixture designs, test samples were prepared with flat surface features with an average thickness of 12 mm and a nominal surface area of 250x250 mm². The components and usage rates of the board mortar designs applied within the scope of the study are given in Table 2. Test samples were prepared by applying the principles stipulated in the TS EN 12467 standard [20]. All test samples were considered for the category of boards designed to be used in places (indoors) that may be exposed to heat and moisture, but not frost.

Table 2. Proportions of trial mixtures (% by weight)

Mixture	OPC	MQS	FIB	MEP	MPU	w/c
CS0	30	64	6	0	0	1.00
CS1	30	55	6	9	0	1.17
CS2	30	55	6	8	1	1.17
CS3	30	55	6	7	2	1.17
CS4	30	55	6	6	3	1.17
CS5	30	55	6	5	4	1.17
CS6	30	55	6	4	5	1.17
CS7	30	55	6	3	6	1.17
CS8	30	55	6	2	7	1.17
CS9	30	55	6	1	8	1.17
CS10	30	55	6	0	9	1.17

Samples coded as CS0 are samples prepared without the use of modified expanded perlite (MEP) and modified pumice aggregate (MPU), and were evaluated as control and comparison mixture designs throughout the study. In all mixture designs, a constant ratio of 30% cement by weight as the main binder material and 6% mixed fiber (FIB) was used. In the other 9 designs (CS1-CS10), MPE and MPU were used in varying amounts, totaling 9% by weight. In the CS1 series, only 9% MEP by weight was used as the modified aggregate component, and this weight ratio was used substituting from the MQS value. Similarly, in the CS10 series, only 9% MPU by weight was used as the modified aggregate component, and this weight ratio was used substituting from the MQS value. In the change from the CS2 series to the CS9 series, the mixture designs were arranged by increasing the MPU ratio, with a 1%

increase in each series. It is aimed to examine the effects of the use of MEP and MPU in these designs on the technical properties of the prepared board test samples. In the design of the CS0 control mixture, the w/c ratio was applied as 1.0, and since porous aggregate was used in the CS1 – CS10 designs, the w/c ratio was used as 1.17 in all series. The consistency (flow value) of the control mixture was balanced as 155 mm on average. The other mixtures in the study were also brought to the consistency value of the control mixture, which could be close to $155 \text{ mm} \pm 2 \text{ mm}$. In the preparation of these samples, prepared wet mortar samples were poured into a mold made of stainless steel with a square surface area, and they were placed evenly by the vibration method. All samples were kept under laboratory conditions for 7 to 14 days as stipulated in the TS EN 12467 standard. 10 test samples for each mixture design were prepared. 5 of these samples were used to determine mechanical properties, and the other samples were used to determine physical and thermal properties. General views of IBFCB test samples after mixing are given symbolically in Figure 3.

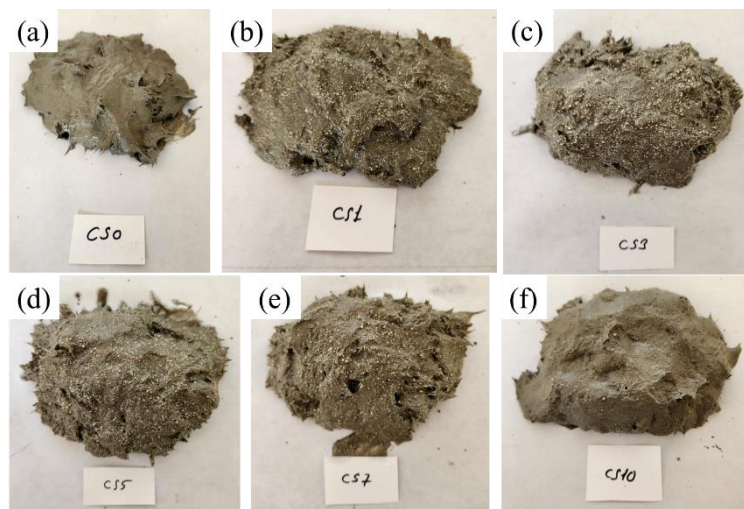


Figure 3. Post-mix symbolic overviews of IBFCB test samples (a) CS0, (b) CS1, (c) CS3, (d) CS5, (e) CS7, (f) CS10

2.2.2. Physical and mechanical tests

As physical properties of IBFCB test samples, apparent unit volume mass values and water absorption values by mass under normal environmental conditions were analyzed according to Article 7.3.1 of the TS EN 12467 standard [20]. In the application of apparent unit volume mass tests, samples to be subjected to mechanical testing were used. After drying for 24 hours in an air circulation oven at 100-105°C, the determined weight was recorded as the mass of the sample. Based on the volume calculated using the external dimensions of the sample, the ratio value of the sample weight to the sample volume was evaluated as unit volume mass. This value expresses the average unit volume mass of the material, including voids (Equation 1).

$$\rho = \frac{m}{V} \quad (1)$$

where, ρ is apparent unit volume mass, (g/cm^3), m is dry mass of the test sample (g), and V is volume of the test sample (cm^3). After the measurements, all values were converted to kg/m^3 and recorded.

To analyze the water absorption value by mass of IBFCB test samples under normal environmental conditions, 3 samples from each mixture were taken and dried in an air circulating oven at 100 – 105 °C for 24 hours and then the unit weight was recorded. Then, the test samples were placed by immersion in a water bath where the temperature was maintained at 20 ± 2 °C, they were taken out of the water bath every 12 hours and their weights were measured, and the process of keeping them in the water bath

continued until the weight of the sample reached a constant weight. Water saturated unit weights of the samples that reached constant weight were recorded and water absorption values were determined using the equation given in equation 2.

$$w = \frac{(m_1 - m_0)}{m_0} \times 100 \quad (2)$$

where, w is water absorption value by mass under normal environmental conditions (%), m_0 is dry mass of the test sample before the test (g) and m_1 is saturated dry mass of the test sample after the water bath (g).

Mechanical evaluation of IBFCB test samples was analyzed on 5 samples of each mixture design as the modulus of rupture value (MOR) at the smallest bending under ambient conditions. In these analyses, samples kept for 14 days in laboratory conditions were tested, taking into account the board conditions stipulated in the TS EN 12467 standard [20], which are designed to be used in places (indoors) that may be exposed to heat and humidity, but will not be exposed to the effect of frost. For the purpose of the modulus of rupture analysis in bending, a bending test machine with a 3-point loading mechanism, which can load at a constant speed while applying the load, and whose accuracy error and repeatability error are $\leq 3\%$, was used (Figure 4). The clearance between supports was used as 200 mm as the loading condition of the test samples, and the condition "The ratio between the span between the supports / the nominal thickness of the sample should be 15 or greater" stipulated in the TS EN 12467 standard was met in all tests.

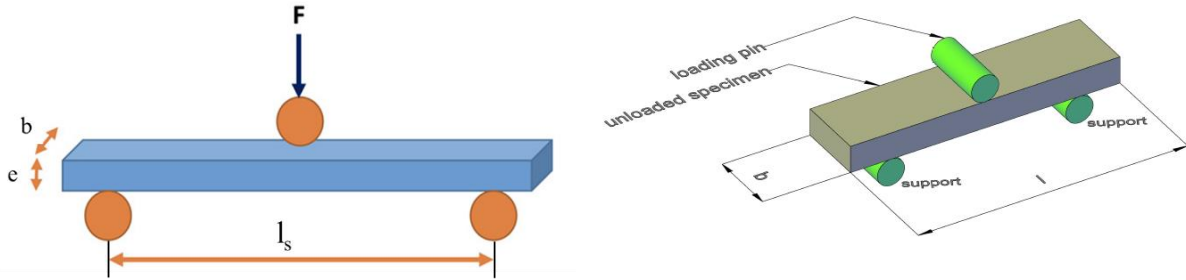


Figure 4. Symbolic general principle of flexural testing machine and testing application.

In the analysis of the modulus of rupture at the smallest bending, the test specimens were placed so that their lower faces rested on the supports, and a load was applied to the specimen with the loading rod placed in the center. A load is applied to the sample at a rate that will cause fracture within a period of 10 seconds to 30 seconds. In the experiment, care was taken to keep the deflection increase rate constant. The flexural modulus of rupture MOR was calculated in megapascal (MPa) unit, using the breaking load determined by the experiment in each direction, with the help of the equation given below (equation 3).

$$MOR = \frac{3 \times F \times l_s}{2 \times b \times e^2} \quad (3)$$

where F is breaking load (N), l_s is clearance between the vertical axes of the support (mm), b is width of the test sample (mm) and e is thickness (mm). The flexural modulus of rupture of the test samples was determined as the arithmetic average of five values (two values in each direction) and was examined based on the limits of the smallest MOR values under ambient conditions specified in Article 5.4.3 (Table 6) of the TS EN 12467 standard [20].

2.2.3. Thermal properties tests of IBFCBs

In order to determine the thermal properties of the samples, the thermal conductivity values and specific heat values of the test samples of each mixture were analyzed using experimental methods. For thermal conductivity value analysis, 3 rectangular samples of each mixture design with a nominal size of

200x400x12 mm³, flat on both sides, were prepared by casting and left to cure for 14 days under ambient conditions. After the curing process, the samples were dried for 24 hours in an air circulating oven at 100 – 105 °C and then tested in (W/mK) unit using a laboratory scale hot box device. This laboratory-scale hot box device is a steady-state measurement device via conduction [40]. However, in specific heat value measurements, 3 cube samples of 50x50x50 mm³ nominal size were prepared and used in a separate steel mold. In order to determine the specific heat value (J/kgK) of IBFCB samples, a calorimeter device with technical features defined in the literature and relevant empirical approaches were used [40, 41].

Using these two thermal properties and the determined physical properties of the test samples, the thermal diffusion value and heat storage amount analyzes of each mixture design were defined using the calculation algorithm. The thermal diffusion of the mixture designs was determined with the approach given in Equation 4 [40, 41].

$$\alpha = \frac{\lambda}{\rho \times C_p} \tag{4}$$

where; α is thermal diffusivity (m²/s), λ is thermal conductivity (W/mK), ρ is dry unit weight (kg/m³) and C_p is specific heat (J/kgK).

The amount of heat stored depends on the specific heat of the medium, the temperature change, and the amount of storage material and it is expressed by Eq. 5 [40, 42].

$$\Delta Q = m \times \int_{T_i}^{T_f} C_p(T).dT \tag{5}$$

Where, ΔQ is the heat stored (J), m is the mass of specimen (kg), C_p is specific heat (J/kgK), dT is temperature difference.

3. RESULTS AND DISCUSSION

3.1. Physical and Mechanical Tests

The physical and mechanical properties of *IBFCB* specimens produced in this study are given in Table 3. Exact values are shared as separate tables, and the experimental results are given and discussed graphically along with regression analyses one by one.

Table 3. Physical and mechanical properties of IBFCB specimens.

Mixture	MEP	MPU	Dry Unit Weight (kg/m ³)	Water Absorption (by mass, %)	Modulus of rupture at smallest bending at 14 days, MOR (N/mm ²)
CS0	0	0	1326	40.7	3.73
CS1	9	0	875	39.1	2.22
CS2	8	1	892	36.4	2.33
CS3	7	2	925	33.8	2.55
CS4	6	3	979	32.5	2.60
CS5	5	4	1000	31.2	2.76
CS6	4	5	1041	30.3	2.83
CS7	3	6	1070	29.7	2.92
CS8	2	7	1125	28.4	3.07
CS9	1	8	1186	27.4	3.44
CS10	0	9	1240	27.0	3.51

The average density value of the CS0 control sample after 14 days of curing under ambient conditions is 1326 kg/m³. This value is almost equivalent to the density values of cement-based fiber reinforced plate products used in the construction industry under current market conditions [23, 24].

It is seen that the density values of all other mixture designs with MEP and MPU aggregate additives under equivalent conditions are lower than the control sample, in other words, they show a lighter plate feature. The lowest density value was obtained in the CS1 mixture with 9% MEP additive by weight, and it is 34% lighter than the control sample. As the MEP contribution rate decreases and the MPU contribution rate increases in mixture designs, the density values of the samples increase in an approach that can be considered linear (Figure 5). The average apparent density value of the CS10 mixture with the highest MPU aggregate additive usage is 1240 kg/m³, which is 6.5% lighter than the control sample. As can be seen here, the use of MEP in mixture designs has played a more active role than MPU in terms of reducing the apparent density. In reducing the building dead load caused by the use of plate in buildings, the use of MEP and/or MPU aggregate in the board mortar is important, provided that other technical features of the board products are taken into account.

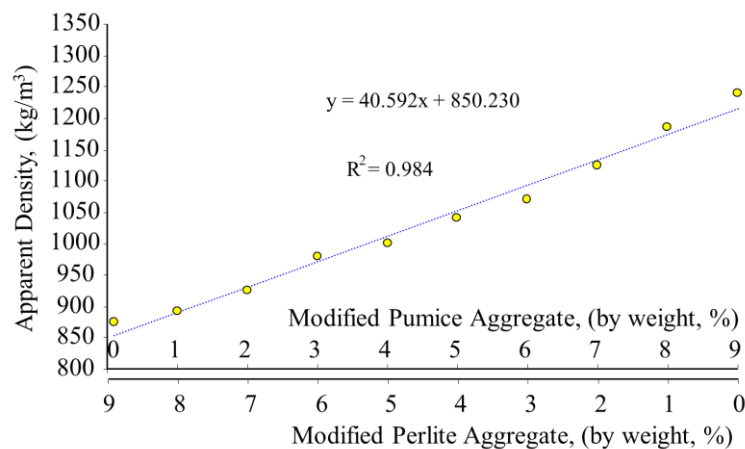


Figure 5. Apparent density change depending on MEP and MPU usage rate of test samples.

The water absorption capacity of inorganic bonded fibrous composite mortars is also considered as a parameter showing the water retention ability. It is inevitable for fibrous composite plates, which have high water absorbency values, to exhibit dimensional mobility in terms of the ratio of absorbed and retained water. Dimensional mobility is not technically desirable, regardless of the orientation of the board. However, it does not seem possible to achieve zero-scale dimensional mobility. For this reason, the minimum acceptable dimensional mobility value should be determined in terms of the usage areas of the boards [43]. Important factors that increase water absorption in composite boards include the structural forms of the aggregate components that make up the board matrix and the water absorption capacities of the fibers that make up the matrix reinforcement. Cellulose fiber additives are generally known as water-retaining components, while glass fiber additives have much lower water retention capabilities due to their structural form [12, 16, 21, 23]. However, the fact that the board mortar matrix contains components with a porous structure and high water retention capacity increases the water absorption ability of the board product and increases the risk of dimensional mobility. In practical applications, it is seen that alternative methods can be used to reduce water absorption ability in board production. For example, adding water-repellent agents of different origins and different proportions to the mixture designs or coating the board product surface with a water-repellent solution. Although these and similar applications provide positive results, it can be seen that they cannot exhibit sustainable material matrix structures due to the risk of losing their water repellency properties over time. In industrial uses, reducing the apparent density value of the board product and minimizing its water absorption ability can be seen as an important technical development. In this context, it is thought that the use of expanded perlite and natural pumice aggregates as modified additives in the board mortar after coating their surfaces with water-repellent material and providing them with a water-impermeable

feature can be successful in this regard. In the experimental study carried out to gain experience with this technical feature development, this interaction was clearly seen in the test samples obtained by adding MEP and MPU aggregate to the mixture in different proportions (Figure 6).

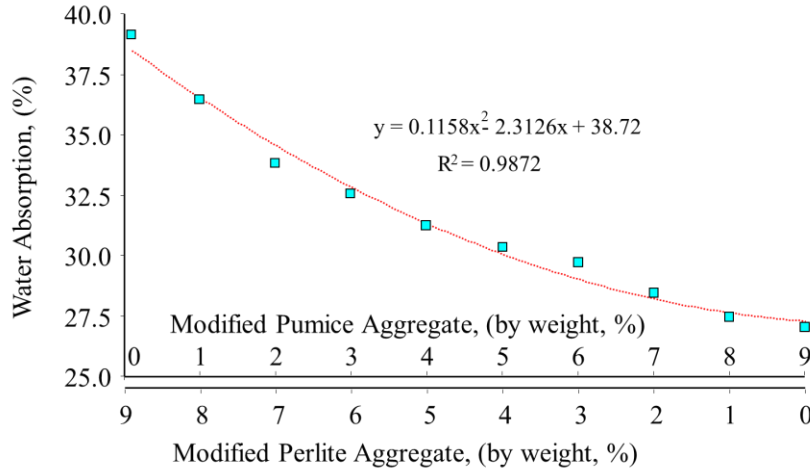


Figure 6. Water absorption change depending on MEP and MPU usage rate of test samples.

In the water absorption rate determination of the CS0 control sample after 14 days of curing under ambient conditions, an average water absorption value of 40.7% by weight was determined. This value not only shows that the matrix structure of the board sample absorbs water on a significant scale, but also represents a potential to exhibit dimensional stability. However, the highest water absorption rate of the CS10 mixture with MPU aggregate additive was obtained as 27% on average. This value is the mixture design with the lowest water absorption value within the scope of the study, and it has approximately 34% lower water absorption ability than the control mixture. This naturally means that this mixture will have a lower risk of dimensional stability. However, it is seen that as the MPU ratio decreases and the MEP ratio increases in mixture designs, the water absorption rate values increase. The average water absorption rate of the CS1 mixture with the highest MEP aggregate additive was 39.1%. This value has approximately 4% lower water absorption ability than the control mixture. These interactions can be examined as the effectiveness of the water absorption rate in the board matrices in the mixture designs (Figure 7). However, it is clearly seen that the water absorption rates of all test samples with MEP and MPU additives are lower than the control mixture. The change in the effectiveness of the water absorption rate in the test samples can also be described as a preliminary criterion of a development that may be positively reflected in the dimensional stability of the board products produced in these design components. Akyuncu and Sanliturk [44] also stated that coating of lightweight aggregates decreased the water absorption values of final products when compared with the one produced with uncoated lightweight aggregates.

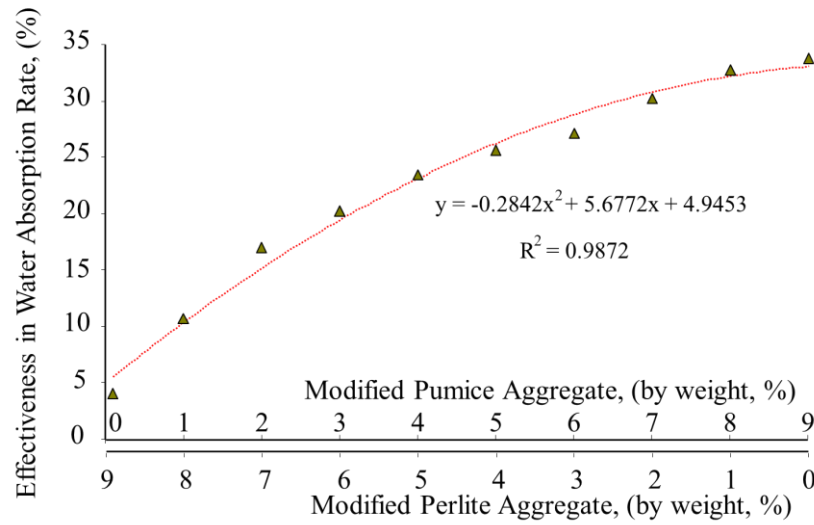


Figure 7. Efficiency analysis on water absorption rate in test samples.

Another important feature of cement and fiber reinforced composite board samples is the lowest modulus of rupture value. This value is also generally known as the MOR value. For building materials to be used as board products, TS EN 12467 standard Article 5.4.3 (Table 6) limits the lowest modulus of rupture values for test samples in wet conditions and ambient conditions. The lowest MOR values under ambient conditions are predicted to vary between 4 MPa and 22 MPa, according to 5 different classes specified in the standard. However, in the test findings, it has been accepted as a rule that the modulus of rupture at the smallest bending in the weakest direction of the test sample should not be smaller than 70% of these defined limit values. Considered in this context, for the suitability of the mixture design for Class 1 at these limit value changes, the smallest MOR value must be greater than $4 \text{ MPa} \times 70\% = 2.8 \text{ MPa}$. When examined in this context, the average MOR value of CS0 control sample in the analysis made after 14 days of curing under ambient conditions is 3.73 MPa. This value appears to provide the limit value prescribed by the standard. The average MOR value of CS10 mixture, on the other hand, with the highest MPU aggregate additive usage is 3.51 MPa. This value is 5.9% lower than the control sample and provides the smallest limit value prescribed by the standard. It has been observed that in mixture designs, as the MPU ratio decreases and the MEP ratio increases, MOR values decrease with an exponential function trend (Figure 8). Therefore, the lowest MOR value was obtained in CS1 mixture and was 2.22 MPa. This value largely does not meet the prescribed limit of the standard. When the changes in all mixture designs were examined, it was observed that CS1 – CS4 mixtures did not similarly meet the predicted limit. In this context, when the MEP and MPU contribution ratio was examined in terms of the mechanical strength of the boards, it was determined that the MEP ratio should be $<5\%$ and the MPU ratio should be $>4\%$ by weight.

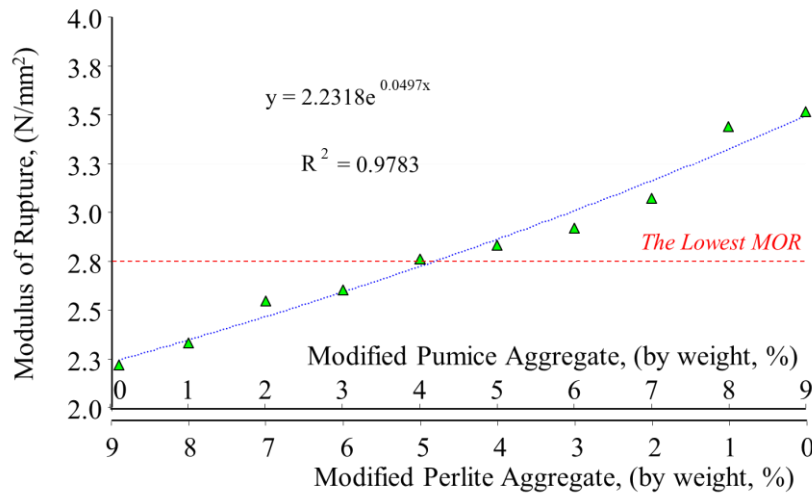


Figure 8. Relation between MEP & MPU ratios in IBFCB mixtures and MOR of IBFCBs

Another situation observed within the scope of the study is that as the apparent density of the test samples decreases, the MOR values also decrease. It is thought that the factor here is that the porosity phenomenon in the matrix structure of the test sample tends to increase in the context of decreasing density and a structural form that is weaker against bending is formed (Figure 9). In order to achieve the lowest MOR value stipulated in the standard, it is seen that the apparent density value of the board must be $>1000 \text{ kg/m}^3$ in designs with MEP and MPU additives.

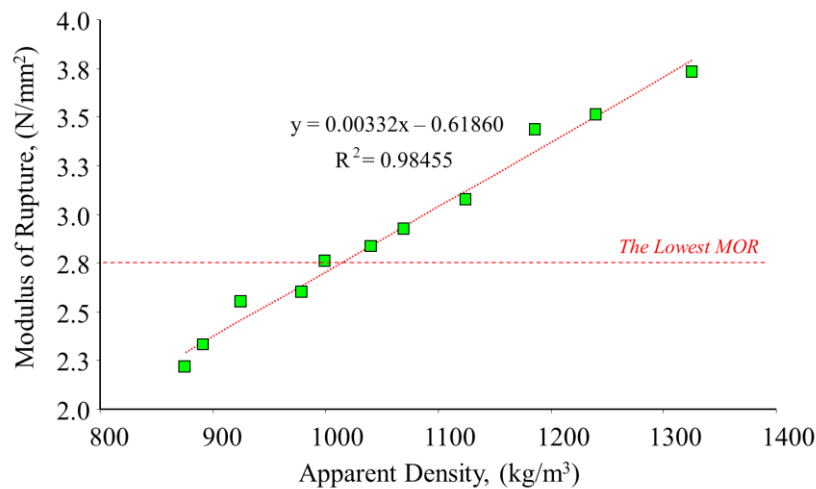


Figure 9. Relation between apparent density and MOR in IBFCB mixtures.

3.2. Thermal Properties Tests of IBFCBs

Thermal properties of all test samples are given in Table 4. The thermal conductivity value of the CS0 control mixture is 0.352 W/mK. The thermal conductivity value of IBFCB mixtures with MEP and MPU aggregates varies between 0.175 W/mK and 0.287 W/mK. The main factor in this change is the MEP and MPU ratios used in the mixture design, and as the MEP ratio increases, the thermal conductivity value decreases. Generally, thermal conductivity in cement-based materials is associated with the porosity and density of the material [45-47]. However, when the optimum mixture design is taken into consideration to ensure the lowest MOR value stipulated in the TS EN 12467 standard and mentioned above, it becomes clear that the variation range in the thermal conductivity values of the test samples is

0.201 W/mK to 0.287 W/mK. The thermal conductivity change of the test samples depending on the MEP and MPU usage rate in mixture designs is given in Figure 10.

Table 4. Thermal properties of tested specimens

Mixture	MEP	MPU	Thermal Conductivity (W/mK)	Cp (J/kgK)	Thermal Diffusivity $\times 10^{-6}$ (m ² /s)	Heat Stored* ΔQ (calories)
CS0	0	0	0.352	785	0.338	2486
CS1	9	0	0.175	944	0.212	1973
CS2	8	1	0.182	938	0.218	1998
CS3	7	2	0.189	922	0.221	2037
CS4	6	3	0.198	891	0.227	2083
CS5	5	4	0.201	872	0.230	2083
CS6	4	5	0.223	857	0.250	2131
CS7	3	6	0.223	846	0.246	2162
CS8	2	7	0.245	833	0.261	2238
CS9	1	8	0.268	812	0.278	2300
CS10	0	9	0.287	805	0.288	2384

*Heat Stored, ΔQ is related to for 10 mm thickness and 1 m² surface application area for a 1°C temperature increase in the surface of board layer.

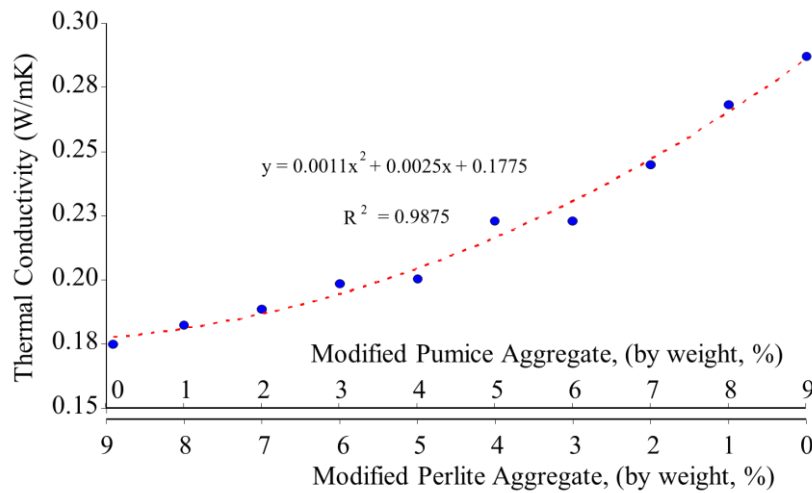


Figure 10. Relation between MEP & MPU ratios in IBFCB mixtures and thermal conductivity of IBFCBs

As can be seen when Figure 10 is examined, as the MEP ratio increases in mixture designs, the matrix structure becomes more insulating, and as the MPU ratio increases, the matrix structure becomes more conductive. In order for board products to contribute to insulation in buildings, it is generally desired that their thermal conductivity values are low. In this context, the necessity of carefully optimizing MEP and MPU usage rates, as far as technical values allow, comes to the fore. Considering only the thermal conductivity value of the test samples, in the most optimum mixture design (CS5), a maximum of 43% insulation could be achieved compared to the control sample.

Another important parameter in examining the thermal comfort properties of building materials is the specific heat (Cp) value of the material. Depending on the matrix structure and components of a material, there may be a difference between the characteristic of the thermal conductivity value and the specific heat value. For example, while the thermal conductivity value of the material increases, the specific heat

value may tend to decrease. Within the scope of this study, the specific heat value of the control sample coded CS0 was determined as 785 J/kgK. On the other hand, the highest specific heat value was determined in the CS1 sample and is $C_p = 944$ J/kgK. The C_p value of this sample with 9% MEP by weight is 20.3% higher than the control sample. However, the C_p value of the 9 wt% MPU added sample is 805 J/kgK, which is 2.5% higher than the control sample. As can be seen here, C_p values decrease as the MEP ratio decreases and the MPU ratio increases in the mixture design. However, the C_p values of all samples with MEP and MPU additives are higher than the control sample (Figure 11).

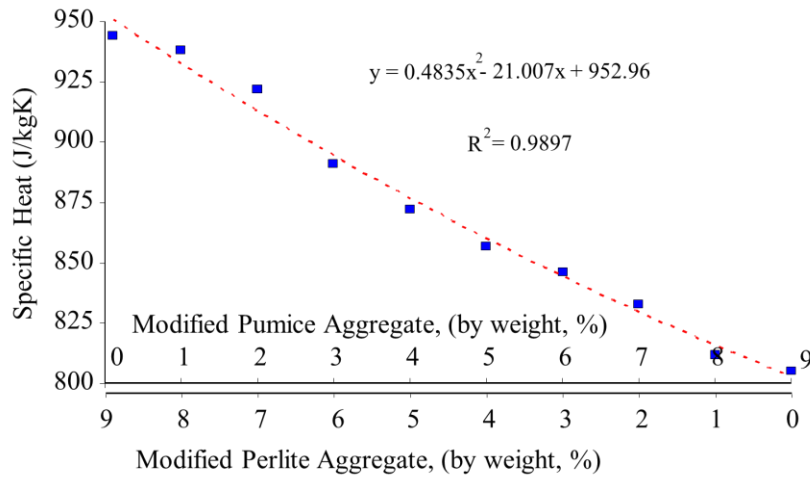


Figure 11. Relation between MEP & MPU ratios in IBFCB mixtures and C_p values of IBFCBs.

The effect of solar radiation and environmental temperature on the building constantly changes throughout the day. Regardless of their origin, all building materials have the ability to store heat, albeit with different characteristics. During the heating of the material, it stores heat, albeit in certain amounts. This phenomenon varies depending on the specific heat of a building component, its density, thickness and the temperature difference it is exposed to [25, 27, 46]. Improvement of thermal insulation performance in a building section can be achieved by keeping the heat storage ability of the components that make up this building section at as low values as possible. Considering cement-based fiber-reinforced composite boards as an important component of building sections, it is desirable to have high insulation values in terms of thermal comfort. It can be thought that the ability to achieve this is due to the low heat storage ability of the form that forms the matrix structures of the board products. Because it is important not to store the heat acting on the surface during use, but to reflect the heat back to the environment where it spreads. The storage of heat by changing the temperature of the substance is called "sensible heat storage", and the storage of heat by phase change is called "latent heat storage" [48-50]. The heat storage ability of many materials used as building materials in buildings is generally seen as "sensible heat storage". When examining the heat transfer in a building element located in a building section, the multiplication value of the density value of the building element to its specific heat value ($\rho \cdot C_p$) is called "heat capacity of the material". The specific heat of the material " C_p " and the heat capacity " $\rho \cdot C_p$ " represent the ability of a material to store heat [46, 48-50].

According to the research findings, the sensible heat storage ability of the control sample coded CS0 was determined as 1.04 J/m³K. On the other hand, the lowest sensible heat storage ability belongs to the square with code CS1 and the highest MEP usage rate, and its value is 0.83 J/m³K. It represents approximately 20.2% less heat storage than the control sample. In the general evaluation of the sensible heat storage capabilities of the test samples, it is seen that as the MPU ratio increases in the mixture design, the heat storage ability increases, in other words, by absorbing the heat acting on the surface, the insulation value weakens. It was determined that the heat storage abilities of MEP and MPU added test samples varied between 0.83 J/m³K - 1.00 J/m³K depending on the increasing MPU ratio. It was

observed that the heat storage abilities of all samples with MEP and MPU additives were lower than the control sample.

Another material property that is important in time-dependent heat transfer is "thermal diffusivity". Thermal diffusivity is a quantity that represents how quickly heat spreads on the surface and body of a material, and its unit is "m²/sec". The thermal diffusivity values of all tested mixtures are given in Table 4. The thermal diffusivity value of the control sample is 0.338x10⁻⁶ m²/s. The thermal diffusivity of MEP and MPU added test samples varies between 0.212 x10⁻⁶ m²/s - 0.288 x10⁻⁶ m²/s depending on the increasing MEP ratio in the mixture. Compared to the control mixture, the thermal diffusivity of all porous aggregate samples is lower than that of the control sample. In other words, if the control sample has a higher thermal diffusivity than other samples, it represents that the thermal diffusivity from the material to the indoor environment will be higher. The algorithmic analysis has shown that as the MEP ratio increases in the mixture design, the thermal diffusivity property decreases due to the decreasing density, and it represents that the heat is converted into heat energy in a large amount of material and is absorbed. However, the magnitude of the thermal diffusivity value can be considered as an indicator that the heat flow through the material is faster and its insulating properties are weakening. In this context, the change in thermal diffusivity of all test samples within the scope of the study compared to the control sample was examined as a "%" value in the context of the comparison criterion. Accordingly, as the MEP ratio in the mixture increases, the change in resistance of the matrix structure of the material to thermal diffusivity increases, whereas as the PMU ratio increases, the change in resistance to thermal diffusivity decreases. This change trend is given graphically in Figure 12.

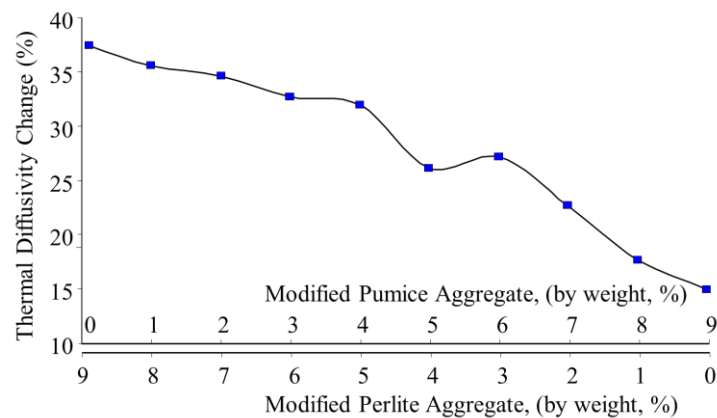


Figure 12. Relation between MEP & MPU ratios in IBFCB mixtures and thermal diffusivity changes of IBFCBs.

As Figure 12 is examined, the changes in thermal diffusivity of MEP and MPU added test samples vary between 15% and 37.4% compared to the control mixture. While the MEP usage rate transforms the matrix structure of the material into a more resistant form against thermal diffusivity, the increase in the MPU usage rate partially negatively affects this feature. However, considering that the board products that can be obtained at these mixed ratios must also meet the minimum MOR value stipulated in the standard, it is seen that a maximum gain of 32% can be achieved compared to the control sample in the optimum mixture design.

Moreover, it can be concluded from Table 4 that the heat storage capacity of the test samples increased from 1973 calories to 2486 calories (see Figure 13). According to Figure 13, in MEP and MPU added mixtures, in the context of the decreasing thermal conductivity value depending on the MEP additive amount, a lower amount of heat is required to increase the temperature on the surface of the board mortar layer by 1°C. This feature represents that the heat value of the board surface can be increased with lower thermal energy, thus creating a more ergonomic usage environment in terms of energy efficiency. In

thermal comfort evaluations, the higher surface temperature of building material components in building sections means that the section will exhibit higher efficiency in terms of thermal insulation. In this context, faster and more economical heating comfort can be achieved in an indoor space with low thermal energy consumption. In order to achieve this rationally, it is desired that the building cross-section absorbs the heat emitted from a heat source indoors at a minimum level, has a low thermal diffusivity despite heat transfer through the cross-section, and has a feature that allows the surface temperature to rise with low calories. In this context, as the MPU ratio increased in the test samples prepared within the scope of the study, the heat storage capacity increased from 1973 calories to 2384 calories. The main factor contributing to this is the increase in the thermal conductivity value of the material matrix structure. However, the heat storage capacity value of all test samples with MEP and MPU additives was lower than the control sample value on a caloric basis. This shows the effect of MEP and MPU contribution on thermal performance.

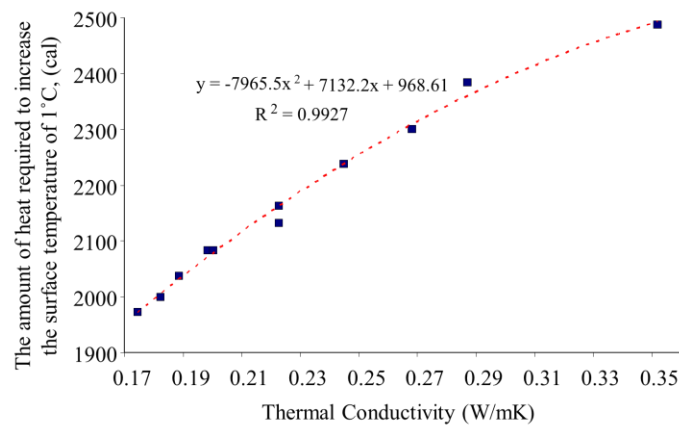


Figure 13. Relation between the amount of heat required to increase the surface temperature of 1°C and thermal conductivity of IBFCBs.

Figure 14 shows the heat storage efficiency of IBFCBs according to thermal diffusivity values. This graphical analysis represents that higher thermal comfort can be achieved by storing less heat within the material due to the decreasing thermal diffusivity value. The improvement of the thermal insulation value in building sections depends on the low value of the heat acting on the material surface, through the diffusion of the heat passing through the material surface and the material section. Conditions where heat storage is minimized, and surface temperature rises with low energy are also important for this situation. In this experimental study, MEP additive having higher porosity creates an effect improving the thermal comfort efficiency. This efficiency reaches up to approximately 21% in samples containing 9% MEP by weight compared to the control mixture. However, the use of pumice aggregate as a component in the mixture, which having lower porosity rate than expanded perlite, has a reducing effect on this efficiency. It is seen that as the MPU ratio increases, this efficiency value decreases up to 4%. In other words, as the MPU ratio increases, the heat flow through the material becomes relatively higher and higher heat energy is needed to increase the material surface temperature.

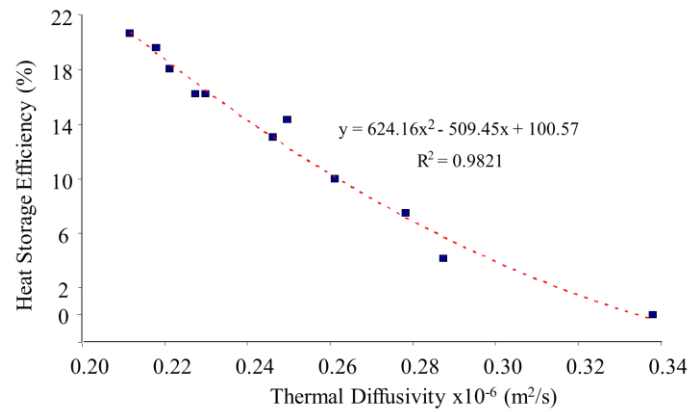


Figure 14. Relation between heat storage efficiency and thermal diffusivity of IBFCBs.

4. CONCLUSION

In this experimental research study, detailed technical analyzes were carried out on the use of modified expanded perlite and modified pumice aggregate components in the production of cement-bonded fiber reinforced boards and their effects on the physical, mechanical and thermal properties of the board, and the findings obtained are discussed comparatively. According to the test results;

1. The use of MEP and MPU was found to be a factor that lightens the plates compared to the control sample. The lowest density value was obtained in the CS1 mixture with 9% MEP by weight, and it is 34% lighter than the control sample.
2. It was observed that the water absorption values of the plate samples produced with aggregates coated to minimize water absorption properties decreased. When comparing CS0 and CS10 samples, a decrease of approximately 34% in water absorption was detected.
3. The average MOR value of CS0 sample is 3.73 MPa. The MOR value of CS10 mixture, with the highest MPU aggregate usage, is 3.51 MPa. This value is 5.9% lower than the control sample and provides the smallest limit value prescribed by the relevant standard.
4. The thermal conductivity value of the CS0 mixture is 0.352 W/mK. The thermal conductivity value of IBFCB mixtures with MEP and MPU varies between 0.175 W/mK and 0.287 W/mK. As the MEP ratio increases, the matrix structure becomes more insulating, and as the MPU ratio increases, the matrix structure becomes more conductive.
5. The specific heat value of the control sample was determined as 785 J/kgK. On the other hand, the highest specific heat value was determined in the CS1 sample and is $C_p = 944$ J/kgK.
6. The sensible heat storage ability of the control sample coded CS0 was determined as 1.04 J/m³K. The lowest sensible heat storage ability belongs to the square with code CS1 and the highest MEP usage rate, and its value is 0.83 J/m³K.
7. MEP addition having higher porosity creates an effect improving the thermal comfort efficiency. This efficiency reaches up to 21% in samples containing 9% MEP compared to control mixture.

The findings reveal significant improvements in providing valuable insights into the potential applications of these composite boards in thermal performance requirements. This research contributes to the ongoing efforts to develop sustainable and high-performance building materials with enhanced properties, offering potential solutions for environmentally conscious and resilient construction practices.

CONFLICT OF INTEREST

The authors stated that there are no conflicts of interest regarding the publication of this article.

CRedit AUTHOR STATEMENT

Lütfullah Gündüz: Writing-Original draft, Writing- Reviewing & Editing, Conceptualization, Methodology, Validation, Investigation, Resources. **Şevket Onur Kalkan:** Writing- Original draft preparation, Writing- Reviewing and Editing, Formal analysis, Visualization, Methodology.

REFERENCES

- [1] Altuma MI, Ghasemlounia R. Effects of Construction Materials to Achieve Sustainable Buildings. *International Journal of Engineering and Management Research* 2021; 11(1): 25-30 .
- [2] Atabay Ş. Determination of exterior material in sustainable buildings by value engineering method according to LEED criteria. *Journal of Sustainable Construction Materials and Technologies* 2023; 8(1): 1-11.
- [3] Yaman K, Muşmul G. Çevre ve ekonomi ilişkisi üzerine genel bir değerlendirme. *Ekonomi İşletme ve Yönetim Dergisi* 2018; 2(1): 66-86.
- [4] Yenilenebilir Enerji Geliştirme Müdürlüğü. (2016). Project development process implementation with an integrated building design approach guide. <https://webdosya.csb.gov.tr/db/meslekihizmetler/ustmenu/ustmenu837.pdf> [Turkish]
- [5] Yalçınkaya Ş, Karadeniz İ. The role of waste material in sustainable architecture design. *Journal of Architectural Sciences and Applications* 2022; 7(2): 750-762.
- [6] Babič NČ, Rebolj D. Culture change in construction industry: from 2D toward BIM based construction. *Journal of Information Technology in Construction (ITcon)* 2016; 21(6): 86-99.
- [7] Alcindor M, Jackson D. Transmitting culture through building systems: The case of the Tile Vault. *Buildings* 2023; 13(4): 873.
- [8] Goicoechea ER. *Antropología Biosocial: Biología, Cultura y Sociedad (Reprint)*; Editorial Universitaria Ramón Areces: 2016, Madrid, Spain.
- [9] Orland-Barak L, Becher A. Cycles of action through systems of activity: Examining an action research model through the lens of activity theory. *Mind, Culture, and Activity* 2011; 18(2): 115-128.
- [10] Rosa A. Acts of psyche. In *The Cambridge Handbook of Sociocultural Psychology*; Valsiner, J., Rosa, A., Eds.; Cambridge University Press: Cambridge, UK; 2007: pp. 205–237.
- [11] Kwayie AT, Zoya KE, Appiah KA. Physical and mechanical properties of composite fiber board for wall surface finishing. *Int J Sci Res* 2016; 5(10): 406-413.
- [12] Singh A, Singh J, Ajay S. Properties of fiber cement boards for building partitions. *International Journal of Applied Engineering Research* 2018; 13(10): 8486-8489.

- [13] Lukmanova LV, Mukhametrakhimov RK, Gilmanshin IR. Investigation of mechanical properties of fiber-cement board reinforced with cellulosic fibers. In IOP Conference Series: Materials Science and Engineering 2019; 570(1): 012113
- [14] Pokorný J, Ševčík R, Šál J, Zárbybnická L. Lightweight blended building waste in the production of innovative cement-based composites for sustainable construction. *Construction and Building Materials* 2021; 299: 123933.
- [15] Ogundipe KE, Ogunbayo BF, Olofinnade OM, Amusan LM, Aigbavboa CO. Affordable housing issue: Experimental investigation on properties of eco-friendly lightweight concrete produced from incorporating periwinkle and palm kernel shells. *Results in Engineering* 2021; 9: 100193.
- [16] Abdellahi SB, Hejazi SM. Effect of glass and polypropylene fibers in cementitious composites containing waste stone powder. *Journal of Industrial Textiles* 2015; 45(1): 152-168.
- [17] Ranachowski Z, Schabowicz K. *The Fabrication, Testing and Application of fibre cement boards.* Cambridge Scholars Publishing 2018.
- [18] Schabowicz K, Gorzelanczyk T. Fabrication of fibre cement boards. In *The Fabrication, Testing and Application of Fibre Cement Boards*, 1st ed.; Ranachowski, Z., Schabowicz, K., Eds.; Cambridge Scholars Publishing: Newcastle upon Tyne, UK, 2018; pp. 7–39. ISBN 978-1-5276-6.
- [19] Ranachowski Z, Schabowicz K. The contribution of fiber reinforcement system to the overall toughness of cellulose fiber concrete panels. *Construction and Building Materials* 2017; 156: 1028-1034.
- [20] TS EN 12467, (2018). *Fibre - cement flat sheets - Product specification and test Methods*, p60, Turkish Standard, November 2018, Ankara, Turkey
- [21] Liu YW, Pan HH. Properties of natural fiber cement boards for building partitions, *Challenges, Opportunities and Solutions in Structural Engineering and Construction – Ghafoori (ed.)* © 2010 Taylor & Francis Group, London, ISBN 978-0-415-56809-8.
- [22] Jarzabek D. Application of advanced optical microscopy. In *The Fabrication, Testing and Application of Fibre Cement Boards*, 1st ed.; Ranachowski, Z., Schabowicz, K., Eds.; Cambridge Scholars Publishing: Newcastle upon Tyne, UK, 2018; pp. 89–106. ISBN 978-1-5276-6.
- [23] Ardanuy M, Claramunt J, Toledo Filho RD. Cellulosic fiber reinforced cement-based composites: A review of recent research. *Construction and building materials* 2015; 79: 115-128.
- [24] Chung SY, Sikora P, Kim DJ, El Madawy ME, Abd Elrahman M. Effect of different expanded aggregates on durability-related characteristics of lightweight aggregate concrete. *Materials Characterization* 2021; 173: 110907.
- [25] Ranachowski Z, Ranachowski P, Dębowski T, Gorzelańczyk T, Schabowicz K. Investigation of structural degradation of fiber cement boards due to thermal impact. *Materials* 2019; 12(6): 944.
- [26] Ferraz PFP, Mendes RF, Ferraz GAS, Damasceno FA, Silva IMA, Vaz LEVSB, ... , Castro JO. Comparison between the thermal properties of cement composites using infrared thermal images. *Agronomy Research* 2020; 18(S1); 806-814.

- [27] Benazzouk A, Douzane O, Mezreb K, Laidoudi B, Quéneudec M. Thermal conductivity of cement composites containing rubber waste particles: Experimental study and modelling. *Construction and Building Materials* 2008; 22(4): 573-579.
- [28] Long HV. Influence of coarse aggregates and mortar matrix on properties of lightweight aggregate concretes. *GEOMATE Journal* 2020; 19(75): 1-7.
- [29] Moreno-Maroto JM, Beaucour AL, González-Corrochano B, Alonso-Azcárate J. Study of the suitability of a new structural concrete manufactured with carbon fiber reinforced lightweight aggregates sintered from wastes. *Materiales de Construcción* 2019; 69(336): e204-e204.
- [30] Ramanjaneyulu N, Rao MS, Desai VB. Behavior of Self-Compacting Concrete Partial Replacement of Coarse Aggregate with Pumice Lightweight Aggregate. In *International Conference on Advances in Civil Engineering ICACE 2019*; 21: 23.
- [31] Zeng Y, Sun P, Tang A, Zhou X. Shear performance of lightweight aggregate concrete with and without chopped fiber reinforced. *Construction and Building Materials* 2020; 263: 120187.
- [32] Çelikten S, Atabey İİ, Özcan ZA, Durak U, İlkentapar S, Karahan O, Atiş CD. Recycling waste expanded polystyrene as aggregate in production of lightweight screed mortar. *Revista de la construcción* 2023; 22(3): 581-596.
- [33] Uluer O, Aktaş M, Karaağaç İ, Durmuş G, Khanlari A, Ağbulut Ü, Çelik DN. Mathematical calculation and experimental investigation of expanded perlite based heat insulation materials' thermal conductivity values. *Journal of Thermal Engineering* 2018; 4(5): 2274-2286.
- [34] Arifuzzaman MD, Kim HS. Development of new perlite/sodium silicate composites. In *International Conference on Mechanical, Industrial and Energy Engineering (ICMIEE)*, Khulna University of Engineering & Technology, Khulna, Bangladesh 2014; 26-27.
- [35] Maxineasa SG, Isopescu DN, Lupu ML, Baciu IR, Pruna L, Somacescu C. The use of perlite in civil engineering applications. In *IOP Conference Series: Materials Science and Engineering* 2022; 1242(1): 012022.
- [36] Yapıcı F, Özçifçi A, Nemli G, Gencer A, Kurt Ş. The effect of expanded perlite on thermal conductivity of medium density fiberboard (MDF) panel. *Technology* 2011; 14(2): 47-51.
- [37] Aras U, Kalaycioglu H, Yel H. The effect of using pumice powder and plasticizer on physico-mechanical and thermal properties of cement-bonded particleboards. *Drvna industrija* 2021; 72(1): 31-37.
- [38] Mohammed TA, Kadhim HM. Sustainable high-strength lightweight concrete with pumice stone and sugar molasses. *Journal of the Mechanical Behavior of Materials*, 2023; 32(1): 20220231.
- [39] İstek A, Gençer A. Çimentolu yonga levha özelliklerine pomza kullanımının etkisi. I. Ulusal Akdeniz Orman ve Çevre Sempozyumu, Isparta, Türkiye, 2014; 560-567.
- [40] Kalkan ŞO, Gündüz L. An analysis of the effectiveness of new generation self-levelling lightweight composite screed for underfloor heating systems. *Journal of Sustainable Construction Materials and Technologies* 2023; 8(3): 16-28.

- [41] Pan J, Zou R, Jin F. Experimental study on specific heat of concrete at high temperatures and its influence on thermal energy storage. *Energies* 2016; 10(1): 33.
- [42] Kumar A, Shukla SK. A review on thermal energy storage unit for solar thermal power plant application. *Energy Procedia* 2015; 74: 462-469.
- [43] Gündüz L, Kalkan ŞO, İsker AM, Güreli B, Hacıoğlu S. Farklı su itici ajanların inorganik bağlı lifli kompozit levhalarda hidrofobik özelliğe etkisi, October 2017, Conference: Uluslararası Yapılarda Kimyasal Katkılar 5. Sempozyumu ve Sergisi, 19-20 Ekim 2017, Ankara
- [44] Akyuncu V, Sanlitürk F. Investigation of physical and mechanical properties of mortars produced by polymer coated perlite aggregate. *Journal of Building Engineering* 2021; 38: 102182.
- [45] Gündüz L, Kalkan ŞO. İnce pomza agreganın çimento esaslı kendiliğinden yayılan tesviye şapının performansına etkisi. *Niğde Ömer Halisdemir Üniversitesi Mühendislik Bilimleri Dergisi* 2023; 12(1): 1-1.
- [46] Gündüz L, Kalkan ŞO. The Effect of Different Natural Porous Aggregates on Thermal Characteristic Feature in Cementitious Lightweight Mortars for Sustainable Buildings. *Iranian Journal of Science and Technology, Transactions of Civil Engineering* 2023; 47(2): 843-861.
- [47] Şapıcı N. Çimento Esaslı Dış Cephe Kaplama Malzemelerinin Üretiminde Kompozit Bileşenli Harçların Teknik Değerlendirilmesi. *El-Cezeri* 2021; 8(2): 981-993.
- [48] Bauer T, Tamme R, Christ M, Öttinger O. PCM-graphite composites for high temperature thermal energy storage. In *Proceedings of the 10th International Conference on Thermal Energy Storage (ECOSTOCK 2006)* 2006; 31:.
- [49] Sharma A, Tyagi VV, Chen CR, Buddhi D. Review on thermal energy storage with phase change materials and applications. *Renewable and Sustainable energy reviews* 2009; 13(2): 318-345.
- [50] Tiari S, Hockins A, Mahdavi M. Numerical study of a latent heat thermal energy storage system enhanced by varying fin configurations. *Case Studies in Thermal Engineering* 2021; 25: 100999.



RESEARCH ARTICLE

SOME GEOMETRIC STRUCTURES RELATED TO DESARGUES CONFIGURATION IN $PG(2,5)$

Elif ALTINTAŞ KAHRİMAN ^{1,*}, Ayşe BAYAR ²

¹ Department of Software Engineering, Faculty of Engineering, Haliç University, İstanbul, Turkey

elifaltintaskahriman@halic.edu.tr  [0000-0002-3454-0326](https://orcid.org/0000-0002-3454-0326)

² Department of Mathematics and Computer Sciences, Faculty of Science, Eskişehir Osmangazi University, Eskişehir, Turkey

akorkmaz@ogu.edu.tr  [0000-0002-2210-5423](https://orcid.org/0000-0002-2210-5423)

Abstract

In this study, we investigate geometric structures related to Desargues configuration in $PG(2,5)$, using an algorithm implemented in C#. We determine different six complete $(11,3)$ -arcs containing Desargues configuration, a $(6,2)$ -arc not containing Desargues configuration, a complete $(16,4)$ -arc, and an affine plane in $PG(2,5)$.

Keywords

Projective plane,
(k,n)-arc,
Complete arc,
Desargues configuration

Time Scale of Article

Received :31 July 2024
Accepted : 30 July 2024
Online date :30 September 2024

1. INTRODUCTION

A set N of points and a set D of subsets of N , referred to lines, make up a projective plane \mathcal{P} . Each pair of points is contained in exactly one line, each pair of distinct lines intersects in exactly one point, and there are four points in a position that together define six distinct lines. When considering the incidence relation provided in \mathcal{P} , a set B of points and lines that is also a projective plane constitutes a subplane of a projective plane \mathcal{P} .

French mathematician Girard Desargues discovered the mathematical statement known as Desargues' theorem in geometry in 1639. Assuming that no two corresponding sides are parallel, the theorem states that if two triangles, $A_1A_2A_3$ and $A_1'A_2'A_3'$, are related to one another in a way that allows them to be viewed perspectively from a single point (i.e., the lines A_1A_1' , A_2A_2' , and A_3A_3' intersect in one point), then the points of intersection of corresponding sides all lie on one line.

In projective geometry, arcs are very important and have many uses in combinatorics and related domains. A k -arc is a set K of k ($k \geq 3$) points in a finite projective plane π (not necessarily Desarguesian) such that no three points of K are collinear (on a line). If the plane π has order p , then $k \geq p + 2$, but the maximum value of k can only be reached if p is even. A $(p + 2)$ -arc is referred to as a hyperoval. Ovals are commonly referred to in the literature, with Hirschfeld being a notable source [1]. A great deal of information has been published about arcs in projective planes, especially about complete $(k,2)$ -arcs with complete quadrangles that generate the Fano plane in the projective planes.

*Corresponding Author: elifaltintaskahriman@halic.edu.tr

These are extensively analyzed in [2], [3]. The procedure for identifying and categorizing Fano subplanes in the projective plane, coordinated by elements of a left nearfield of order 9, is described in [4].

Fano configurations in $PG(5,2)$ are discovered in [5]. The smallest Cartesian Group methods for categorizing $(k,3)$ -arcs in the projective plane of order 9 and order 25 are given in [6], [7]. In [15] by Altıntaş, the algorithm (written in C#) is used to examine $(k,2)$ -arcs of the projective plane of order 5 coordinatized by elements of $GF(5)$ [15].

The main purpose of this study is to investigate some arcs and geometric structures with related to Desargues configuration in $PG(2,5)$. In Section 2, we give some definitions that are important in our study. In Section 3, we constructed the projective plane of order 5 with their lines, points and incidence relation over $GF(5)$ and we determine a Desargues configuration. In Section 4, we introduce our algorithm and method to find all the results that related to (k,n) -arcs. Here in, different six complete $(11,3)$ -arcs related to Desargues configuration and a $(6,2)$ -arc using the points outside the Desargues configuration are found. And also, the 16 points obtained as a result of applying the algorithm to a $(6,2)$ -arc indicate a $(16,4)$ -arc, and the common points of $(16,4)$ -arc and Desargues configuration specifies an affine plane. In Section 5, we give our results.

2. PRELIMINARIES

This section presents to review some relevant definitions and theorems in projective planes. Here in, some properties of arcs in projective planes are given.

Definition 1. A (axiomatic) projective plane \mathcal{P} with N being a set of points, D being a set of lines, and \circ being an incidence relation, \mathcal{P} is an incidence structure (N,D,\circ) that satisfies the following axioms:

- i) Each pair of distinct points lies on exactly one unique line;
- ii) For every pair of distinct lines, there is exactly one unique point where they intersect.;
- iii) \mathcal{P} contains a set of four points such that no three of them lie on a single common line.

In \mathcal{P} , a closed configuration S is a subset of $N \cup D$ that remains closed under the intersections of any lines in S and the lines defined by any two distinct points in S . We denote the line through points p and q in \mathcal{P} as $\langle p, q \rangle$.

Definition 2. [9] The set $V(n + 1, K)$ is $(n + 1)$ -dimensional vector space over the field K and is taken to be the set of vectors $X = \{x_0, x_2, \dots, x_n\}$, $x_i \in K$. Correspondingly, $PG(n,K)$ is n -dimensional projective space over K and is the set of elements, called points, $P(x)$ with $x \in V(n + 1, K) \setminus \{0\}$. When $K = GF(q) = F_q$, the finite field of q elements, also called the Galois field of q elements, then $V(n + 1, K)$ is written $V(n + 1, q)$ and $PG(n,K)$ is written $PG(n,q)$. The order of $PG(n,q)$ is q . The number of points in $PG(n,q)$ is

$$\theta(n) = \frac{q^{n+1}-1}{q-1}.$$

(x_1, x_2, \dots, x_n) represents any point in N , where x_1, x_2, \dots, x_n are non-zero. A triple's nonzero multiples correspond to the same point. Likewise, $[a_1, a_2, \dots, a_n]$ represents any line in D , where a_1, a_2, \dots, a_n are not all 0. P_2F represents this projective plane, which is a point-line geometry (N, D, \circ) described by F . Incidence Relation: $\circ: (x_1, \dots, x_n) \circ [a_1, \dots, a_n] \Leftrightarrow a_1x_1 + a_2x_2 + a_3x_3 + \dots + a_nx_n = 0$.

Let p be a prime number and r be a positive integer, respectively. The projective plane of order $n = p^r$ over the finite field $F = GF(p^r)$, where p^r is the number of elements, is represented by $P_2F = PG(2, p^r)$ [9].

Theorem 1. (Desargues Theorem) *In the projective plane, let ABC and $A'B'C'$ represent two triangles. If and only if the intersections of the corresponding sides $(AB, A'B')$, $(BC, B'C')$, $(CA, C'A')$ lie on a single line, then the lines AA' , BB' , CC' intersect in a single point.*

Desarguesian projective planes are projective planes which satisfy the Desargues theorem. Every projective plane over a field is Desarguesian.

Definition 4. [10] *In a projective plane, a (k, n) –arc \mathcal{K} is a set of k points such that some line intersects \mathcal{K} in n points, and no line intersects \mathcal{K} in more than n points, where $n \geq 2$.*

Definition 5. [11] *A line l of projective plane is an μ –secant of (k, n) –arc \mathcal{K} if l intersects \mathcal{K} in μ points. Let τ_i be the total number of i -secants to \mathcal{K} . The number of i -secants to \mathcal{K} through a point Q of $\mathcal{P} \setminus \mathcal{K}$ is denoted by σ_i or $\sigma_i(Q)$. Moreover, a point Q of $\mathcal{P} \setminus \mathcal{K}$ is called point of index zero if $\sigma_n(Q) = 0$.*

If there isn't a $(k + 1, n)$ –arc that contains a (k, n) –arc, then it is complete.

3. PG(2,5) PROJECTIVE PLANE

In this work, we take $PG(2,5)$, which is constructed over $GF(5)$ with 31 points and 31 lines under the irreducible polynomial $f(x) = x^3 + 2x^2 + x - 1$, where the elements 0, 1, 2, 3, 4 of $GF(5)$. Every line has six points, and every point has six lines passing through it in $PG(2,5)$ [8].

The projective plane $PG(2,5)$ has a point set N that is $N = \{N_i | i = 1, 2, \dots, 31\}$, where

$$N_1 = (0,0,1), N_2 = (1,1,1), N_3 = (1,2,2), N_4 = (1,4,2), N_5 = (1,4,3), N_6 = (1,3,4), N_7 = (1,0,3), N_8 = (1,3,1), N_9 = (1,2,4), N_{10} = (1,0,4), N_{11} = (1,0,1), N_{12} = (1,2,1), N_{13} = (1,2,3), N_{14} = (1,3,0), N_{15} = (0,1,3), N_{16} = (1,1,3), N_{17} = (1,3,3), N_{18} = (1,3,2), N_{19} = (1,4,0), N_{20} = (0,1,4), N_{21} = (1,1,0), N_{22} = (0,1,1), N_{23} = (1,1,2), N_{24} = (1,4,4), N_{25} = (1,0,2), N_{26} = (1,4,1), N_{27} = (1,2,0), N_{28} = (0,1,2), N_{29} = (1,1,4), N_{30} = (1,0,0), N_{31} = (0,1,0).$$

Table 1 provides the $PG(2,5)$ incident relation table. Each row represents points located on the line $D_i, i = 1, 2, \dots, 31$.

Table 1. The lines of $PG(2,5)$

D_1	N_2	N_3	N_{17}	N_{22}	N_{24}	N_{30}
D_2	N_3	N_4	N_{18}	N_{23}	N_{25}	N_{31}
D_3	N_4	N_5	N_{19}	N_{24}	N_{26}	N_1
D_4	N_5	N_6	N_{20}	N_{25}	N_{27}	N_2
D_5	N_6	N_7	N_{21}	N_{26}	N_{28}	N_3
D_6	N_7	N_8	N_{22}	N_{27}	N_{29}	N_4
D_7	N_8	N_9	N_{23}	N_{28}	N_{30}	N_5
D_8	N_9	N_{10}	N_{24}	N_{29}	N_{31}	N_6
D_9	N_{10}	N_{11}	N_{25}	N_{30}	N_1	N_7
D_{10}	N_{11}	N_{12}	N_{26}	N_{31}	N_2	N_8
D_{11}	N_{12}	N_{13}	N_{27}	N_1	N_3	N_9
D_{12}	N_{13}	N_{14}	N_{28}	N_2	N_4	N_{10}
D_{13}	N_{14}	N_{15}	N_{29}	N_3	N_5	N_{11}
D_{14}	N_{15}	N_{16}	N_{30}	N_4	N_6	N_{12}
D_{15}	N_{16}	N_{17}	N_{31}	N_5	N_7	N_{13}
D_{16}	N_{17}	N_{18}	N_1	N_6	N_8	N_{14}

D_{17}	N_{18}	N_{19}	N_2	N_7	N_9	N_{15}
D_{18}	N_{19}	N_{20}	N_3	N_8	N_{10}	N_{16}
D_{19}	N_{20}	N_{21}	N_4	N_9	N_{11}	N_{17}
D_{20}	N_{21}	N_{22}	N_5	N_{10}	N_{12}	N_{18}
D_{21}	N_{22}	N_{23}	N_6	N_{11}	N_{13}	N_{19}
D_{22}	N_{23}	N_{24}	N_7	N_{12}	N_{14}	N_{20}
D_{23}	N_{24}	N_{25}	N_8	N_{13}	N_{15}	N_{21}
D_{24}	N_{25}	N_{26}	N_9	N_{14}	N_{16}	N_{22}
D_{25}	N_{26}	N_{27}	N_{10}	N_{15}	N_{17}	N_{23}
D_{26}	N_{27}	N_{28}	N_{11}	N_{16}	N_{18}	N_{24}
D_{27}	N_{28}	N_{29}	N_{12}	N_{17}	N_{19}	N_{25}
D_{28}	N_{29}	N_{30}	N_{13}	N_{18}	N_{20}	N_{26}
D_{29}	N_{30}	N_{31}	N_{14}	N_{19}	N_{21}	N_{27}
D_{30}	N_{31}	N_1	N_{15}	N_{20}	N_{22}	N_{28}
D_{31}	N_1	N_2	N_{16}	N_{21}	N_{23}	N_{29}

Since $PG(2,5)$ is a plane over a field, any two triangles that are perspective from a center are also perspective from an axis. For example, let triangles $A_1A_2A_3$ and $A_1'A_2'A_3'$ be taken perspective from a point center point N_1 such that $A_1 = N_3, A_2 = N_2, A_3 = N_6$ and $A_1' = N_9, A_2' = N_{23}, A_3' = N_{14}$. Thus we have intersections points with the lines of these triangles:

$$\begin{aligned} A_1A_2 \cap A_1'A_2' &= N_{30} \\ A_1A_3 \cap A_1'A_3' &= N_{26} \\ A_2A_3 \cap A_2'A_3' &= N_{20} \end{aligned}$$

It is seen that N_{20}, N_{26}, N_{30} intersection points are collinear and their perspective axis the line D_{28} .

4. THE ALGORITHM USING DESARGUES CONFIGURATION TO CONSTRUCT (k,n) -ARCS IN $PG(2,5)$

In this section, we illustrate the algorithm that used to construct (k, n) –arcs in $PG(2,5)$, and determined $(k, 3)$ –arcs up to no-secant, bisecant or secant distributions.

4. 1. Method: Finding (k, n) –arcs

Step 1: Finding the points and lines of $PG(2,5)$ by irreducible polynomial.

In this case, we get 31 points and 31 lines as shown in Table 1.

Step 2: Consider a Desargues Configuration in $PG(2,5)$, Then, there is ten points and in this Desargues configuration forms $(10, 3)$ –arc in $PG(2,5)$ which is not complete. For example,

$$\mathcal{A} = \{N_1, N_2, N_3, N_6, N_9, N_{14}, N_{20}, N_{23}, N_{26}, N_{30}\}$$

Step 3: There are 6 points not on the Desargues configuration. Adding these points to \mathcal{A} gives us six different complete $(11, 3)$ –arcs in $PG(2,5)$.

If we take into consideration the points of the Desargues configuration $\mathcal{A} = \{N_1, N_2, N_3, N_6, N_9, N_{14}, N_{20}, N_{23}, N_{26}, N_{30}\}$, it is $(10, 3)$ –arc but not complete arc. In this projective plane, the points of this $(10, 3)$ –arc are deleted, then $N_4, N_{10}, N_{11}, N_{15}, N_{19}, N_{31}$ points are remained. Six lines pass through each of these points. Five of them intersect the Desargues configuration at two points, and one is the remaining line, which does not intersect it at all. See Table 2.

Table 2. Desargues Configuration and remaining points incidence relations

Point	Secant lines	Not intersect
N_4	$D_2, D_3, D_{12}, D_{14}, D_{19}$	D_6
N_{10}	$D_8, D_9, D_{12}, D_{18}, D_{25}$	D_{20}
N_{11}	$D_9, D_{10}, D_{13}, D_{19}, D_{21}$	D_{26}
N_{15}	$D_{13}, D_{14}, D_{17}, D_{25}, D_{30}$	D_{23}
N_{19}	$D_3, D_{17}, D_{18}, D_{21}, D_{29}$	D_{27}
N_{31}	$D_2, D_8, D_{10}, D_{29}, D_{30}$	D_{15}

Step 4: Adding the remaining points $\{N_4, N_{10}, N_{11}, N_{15}, N_{19}, N_{31}\}$ to $(10,3)$ -arc will give us $(11,3)$ -arcs.

Now we take the set $\mathcal{A} = \{N_1, N_2, N_3, N_6, N_9, N_{14}, N_{20}, N_{23}, N_{26}, N_{30}\}$ such that these points construct Desargues Configuration. We provide the following algorithm (written in C#) to find complete $(11,3)$ -arcs of $PG(2,5)$:

Steps of Algorithm

```

A ← Read(Excel File)
B ← Read(Text File)
C ← A
while s(C)>0
    Bi ← input(b), {b|b ∈ C, b ∉ B, i = s(B) + 1}
    j=1
    while j ≤ s(B)
        for k=(j+1) to s(B)
            m ← the index of row on Bj, Bk
            D ← Amn; {Amn|Amn ≠ Bj, Amn ≠ Bk, n = 1, ..., 10}
            Remove a from A; {a|a ∈ A, a ∈ D}
            C ← c; {c|c ∈ A, c ∉ C}
        end for
        j=j+1
    end while
end while

```

Since $PG(2,5)$ is Desarguesian, choosing a specific Desargues configuration in the proofs provided throughout the paper does not affect the generality.

Theorem 1. Let \mathcal{A} be Desargues configuration in $PG(2,5)$. If the given algorithm is applied to the points of Desargues configuration to find $(k,3)$ -arcs, there is a $(6,2)$ -arc constructing with the remaining points.

Proof. Let $\mathcal{A} = \{N_1, N_2, N_3, N_6, N_9, N_{14}, N_{20}, N_{23}, N_{26}, N_{30}\}$ be Desargues configuration in $PG(2,5)$. If we apply the algorithm to \mathcal{A} , the points $N_4, N_{10}, N_{11}, N_{15}, N_{19}$, and N_{31} are remained in $PG(2,5)$. Since all points of a projective plane lie on a pencil of lines through a single point, then the points of a Desargues configuration lie on a pencil of lines through a point. In this case, each line through any point outside the configuration contains two points of the Desargues configuration, while one line not contain any points of the Desargues configuration. In projective plane, there is only one line passing through any two points. So, the line passing through any two of the remaining points does not intersect the Desargues configuration. Hence, the remaining point set $\{N_4, N_{10}, N_{11}, N_{15}, N_{19}, N_{31}\}$ is a $(6,2)$ arc.

From this point on, we will denote the remaining points set $\{N_4, N_{10}, N_{11}, N_{15}, N_{19}, N_{31}\}$ by C .

Theorem 2. There are six different complete (11,3) –arcs containing a Desargues configuration in $PG(2,5)$.

Proof. Let \mathcal{A} be a Desargues configuration. It is obtained (6,2)-arc by applying the algorithm to \mathcal{A} from Theorem 1. Every point of this (6,2)-arc is on six lines such that five of them intersect Desargues configuration \mathcal{A} in two points and one of them don't have common point with \mathcal{A} . If each of these points are added to \mathcal{A} that is (10,3)-arc, it is obtained six different complete (11,3)-arc.

Example Let be Desargues configuration \mathcal{A} , following the implementation of this algorithm, all complete (11,3)-arcs are given in Table 3.

Table 3. Complete (11,3)-arcs

Name of the arc	Completion of (10,3) Arc \mathcal{A}	Complete (11,3)-arcs
\mathcal{A}_1	$\mathcal{A} \cup \{N_4\}$	$\{N_1, N_2, N_3, N_4, N_6, N_9, N_{14}, N_{20}, N_{23}, N_{26}, N_{30}\}$
\mathcal{A}_2	$\mathcal{A} \cup \{N_{10}\}$	$\{N_1, N_2, N_3, N_6, N_9, N_{10}, N_{14}, N_{20}, N_{23}, N_{26}, N_{30}\}$
\mathcal{A}_3	$\mathcal{A} \cup \{N_{11}\}$	$\{N_1, N_2, N_3, N_6, N_9, N_{11}, N_{14}, N_{20}, N_{23}, N_{26}, N_{30}\}$
\mathcal{A}_4	$\mathcal{A} \cup \{N_{15}\}$	$\{N_1, N_2, N_3, N_6, N_9, N_{14}, N_{15}, N_{20}, N_{23}, N_{26}, N_{30}\}$
\mathcal{A}_5	$\mathcal{A} \cup \{N_{19}\}$	$\{N_1, N_2, N_3, N_6, N_9, N_{14}, N_{19}, N_{20}, N_{23}, N_{26}, N_{30}\}$
\mathcal{A}_6	$\mathcal{A} \cup \{N_{31}\}$	$\{N_1, N_2, N_3, N_6, N_9, N_{14}, N_{20}, N_{23}, N_{26}, N_{30}, N_{31}\}$

Theorem 3. Let $P_1, P_2, \dots, P_6, i = 1, 2, \dots, 6$ be the vertices of 6-gon determining by (6,2)-arc C . If the algorithm is applied to the points on the diagonals $P_i P_{i+3}, i=1, 2, 3$ of 6-gon, the remaining point set forms a complete (16,4)-arc.

Proof. We consider $P_1, P_2, \dots, P_6, i = 1, 2, \dots, 6$ as the vertices of 6-gon determining by (6,2)-arc C , there are the remaining 16 points in $PG(2,5)$. It is easily seen that the remaining 16 points construct complete (16,4)-arc by applying algorithm.

From this point onward, this complete (16,4)-arc will be denoted by D .

Theorem 4. There is an affine plane determined by the common points of (16,4)-arc D and Desargues configuration \mathcal{A} in $PG(2,5)$.

Proof. Since $PG(2,5)$ is Desarguesian, it applies to all Desargues configurations. For example, we consider Desargues configuration $\mathcal{A} = \{N_1, N_2, N_3, N_6, N_9, N_{14}, N_{20}, N_{23}, N_{26}, N_{30}\}$ and the complete (16,4)-arc $D = \{N_1, N_5, N_7, N_9, N_{13}, N_{14}, N_{17}, N_{18}, N_{21}, N_{22}, N_{23}, N_{24}, N_{25}, N_{27}, N_{28}, N_{29}\}$ from Theorem 3. From this, the intersection set of \mathcal{A} and D is $\{N_1, N_9, N_{14}, N_{23}\}$. If we define the set of points as $\{N_1, N_9, N_{14}, N_{23}\}$, the set of lines as $\{N_1 N_9, N_9 N_{23}, N_1 N_{14}, N_{14} N_{23}, N_1 N_{23}, N_9 N_{14}\}$, and the incidence relation \circ as every point being on the line that contains it, the geometric structure (N, D, \circ) is an affine plane.

6. CONCLUSION

In this work, it is determined that some arcs and geometric structures in $PG(2,5)$ by giving the algorithm implemented in C#. The following conclusions are found:

1. In $PG(2,5)$, there is exactly one (6,2)-arc that does not contain any common points with the (10,3)-arc determined by each Desargues configuration.
2. In $PG(2,5)$, there are six different complete (11,3)-arcs containing each Desargues configuration.

3. In $PG(2,5)$, by applying the algorithm to $(6,2)$ -arcs that do not intersect with the Desargues configuration, a $(16,4)$ -arc is obtained.
4. An affine plane can be defined with the intersection points of the obtained $(16,4)$ -arc D and the Desargues configuration \mathcal{A} .

These findings provide significant insights into the relationships between Desargues configurations and arcs, enhancing our understanding of their roles in $PG(2,5)$.

CONFLICT OF INTEREST

The author(s) stated that there are no conflicts of interest regarding the publication of this article.

CRedit AUTHOR STATEMENT

Elif Altıntaş Kahrıman: Methodology, Formal analysis, Investigation, Resources, Writing – Original Draft, Writing – Review & Editing, Visualization, **Ayşe Bayar:** Conceptualization, Methodology, Validation, Formal analysis, Resources, Writing – Review & Editing, Visualization

REFERENCES

- [1] Hirschfeld JWP, Thas JA. General Galois Geometries, Springer Monographs in Mathematics. Springer- Verlag London, 2016.
- [2] Bayar A, Akca Z, Altıntaş E, Ekmekci S. On the complete arcs containing the quadrangles constructing the Fano planes of the left near field plane of order 9. New Trends in Mathematical Science. 2016, 4(4), 266-266.
- [3] Ekmekci S, Bayar A, Altıntaş E, Akca Z. On the Complete $(k,2)$ - Arcs of the Hall Plane of Order 9. International Journal of Advanced Research in Computer Science and Software Engineering. 2016, 6 (10), 282-288.
- [4] Akca Z, Ekmekci S, Bayar A. On Fano Configurations of the Left Hall Plane of order 9. Konuralp journal of mathematics. 2016, 4 (2), 116-123.
- [5] Akca Z, Altıntaş A. A Note on Fano Configurations in the Projective Space $PG(5,2)$, Konuralp Journal of Mathematics. 2021, 9(1), 190-192.
- [6] Akca Z. A numerical computation of $(k, 3)$ -arcs in the left semifield plane order 9, International Electronic Journal of Geometry. 2011, 4(2), 13-21.
- [7] Akca Z, Günaltılı I On the $(k, 3)$ - arcs of $CPG(2,25,5)$, Anadolu University Journal of Science and Technology-B Theoretical Sciences. 2012, 1(0), 21-27.
- [8] Qassim BA. The construction for the arcs $(8,4)$ -from the two arcs $(7,4)$ -in $PG(2,q)$, $q=5$. J. Phys.: Conf. Ser. 2020, 1664012039.
- [9] Hirschfeld JWP, Thas JA. General Galois Geometries, The Charendon Press, Oxford, 1991.
- [10] Hirschfeld JWP, Voloch JF. Group-arcs of prime order on cubic curves, Finite Geometry and Combinatorics, 2015, 191, 177-185.

- [11] Hirschfeld JWP. Projective Geometries over Finite Fields, Oxford Mathematical Monographs, The Clarendon Press Oxford University Press, New York, second edition, 1998.
- [12] Hall M. Projective planes. Trans. Am. Math. Soc. 1943, 54, 229-277 .
- [13] Hall M, Swift Jr, J.D, Killgrove R. On projective planes of order nine. Math. Tables and Other Aids Comp. 1959, 13, 233-246 .
- [14] Pichanick EVD, Hirschfeld JWP. Bounds for arcs of arbitrary degree in finite Desarguesian Planes. Journal of Combinatorial Designs. 2016, 24(4), 184-196.
- [15] Altıntaş E, Bayar A. Complete $(k,2)$ -Arcs in the Projective Plane Order 5. Hagia Sophia Journal of Geometry. 2023, 5(1), 11-14.